Experimental and finite element analysis of mechano-electrochemical effects in intervertebral disc biomechanics

This thesis is submitted to the

Department of Biomedical Engineering

at

the University of Strathclyde

by

Mark D. Farrell

in partial fulfilment of the requirements for the degree of

Doctor of Philosophy

2013

Declaration

This thesis is the result of the author's original work. It has been composed by the author and has not been previously submitted for examination which has led to the award of a degree.

The copyright of this thesis belongs to the author under the terms of the United Kingdom Copyright Acts as qualified by the University of Strathclyde regulation 3.50. Due acknowledgement must always be made of the use of any material contained in, or derived from, this thesis.

Signed:
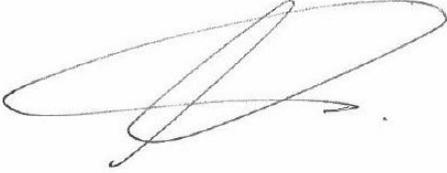
Date: 19th September 2013

Acknowledgements

Contents

List of figures

List of tables

Abstract

Lower back pain places an enormous economic burden on society and health authorities as it affects up to 80% of the population and has been attributed to intervertebral disc injury as well as the degenerative adaptations which occur with advancing age. Much of our understanding of disc mechanics comes from mathematical and finite element models; however, there is a lack of empirical data which is required for model validation. Additionally, the influence of mechano-electrochemical phenomena on fundamental mechanical properties such as permeability and Poisson's ratio is still not fully understood. Therefore, this thesis aimed to investigate the influence of such phenomena on disc mechanics whilst providing a comparison between multiphasic FE models and experimental data.

Direct permeation experiments found that fluid velocity may be augmented through the nucleus pulposus via ionic osmotic pressure gradients which consist of fixed charge, mobile ion and electrical potential gradients. A novel method to fully characterise, for the first time, the Poisson's ratio of the disc was developed. Poisson's ratio of the nucleus pulposus was found to be strain dependent and lower than previously thought, whilst solid matrix viscoelasticity may influence disc mechanics at high strain-rates. Confined compression experiments on the degenerate human nucleus pulposus found that the solid matrix bears the majority of load under axial compression due to the depletion of proteoglycans and the consequential reduction in mechano-electrochemical effects in this tissue. Poor agreement with biphasic theory may provide evidence of the degenerate nucleus pulposus exhibiting a heterogeneous structure and a dual permeability phase.

Multiphasic models were developed and compared to experimental data. Differences were found between biphasic and triphasic models which resulted in varying agreement with experimental data thus the correct selection of numerical framework was found to be crucial when investigating disc mechanics.

The data presented in this thesis are important for informing our overall understanding of disc mechanics, aiding the development future models as well as providing a benchmark for potential replacement materials to be critiqued against, particularly in terms of permeability and fluid pressurisation which are crucial to the load bearing capacity of the tissue.

Publications

I.   Farrell, M.D and Riches, P.E. On the Poisson's Ratio of the Nucleus Pulposus. Journal of Biomechanical Engineering, 2013. DOI: 10.1115/1.4025180.

II. Farrell, M.D. and Riches, P.E. Ionic osmotic effects increase fluid flow during permeation tests. Journal of Mechanics in Medicine and Biology, 12(4), 2012.

III. Farrell, M.D. and Riches, P.E. The Poisson's ratio of the nucleus pulposus is strain-dependent. Journal of Biomechanics, 45(S1), 2012.

IV. Farrell, M.D. and Riches, P.E. Poisson's ratio of nucleus pulposus tissue: Comparison of experimental results with a biphasic poroviscoelastic finite element model. EUROMECH534, 2012.

V.   Farrell, M.D. and Riches, P.E. The apparent permeability of the nucleus pulposus is increased by electrochemical effects. Proceeding from the International Society of Biomechanics, 2011.

1. Introduction

Lower back pain (LBP) is a major public health problem. It has been reported that up to 80% of the population will experience LBP during their lifetime (Freburger et al., 2009) with around 10% of sufferers considered to be chronically disabled (Urban and Roberts, 2003). This places an enormous economic burden on society as well as medical services.

LBP is a major cause for disability and work loss, and instances have increased more rapidly over the past 25 years than any other form of incapacity in the UK (Maniadakis and Gray, 2000). The direct cost of health care in the UK as a result of LBP in 1998 was £1.6 billion, however, when the added burden of informal care and losses due to work absenteeism are considered, the total cost was some £10.7 billion (Maniadakis and Gray, 2000). In the US, suggestions of the total economic burden of LBP vary greatly with figures ranging from $19.6 to $118.8 billion (Dagenais et al., 2008). Although it is extremely difficult to conclude the total economic burden of LBP, it remains a huge socio-economic burden, and despite technological advances it appears to be worsening (Dagenais et al., 2008).

The vertebral column consists of 24 articulating vertebrae which are separated by intervertebral discs (IVDs) allowing flexibility to the spine. The column is generally regarded as being composed of five different areas from the head downward known as the cervical, thoracic, lumbar, sacral and coccygeal regions (Figure 1.1). The lumbar spine is situated above the sacrum and is considered the lower back region. It consists of five vertebral bodies and adjacent IVD's which withstand the highest

loads of the spine. A number of studies have shown a relationship between some types of LBP and IVD degeneration (Borenstein et al., 2001, Jensen et al., 1994, MacGregor et al., 2004, Luoma et al., 2000) with the lumbar region the most frequent source due to the significant mechanical loads subjected to this area (Adams and Dolan, 2005, Andersson, 1999). The IVD's are under constant mechanical stress and alteration to the physiochemical properties of the discs can result in LBP. For example, a reduction in the discs load bearing capacity as a result of degeneration can cause a transfer of load to the surrounding joints and ligaments, while some regions of the disc become innervated and can become painful (Freemont et al., 1997).

Chapter 2 provides a general review of the existing literature on IVD biomechanics with particular interest paid to the research streams pertinent to the experimental and numerical chapters of this thesis. This includes an overview of current knowledge of the IVD's mechanical and biological function with a view to gaining insight to discogenic pain. The general structure of the disc is first considered, before discussing the main mechanical and biological characteristics appropriate to this thesis such as permeability, osmotic pressure and Poisson's ratio. Finally, mathematical and finite element modelling of the disc is considered with reference to the aforementioned disc properties and includes an overview of disc function, structure, constituents, biology and in vivo loading conditions.

Each analysis chapter has been written in manuscript format consisting of a detailed introduction, methods, results and discussion. This layout has been chosen to allow each chapter to be read both holistically and as an isolated piece of work. The body

of this thesis consists of three experimental chapters; two of which are complimented with the related numerical analyses.

An overall discussion, limitations and recommendations chapter is then presented which considers all chapters as a unified body of work.
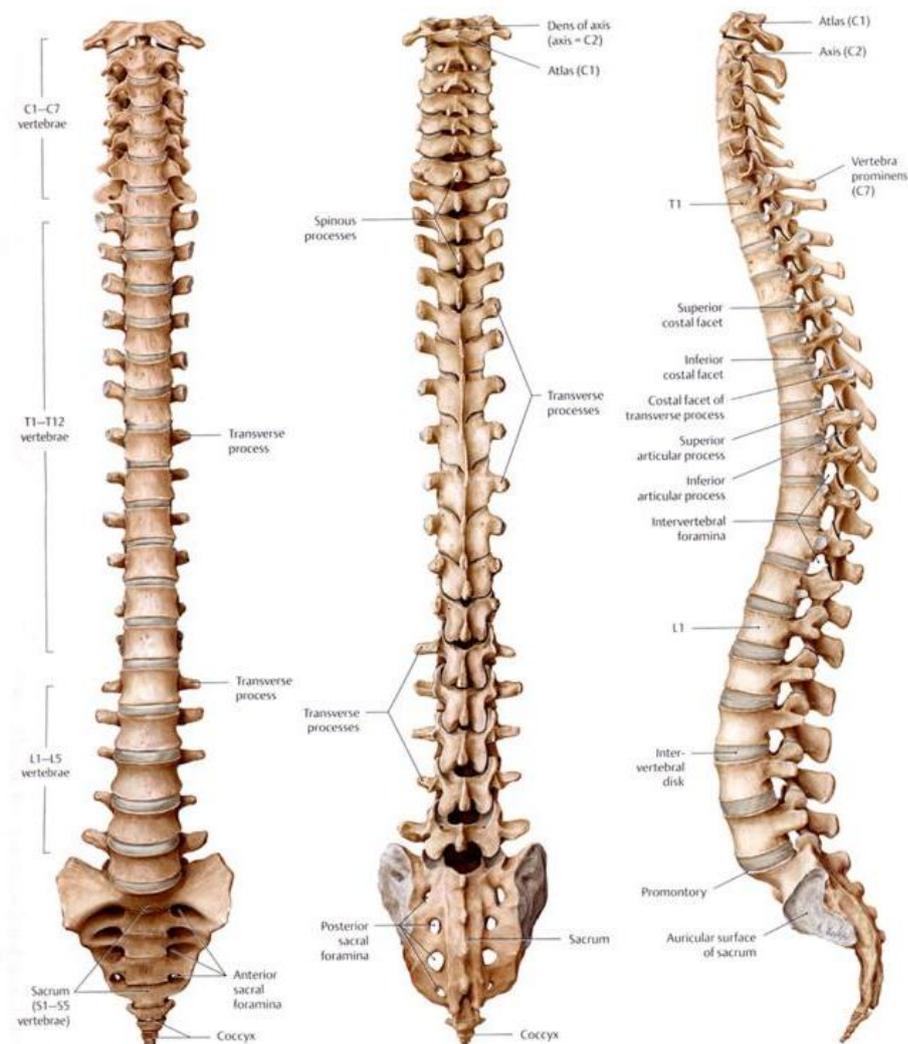
Figure 1.1 The spinal column. Taken from http://3.bp.blogspot.com/-T4lF8OsVyiY/TZSk6rNyHFI/AAAAAAAAABCw/h72rBFU40/s1600/spine_trio_vw1.jpg

2. Literature review

2.1. The intervertebral disc

The intervertebral disc (IVD) consists of a central gel-like region known as the nucleus pulposus (NP); an outer annulus fibrosus (AF) which surrounds the NP (Figure 2.1) and the cartilage end-plates (CEPs) which are located on the superior and inferior surfaces between the disc and the vertebral bodies. In the lumbar spine the discs are approximately 7 to 10 mm thick, ~40 mm in diameter and occupy approximately one third of the height of the spinal column (Raj, 2008). The lumbar disc is generally wedge shaped, with the posterior region being thinnest and the anterior being thickest which is a result of the curvature of the spine (Roberts et al., 1989). Constituents of the disc vary dramatically between regions resulting in the disc's anisotropic structure (Horner et al., 2002) and mechanical behaviour. The disc undergoes degenerative adaptations with advancing age, a phenomenon which often starts earlier than that experienced by other musculoskeletal tissues, and often leads to lower back pain (LBP) (Urban and Roberts, 2003).

2.2. The Nucleus Pulposus (NP)

The NP is the central region of the disc and in the healthy state is a highly hydrated gel-like material. This gelatinous structure contains randomly organised collagen fibres (Inoue, 1981), radially orientated elastic fibres (Yu et al., 2002) and sparsely located chondrocytes, all of which are embedded in a proteoglycan (PG) rich matrix. PG content is highest in the NP region of the disc (Urban et al., 2000) and accounts for 30-35% of the dry weight (Perie et al., 2006a, Perie et al., 2006b, Johannessen

and Elliott, 2005). The tissue exhibits an extremely high water content accounting for approximately 70-90% of the overall weight (Urban and McMullin, 1988, Iatridis et al., 1997b, Roberts et al., 1989, Urban et al., 1979). Both PG and water content have been found to decrease with increasing age and with the advancement of degeneration (Iatridis et al., 1997a, Johannessen and Elliott, 2005, Urban et al., 1978, Urban and McMullin, 1988). Collagen content in the NP is predominantly type II (~85%) with a gradual increase in type I in the areas approaching the AF (Eyre and Muir, 1976).

2.2.1. The Annulus Fibrosus (AF)

The AF laterally confines the NP and consists of concentric sheets of lamellae. In the AF, collagen has a high level of structural organisation, with fibre orientation alternating between lamellae at angles of $\pm 60^{o}$ (Houben et al., 1997) (Figure 2.1). The biochemical composition of the AF is dependent on radial site, with the highest collagen content found in the outer AF (OAF), and the highest PG, and water content found in the inner AF (IAF). The high content of type I collagen in the AF gives the
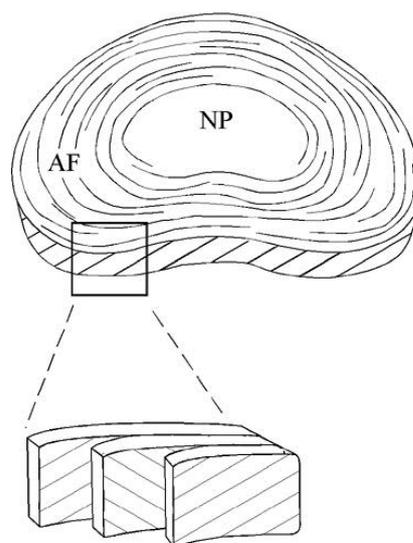
Figure 2.1 Image illustrating the structure of the AF and the alternating fibre direction. Image taken from http://www.uphs.upenn.edu/orl/research/bioengineering/afstructure.jpg.

tissue its high tensile strength (Ebara et al., 1996) which allows it to confine the NP during compression. Elastic fibres lie between the lamellae which may help the disc to return to its natural shape after deformation (Urban and Roberts, 2003). They may also help to bind the sheets of lamellae together, as fibres pass radially from one lamella to the next (Yu et al., 2002). The cells in the AF, and in particular the OAF, tend to be fibroblast-like and arranged parallel to collagen fibres. Towards the IAF, the cells appear to be more oval (Urban and Roberts, 2003).

2.2.2. The Cartilage Endplate (CEP)

The cartilage endplates (CEPs) are located between the vertebral bodies and the IVD's. They consist of layers of hyaline cartilage and are approximately 0.6mm thick with the thinnest region adjacent to the NP. It is thought that the CEPs play an important role in nutrient transport to the disc as variation in permeability and porosity may reduce cell function (Rodriguez et al., 2011). It is consequently of great interest when studying degeneration and the causes of LBP (Roberts et al., 1989). The CEPs are located on both the superior and inferior surfaces of the disc and are composed of a PG gel and a collagen fibre network (Roberts et al., 1989). An inhomogeneous constituent organisation exists with an increase in collagen content and decrease in PG content radially towards the periphery and axially towards the vertebral body (Roberts et al., 1989). PG content of the healthy CEP is between 10% and 30% of dry weight (Roberts et al., 1989) with this value found to decrease with advancing age and degeneration (Antoniou et al., 1996). Collagen content in the CEPs is almost entirely type II and has been found to be between 15% and 20% of the dry weight (Roberts et al., 1989). Collagen fibres in the CEP are a continuation of

the fibres found in both the NP and AF, and run both axially and radially (Roberts et al., 1989).

2.3. IVD Constituents

2.3.1. Collagen

Collagen is the most abundant protein in the body (Eyre, 1980). It is the basic structural element for soft tissue and contributes to the material's mechanical properties. The most important mechanical property of a collagen fibre is its ability to withstand tensile forces. Soft tissues, which are abundant in collagen, demonstrate extremely high tensile stiffness; for example, tendons. However, due to their large length to thickness ratio they are prone to buckling under compressive force and consequently offer little resistance to this form of loading.

The main types of collagen found in the disc are type I and type II. Type I is the most abundant protein in the body and exhibits high tensile strength. Diameters of fibre bundles vary from 2 to 10µm (Mow et al., 1991) and are commonly found in areas of the disc which experience high tensile stresses. Type II fibres are found in articular cartilage (AC), the IVD and sternal cartilage, i.e. areas under high compressive stress. Estimated fibre diameters vary from 20 to 200nm (Mow et al., 1991). In addition, an array of different collagen types (III, VI, IX, X) can be found in minor amounts in IVD tissue (Roberts et al., 1991).
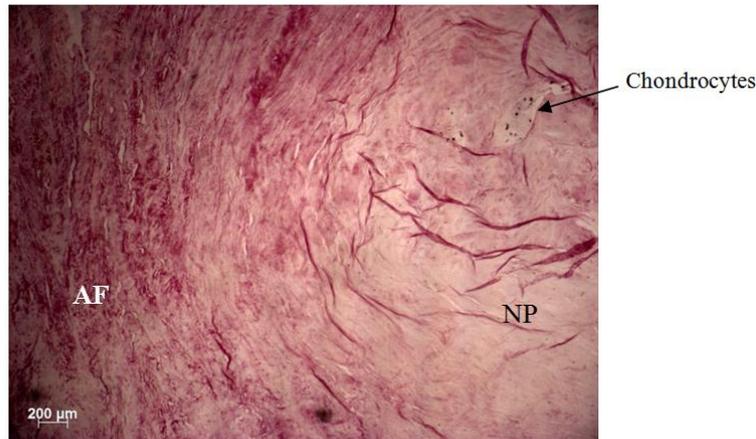
Figure 2.2 Sagittal section of bovine tail IVD stained for collagen (unpublished work by the author).

Collagen fibers have been reported to demonstrate intrinsic viscoelasticity which may significantly affect IVD mechanics. Shen et al., (2011) applied a Maxwell-Weichert model to experimental data obtained from stress relaxation experiments on individual collagen fibrils. The fibrils were shown to exhibit an elastic modulus of 123 ± 46 MPa whilst the time-dependent behaviour demonstrated a fast-time response of 7 ± 2 s and a slow time response of 102 ± 5s. Shen et al., (2011) proposed that the mechanism by which individual fibrils may demonstrate viscoelasticity is through molecular rearrangement of collagen molecules and water molecules in reaction to an applied stress.

2.3.2. Proteoglycan (PG)

The high concentration of proteoglycan (PG) in the disc matrix is crucial to the biomechanical and physiochemical properties of the tissue. A PG is a large protein-polysaccharide molecule composed of one or more glycosaminoglycans (GAGs) which are attached to a core protein (Muir, 1983). A GAG is a hetropolymer of

repeating disaccharide sequences which contains hexosamine and hexuranic acid or hexose (Carney and Muir, 1988). The primary type of PG in the disc is aggrecan, whilst other forms such as biglycan and decorin may also be present. Aggrecan consists of keratan sulphate (KS) and chondroitin sulphate (CS) chains which are covalently bonded to a protein core which, in turn, is composed of three globular regions known as keratan sulphate-rich and chondroitin-rich regions (Nordin and Frankel, 2001). Each KS chain is made up of 13 disaccharide units, whereas each CS chain is made up of 25 to 30 disaccharide units (Muir, 1983). PGs exhibit a high negative charge which is generally quantified in terms of their negative fixed charge density (FCD) which has been shown to be between 0.1 and 0.5 milliequivalents per gram of water (Urban et al., 1979). The basic functional importance of PG to the disc is their ability to restrict fluid loss from the disc during compression, and to encourage the reimbibition of fluid during periods of reduced loading due to their hydrophilic nature. PG distribution is generally considered to be homogenous throughout the NP, however, slight axial variation has been observed with more PG found in the mid-plane of disc with a slight reduction towards to the disc-CEP boundary (Iatridis et al., 2007).
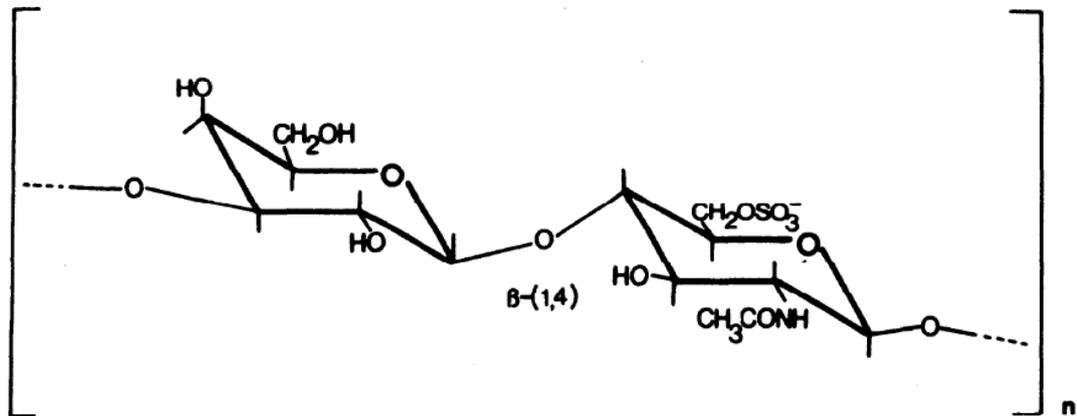
Figure 2.3 Structure of repeating disaccharide unit of keratan sulphate (Carney and Muir, 1988).

Proteoglycan Type	Mol Wt	Interaction with HA	Mol Wt of Core Protein
Aggregating CS-rich	3.5×10^6	+	>200,000
Aggregating KS-rich	1.3×10^6	+	~95,000
High mol wt, nonaggregating	$<1.3 \times 10^6$	–	Not determined
Low molecular wt, nonaggregating	76,000	–	42,300
Self-associating DS-PG	200,000	–	45,000 (found as dimer)
Nonassociating DS-PG	80,000–120,000	–	45,000
Type IX collagen	115,000	Not known	68,000

Table 2.1 Properties of the major cartilage proteoglycans. CS, chondroitin sulphate. DS-PG, dermatan sulphate proteoglycan. KS, keratan sulphate. HA, hyaluronic acid. Molecular weights are relative to collagenous standards (Carney and Muir, 1988).

2.3.3. Water

Approximately 70% of the total volume of a healthy adult lumbar disc is composed of water (Scott et al., 1994). Water content in the disc is split into two compartments; intrafibrillar (IF) and extrafibrillar (EF), with a small amount of water located between collagen fibres (IF) and the rest as EF (Maroudas and Bannon, 1981). The level of hydration is an important factor in controlling the chemical and mechanical functioning of the disc. Disc fluid contains numerous free mobile cations (for example, Na^+, K^+, Ca^{2+}) which are thought to play an important role in the mechanical response of the tissue (Lai et al., 1991, Gu et al., 1998). Fluid is also essential for the transport of nutrients, due to the avascular nature of the IVD, with the tissue's hydraulic permeability playing an important factor. The flow of fluid to and from the disc permits the convective and diffusive transport of gas, nutrients and waste products to and from disc cells. The interaction between water, PG's and the collagen fibres via the Donnan osmotic pressure (section 2.3.2) has an important function in controlling the structure and swelling properties of the ECM (Maroudas, 1975). When disc tissue is loaded in compression, most of the water is free to move interstitially which is important for the control of the mechanical behaviour of the disc.

2.3.4. Other constituents

2.3.4.1.   *Disc cells*

The sparsely distributed chondrocyte-like disc cells found in the NP are rounded and enveloped within a lacuna (Figure 2.4), whilst those found in the AF have an elongated fibroblastic appearance and are orientated in the same axis as the collagen

fibres (Roberts et al., 1991). Disc cells account for less than 10% of the tissue volume in AC (Stockwell, 1979) yet are responsible for the production and maintenance of the organic component of the ECM (Muir, 1983). Somewhat surprisingly, however, very little is known of the phenotype of the cells in either normal or degenerate discs (Sive et al., 2002). Cultured NP cells removed from both animal (Poiraudeau et al., 1999) and human discs (Chelberg et al., 1995) demonstrate expression of type II collagen, as well as both keratan and chondroitin sulphate.

2.3.4.2. *Elastin & other minor constituents*

The main macromolecular components of the disc are collagen (type I and II) and the proteoglycan, aggrecan. However, there are many other minor components which aid the function of the disc, such as; lumican, decorin, biglycan and minor collagens (Roberts et al., 1991). There also exists an elastic fibre organisation in both the NP and AC which is thought to aid the mechanical recovery of the tissue (Yu et al., 2002, Barbir et al., 2010). Elastic tissues in the body owe their ability to resume original geometry after deformation to the protein elastin. Unlike the relatively inextensible collagen fibre, the elastic fibre occurs in a pre-contracted state but has the potential to extend to twice its original length (Bailey, 1978). Elastic fibres, have been found to demonstrate an organised structure in the IVD; in the NP, they have been found to run vertically and perpendicularly to the CEP in the superficial zones and radially towards the AF in the inner zone (Yu et al., 2002) (Figure 2.5).
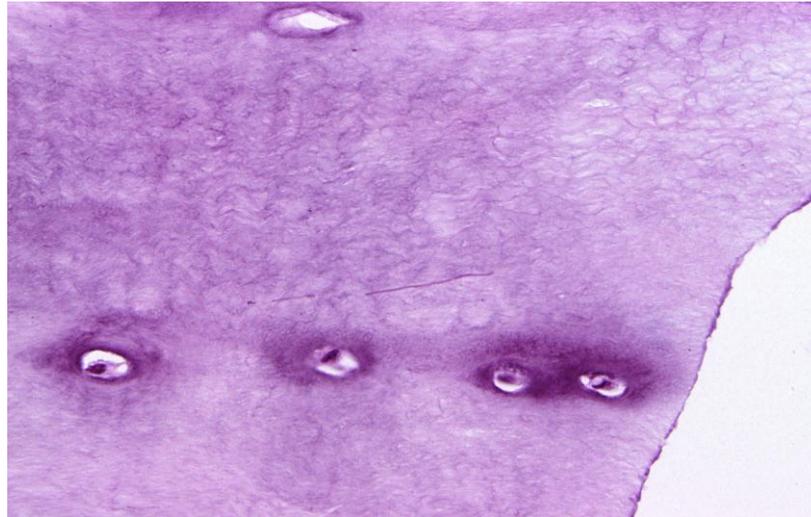
Figure 2.4 Chondrocytes in the bovine tail NP (unpublished work by the author).
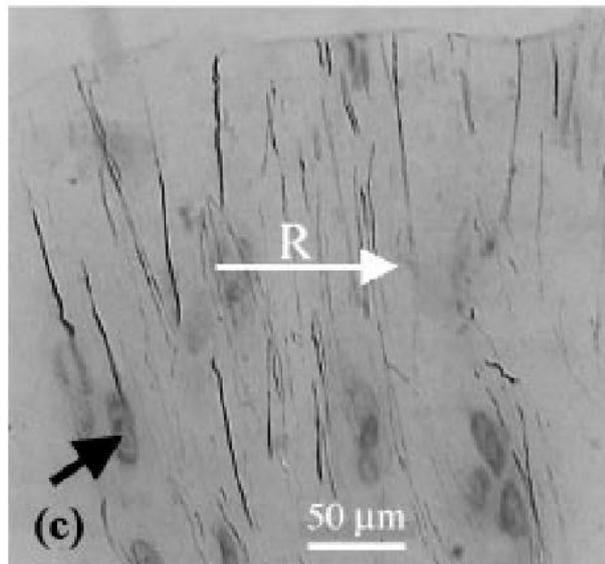
Figure 2.5 Elastic fibres in the outer zones of the bovine tail NP (adjacent to the CEP) indicated by black arrow. R indicates the radial direction (Yu et al., 2002).

2.4. Disc Mechanics

In order to further our understanding of the mechanical consequences of disc injury and degeneration, as well as to advance constitutive modelling of the disc, an understanding of disc mechanics is essential. Mechanical tests on hydrated soft tissues such as IVD and AC elucidate the essential characteristics and material properties which enable these materials to function within the body, as well as shed light on possible problems associated with injury and degeneration.

2.4.1. Disc loading

In vivo, the disc is subjected to constant non-zero mechanical stress. Primarily, this is a compressive loading mechanism which generates an increased fluid pressure within the disc. Nachemson (1960) investigated the lumbar IVD intradiscal pressure as a result of in vitro loading reporting that the stress state in the NP is hydrostatic and is generally 1.3 to 1.5 times that of the applied stress. McNally and Adams (1992) also suggested that the hydrostatic pressure in the NP is close to being proportional to the applied stress. An applied mechanical stress is counteracted by the hydrostatic pressure, whilst a pressure gradient between the disc and the vertebral fluid results in fluid flow from the disc through the CEP (Adams et al., 1996, Brinckmann et al., 1983, Oloyede et al., 1998, Riches et al., 2002). This phenomenon is dependent on a number of factors which govern the rate of fluid flux; the tissue's intrinsic hydraulic permeability, fluid pressure and osmotic pressure gradients. Tissue permeability in the disc is extremely low, which results in a slow rate of fluid exudation during compression, resulting in only a gradual reduction in pressure (Lu et al., 1998, Oloyede et al., 1998, Riches et al., 2002, Heneghan and Riches, 2008a). Oloyede et

al.(1998) investigated the effect of short-term static axial-loading on the response of the IVD. Figure 2.6 illustrates the typical pore pressure over time when subjected to a constant external stress of 1.9MPa. It can be seen that the maximum pore pressure was created within the first hour of loading before gradually reducing to almost zero.
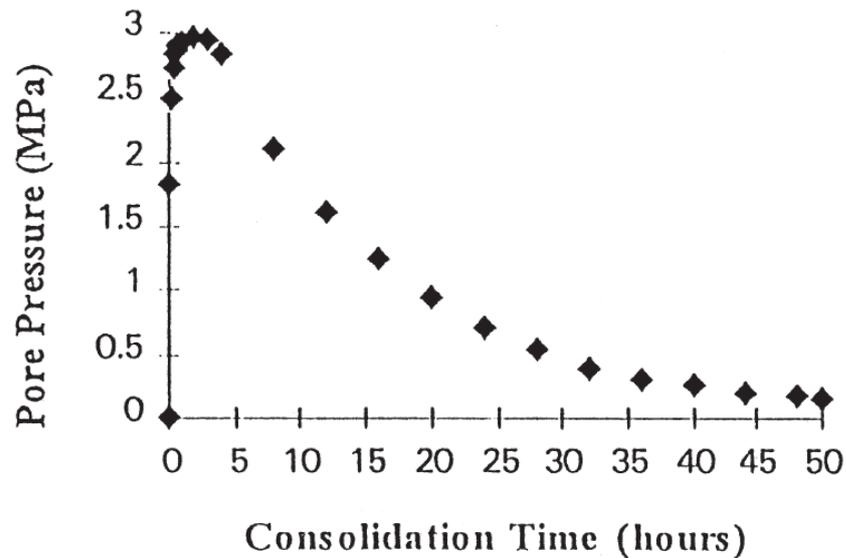
Figure 2.6 Pore pressure under a static compressive stress of 1.9 MPa (Oloyede et al., 1998).

The application of compressive load to a motion segment causes the CEP to bulge axially, reducing stress on the disc (Brinckmann et al., 1983). Additionally, the increase in NP pressure during compression can result in the AF bulging radially, with the lamellae fibres extending: the diameter of the outer annulus fibrosus (OAF) can extend by as much as 13% in the healthy disc (McNally and Adams, 1992).When the applied load is removed from the disc, the osmotic pressure re-imbibes fluid and the bulging of the disc recovers. Fluid is also significantly contributed to by the hydrophilic nature of the PGs. However, the recovery of the solid matrix, attributed,

in part to solid matrix viscoelasticity, may also play a role in disc recovery after deformation.

A variation in intradiscal pressure with posture has been documented in a number of studies (Nachemson and Elfstrom, 1970, Sato et al., 1999, Wilke et al., 1999). It was found that the lowest intradiscal pressure was found when in the supine position and the highest found when bending forward whilst lifting a weight. Additionally, it has been suggested that bending forward, even without additional weight, can increase intradiscal pressure and apply enough tensile stress to the posterior AF so that it is at risk of failure (Hickey and Hukins, 1980).

In vivo, the disc experiences global compressive strains of up to 20% (Botsford et al., 1994), however, mathematical models have suggested that significant strain gradients (up to 70%) occur with areas of high localised strain near the boundary of the applied load (Holmes and Mow, 1990, Mow et al., 1980, Riches et al., 2002). As yet, there is no experimental evidence to verify the existence of strain gradients; however, the possible ramifications of such a localised deformation may impact many of the mechano-biological functions of the tissue such as matrix formation and restoration.

2.4.2. Diurnal changes

The disc exhibits its highest hydration state in the morning due to ~8h of reduced loading at night which allows for fluid reimbibition. The loss in one's height throughout the day is generally considered to be a direct result of fluid exudation from the discs which are under constant compressive load throughout the day. Botsford et al. (1994) found that the average diurnal disc volume decrease in the lower lumbar disc was 16%, and Tyrell et al. (1985) found that throughout a day of

non-strenuous activity, subjects lost an average of 1.1% of their height, with 50% of the loss occurring in the first hour after rising and 83% lost in the first 3.25 hours. Pollock et al., (2008) examined the effect of body weight unloading on spinal height during 1h walking on a treadmill and found that the length of the spine increased. A more recent study investigated the effect of load carriage on spinal compression (Chow et al., 2011), where subjects were tasked with carrying a load equivalent to 15% of their body weight either anteriorly or posteriorly for 20 min followed by 10 min of unloading. They found the magnitude of spinal compression was dependent on loading duration, with anterior loading resulting in more compression than posterior loading whilst there was only a mild recovery after a period of unloading (Figure 2.7).
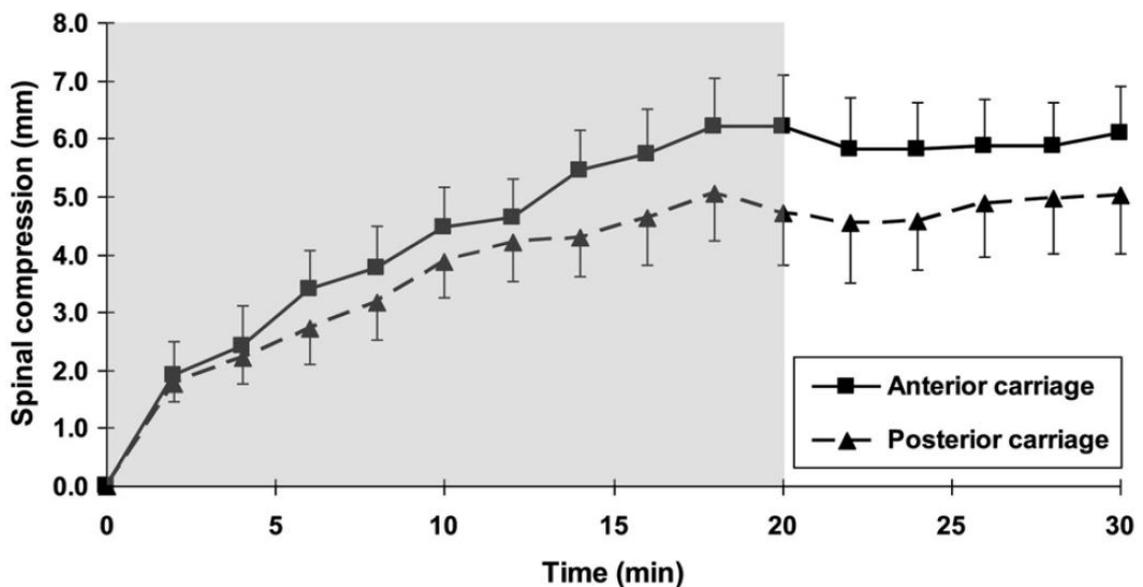
Figure 2.7 Changes in spinal compression for anterior and posterior carriages over time. The shaded area indicates the period of load whilst the un-shaded area indicates a period on unloading (Chow et al., 2011).

2.4.3. Osmotic pressure

The disc exhibits a high concentration of fixed negative charges as a result of the sulfate and carboxyl charge groups on the CS and KS chains dissociating in solution at physiological pH (Nordin and Frankel, 2001). This negative fixed charge density (FCD) creates strong intramolecular and intermolecular charge repulsive forces. When the tissue is immersed in physiological saline, the sum of these forces is equivelent to the Donnan osmotic pressure (Buschmann and Grodzinsky, 1995, Donnan, 1924, Gu et al., 1998, Lai et al., 1991). In vivo, these repulsion forces serve to increase the stiffness of the tissue. The charged sulfate and carboxyl groups fixed along the PGs attract various ions in a bid to maintain electroneutrality, mainly Na^+, Ca^{2+} and Cl^-. When such a tissue is in contact with a monovalent salt solution, the diffusion of salt ions and the flow of fluid takes place between the tissue and the external solution until equilibrium is achieved.

The large molecular size of PGs restricts their movement with respect to the external solution and consequently, the tissue may be considered to be semi-permeable thus creating an environment where fluid exudation and imbibition occurs to balance osmotic stresses. Osmotic pressure allows the tissue to withstand compression as well as aid fluid transport and nutrition (Ferguson et al., 2004, Urban et al., 1979). During daily loading, the resultant hydrostatic pressure, 0.6 to <1.0MPa, is approximately three to five times greater than the counteracting osmotic swelling pressure, 0.15 to 0.2 MPa, resulting in fluid flow out of the disc (Ayotte et al., 2000). This fluid loss has been found to be greatest from the NP when compared to the AF (Adams and Hutton, 1983). It is generally agreed that the loss in one's height during daily activity can be attributed to the loss in volume of the IVD's. During the diurnal

cycle, the disc experiences reduced loading during rest periods which allows the disc to rehydrate due to osmotic gradients and consequently restores body height. The mechanism which allows this recovery has been suggested to include a direction dependent tissue permeability enabling fluid to be reimbibed more easily than it is lost (Ayotte et al., 2000, Ayotte et al., 2001, Riches et al., 2002).

There are three components which form the osmotic pressure: i) components due to Donnan osmotic effects, ii) component due to excluded effects and iii) the component due to the interactions between the charged ions and electrolyte. The ionic component of the osmotic pressure as an aggregate of components i) and iii) and is the main source of interest as it represents ~85% of the total pressure magnitude (Urban et al., 1979). The ionic effect can be negated by subjecting the tissue to a sufficiently hypertonic external solution (>3M NaCl). By increasing the concentration of the external solution, an increase in the negative chloride ions, Cl^-, results in a reduction in charge imbalance between the tissue and external solution. The consequence is a reduction in the Donnan osmotic pressure.

Figure 2.8 illustrates how the osmotic swelling pressure of disc and AC is affected by 0.15M and 1.5M NaCl, with much lower osmotic pressure present when subjected to the latter (Urban et al., 1979). Additionally, a significant reduction in NP compressive stiffness was observed when subjecting the tissue to 3M and 6.1M NaCl (Heneghan and Riches, 2008b) (Figure 2.9). The reduction in ionic osmotic pressure, π_{ionic}, with increasing NaCl concentration is in agreement with the fact that π_{ionic} relates to the effective fixed charge density, c^F ($mol.m^{-3}$), and the molar concentration of the external solution, $c*$ ($mEq.ml^{-1}$). However, in hypertonic NaCl bathing solutions, $c*$ is far greater than c^F, rendering π_{ionic} negligible (Lu et al.,

2004b). This allows π_{ionic} effects to be determined by comparing experimental results when the sample is tested in isotonic (~0.15M NaCl) and hypertonic (>>0.15 NaCl, e.g. 3M NaCl).
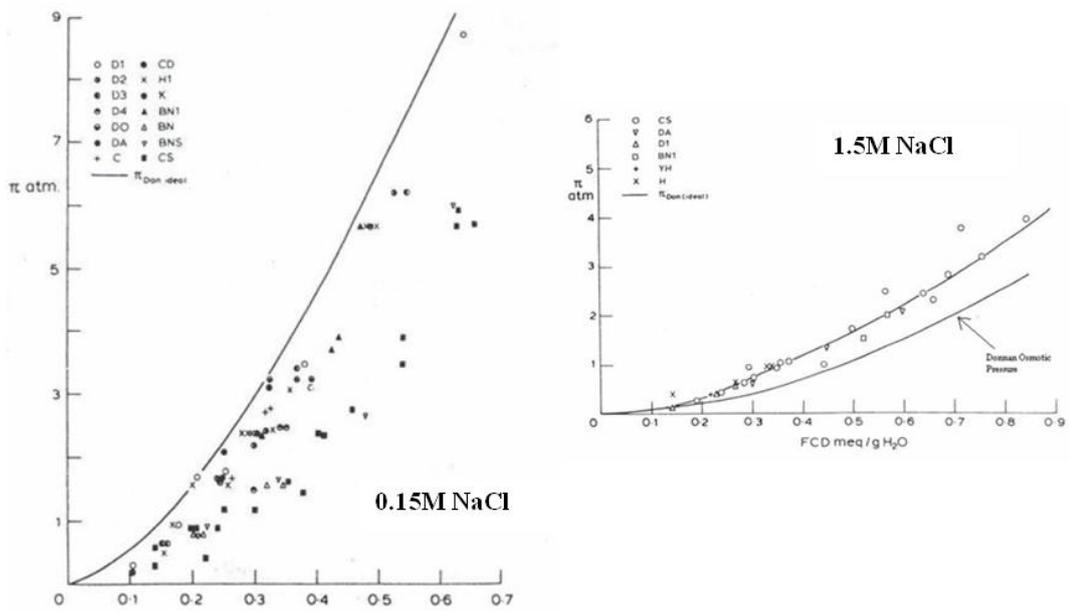
Figure 2.8 Osmotic pressure against fixed charge density for samples bathed in isotonic and hypertonic external solutions (Urban et al., 1979).
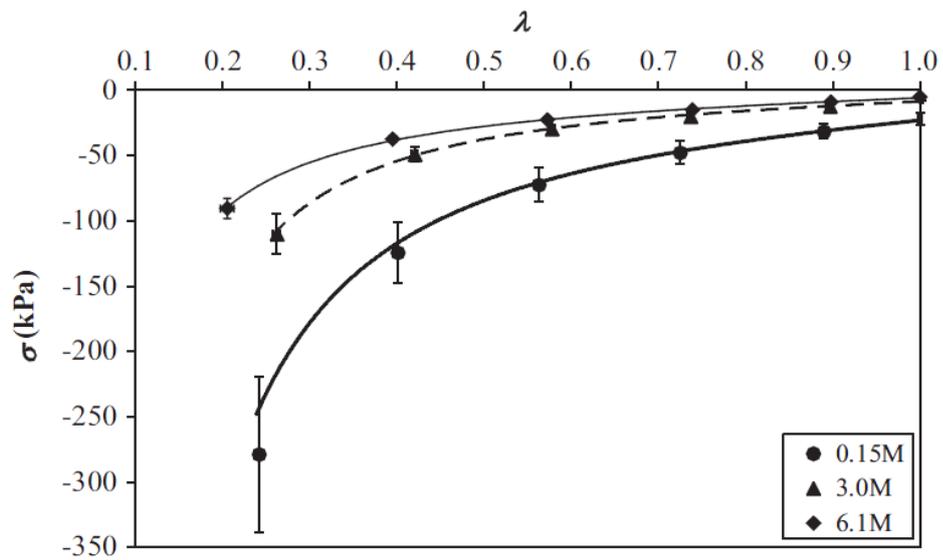
Figure 2.9 Plot of σ against λ for multiple strain samples (Heneghan and Riches, 2008b).

2.4.4. Hydraulic Permeability

The disc's intrinsic hydraulic permeability plays an important role in governing the mechanical response to applied stress. Disc tissue exhibits an extremely low permeability (Heneghan and Riches, 2008a) which allows it to maintain high fluid pressure when in compression (Lu et al., 1998, Mow et al., 1980, Riches et al., 2002). Darcy's Law defines permeability, k, as the constant of proportionality between the magnitude of the relative fluid velocity of solid and fluid, w, the dynamic viscosity, μ, and the pressure drop, P, over a given distance, x. Given by

$$w = \frac{-k}{\mu} \frac{\partial P}{\partial x} \qquad (2.1)$$

Within the disc, however, fluid flow is also governed by osmotic pressure, π, and was incorporated by Vignollet et al., (2010) via

$$w = \frac{-k}{\mu} \left(\frac{\partial P}{\partial x} - \frac{\partial \pi}{\partial x} \right) \qquad (2.2)$$

The hydraulic permeability, κ, is defined as

$$\kappa = \frac{k}{\mu} \qquad (2.3)$$

The tissue's intrinsic hydraulic permeability is governed by the fluid-solid constituent interactions. The NP exhibits a very low permeability and thus high frictional forces are created when a fluid is permeated through the solid matrix. Since the collagen network in the NP has a widely spaced architecture, it is the PGs that

contribute mostly to the tissue's low permeability due to their hydrophilic nature and bottlebrush structure creating a physical barrier. A low hydraulic permeability allows the tissue to maintain structural integrity during compression as it opposes fluid flow from the disc. Experimentally, the hydraulic permeability of a tissue sample can be determined via a direct permeation experiment (Figure 2.10) (Mansour and Mow, 1976, Heneghan and Riches, 2008a, Gu et al., 1999b).
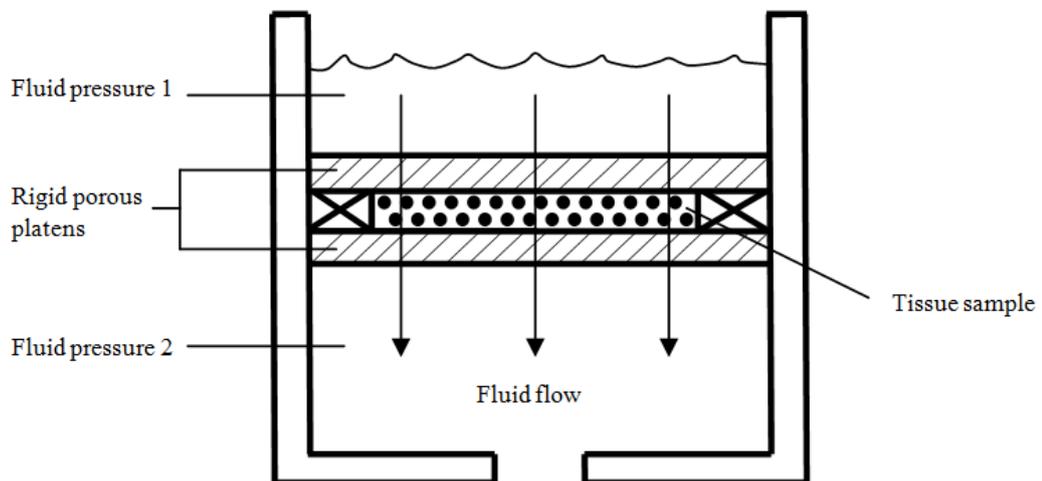
Figure 2.10 Experimental setup to measure the hydraulic permeability of a tissue sample. Involves applying a pressure gradient across the sample to induce fluid flow. k is calculated by applying Darcy's law to the experimental parameters.

One major flaw exists when conducting a direct permeation experiment as the one above; it assumes constant sample height throughout infusion. Flow induced deformation occurs when the flow of fluid through a tissue sample exerts a viscous drag on the solid matrix which directly affects the specimen thickness. An ideal

experimental configuration would involve the monitoring of specimen thickness during the infusion, however, this is extremely challenging.

A more common method to calculate the hydraulic permeability of cartilaginous tissue is by indirectly fitting a biphasic model to experimental data (Best et al., 1994, Drost et al., 1995, Ateshian et al., 1997, Houben et al., 1997, Chen et al., 2001, Johannessen and Elliott, 2005, Perie et al., 2005). The zero strain permeability can be determined from this technique; however, the accuracy of this approach depends on the suitability of the model and the ability of the numerical schemes to extract the relevant parameters (Riches, 2012).

2.4.5. Strain-dependent permeability

Flow induced deformation occurs when the fluid flowing through a soft tissue sample creates a drag force on the solid matrix. The strain-dependent permeability of both disc and AC is of importance as it results in an apparent direction-dependent resistance to flow which aids the reimbibition of fluid during periods of reduced loading (Ayotte et al., 2000, Riches et al., 2002, Heneghan and Riches, 2008a). The permeability of both NP (Heneghan and Riches, 2008a) and AC (Mansour and Mow, 1976) was found to decrease with increasing strain due to a compaction of the collagen network, resulting in a reduction of extrafibrillar space through which fluid can flow. This phenomenon has also been observed through mathematical modelling of the disc (Perie et al., 2005) and AC (Ateshian et al., 1997, Chen et al., 2001) which includes a strain-dependent permeability term.

Heneghan and Riches (2008a) investigated the effect of strain on the hydraulic permeability of bovine NP and found that the relationship is best described by the

equation of Holmes and Mow (1990), which is based on finite deformation theory and is given by:

$$k(\lambda) = k_0 \left(\frac{\lambda - 1 + \emptyset_0}{\emptyset_0}\right)^{\kappa} e^{[M(\lambda^2 - 1)/2]} \qquad (2.4)$$

where k_0 is the zero strain permeability, M, and κ are non-dimensional parameters relating k to λ, and $\emptyset$ is the tissue porosity; the subscript 0 indicates zero strain values.

2.4.6. Poisson's ratio

The nature of the NP is such that it is neither fully confined nor fully unconfined, as radial expansion is transferred to the AF during compression. Poisson's ratio is a material property which describes the relationship between axial and lateral strain and is a key parameter when modelling the NP in unconfined geometry (Figure 2.11).
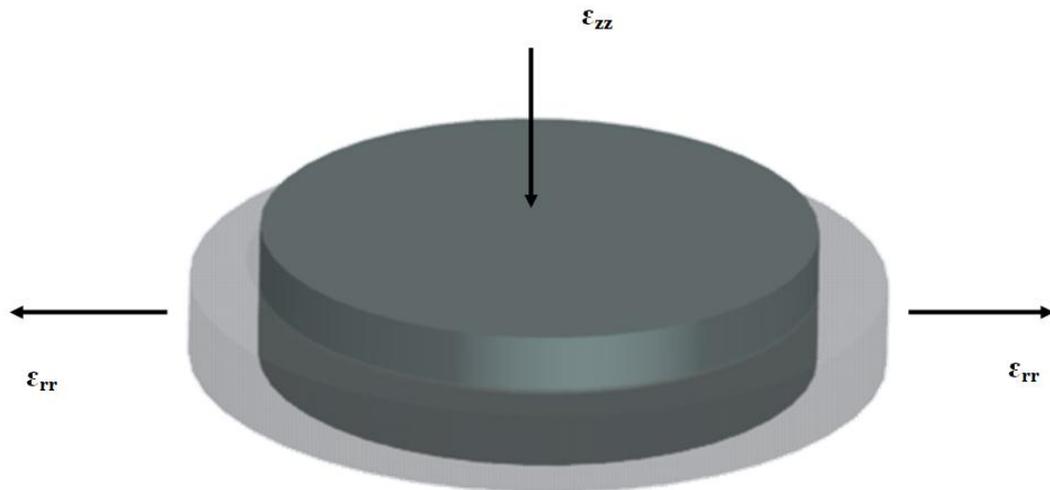
Figure 2.11 Poisson's ratio: relationship between axial strain, ε_{zz}, and resultant radial strain, ε_{rr}.

Poisson's ratio is defined as the negative of the ratio of radial strain to axial strain. It is negative to ensure that v is a positive number.

$$v = -\frac{\varepsilon_{rr}}{\varepsilon_{zz}} \qquad (2.5)$$

An incompressible material has $v = 0.5$. Values less than this imply a loss of volume with deformation. Values higher than this imply the opposite. With Poisson's ratio data, the aggregate modulus, H_A, which is a measure of stiffness in confined compression can be converted to Young's modulus, E, via

$$H_A = E(1 - v)/[(1 + v)(1 - 2v)] \qquad (2.6)$$

Commonly, the NP is described as an incompressible fluid and studies have adopted a Poisson's ratio value of ~0.5, whilst others have adopted values between 0.35 and 0.49 (Meakin and Hukins, 2001, Kulak et al., 1976, Iatridis et al., 2003, Lu et al., 1998, Argoubi and Shirazi-Adl, 1996, Goel et al., 1993, Lee et al., 2000, Natarajan et al., 1994). However, to the author's knowledge, only one experimental study has attempted to directly determine the Poisson's ratio of the NP. This was achieved using an optical measurement technique coupled with an unconfined compression experiment, reporting a significantly higher value of 0.62 ± 0.15 (Figure 2.12) (Cloyd et al., 2007). This implies an increase in volume with compression. The

reason for this high value may have been the result of methodological sensitivity which will be discussed in chapters 5 and 6. One possible explanation for the lack of experimental data on NP Poisson's ratio is the difficulty in sample preparation and measurement of lateral displacement. The tissue is inherently viscid and, as such, presents the problem of specimen-platen interfacial frictional effects which may serve to influence lateral expansion during an unconfined compression experiment.
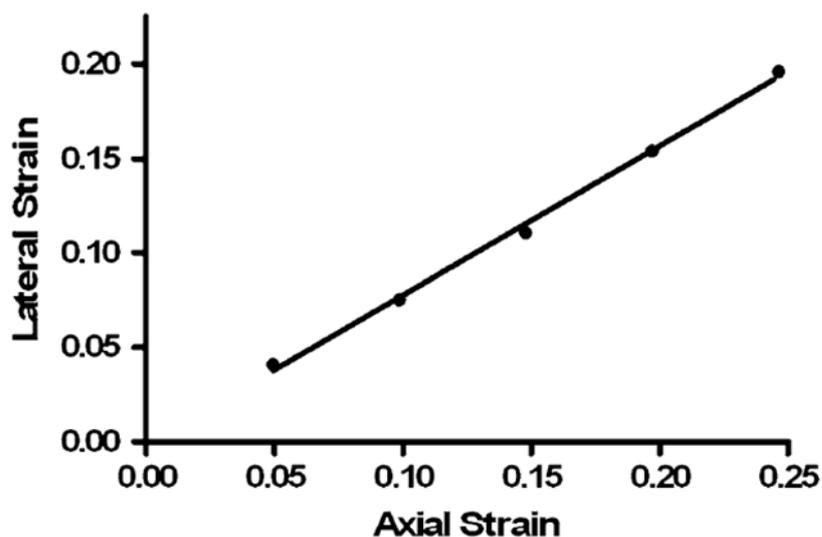
Figure 2.12 Representative linear regression for calculation of NP Poisson's ratio (Cloyd et al., 2007).

However, there have been more studies on the Poisson's ratio of AC, some of which report a depth dependency. Chegini and Ferguson (2010) highlighted that the highest Poisson's ratio is found in the deep zone and the lowest in the superficial zone. Due to the composition of AC, these findings are in keeping with a study which indicated that Poisson's ratio is controlled, primarily, by collagen fibres (Kiviranta et al., 2006). Collagen controls the tensile modulus of AC and this, in turn, controls the depth dependent Poisson's ratio of AC.

The linear biphasic theory utilised in unconfined compression between impermeable platens (Armstrong et al., 1984) predicts that, immediately after compression, the tissue should experience a peak lateral expansion as a result of an instantaneous build-up of fluid pressure with $v = 0.5$. During the hold phase, the tissue should partially recoil due to the additional flow induced deformation radially stressing the fibres in tension. Chegini and Ferguson (2010) highlighted that the Poisson's ratio of AC is lowest in the superficial zone, which has the highest tensile modulus (Figure 2.13).
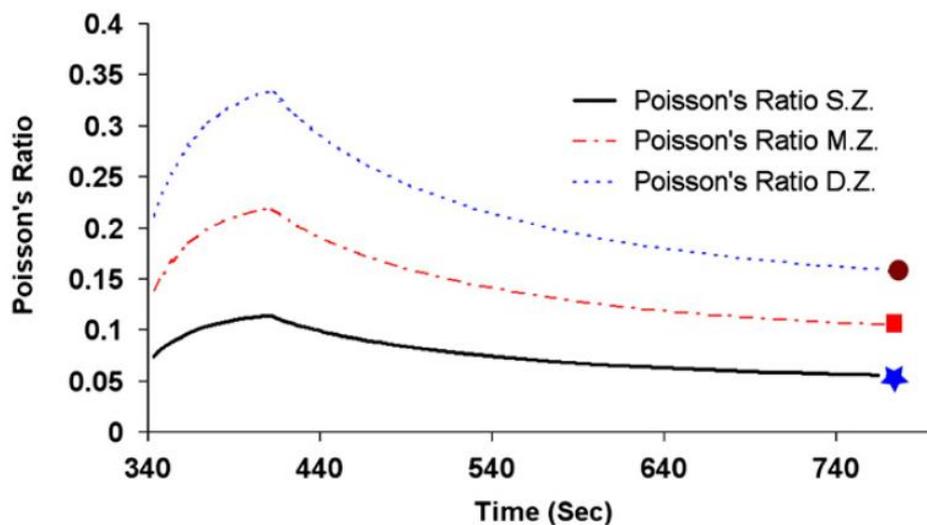
Figure 2.13 Depth dependent Poisson's ratio of AC (Chegini and Ferguson, 2010).

Since elastic fibres play an integral role in the recovery of the tissue after deformation (Yu et al., 2002) and that collagen and elastic fibres only contribute to the mechanical functioning of the disc when stressed in tension, the orientation of these fibres may influence Poisson's ratio. It has been well documented that collagen content in the NP is unorganised and homogenous, whereas elastic fibres have been found to show a degree of organisation with fibres predominantly running radially in

the central zone and predominantly perpendicular to the CEP in the superficial zones (Yu et al., 2002). The effect of this depth dependent elastic fibre orientation on the mechanical response to deformation in unconfined geometry is yet to be determined.

2.5. Mechanobiology of the IVD

2.5.1. Nutrition

The nutrition of the IVD is a topic of much interest as it may be directly implicated in the initiation of degeneration. Since the disc is avascular, it relies on diffusion for the transport of small molecules. The outer AF is surrounded by a capillary network allowing adequate nutrient supply to this region (Stairmand et al., 1991). The supply to the nucleus, however, is far more obstructed with capillaries approximately 7 to 8mm from the centre of the adult lumbar disc (Urban et al., 2004). Blood vessels penetrate the subchondral bone of the adjacent vertebral body and the calcified zone of the CEP, and nutrients must then diffuse from the blood vessels through the cartilage and into the NP (Stairmand et al., 1991). Free diffusion is permitted when the nutrient itself is smaller in cross-sectional area than the extra-fibrillar spaces in the PG-collagen network. The most permeable region of the CEP is the central area, with 85% of the NP-CEP region found to be permeable to diffusion (Maroudas et al., 1975, Nachemson et al., 1970, Urban et al., 1978). The solute concentration gradient between disc tissue and external solution also plays an important factor in governing the rate of diffusion. Negatively charged solutes are excluded to a greater extent than positively charged solutes, which is due to the high negative charge of the PGs, with the CEP route being of primary importance to the transport of positively charged solutes (Maroudas et al., 1968, Urban et al., 1978).

Diffusion is the primary mechanism required for the transport of small molecules such as oxygen and glucose, however, the transport of larger metabolites is aided by convective fluid flow (Ferguson et al., 2004, Urban et al., 1982, McMillan et al., 1996). Because larger metabolites have a low diffusion coefficient, loading of the disc is necessary to aid transport throughout the tissue. One study has demonstrated that the transport of a 28kDa solute through AC was enhanced by fluid flow (Garcia et al., 1998). These results have been verified by mathematical modelling of nutrient transport in AC, where the net increase in large nutrient transport during daily loading was found to be 30% when compared to diffusion alone (Ferguson et al., 2004). The main routes for the convective transport of nutrients are axially through the CEP and radially through the AF (Nachemson et al., 1970, Ogata and Whiteside, 1981, Urban et al., 1977). One problem related to the convective transport of nutrients through the CEP is the calcification and resultant reduction in permeability which affects the marrow contact channels with advancing age. The reduction in permeability obstructs the convective transport of large molecular weight molecules, which may impact on the cellular function of the disc (Ferguson et al., 2004, Nachemson et al., 1970, Riches and McNally, 2005). Although mechanical loading enhances the convection of larger metabolites, Arun and co-workers (2009) found that sustained creep loading in fact reduced the diffusion of small solutes into the centre of the disc.

2.6. Ageing and Degeneration

The spine experiences structural and compositional changes with advancing age and with the progression of degeneration. Ageing causes inevitable changes in the

appearance and composition of spinal tissues e.g. a loss in height and PG content, but these were previously thought to be largely unrelated to pain (Boden et al., 1990). However, more recent large population studies, though varied, have indicated that an association may indeed exist between disc degeneration and LBP (Bendix et al., 2008, Cheung et al., 2009, de Schepper et al., 2010). Additionally, structural changes associated with degeneration such as Schmorl's nodes and disc herniation are closely associated with pain (Videman et al., 2003). Degeneration of the IVD is an extensive area of interest which has been studied for many years, so this section will only briefly describe the fundamentals of this phenomenon.

The morphology of the IVDs is of particular importance due to the occurrence of LBP which has been attributed, in part, to the degeneration of the disc (Borenstein et al., 2001, Jensen et al., 1994, MacGregor et al., 2004, Luoma et al., 2000). Disc degeneration is a complex process characterised by biochemical adaptations in the NP and IAF, as well as the formation of fissures orientating from the central areas of the disc towards the periphery (Fraser et al., 1993). Additionally, stress induced defects in the OAF may accelerate degeneration of the inner zones and ultimately lead to pain (Fraser et al., 1993).

The disc is generally considered an avascular structure, however, until the second year of life blood vessels can be found between the lamellae of the AF. After the second year of life, these vessels degenerate which results in the reduction of cell density in the disc, probably due to hindrance in metabolite transport. The hydration of the disc also decreases (Figure 2.14 and Figure 2.15) with advancing age (Prescher, 1998) which can be attributed to a loss of proteoglycan content and increased cross-linking of collagen fibres (Adams and Dolan, 2005). The mechanical

implications of these adaptations is that the gelatinous NP may reduce in size, and is no longer able to maintain the high hydrostatic pressure required to withstand compression during daily loading. Peak compressive stresses may then occur in the AF of the degenerate disc (McNally and Adams, 1992). Cell death also occurs, with the presence of cells with necrotic and apoptotic appearance. These adaptations are extremely common and it has been reported that more than 50% of cells in adult disc are necrotic (Buckwalter, 1995, Gruber and Hanley, 1998). A recent review by Adams and Dolan (2012) indicated that there is evidence of two disc degeneration phenotypes. The first form stems from degenerative changes associated with the end-plate and the second stemming from the AF.
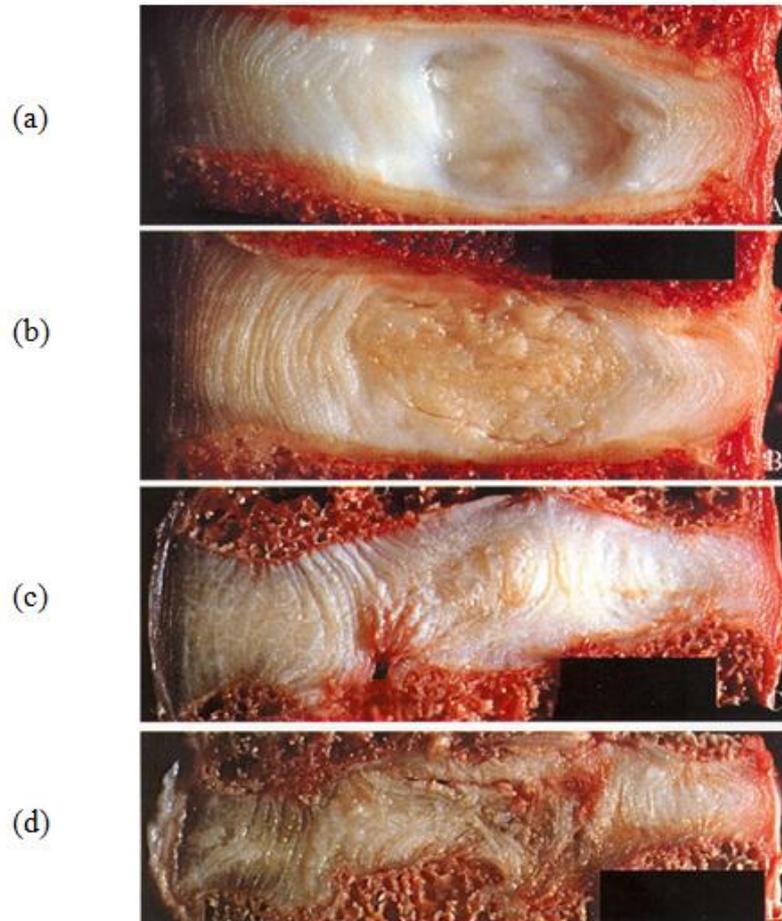
Figure 2.14 Grades of disc degeneration (Adams et al., 2002).
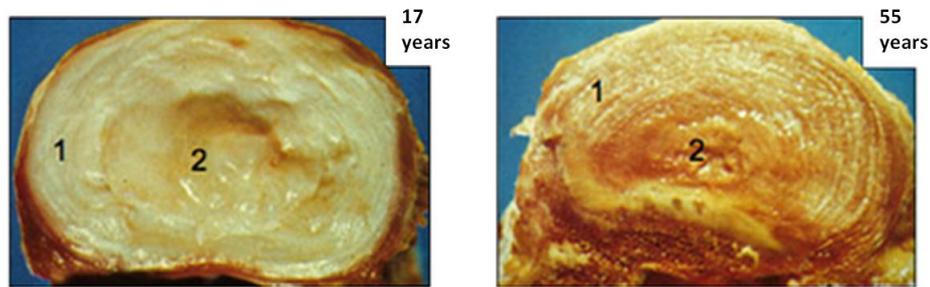
Figure 2.15 Left: Young healthy disc with annulus fibrosus (1) and nucleus pulposus (2). Right: Degenerative disc with loss of water content. Taken from http://www.eurospine.org/p31000298.html.

Although the source of LBP is a complex and much debated subject area, structural changes such as disc prolapse, (Videman et al., 2003), when nuclear material impinges on a nerve ending from the central nervous system (CNS), can certainly lead to LBP (Figure 2.16). Although prolapse is usually considered to be the result of a mechanically induced rupture, it can only be recreated in vitro in healthy discs by mechanical forces far greater than those which are normally experienced in vivo. In the majority of laboratory tests, it is the vertebral body that fails rather than the disc (Adams and Hutton, 1982), however, McNally et al., (1993) suggested via in vitro experiments that some discs may experience prolapse as a result of localised stress concentrations in the posterior AF when subjected to anterolateral bending and compression. Degenerative changes, such as the migration of degenerate sections of NP tissue through tears in the AF, allow the disc to herniate in vivo (Moore et al., 1996). Although mechanical factors alone may not induce disc failure, mechanical stimulus can contribute to compositional changes in the IVD. For example, Ishihara

et al (1996) found that high hydrostatic pressure can reduce matrix synthesis by up to 60%.

The role of the CEP in the degeneration of the disc has been considered crucial. Alteration in the composition of the CEPs has been shown to correlate closely with the degeneration of the disc (Nachemson et al., 1970). The CEP contains type X collagen which can be involved in the calcification of the marrow contact channels which can consequently reduce the permeability of the tissue (Nachemson et al., 1970). The result is a significant reduction in the transport of nutrients into the IVD (Roberts et al., 1996).

The posterior longitudinal ligament and peripheral AF contain nerve endings from the sinuvertebral nerve (Groen et al., 1990). In degenerated discs, nerve endings can sometimes be found to grow into the NP as a result of a loss of hydrostatic pressure (Freemont et al., 1997) and PG depletion (Melrose et al., 2002) which could result in the disc itself becoming a source of pain. Pain-provocation studies on sedated patients have confirmed that a full symptomatic pain response can be reproduced by gentle probing of the posterior AF (Kuslich et al., 1991). Additionally, a number of studies have found that the apophyseal and sacroiliac joints are common sources of back pain (Schwarzer et al., 1994, Schwarzer et al., 1995).

Recent work has suggested that genetic factors play an important role in disc degeneration and LBP, with a number of studies reporting a strong hereditary tendency for disc degeneration (Heikkila et al., 1989, Matsui et al., 1998, Varlotta et al., 1991). MRI scans of identical twins, who were both free of possible abnormal factors which may influence disc degeneration, showed extremely similar variations

in spinal column shape and disc degeneration (Battie et al., 1995). Additionally, family studies have indicated that first-degree relatives are twice as likely to develop generalised osteoarthritis (Kellgren et al., 1963). Sambrook and co-workers (1999) reported that disc height and bulge are extremely heritable, and osteophytes are heritable in the lumbar region via MRI.

This section has outlined the fundamental disc adaptations and possible problems associated with ageing and degeneration, however, for a fuller understanding of these mechanisms the reader is suggested to undertake a more thorough investigation of the field e.g. Buckwalter et al., (1995), Urban and Roberts (2003), Adams and Roughley (2006).

Figure 2.16 Intervertebral disc prolapse at L4/5. Image taken and edited from
http://jnnp.bmj.com/content/73/suppl_1/i42.full.

2.7. Constitutive modelling of cartilaginous tissue

2.7.1. Mathematical modelling

An important, and indeed extensive, area of soft tissue biomechanics is the mathematical modelling of mechanical response. As such, the area will only be briefly described with emphasis on the particular subject matter which is important to this thesis.

Macroscopic models which have been extrapolated from solid mechanics have been traditionally utilised in the modelling of cartilaginous tissue (Taylor and Miller, 2006), many of which are based on poroelastic theory (Biot, 1941, Biot, 1962). A porous medium is one which is constructed of a solid matrix which has an interconnected network of pores filled with fluid. The most commonly used model is the linear biphasic theory (Mow et al., 1980) (KLM model) and its extensions to finite deformation (Kwan et al., 1990, Holmes and Mow, 1990), transverse isotropy (Cohen et al., 1998) and nonlinear permeability (Holmes, 1986). In confined compression experiments, the aggregate modulus, H_A, and hydraulic permeability, k, can be derived by curve fitting experimental data to the linear biphasic equation:

$$\frac{\partial^2 u}{\partial z^2} = \frac{1}{H_A k} \frac{\partial u}{\partial t}$$

(2.7)

where u is the axial (z) displacement and t is the time. Biphasic theory was further developed to account for strain-dependent H_A and k in confined compression (Holmes and Mow, 1990, Holmes, 1986) via the non-linear biphasic model:

$$\sigma_e = \frac{1}{2} H_{A0} \left(\frac{\lambda^2 - 1}{\lambda^{2\beta + 1}} \right) e^{\beta(\lambda^2 - 1)}$$

(2.8)

where, σ_e is the equilibrium stress, H_{A0} is the zero strain aggregate modulus, λ is the stretch ratio defined as deformed height divided by original height or $1 + \text{strain}$, and β is a non-dimensional parameter which relates σ_e to λ. Hydraulic permeability can be related to λ by,

$$k = k_0 \left(\frac{\lambda - \emptyset_0^s}{1 - \emptyset_0^s}\right)^\kappa e^{M(\lambda^2 - 1)/2} \tag{2.9}$$

where, k_0 is the zero strain permeability, $\emptyset_0^s$ is the zero strain solid volume ratio, and M and κ are non-dimensional parameters controlling the loss of k with λ. The reason for biphasic formulations proving popular when modelling the behaviour of cartilaginous tissue is that they allow for the analysis of the stresses in the solid and fluid phases which is important, for example, when considering the resistance to compressive loading in both the degenerate and non-degenerate cases (Ateshian et al., 1994). Heneghan and Riches (2008a) showed that biphasic mathematic models can be used to predict the mechanical behaviour of the NP by comparing hydraulic permeability experimental data with the model of Holmes and Mow (Holmes and Mow, 1990). However, as a result of difficulty in replicating experimental boundary conditions, biphasic formulations have also been shown to be inadequate at describing many of the tissues mechanical characteristics which has led to the development of a number of extensions.

Recently, poroelastic models have become more sophisticated with the implementation of strain-dependent properties such as hydraulic permeability and osmotic pressure. One modification of the KLM model has come in the form of the conewise linear biphasic model (CLB) (Stoltz and Ateshian, 2000) which has been

formulated to account for the apparent tension-compression non-linearity of AC by incorporating anisotropic material properties. This model has been found to account well for the reaction forces observed in confined and unconfined compression experiments, however, it failed to successfully fit lateral expansion data in unconfined geometry.

A significant development has come in the form of poroviscoelastic models (PVE) which are generalisations of linear biphasic models but include flow independent solid matrix viscoelasticity. These models are isotropic formulations and, as such, are constructed by adapting the general KLM linearly elastic solid stress equation (Taylor and Miller, 2006). PVE models have been widely used in the analysis of AC mechanics with a high degree of success (DiSilvestro et al., 2001b, DiSilvestro et al., 2001a, DiSilvestro and Suh, 2002, Huang et al., 2001, Mak, 1986a, Mak, 1986b, Setton et al., 1993, Suh and DiSilvestro, 1999).

The chemical structure and physical interations of the PGs in the disc influence the mechanical properties of the tissue, and in particular the ECM. For an understanding of the contribution of the PG charges and ions, consideration has to be made to at least three distinct phases known as triphasic theory. This complex theory models cartilaginous tissue as a mixture of three phases: a charged solid phase which represents the collagen-PG network, a fluid phase, and an ion phase comprising the monovalent cation Na^+ and anion Cl^- as well as other multivalent species such as Ca^{2+} (Gu et al., 1998, Lai et al., 1991). The triphasic theory, however, neglects electrical fluxes which may not be appropriate which considering disc tissue due to the high concentration of FCD associated with this tissue (Frijns et al., 1997). The quadriphasic theory developed by Huyghe and Janssen (1997) distinguishes between

cations and anions thus resulting in an additional phase which allows for agreement with experimental data whilst using realistic diffusion coefficients (Frijns et al., 1997). These models have been used to predict the mechanical properties of disc tissue; however, the validity of these poroelastic models is yet to be fully ascertained. Due to their complexity they have not been extensively and rigorously tested against experimental data.

Experimental data is essential for providing verification and validation of mathematical models and numerical simulations (Jones and Wilcox, 2008). The requirement for empirical data for the continued verification of mathematical models was highlighted by the poroelastic model of Riches et al. (2002), which also demonstrated good agreement with experimental data from spinal motion segments.

2.7.2. Finite Element (FE) modelling

This section outlines the general theory with regards to FE modelling and its application to the study of cartilaginous tissue. A more detailed review of the subject matter exists within the appropriate chapters.

Due to the difficulty in determining the mechanical, biological and electrical behaviour of cartilaginous tissue experimentally, computational descriptions of the tissue are often used for such analyses via the finite element method. FE modelling allows for the solving of a series of complex partial differential equations by dividing a structure into simple disjointed geometrical *elements*. Elements are connected to one another by nodes thus forming a system of equations for the structure. Each element is solved in relation to each other, with unknowns at the nodes (e.g. stresses) thus allowing for an approximate solving of the total system.

FE modelling is a method commonly adopted for the investigation of disc mechanics; for both full disc geometry and isolated tissue. The early work by Belytschko et al., (1974) demonstrated the usefulness of a full disc FE model in predicting material properties by investigating stress distributions within the disc, NP hydrostatic pressure and the deformations of the AF and vertebral body. Shirazi-Adl et al., (1984) made the first attempt to capture the non-linear composite nature of the AF in a full disc FE model and it was compared to experimental load, disc bulge, end-plate bulge and intradiscal pressure data. More recently Wang et al.,(1997) investigated the viscoelastic behaviour of the disc via an FE model and demonstrated that a motion segment experiences lesser deformation at high loading rates thus transferring lesser loads onto the facet joints and surrounding ligaments. Galbusera et al., (2011) compared four methods of simulating swelling in poroelastic FE models of the IVD. A non-linear

3D FE model was developed by Rohlmann et al., (2006) to investigate the effect of degeneration on the mechanics of a lumbar motion segment by varying disc height and bulk modulus of the NP.

In addition to the analysis of modelling of IVD's, a number of studies have developed full spine models to investigate daily loading. One recent example of this is the work of Schmidt et al., (2010) who investigated spinal response to dynamic physiological loading via a non-linear poroelastic FE model of the lumbar spine (Figure 2.17). Fairly good agreement was achieved with in vivo and in vitro measurements; findings suggested that axial displacement, fluid loss, axial stress and disc radial strain increased whilst pore pressure and collagen fibre strains decreased throughout the diurnal cycle. Wang et al., (2005) developed a novel technique which allows FE models of the spine to be based on patient specific geometries obtained from medical data sets.

In order to investigate the micromechanical behaviour of the disc and to validate current models, simple-geometrical FE models have proven to be a useful tool. This method allows for the exclusion of the complex geometries, boundary conditions and the intrinsic property simplifications often associated with full disc and spine models.

Chegini and Ferguson (2010) investigated the depth dependent Poisson's ratio of AC through an inhomogeneous orthotropic fiber embedded biphasic model. Cao et al., (2011) modelled the stress-strain, fluid pressure and flow fields for cells and their surrounding pericellular matrix in the NP using 3D models based on the in situ morphology of cell-PCM regions of the NP, whilst the complex mechanochemical interactions which occur in neutral deformable porous media under finite deformation were investigated by Ateshian et al., (2011). The quadriphasic theory was also successfully incorporated into a 3D FE model by van Loon et al., (2003) and found

consistent results when compared to an analytical solution for 1D consolidation and swelling.
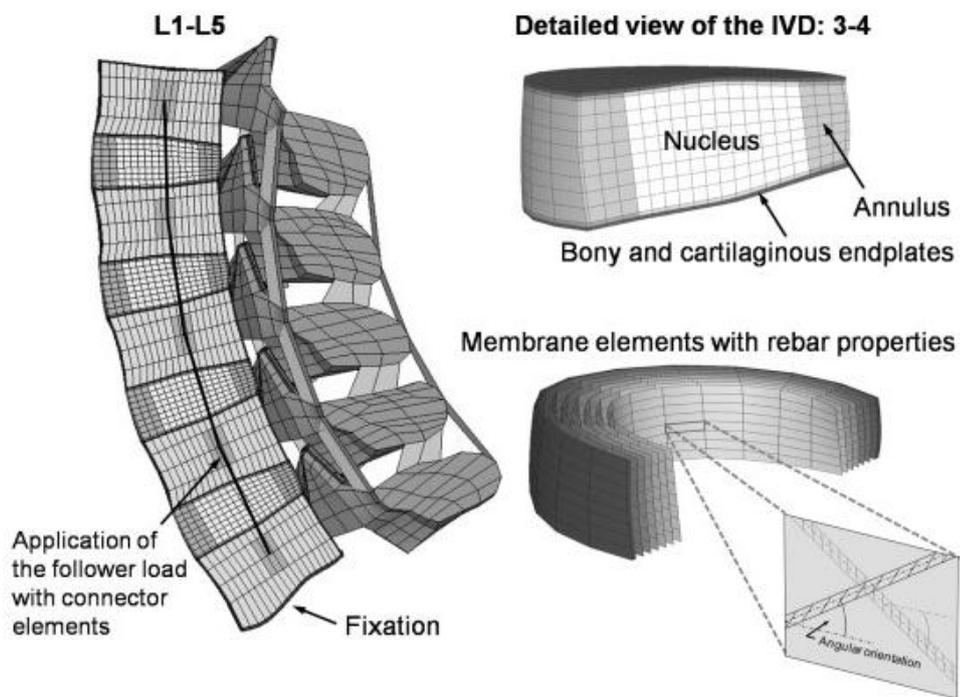
Figure 2.17 FE model of the lumbar spine (Schmidt et al., 2010)**.**

2.8.   Thesis aims

The importance of furthering our understanding of disc biomechanics has been presented; however, there remain a number of unknowns in terms of fundamental material properties and their sensitivities to deformation which are required to further our modelling of this tissue. Additionally, the influence of mechano-electrochemical phenomena, arising from the high concentration of PG's, on the disc's mechanical response requires investigation via the coupling of experimental data and multiphasic FE modelling. To further complicate the analysis of such mechanisms, the effect of the degenerative cascade must also be considered.

Therefore, this thesis aims to investigate the influence of mechano-electrochemical phenomena on IVD biomechanics via the 3 commonly adopted mechanical testing configurations for this tissue: direct permeation, unconfined compression and confined compression.

Multiphasic modelling, via the open source FE package "FEBio", will compliment experimental analysis to allow a clearer understanding of the micromechanical interactions with take place during such experimental configurations whilst the effect of degeneration on such mechanisms will also be investigated. A comparison between the commonly adopted biphasic and triphasic mathematical frameworks will determine whether models which consider electrical phenomena are worth the additional computational expenditure. Although "FEBio" has been validated against alternative and verified FE codes (Maas et al., 2012), the current work aims to compare it to experimental data which has not previously been reported in the literature.

Results from this thesis will aid our overall understanding of disc mechanics, nutrient transport and the sensitivity of the disc's response to various deformations and external conditions. Perhaps the most important use for the results from this thesis will be the potential advancement of our modelling capability which will, in turn, aid the future design and engineering of potential disc replacement devices and engineered constructs.

2.9. Outline of studies

2.9.1. Study 1: Experimental determination of the influence of mechano-electrochemical phenomena on fluid flow in the nucleus pulposus

The influence of flow induced strain gradients within the NP has not been fully investigated. Assuming an initial homogeneous distribution of PG, strain gradients may develop FCD gradients which will, in turn, affect mobile ion concentrations and electrical potential gradients. The influence of such relations on the global fluid pressure gradient is not understood. If indeed such interactions occur then mathematical models which account for such phenomena may be required. A direct permeation study whereby solutions of differing salinity will be inflused through the tissue at varying fluid pressures to highlight the influence of mechano-electrochemical effects on fluid flow within the NP. It is hypothesised that the fluid flow is decreased by both hypotonic and hypertonic permeating solutions compared to an isotonic permeating solution as a result of ionic gradients only being apparent in the latter.

2.9.2. Study 2: Finite element modelling of the influence of mechano-electrochemical phenomena on fluid flow in the nucleus pulposus

Multiphasic FE poroelastic models which simulate Study 1 will be developed using both biphasic and triphasic theory to further investigate the mechano-electrochemical interactions which may occur during such a configuration. Comparing numeric results to experimental data will allow for the assessment of the capability of both mathematical frameworks for the description of fluid flow within the NP. It is hypothesised that FCD and electric potential gradients play an important role in governing fluid flow within the NP and consequently a triphasic poroelastic model should be used when modelling fluid flow in this tissue.

2.9.3. Study 3: Experimental determination of the Poisson's ratio of the IVD

The Poisson's ratio, a fundamental material property, of the NP remains a relative unknown which has resulted in various values being utilised in models of this tissue. This study, therefore, aims to fully characterise the Poisson's ratio of the NP and determine how sensitive this property is to strain, strain-rate and axial location in the disc as well as the influence of the AF via unconfined compression experiments. It is hypothesised that the Poisson's ratio of the NP is both strain and strain-rate-dependent, there is a significant effect of axial location and the AF will provide a confining effect to the NP and reduce the overall Poisson's ratio of the disc.

2.9.4. Study 4: Finite element modelling of the nucleus pulposus in unconfined compression: the effect of mechano-electrochemical phenomena

The transient and equilibrium mechano-electrochemical interactions which occur during the unconfined compression will be investigated via multiphasic FE

modelling. In a similar fashion to Study 2, biphasic and triphasic simulations will be compared to experimental data to assess the capability of these mathematical frameworks in predicting the mechanical response of the NP to such experimental conditions. Ionic environment will be a key changeable parameter thus allowing for the analysis of ionic effects. It is hypothesised that the ionic environment has a significant effect on results and mechano-electrochemical interactions play an important role in governing tissue response in an unconfined compression experiment.

2.9.5. Study 5: Confined compression of the human nucleus pulposus: mechano-chemical effects in the degenerate case

The effect of degeneration on the influence of mechano-electrochemical interactions on the mechanical response of the NP is yet to be understood. Isotonic and hypertonic confined compression experiments will be conducted on degenerate human NP tissue with inverse analytical methods applied to the resultant load data. It is hypothesised that there will be minimal effect of external solution on the mechanical response of the tissue as a result of diminished mechano-electrochemical interactions occurring in the degenerate case.

3. Experimental determination of the influence of mechano-electrochemical phenomena on fluid flow in the nucleus pulposus

3.1.   Introduction

As discussed in section 2.1, the IVD is avascular and as such relies on diffusion and convective fluid flow for nutrient supply (Ferguson et al., 2004). Although small molecules such as oxygen and glucose are transported via diffusion, convection may play an important role in the transport of larger metabolites when diffusion alone is not sufficient (Ferguson et al., 2004, McMillan et al., 1996, O'Hara et al., 1990, Roberts et al., 1996, Tomlinson and Maroudas, 1980, Urban et al., 2004, Urban et al., 1982). It has been predicted, via numerical analyses, that there is a 30% increase in the transport of large metabolites over the diurnal cycle when convection is coupled with diffusion, compared to diffusion alone (Ferguson et al., 2004). The main route for transport to the NP is axially through the CEPs (Holm et al., 1981, Nachemson et al., 1970, Ogata and Whiteside, 1981) with the rate of convective transport governed by the tissues hydraulic permeability. It has been found that, in the healthy disc, the permeability of the NP dominates fluid movement, whilst CEP permeability only has a significant effect when degeneration or calcified occlusion reduces its permeability to a level lower than that of the NP (Riches and McNally, 2005).

Additionally, hydraulic permeability plays an essential role in disc mechanics. The disc can withstand high compressive strains due to a high hydrostatic pressure which dissipates slowly due to the tissues low permeability (Lu et al., 1998, Riches et al., 2002, Oloyede et al., 1998, McNally and Adams, 1992), this is discussed in more detail in 2.4.4. Heneghan and Riches (2008a) investigated the strain-dependent

hydraulic permeability of the compressed bovine NP and demonstrated that the permeability decreased with compression, which is in agreement with earlier studies on bovine AC (Mansour and Mow, 1976, Reynaud and Quinn, 2006), human AF (Gu et al., 1999b) and linear and non-linear models (Perie et al., 2005).

To measure tissue permeability directly, a pressure differential technique together with Darcy's law can be applied, and has been utilised on the NP (Heneghan and Riches, 2008a), AF (Gu et al., 1999b) and bovine AC (Mansour and Mow, 1976, Reynaud and Quinn, 2006). However, permeability is more commonly determined by fitting a biphasic model to experimental data (Best et al., 1994, Drost et al., 1995, Ateshian et al., 1997, Houben et al., 1997, Chen et al., 2001, Johannessen and Elliott, 2005, Perie et al., 2005). The zero-strain permeability is extracted from this technique, but the accuracy of this inverse approach depends on the suitability of the model and the ability of the numerical schemes to extract the relevant parameters.

When a fluid pressure gradient is applied to a sample in confined compression, the linear biphasic equation (Mow et al., 1980) or nonlinear biphasic equation (Holmes, 1986) predict that, at equilibrium, under a constant fluid velocity, there is a variation in strain through the tissue: with higher localised strain occuring toward to the downstream surface due to the applied fluid pressure inflating the upstream pores. A strain distribution through the tissue will result in a permeability distribution through the tissue as a result of reduced pore size and increase PG concentration in areas of high compressive strain. Thus, direct permeation tests determine the apparent permeability of the sample, not a localised permeability value. The occurence of localised strain gradients has yet to be verified experimentally.

Many biological tissues exhibit a swelling potential which is caused by the fixed electric charges in the solid matrix (FCD) which are counteracted by charges in the fluid (Lai et al., 1991, Huyghe and Janssen, 1997, Lai et al., 2000, Gu et al., 1993), see section 2.4.3. Modelling that includes mobile ions as separate phases, together with fixed charges associated with the concentration of PG in the sample (Gu et al., 1993, Gu et al., 1998, Lai et al., 2000, Huyghe and Janssen, 1997), have implied that electrical potential, mobile ion and fixed charge gradients will all affect fluid flow. The development of finite element models, which are based on the theory of porous media, allowing for the simulation of mechano-electrochemically active soft tissue, has followed suit (Ehlers et al., 2009, Yang et al., 2011), however, the integration of tri- or quadriphasic theory has proved challenging.

Theoretically, strain gradients may develop FCD gradients which will, in turn, affect mobile ion concentrations and electrical potential gradients. However, the relative influence of mobile ion and fixed charge gradients compared to the global fluid pressure gradient has not been ascertained to date. If such interactions have significant influence on disc mechanics, then mathematical models which include such phenomena must be used. Experimentally, permeating a solution with a very high mobile ion concentration would render mobile ion, fixed charge and electrical potential gradients negligible, thus leaving flow to be dependent on the fluid pressure gradient. On the other hand, permeating a solution with no mobile ions would remove any gradients associated with mobile ion concentrations. However, permeating a low mobile ion concentration, such as isotonic NaCl, would leave all gradients in situ: fluid pressure, mobile ion, fixed charge and electric potential.

3.2. Aims and hypotheses

The aim of this chapter was to determine the fluid flow within the bovine NP with regards to the experimental variables of applied fluid pressure gradients and mobile ion concentration. It was hypothesised that fluid flow is decreased by both hypotonic and hypertonic permeating solutions compared to an isotonic permeating solution as a result of ionic gradients only being apparent in the latter.

3.3. Methods

3.3.1. Materials

Due to the difficulty in obtaining fresh human discs, bovine tail IVDs are commonly used due to their similar size and availability. Previous studies have used this tissue to study IVD composition (Nerlich et al., 1997, Roberts et al., 1991), metabolism (Horner et al., 2002, Horner and Urban, 2001, Ishihara et al., 1997), function (Aguiar et al., 1999), mechanics (Oloyede et al., 1998, Perie et al., 2005, Perie et al., 2006b, Perie et al., 2006a, Heneghan and Riches, 2008a, Heneghan and Riches, 2008b) and regulation (Razaq et al., 2000) due to their structural and compositional similarity to human discs.

Ishihara et al., (1996) demonstrated that the pressure profile across the bovine disc is similar to that of a healthy human disc whilst Demers et al., (2004) found that the water content of the bovine disc is similar to that found in the healthy human lumbar disc at approximately 77%. The same study, however, found that the PG content of the animal disc was slightly lower, at 30% of dry weight, than what has been observed in the human disc (40-50%) (Johannessen and Elliott, 2005). Even though

the bovine tail is subjected to lesser loading than the human lumbar disc, the swelling pressure of the bovine tail disc is of the same magnitude whilst in a prone position (Oshima et al., 1993, Ishihara et al., 1996).

Bovine tails were obtained from a local abattoir (Sandyford abattoir, Paisley, Scotland) within 2 hours of slaughter. Tails were dissected fresh, and all surrounding soft tissue was dissected with a scalpel to reveal the spinal column and IVD's (Figure 3.1). The 3 largest IVD's were removed from the adjacent vertebral end-plates with a scalpel, and subsequently frozen at -20°C until testing. A total of 24, ø10 mm, 1020 ± 122 µm (mean ± SD) thick plugs of NP tissue, orientated in the axial direction, were harvested with a cork borer and sectioned with a custom built cutting tool (Appendix 9.1) prior to placement in a direct permeation rig, described previously (Heneghan and Riches, 2008a).

Figure 3.1 Surrounding soft tissue was removed to reveal the spinal column and allow removal of IVD's.

3.3.2. Experiments

A schematic diagram of the permeation rig is shown in Figure 3.2. It consisted of an upper cylindrical permeation chamber which was attached to the adjustable crosshead of a materials testing machine (model Z005, Zwick Roell, Ulm, Germany), and a lower chamber secured to the stationary base. Both chambers were manufactured from acrylic. An image of the upper chamber can be viewed in Figure 3.3.
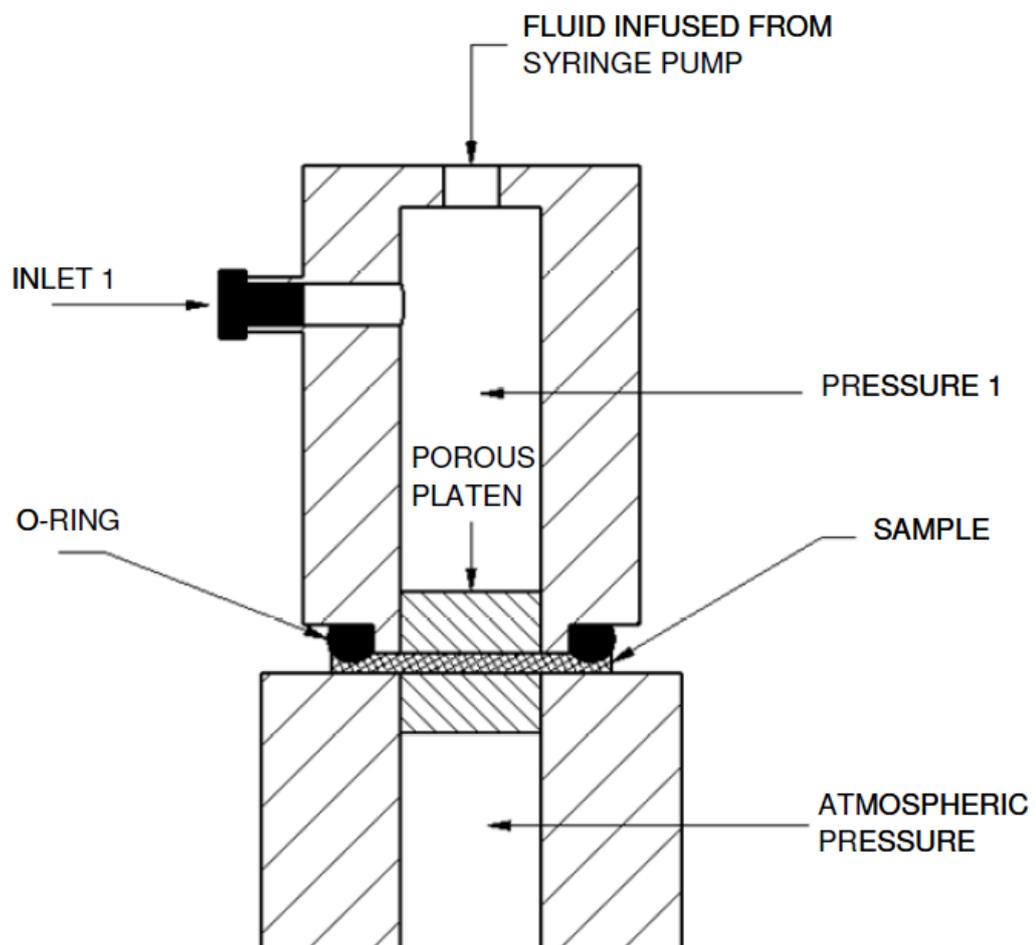
Figure 3.2 Schematic of the apparatus used to measure the permeability of the NP (Heneghan and Riches, 2008a).
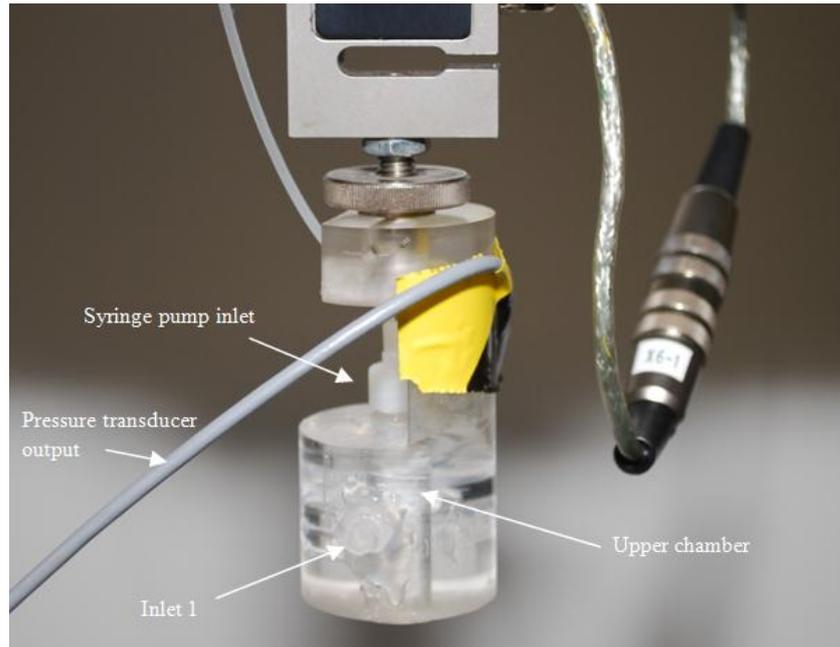
Figure 3.3 Photograph of the upper acrylic chamber used to infuse fluid through the sample.

NP samples were confined between two porous platens (stainless steel; average pore size, 100µm; ø5mm) which had a permeability of at least 4 orders of magnitude greater than previously reported for bovine NP tissue, thus causing negligible resistance to flow. Sample thickness was determined by lowering the upper platen onto the sample until a load of 0.3N was detected by the load cell. The platen was then removed and an 8mm diameter o-ring positioned on the superior surface (upstream) of the sample. The upper chamber was lowered again using displacement control to the previously determined sample height, embedding the o-ring into the tissue and thus confining fluid flow to the axial direction only. The upper chamber was filled with the permeating solution and vented of any air bubbles via inlet 1. Aqueous NaCl solution was then pumped through the sample by a dual syringe infusion/withdrawal pump (model 200 series, Cole-Parmer, London, UK) fitted with a 250µl Hamilton syringe (Figure 3.4).
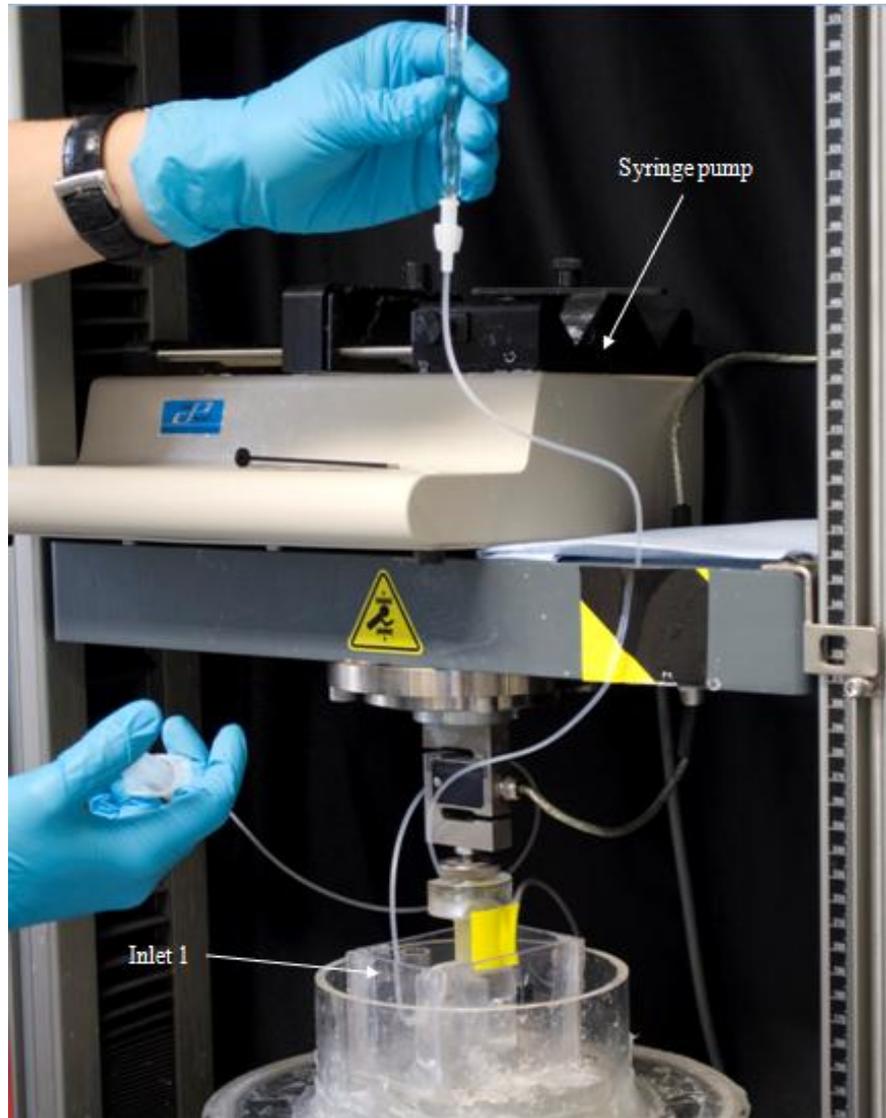
Figure 3.4 Filling the upper chamber with solution, and venting air out through syringe.

Calibration of the dual syringe pump was conducted by comparing the flow rate and expelled fluid weight against time. The 250µl syringe was filled with saline solution and subsequently mounted onto the syringe pump. The flow rate was set to 0.25ml/min to expel the full volume within a short period of time. The fluid was collected and weighed on laboratory scales (model XT220A, Precisa, Switzerland). The process was timed to check the flow rate on the syringe pump. The syringe pump was found to expel fluid at 0.245ml/min, and as such was considered adequately calibrated.

The pressure difference across the sample was measured using a Honeywell 15 psi (103kPa) compensated gauge pressure transducer (model 26PCCFA1G, RS Components, Glasgow, UK). This was calibrated in situ against a mercury column by blocking the porous channel with a sheet of aluminium (Figure 3.5), filling the upper chamber with saline solution, and applying incremental pressures of 10kPa to 60kPa via the syringe pump inlet and recording the resultant reading on a voltmeter (Figure 3.6). The calibration curve can be seen in Figure 3.7.
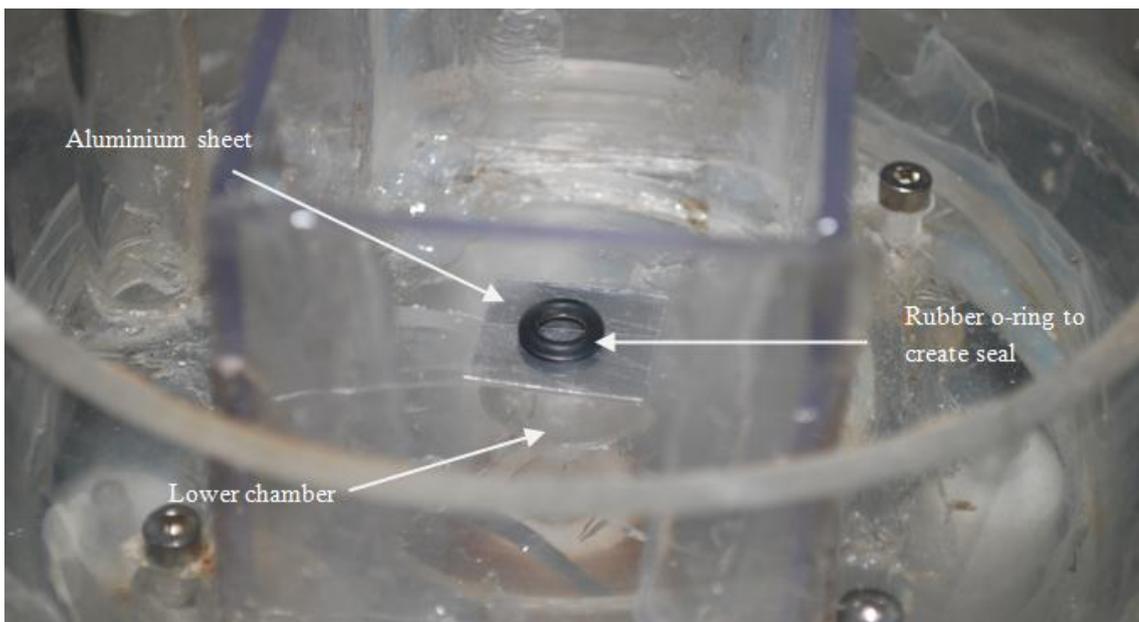
Figure 3.5 Photograph of lower chamber and aluminium sheet to block porous channel for pressure transducer calibration. A rubber o-ring was used to create an air-tight seal between upper and lower chambers.
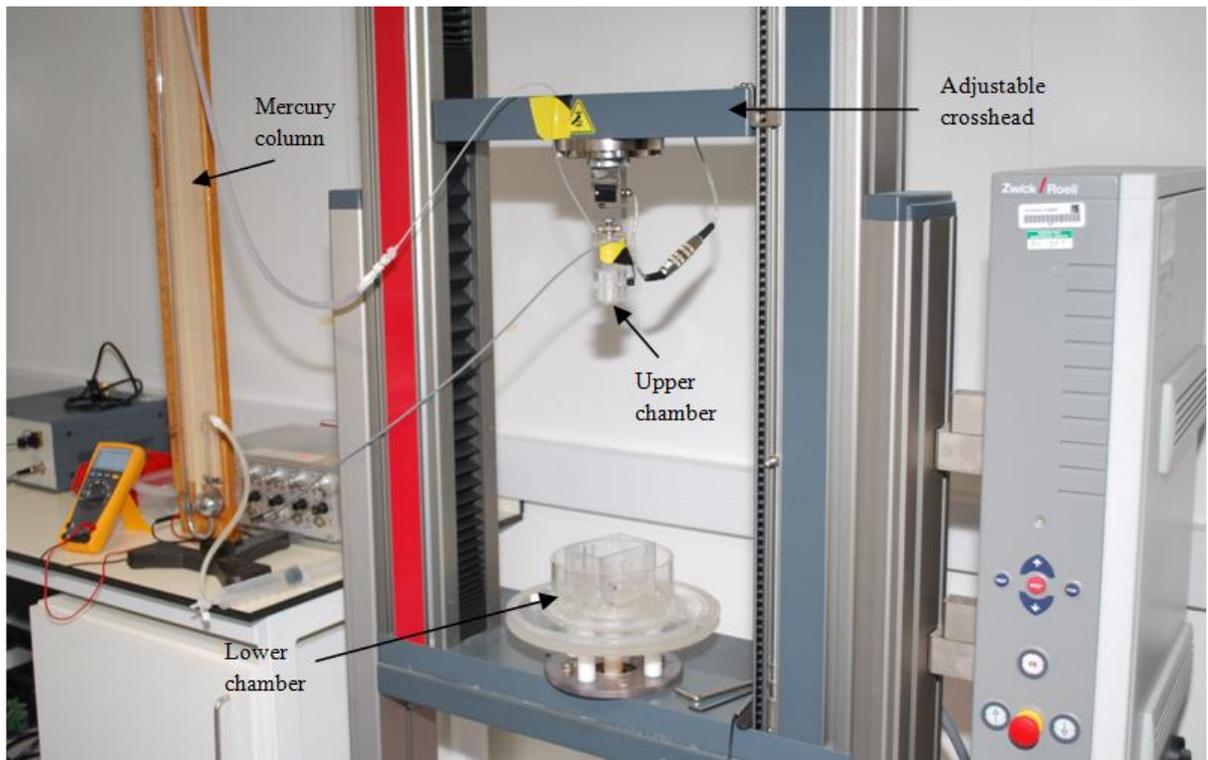
Figure 3.6 Pressure transducer calibration setup.
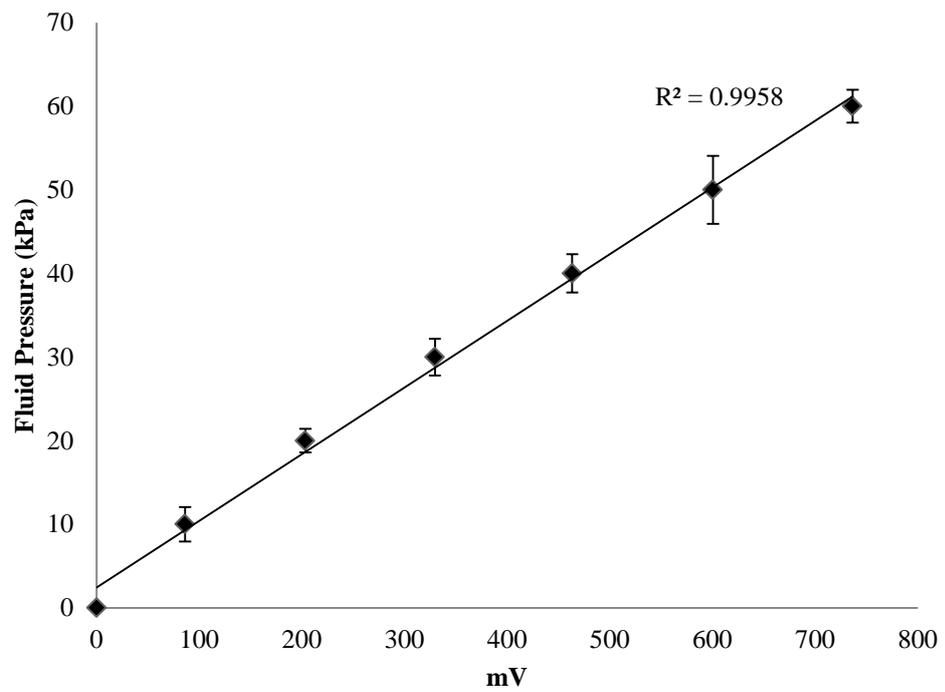
Figure 3.7 Calibration of the pressure transducer against a mercury column.

A total of 24 tissue samples were tested in either of 0M NaCl (hypotonic), 0.15M NaCl (isotonic) and 3M NaCl (hypertonic). For each sample, the flow rate was adjusted to maintain a pressure gradient of either: 30, 45, or 60 kPa across the sample in a random sequence. Infusion was conducted slowly to allow each sample to reach equilibrium during the first pressure ramp (~2h per pressure). Equilibrium was assumed when the pressure gradient across the sample did not alter more than ± 1% over a period of 15 minutes.

3.3.3. Theory

The electro-chemo-mechanics of porous media has been well described (Huyghe and Janssen, 1997) whereby the mechanical effect of the gradients of pressure, ion concentration and electric field may be related to fluid flow in a tissue. The reader is referred to this paper for a fuller description of the theory. However, the theory with regards to Darcy's equation is briefly reiterated here in the same nomenclature.

Defining the fixed charge density of a tissue, c^{fc}, to be positive for positive charges, the electroneutrality condition of a tissue in a monovalent salt solution is

$$c^- = c^+ + c^{fc} \qquad (3.1)$$

where c denotes the concentration of the superscripted ion species. Electroneutrality of the external solution (represented by overlined symbols) dictates:

$$\bar{c}^- = \bar{c}^+ = \bar{c} \tag{3.2}$$

The equations that describe Donnan equilibrium concentration of ions are:

$$2c^+ = -c^{fc} + \sqrt{(c^{fc})^2 + 4f^2\bar{c}^2} \tag{3.3a}$$

$$2c^- = c^{fc} + \sqrt{(c^{fc})^2 + 4f^2\bar{c}^2} \tag{3.3b}$$

where

$$f^2 = \frac{\bar{f}^+\bar{f}^-}{f^+f^-} \tag{3.4}$$

in which

$$f^\beta = \frac{a^\beta}{c^\beta}, \beta = +, - \tag{3.5}$$

are the activity coefficients, based on the activities, a, of components β. Furthermore, the osmotic pressure, π, may be given as:

$$\pi = RT\left[\phi^f(c^+ + c^-) - 2\bar{\phi}^f\bar{c}\right] \tag{3.6}$$

Finally, Darcy's equation (Eq. 53) (Huyghe and Janssen, 1997) may be written as

$$n^f v^{fs} = -K \cdot \left[\nabla_0(p - \pi) + RT(\phi^+ \nabla_0 c^+ + \phi^- \nabla_0 c^-) - F c^{fc} \nabla_0 \xi \right] \qquad (3.7)$$

In Eq. (3.7) R is the universal gas constant; T the absolute temperature; ϕ^f, $\bar{\phi}^f$, ϕ^+ and ϕ^- are the osmotic coefficients of the various constituents, n^f and v^{fs} are the volume fraction of the fluid phase and relative velocity of the fluid and solid respectively; K the permeability tensor; F is Faraday's constant and ξ the electrical potential. The electrical potential can be shown to be

$$\xi - \bar{\xi} = \frac{RT}{2F} Ln\left(\frac{a^- \bar{a}^+}{a^+ \bar{a}^-}\right) \qquad (3.8)$$

Substituting Eq. (3.1) and Eq. (3.6) into Eq. (3.7), and under the assumption that $\nabla_0 \bar{c} = 0$, we find

$$n^f v^{fs} = -K \cdot \left[\nabla_0 p - RT[(2\phi^f - \phi^+ - \phi^-)\nabla_0 c^+ + (\phi^f - \phi^-)\nabla_0 c^{fc}] - F c^{fc} \nabla_0 \xi \right] \qquad (3.9)$$

Eq. (3.9) shows that the fluid flow can be ascribed to a fluid pressure gradient, a cationic gradient (there exists an equivalent equation using an anionic gradient), a gradient of fixed charges and an electric potential gradient. In the absence of mobile

ions in the external solution, i.e. $\bar{c}^- = \bar{c}^+ = \bar{c} = 0$, then $c^- = c^{fc}$ and $c^+ = 0$. In

this case, Eq. (3.6) becomes

$$\pi = RT\phi^f c^{fc} \tag{3.10}$$

and Eq. (3.9) becomes

$$n^f v^{fs} = -K \cdot \left[\nabla_0 p - \left(\phi^f - \phi^- \right) \nabla_0 c^{fc} - F c^{fc} \nabla_0 \xi \right] \tag{3.11}$$

implying that fluid flow is only affected by a fluid pressure gradient, a concentration gradient of the fixed charges, potentially occurring through deformation, and an electrical potential gradient. Furthermore, in the absence of mobile ions, any electrical potential gradient can be attributed to gradients of fixed charges.

In a hypertonic external salt solution, $\bar{c} \gg c^{fc}$, leading to $c^+ = c^- = \bar{c}^- = \bar{c}^+ = \bar{c}$, and $\nabla_0 \xi = 0$. Thus Eq. (3.6) becomes

$$\pi = 2RT\bar{c}\left[\phi^f - \bar{\phi}^f \right] \tag{3.12}$$

Under the simplifying assumption that $\phi^f = \bar{\phi}^f$, then $\pi = 0$, and Darcy's equation reduces to the familiar

$$n^f v^{fs} = -K \cdot \nabla_0 p \qquad (3.13)$$

In Huyghe and Janssen the permeability tensor was expressed in terms of the frictional tensors resulting from the interactions between fluid, solid and ions (Huyghe and Janssen, 1997). In this work, it is assumed that

$$K = \frac{k}{\mu} \qquad (3.14)$$

in which the frictional components are incorporated into the empirical values of viscosity of the permeating solutions and k is the intrinsic permeability of the solid matrix.

3.3.4. Data analysis

For each sample, Eq. (3.13) and Eq. (3.14) were used to determine the apparent intrinsic permeability, k, of the sample at equilibrium:

$$k = \frac{\mu v h}{\Delta P} \qquad (3.15)$$

where $v = n^f v^{fs}$ is the global fluid velocity through the sample, ΔP the applied fluid pressure difference and h the thickness of the sample. The viscosity of the permeating solution, μ, is given by $\mu_{0M} = 0.001002$ Pa.s, $\mu_{0.15M} = 0.001015$ Pa.s and $\mu_{3M} = 0.001375$ Pa.s at 20°C (Haynes, 2010). In the tissue mechanics literature,

permeability is often expressed as hydraulic permeability, or k/μ (m^4/Ns). Since viscosity is a varying parameter in this experiment, it was chosen to present actual permeability values in m^2, however the conversion to k/μ is trivial with the factors presented above.

By applying a fluid pressure gradient across the tissue sample, the external fluid pressure will exert a stress at the boundary on the solid matrix. Flow induced viscous drag on the solid matrix will cause axial deformation of the sample during testing. To estimate the flow induced deformation during the test the stress-strain relationship of this tissue can be used:

$$\sigma = \frac{1}{2} H_{A0} \left(\frac{\lambda^2 - 1}{\lambda^{2\beta+1}} \right) e^{\beta(\lambda^2 - 1)} + \sigma_0 \qquad (3.16)$$

in which H_{A0} is the zero-strain aggregate modulus, β is a dimensionless coefficient, λ is the stretch ratio, and σ_0 is the stress at zero strain ($\lambda = 1$). Table 3.1 provides the parameters for this equation in both 0.15M and 3M NaCl (Heneghan and Riches, 2008b). Unfortunately the parameters required to apply this equation to the hypotonic case are not available, so this analysis was only performed on data obtained from the isotonic and hypertonic permeations.

	0.15M	3M
H_{A0} (kPa)	69.4	31.2
β	0.256	0.328
σ_0 (kPa)	-22.7	-8.3

Table 3.1 Parameter values for the stress-strain relationship of NP tissue for the two permeating solutions.

By assuming that the fluid pressure gradient was equivalent to an applied mechanical stress, Eq. (3.16) was used to estimate the stretch ratio, λ, which in turn was used to determine the height of the sample during the test, since

$$\lambda = \frac{h}{h_0} \tag{3.17}$$

where h_0 is the initial height of the sample. This data was then reused in Darcy's equation to calculate a predicted strain-dependent permeability. Since the current experimental setup was not able to measure and verify flow induced deformation, this is only a theoretical adjustment, and consequently analyses with and without this correction for sample height changes are provided.

Based on Eq. (3.13), the permeability in the hypertonic solution may be deemed representative of the intrinsic apparent permeability of the tissue, since ionic gradients are minimised in such external solutions (Mow and Schoonbeck, 1984). An effective pressure difference can then be defined as the total pressure difference required across the sample to achieve the measured flow velocity, but with the intrinsic apparent tissue permeability measured in the hypertonic case. This may be expressed as:

$$\Delta P_{eff,\beta} = \frac{\mu_\beta v_\beta h_\beta}{k_{3M}}; \quad \beta = 0M, 0.15M, 3M \tag{3.18}$$

Individual samples were not tested in all permeating solutions and so Eq. (3.18) can only be utilised with average values. The effective pressure includes an overall ionic osmotic effect:

$$\Delta\pi = \Delta P - \Delta P_{eff} \tag{3.19}$$

By combining Eq. (3.8), Eq. (3.11), Eq. (3.13) and Eq. (3.19) the overall ionic osmotic effect can be divided into mobile ion and fixed charge components and the effective pressure gradient due to mobile ion and/or fixed charge gradients can then expressed as a percentage of the applied fluid pressure, ΔP.

Fluid velocities and apparent permeability were analysed using repeated measures ANOVA, with the applied fluid pressure being a within-sample factor and external salt concentration being a between-sample factor. Where significant differences with the applied fluid pressure were found, subsequent t-tests with Bonferroni adjustment were conducted to identify differences between specific pressures and solutions. Significant differences were assumed when $p \leq 0.05$.

3.4.   Results

All samples reached equilibrium within 2 hours and a total fluid volume of at least equal to the average sample tissue volume was permeated during each test ensuring sufficient infusion. A significant increase in velocity and decrease in permeability was observed with increasing fluid pressure gradient (Table 3.2) ($p < 0.001$). Furthermore, a significant reduction in fluid velocity ($p \leq 0.001$) and k ($p \leq 0.001$) was observed when 3M NaCl was permeated compared to both 0M and 0.15M NaCl.

Whilst there was no significant difference between v and k for 0M and 0.15M (p > 0.05) average results for the former were consistently lower for all pressure gradients (Figure 3.8). The stress-strain relationship for this tissue in each solution dictated that the stretch ratio of the tissue reduced with increasing applied fluid pressure, with greater flow-induced deformation occurring in the hypertonic case (Table 3.3). This hypothesised flow induced deformation serves to lower the permeability of the tissue.
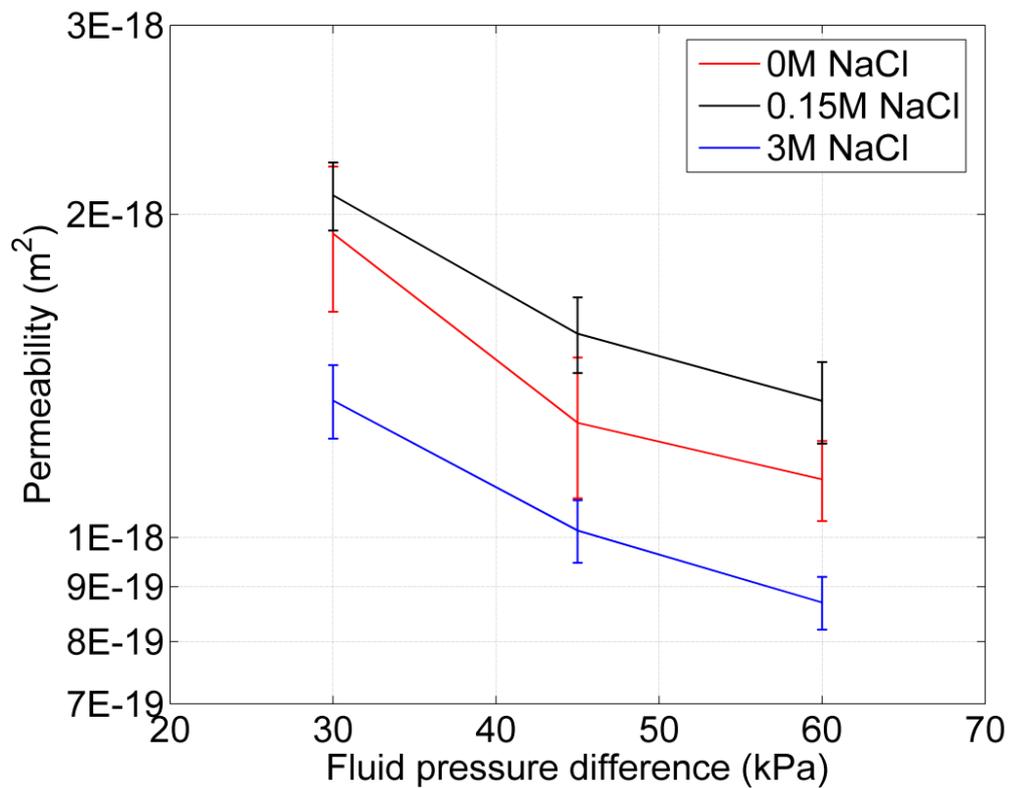
Figure 3.8 Apparent permeability results for 0M, 0.15M and 3M NaCl permeating solutions.

ΔP (kPa)	0M v ($\times 10^{-8}$ m/s)	0M k ($\times 10^{-18}$ m^2)	0.15M v ($\times 10^{-8}$ m/s)	0.15M k ($\times 10^{-18}$ m^2)	3M v ($\times 10^{-8}$ m/s)	3M k ($\times 10^{-18}$ m^2)
30	5.31 ± 2.74	1.92 ± 0.84	6.62 ± 1.67	2.08 ± 0.43	2.90 ± 0.57	1.34 ± 0.32
45	5.31 ± 2.67	1.25 ± 0.55	7.31 ± 1.61	1.54 ± 0.35	3.31 ± 0.66	1.02 ± 0.19
60	6.21 ± 1.84	1.17 ± 0.28	8.41 ± 1.88	1.34 ± 0.33	3.79 ± 0.75	0.87 ± 0.14

Table 3.2 Direct permeation results for each of the external solutions. v is the flow velocity and k is the apparent permeability.

ΔP (kPa)	0.15M v ($\times 10^{-8}$ m/s)	0.15M k ($\times 10^{-18}$ m^2)	0.15M Predicted λ	0.15M k_{adj} ($\times 10^{-18}$ m^2)	3M v ($\times 10^{-8}$ m/s)	3M k ($\times 10^{-18}$ m^2)	3M Predicted λ	3M k_{adj} ($\times 10^{-18}$ m^2)
30	6.62 ± 1.67	2.08 ± 0.43	0.90	1.88 ± 0.39	2.90 ± 0.57	1.77 ± 0.46	0.57	1.03 ± 0.23
45	7.31 ± 1.61	1.54 ± 0.35	0.74	1.14 ± 0.26	3.31 ± 0.66	1.34 ± 0.32	0.45	0.61 ± 0.12
60	8.41 ± 1.88	1.34 ± 0.33	0.62	0.83 ± 0.21	3.79 ± 0.75	1.18 ± 0.19	0.37	0.44 ± 0.07

Table 3.3 Direct permeation results for isotonic and hypertonic external solutions. v is the flow velocity; k is the unadjusted apparent permeability and k_{adj} data pertain to the analysis based on the predicted flow induced deformation (λ) of the samples

3M ΔP_{eff} (kPa)	0M ΔP_{eff} (kPa)	0M $\Delta\pi$ (kPa)	0M % increase ΔP_{eff}	0.15M ΔP_{eff} (kPa)	0.15M $\Delta\pi$ (kPa)	0.15M % increase ΔP_{eff}
30	43.0 ± 18.8	-13.0 ± 18.8	43	46.6 ± 9.6	-16.6 ± 9.6	55
45	56.5 ± 23.9	-11.5 ± 23.9	26	68.6 ± 15.7	-23.6 ± 15.7	52
60	78.2 ± 19.0	-18.2 ± 19.0	31	92.4 ± 22.8	-32.4 ± 22.8	54

Table 3.4 The effective fluid pressure difference and osmotic pressure difference across the sample as a function of the applied fluid pressure (mean ± SD).

Associating the change in fluid velocity with an effective fluid pressure difference, Table 3.4 demonstrates that both fixed charge gradients and mobile ion gradients combine to increase the effective pressure by between 50 and 55%. Of this 55%, over half (between 26 and 43%) can be associated with fixed charges, with the remaining related to mobile ion gradients.

3.5.   Discussion

An experimental setup was developed to determine the influence of mechano-electrochemical effects on fluid flow in the NP. Permeating solutions of differing salinity were infused through tissue samples at 30, 45 and 60kPa in a random sequence. The permeability for each solution, at each pressure gradient was calculated at equilibrium. The main finding of this study is that if a fluid pressure gradient exists across a tissue then, in the physiologic condition there exists an ionic osmotic pressure gradient, which is comprised of a fixed charge gradient, a mobile ion gradient and an electric potential gradient. This phenomenon can augment fluid flow by up to 55% of the applied fluid pressure, whereby fixed charges are responsible for 26-43% and the mobile ion gradient responsible for 12-26%.

Assuming an initial homogenous vertical distribution of PG in the tissue sample, this suggests significant strain gradients develop across the sample as a result of applied fluid pressure gradients. This provides the first empirical evidence for the existence of localised deformation gradients existing within cartilaginous tissue. Indeed, the strain resultant fixed charge and mobile ion gradients serve to lessen localised deformations, attracting fluid flow into regions of compaction, as depicted in Figure 3.9. Since, under physiological loads, deformations are predicted to occur mainly at

the boundaries (Mow et al., 1980) and that the disc cell density is greatest in these regions (Stairmand et al., 1991), this may be an important mechanism for reducing the strain experienced by the cells and thus maintaining cell viability (Setton and Chen, 2005).

Fluid flow, and thus apparent permeability, was found to be lowest when 3M NaCl was permeated, due to the high mobile ion concentration of this solution rendering all gradients, except the fluid pressure, negligible, thus leaving the flow to be representative solely of the intrinsic tissue permeability. Fluid flow increased for the same fluid pressure differences when 0M NaCl was permeated, compared to 3M, due to only the mobile ion gradients being rendered negligible but retaining the effects of the fixed charges. Whereas, permeating 0.15M NaCl left all gradients in situ and resulted in the greatest fluid velocity. This result is entirely in keeping with quadriphasic theory (Huyghe and Janssen, 1997).

The reduction in apparent permeability with increased applied fluid pressure is in keeping with the results obtained from direct permeation experiments on AC (Mansour and Mow, 1976) and bovine NP (Heneghan and Riches, 2008a). The fluid pressure increases tissue compaction of the collagen and proteoglycan network which will increase the resistance to the flow of fluid through the tissue. This again demonstrates the importance of using a strain dependent permeability value in mathematical models.

This study has quantified an important constitutive relationship for cartilaginous tissue. Modelling that includes mobile ions as separate phases, together with fixed charges associated with the concentration of PG's in the sample, is important for

describing fluid flow within tissue. If this relationship is not employed within a model then this may have a consequence of misreporting fluid flow within the tissue, with important ramifications for the convective transport of metabolites in the tissue. It may also lead to the overestimation of localised compressive strain with potential consequences for studies into cell mechanobiology.

The permeability values achieved in this study, in the isotonic case, are very similar to those measured previously for this tissue (Heneghan and Riches, 2008a) (Table 3.5). Typically, experiments which determine permeability through permeation tests do not adjust for flow-induced compression (Gu et al., 1999b, Heneghan and Riches, 2008a). The use of Darcy's law, when calculating tissue permeability, relies on the assumption of constant tissue thickness throughout the experiment. The current configuration was not able to quantify sample height changes due to the applied fluid pressure; however, by assuming that the fluid pressure gradient was equivalent to an applied mechanical stress, a mathematical estimate of the flow induced deformation during the 0.15M and 3M NaCl infusions was made. The stress - strain relationship of the tissue was applied to experimental data whilst utilising the parameters defined by Heneghan and Riches (2008b), and the experimentally determined permeability values adjusted accordingly. Since the aggregate modulus of the tissue decreases when ionic gradients are rendered negligible (Heneghan and Riches, 2008b); the mechanical stress due to the applied fluid pressure will compress the tissue more than in the isotonic case. An increased compression will reduce permeability, further increasing the difference between the hypertonic and isotonic conditions, which will serve to further increase the importance of the fixed charge and mobile ion gradients in affecting fluid flow. It can be concluded that the fluid velocity augmentation

calculated here is a minimum, and the actual augmentation may be significantly greater.
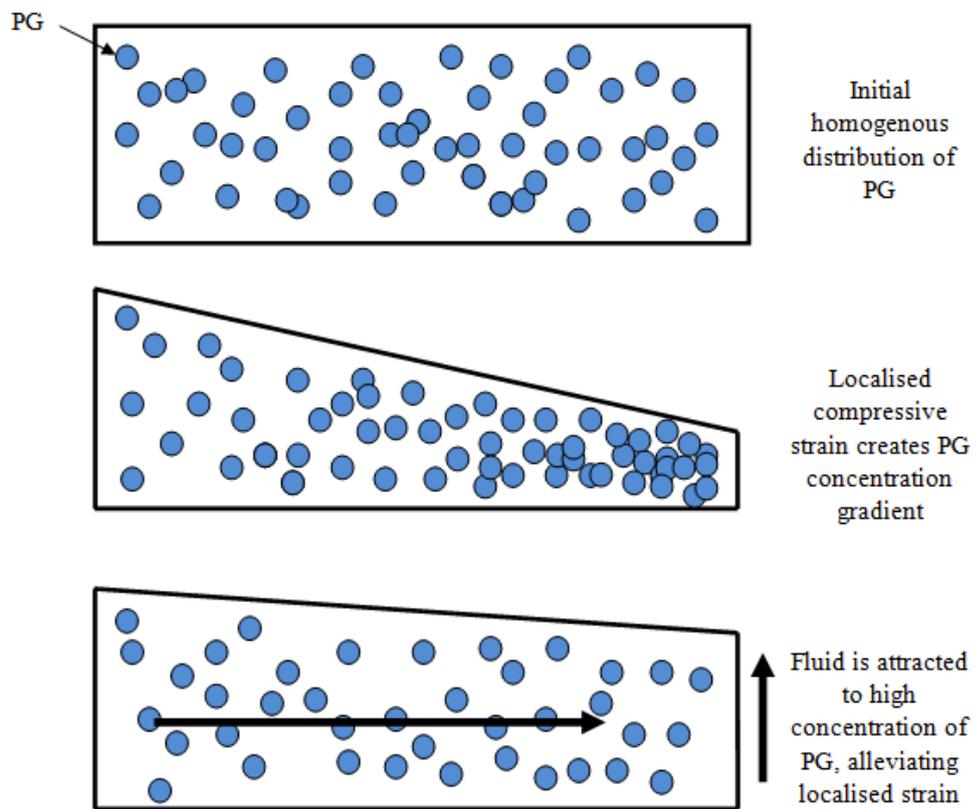
Figure 3.9 Attraction of fluid to regions of high localised compressive strain via PG gradients.

Study	Tissue	Method	λ	Permeability $(m^4/N.s) \times 10^{-15}$
Current	Bovine NP	Direct permeation	0.9 Estimated	2.05
Heneghan and Riches (2008)	Bovine NP	Direct permeation	0.95	1.74
Gu et al. (1999)	Human AF	Direct permeation	0.71	1.53
Perie et al. (2005)	Bovine NP	Linear biphasic model	0.95	1.20
Perie et al. (2005)	Bovine NP	Non-linear biphasic model	0.95	0.60
Perie et al. (2005)	Bovine AF	Linear biphasic model	0.95	0.30
Perie et al. (2005)	Bovine AF	Non-linear biphasic model	0.95	0.90
Johannessen et al. (2005)	Human NP	Linear biphasic model	0.95	0.90
Riches et al. (2002)	Human lumbar disc	Poroelastic model	-	0.2-0.91

Table 3.5 Comparison of literature values of NP and AF permeability.

Degeneration of the disc is associated with a loss of proteoglycan and thus a reduction in the overall ionic osmotic pressure. Whilst the ionic osmotic pressure was artificially reduced by permeating a hypertonic solution, the results cannot be extrapolated to the degenerate case, since the proteoglycans are present and still being a physical barrier to fluid flow, even if they are not providing a mechano-electrochemical gradient.

3.6.   Experimental artefacts

One possible source of error in this experiment is the potential leaching of PGs from the sample during testing. As each sample was permeated for approximately 6h (2h for each pressure condition, randomly counterbalanced), permeability was analysed with respect to the running order of each pressure condition. If leaching occurred, one would expect to witness a reduction in permeability with running order. However, there was no significant difference when analysed (Appendix 9.1), leading to the conclusion that there was negligible leaching.

Another possible source of error is a potential decalibration of the pressure transducer over time. In order to maintain accurate regulation of fluid pressure in the system, the pressure transducer was recalibrated every month. This was conducted in situ with the permeation rig as detailed in section 3.3.

A scanning electron microscope (model TM-1000, Hitachi, Tokyo, Japan) was used to image the surface of samples infused with 3M NaCl to elucidate the extent of salt crystal deposition in the tissue during infusion. Excessive amounts of crystal deposition may have resulted in the rupturing of tissue fibres which may have affected the flow of solution through the sample.

Low magnification images taken of the upstream surface of samples tested in 3M NaCl indicated large amounts of deposition (Figure 3.10). The larger of these crystals will have formed after testing, during subsequent dehydration of the sample during storage, and will not have affected the tissue during infusion. It is possible, however, that the smaller crystals may have been present. However, images taken at higher magnification, where tissue fibres are visible, indicate that tissue rupturing did not occur (Figure 3.11). Unfortunately it was not possible to image subsurface salt deposition; however, since the upstream surface of the tissue was exposed to the highest fluid pressure gradient, fibre rupturing would have been most evident on this surface. Since there was no visible rupturing on the upstream surface, it is assumed that this was the case for the full thickness of the sample. Consequently, the flow velocities produced in this experiment are considered valid.
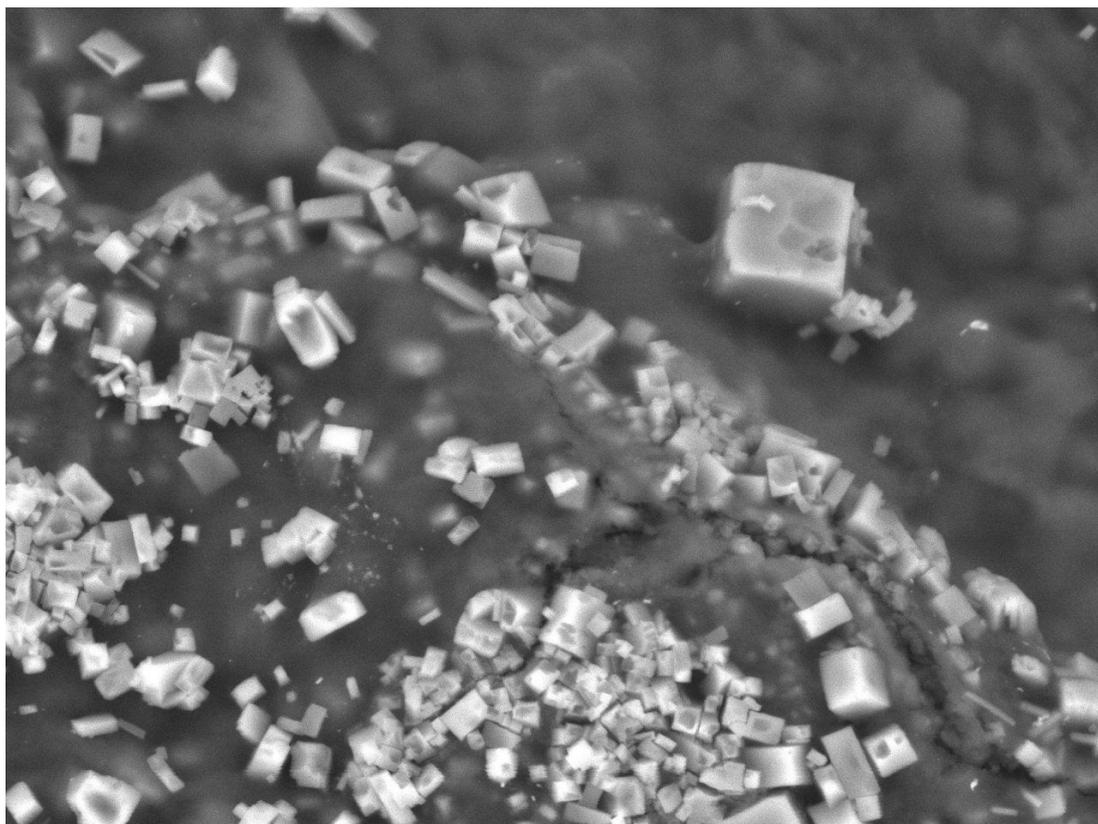
TM-1000_2232   2010/11/17 15:13 L   30 um

Figure 3.10 SEM image showing salt crystals deposited on a sample surface after 3M NaCl infusion.
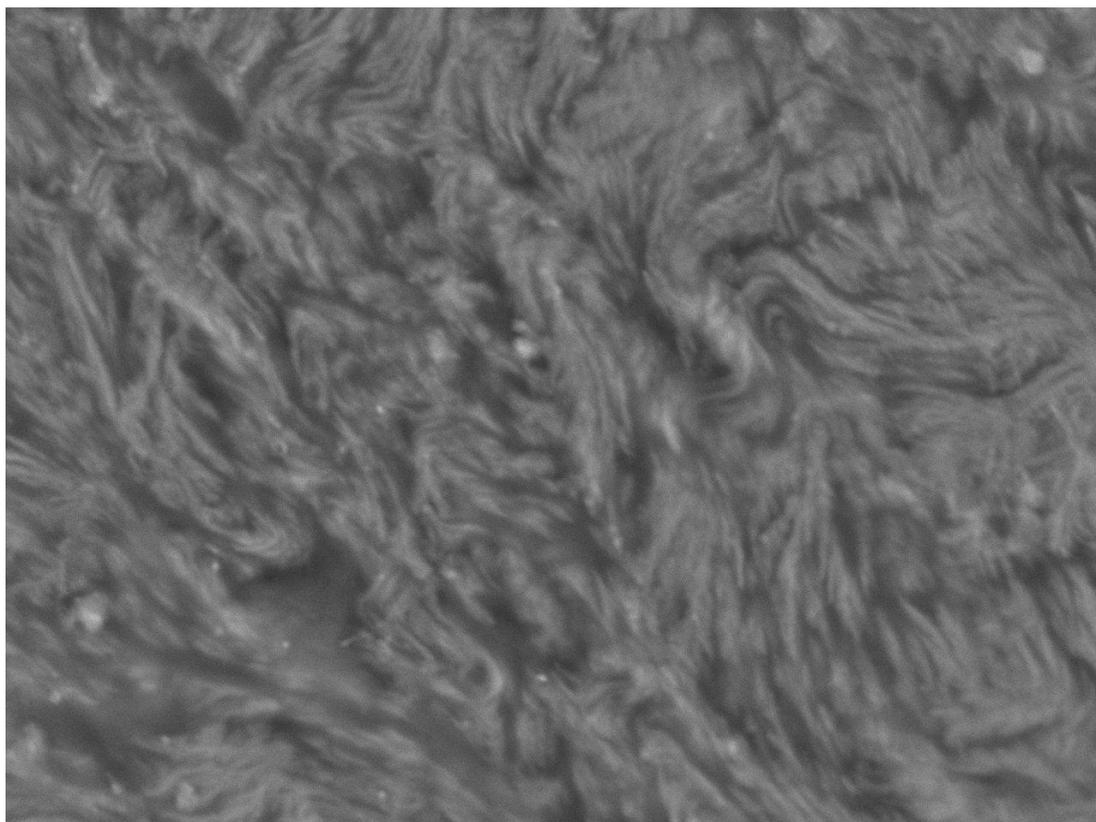
TM-1000_2237   2010/11/17 15:26 L   30 um

Figure 3.11 SEM image showing no visible signs of tissue rupture after 3M NaCl infusion.

3.7. Conclusions

This experimental chapter has provided evidence that fluid velocity may be augmented through tissue via ionic osmotic pressure gradients which consists of fixed charge, mobile ion and electrical potential gradients. When combined, these gradients can augment flow through tissue by up to 55% of the applied pressure compared to fluid pressure alone. This demonstrates the importance of using a constitutive equation that includes mobile ions and fixed charges as separate phases when modelling cartilaginous tissue in order to better describe the convective transfer and strain distribution within the tissue, which are both important input conditions for future mechanobiological studies. The considerable influence of electrochemical effects in the disc may lead to complexities when considering the signals which control cell biosynthesis. The experimental results presented in this chapter demonstrate the influence of electro-chemical interactions on fluid transport, which may suggest to the use of non invasive electro-therapy treatments whereby an applied electric potential is administered to encourage convective nutrient transport in degenerated discs.

4. Finite element modelling of the influence of mechano-electrochemical phenomena on fluid flow in the nucleus pulposus

4.1. Introduction

Much of current understanding of disc mechanics has come from finite element (FE) modelling. The accuracy of this approach, however, relies on appropriate material characteristics being modelled by the numerical schemes i.e. material constitutive behaviour. In order to have complete faith in a model, FE simulations must be compared to experimental data from isolated tissue (Stokes et al., 2010).

Biological tissues are often modelled as porous media which consist of a solid matrix and interstitial fluid. Numerous models adopt this framework but individual models usually augment the model behaviour with further complexity (see chapter 2.7). There is a requirement for the incorporation of the disc's complex mechanical and chemical properties into FE models as they aid the design of artificial devices, allow for the assessment of potential tissue engineered replacements and support our understanding of mechanical and biological functioning in the disc.

As discussed in chapter 3, due to the disc's avascular nature, fluid flow in the disc is essential for the transport of nutrients as well as dominating the mechanical properties of the disc. Understanding the transport of both interstitial fluid and solutes in the disc is of extreme importance as these mechanisms may be involved in a range of biological processes (Ateshian et al., 2011). Currently, several models which are used for describing full spine biomechanics adopt a simplistic approach to

the IVD and generally utilise a single-phase material definition, therefore neglecting fluid flow effects (Ehlers et al., 2009). Simplifying a model in such a way may have ramifications when investigating how disc mechanics translates to spinal segment motion and load bearing potential. To account for the effects of fluid flow within the disc, biphasic models have been developed which incorporate interstitial fluid within a porous solid matrix (Mow et al., 1980, Argoubi and Shirazi-Adl, 1996, Iatridis et al., 1998, Ayotte et al., 2000, Li et al., 1999, Riches et al., 2002). Biphasic models have provided great insight to internal disc mechanics, however, the limitations in describing localised and global fluid flow when considering solid-solute interactions are yet to be fully investigated.

As discussed in chapter 3, mechano-electrochemical effects greatly influence fluid flow within the disc and biphasic models do not account for such phenomena. The transport of ions in a charged, deformable matrix has been an area of particular interest in the field of tissue biomechanics. Mechano-electrochemical phenomena, based on the triphasic theory of Lai et al. (1991), the quadriphasic theory of Huyghe and Janssen (1997), and the multi-electrolyte theory of Gu et al. (1998), concerned with the transport of charged ions in a charged solid matrix have been implemented in FE models by several authors which are applicable to infinitesimal strains (Frijns et al., 1997, Sun et al., 1999, Yao and Gu, 2007a, Magnier et al., 2009) and finite deformations (van Loon et al., 2003). However, the validity of these models in describing fluid flow within the disc is yet to be determined due to a lack of empirical data. The background to biphasic and triphasic modelling was discussed in section 2.7, however, the details with regards to the frictional interactions between

charged solutes and the solid matrix and how these interactions may affect fluid flow in the disc will be discussed here in more detail.

At equilibrium, the concentrations of dissolved ions in the interstitial fluid is given by the Donnan ion distribution law (Donnan, 1924) which states that a balance must exist between the electric potential of the ions in the external solution and the ions in the tissue (Lai et al., 1991, Gu et al., 1998). These ions may be transported within the tissue by a number of mechanisms; convection of the interstitial fluid (due to fluid pressure gradients), diffusion through the fluid (due to ion concentration gradients) or via conduction (due to an electric field) (Lai et al., 2000). Conduction occurs when a charged particle is subjected to a Coulomb force when in the presence of an electric potential. As such, electric potential is considered to play an important role in governing fluid flow within the disc, and is thought to be associated with variations in tissue composition which alters dramatically with degeneration and deformation (Gu et al., 1999c). Since FCD is a function of PG content, electric potential is related to the tissue deformation gradients associated with applied fluid pressure during a permeation experiment as discussed in chapter 3.

The overall electric potential within a charged hydrated tissue consists of two electro-chemical phenomena which have the potential to individually and aggregately influence fluid flow; streaming potential and diffusion potential. In a charged hydrated tissue, an electric potential difference will occur within the NP when a fluid containing charged ions is passed through, known as the streaming potential (Gu et al., 1993), and is caused by the high concentration of negatively charged PGs within the tissue. The streaming potential of AC has been studied in relation to a number of loading conditions, and has been found to be correlated to

fixed charge density (FCD), stiffness, ion concentrations, ion diffusivity and hydraulic permeability (Chen et al., 1997, Gu et al., 1993). A diffusion potential arises when an inhomogeneous distribution of FCD causes a concentration gradient of cations and anions. The diffusion tendency of the cations and the anions are in opposite directions resulting in a separation of the oppositely charged ions. Consequently, a gradient of electric potential exists in the tissue i.e., the diffusion potential which influences fluid and ion transport (Gu et al., 1993, Lai et al., 2000). A triphasic investigation into the nature of these electric fields in AC was carried out by Lai and co-workers (2000), who reported that diffusion potential and streaming potential effects compete against one another for governance inside the tissue. An interesting finding of this study was that, when FCD concentrations are the same, streaming potential dominates the electric field in tissues with higher aggregate modulus whereas diffusion potential dominates the electric field in tissues with lower aggregate modulus as a result of greater deformation and FCD gradients.

Gu et al. (1993) and more recently Lai et al. (2000) used triphasic theory to study the convection and diffusion of interstitial fluid and ions in a charged hydrated soft tissue. However, the effect of solute concentration dependent mechano-electrochemical interactions on global fluid flow in the NP is yet to be comprehensively investigated by way of FE modelling. Studying the effects of such phenomena will help elucidate how fluid flow in the disc is affected by physical alterations such as deformation and degeneration and allow for the advancement of possible tissue engineered replacements and potentially non invasive disc treatments. Since both biphasic and triphasic models are frequently applied in the disc and

cartilage literature, it is useful to compare the predicted mechanical responses of each to experimental data (Ateshian et al., 2004).

4.2. Aims and hypotheses

The objective of this study was to develop both biphasic and triphasic poroelastic FE models capable of describing the flow of interstitial fluid and solutes through the solid matrix of the NP. The permeation of NaCl solutions of differing salinity, via an applied fluid pressure, was modelled whilst incorporating two important phenomena: (1) Solute transport through a deformable solid matrix, including strain-induced alterations in permeability and stiffness. (2) Consideration of the mechano-electrochemical effect of solute concentration. Results are compared to experimental data from chapter 3, and recommendations made for the future use of poroelastic models in describing fluid flow in the NP. It was hypothesised that FCD and electric potential gradients play an important role in governing fluid flow within the NP and consequently a triphasic poroelastic model should be used when modelling fluid flow in cartilaginous tissue.

4.3. Methods

4.3.1. FEBio

FEBio is a nonlinear finite element program which has been specifically developed for the solving of biomechanical problems, and as such has been used in this study for modelling the NP. It supports two analysis types; quasi-static and dynamic. It is an open source program downloadable from *http://mrl.sci.utah.edu/software*.

The program allows for the implementation of an array of materials to custom geometries. The following sections will describe the materials, geometry, constraints and reiterate the governing equations, obtained from the program's theory manual, utilised by the software when applied to the current study.

4.3.2. FEBio Biphasic-solute material

The biphasic-solute material definition may be used to model the flow of a solvent and a solute through a non-charged porous material which includes diffusion and convection. Quasi-static conditions are assumed for momentum balance by neglecting the inertia effects. As the solute permeates through the porous material, frictional interactions between the solid matrix and solvent may occur which may affect solute transport. These frictional interactions are accounted for by a diffusivity term which includes; free diffusivity representing the diffusivity of the solute in the solvent only, and mixture diffusivity with represents the diffusivity of the solute in the solid matrix.

The governing equations adopted by FEBio for the modelling of the transport of a solute through a non-charged deformable porous media are based on the mixture theory by Mauck et al. (2003) and Ateshian et al. (2006). The reader is referred to these manuscripts for a full description of the theory; however, the details pertinent to the analyses conducted in this study will be reiterated in the same nomenclature in a similar fashion to that of Ateshian et al. (2011).

The mixture constituents are the porous solid matrix, $\alpha = s$, the solvent, $\alpha = w$, and the solute, $\alpha = u$ whilst the interstitial fluid pressure is p, and the solute concentration is c. The mixture stress is described by the Cauchy stress tensor

$$\sigma = -p\mathrm{I} + \sigma_\varepsilon \tag{4.1}$$

where I is the identity tensor and σ_ε is the elastic stress in the solid matrix. The mixture is compressible due to the ability of the pores to collapse when fluid exudes the matrix. Accordingly, the balance of linear momentum for the mixture is

$$\nabla\sigma = -\nabla p + \nabla\sigma_e = 0 \tag{4.2}$$

The balance of linear momentum equations for the solvent and solute are given by

$$\rho^w \nabla\tilde{\mu}^w + f^{ws} \cdot (v^s - v^w) + f^{wu} \cdot (v^u - v^w) = 0 \tag{4.3}$$

$$-\rho^u \nabla\tilde{\mu}^u + f^{us} \cdot (v^s - v^u) + f^{uw} \cdot (v^w - v^u) = 0 \tag{4.4}$$

where ρ^α is the apparent density (mass of constituent α per volume of the mixture), v^α is the velocity of constituent α and $\tilde{\mu}^\alpha$ is the mechano-chemical potential. $f^{\alpha\beta}$ is the diffusive drag tensor between α and β, representing the momentum exchange via frictional interactions, satisfying $f^{\alpha\beta} = f^{\beta\alpha}$.

The mechano-chemical potential, $\tilde{\mu}^w$, of the solvent is given by

$$\tilde{\mu}^w = \mu_0^w(\theta) + \frac{1}{\rho_T^w}(p - R\theta\Phi c) \tag{4.5}$$

where μ_0^w is the solvent chemical potential, ρ_T^w, is the true density of the solvent (mass of α per volume of α), c is the solute concentration and Φ is the osmotic coefficient which represents by how much the solute concentration affects the solvent chemical potential.

The mechano-chemical potential of the solute is almost equal to its chemical potential because of assumed negligible solute volume fraction. Momentum and energy balances which are evaluated across a boundary surface in the biphasic-solute material require that the mechano-chemical potentials of the solvent and solute be continuous across said surface. These requirements are enforced by defining the effective fluid pressure, $\tilde{p}$, and effective solute concentration, $\tilde{c}$, as

$$\tilde{p} = p - R\theta\Phi c \tag{4.6}$$

$$\tilde{c} = \frac{c}{\tilde{\kappa}} \tag{4.7}$$

where $\tilde{\kappa}$ is the effective solubility due to steric volume exclusion and electrostatic interactions.

The biphasic-solute flux relations, where w is the volumetric flux of the solvent and j is the molar flux of the solute, are given by

$$\text{w} = -\tilde{\text{k}} \cdot \left(\nabla\tilde{p} + R\theta\frac{\tilde{\kappa}}{d_0}\text{d} \cdot \nabla\tilde{c}\right) \tag{4.8}$$

where

$$\tilde{\text{k}} = \left[\text{k}^{-1} + \frac{R\theta}{\varphi^w}\frac{\tilde{\kappa}c}{d_0}\left(\text{I} - \frac{\text{d}}{d_0}\right)\right]^{-1} \tag{4.9}$$

is the effective hydraulic permeability of the interstitial fluid (solvent and solute). k is the hydraulic permeability of the solvent through the porous solid matrix, d is the solute diffusivity through the mixture incorporating solvent-solid frictional

interactions, d_0 is the solute free diffusivity incorporating solvent-solute frictional interactions and φ^w is the solid matrix porosity.

4.3.3. FEBio Triphasic-solute material

A triphasic material is an extension to the biphasic-solute material whereby charged or neutral solutes may be contained in the mixture. Additionally, the solid matrix may also be charged (allowing for the incorporation of FCD) affecting the interaction between solute and solid matrix considerably. The triphasic material model is based on the mixture theory of Lai et al. (1991) and considers the charged solid phase, the incompressible fluid phase, and ion phase with two monovalent ion species, i.e., anion (-) and cation (+) (Sun et al., 1999).

When an electrically charged mixture undergoes deformation, the electro-chemical interactions between the solid and fluid phases may result in numerous mechano-electrochemical phenomena such as FCD, electric potential and streaming potential gradients. These phenomena may have significant implications when considering the mechanical response of the tissue to deformation as well as fluid flow mechanisms.

The reader is referred to the biphasic-solute material review in section 4.3.2 for a description of the general conditions associated with biphasic and triphasic analyses. However, the governing equations which describe the transport of a charged solute through a charged porous matrix will be described here.

The mechano-chemical potential of the solvent is given by

$$\tilde{\mu}^w = \mu_0^w(\theta) + \frac{1}{\rho_T^w}\left(p - p_0 - R\theta\Phi\sum_\alpha c^\alpha\right) \qquad (4.10)$$

where $\mu_0^w(\theta)$ is the solvent chemical potential in the standard state, θ is the absolute temperature, ρ_T^w is the true density of the solvent (invariant due to incompressibility), p is the fluid pressure, p_0 is the fluid pressure in the standard state, R is the universal gas constant, Φ is the non-dimensional osmotic coefficient and c^α is the solution volume based concentration of solute α.

The mechano-chemical potential of a charged solute, α, is given by

$$\tilde{\mu}^\alpha = \mu_0^\alpha(\theta) + \frac{R\theta}{M^\alpha}\left(\frac{z^\alpha Fc}{R\theta}(\psi - \psi_0) + \ln\frac{\gamma^\alpha c^\alpha}{\kappa^\alpha c_0^\alpha}\right) \qquad (4.11)$$

where $\mu_0^\alpha(\theta)$ is the solute chemical potential in the standard state, M^α is the molar mass of the solute, γ^α is the activity coefficient, κ^α is its solubility, Fc is Faraday's constant, ψ is the electric potential of the mixture which is the resultant of all charges in the tissue combined with any electric and/or magnetic effects which may be exerted on the tissue, and ψ_0 is the electric potential in the standard state.

In triphasic analyses, electroneutrality must be satisfied at every point during the continuum. Therefore, the sum of all electrical charges must reduce to zero. The solvent is always considered neutral, so the electroneutrality condition can be written as

$$c^f + \sum_\alpha z^\alpha c^\alpha = 0 \qquad (4.12)$$

where c^f is the FCD and z^α is the charge number of solute α. The fluid pressure and solute concentrations are not continuous across the boundaries; therefore the following continuous variables are used as nodal degrees of freedom

$$\tilde{p} = p - R\theta\Phi\sum_{\alpha \neq s,w} c^\alpha \tag{4.13}$$

which is the effective fluid pressure, and

$$\tilde{c}^\alpha = c^\alpha/\tilde{\kappa}^\alpha \tag{4.14}$$

which is the effective solute concentration where $\tilde{\kappa}^\alpha$ is the partition coefficient which is related to the effective solubility and electric potential by

$$\tilde{\kappa}^\alpha = \hat{\kappa}^\alpha exp\left(-\frac{z^\alpha Fc\psi}{R\theta}\right) \tag{4.15}$$

The solvent, w, and solute, j^α, flux relations are given by

$$w = -\tilde{k} \cdot \left(\nabla\tilde{p} + R\theta\sum_{\beta \neq s,w}\frac{\tilde{\kappa}^\beta}{d_0^\beta}d^\beta \cdot \nabla\tilde{c}^\beta\right) \tag{4.16}$$

and

$$j^\alpha = \tilde{\kappa}^\alpha d^\alpha \cdot \left(-\varphi^w\nabla + \frac{\tilde{c}^\alpha}{d_0^\alpha}w\right) \tag{4.17}$$

where

$$\tilde{k} = \left[k^{-1} + \frac{R\theta}{\varphi^w}\sum_{\alpha \neq s,w}\frac{c^\alpha}{d_0^\alpha}\left(I - \frac{d^\alpha}{d_0^\alpha}\right)\right]^{-1} \tag{4.18}$$

4.3.4. Biphasic and triphasic solid phase and permeability constitutive relations

4.3.4.1.   *Solid phase constitutive relation*

Both the biphasic and triphasic models adopt the same solid constitutive relations for modelling the deformable solid matrix of the tissue, whilst incorporating the additional properties discussed above. The chosen solid type is based on the non-linear framework of Holmes and Mow (1990) which allows for the modelling of strain-dependent stiffness. This isotropic, hyper elastic material model has been implemented successfully in modelling the solid matrix of both AC (Holmes and Mow, 1990, Ateshian et al., 1997) and IVD tissue (Iatridis et al., 1998, Heneghan and Riches, 2008b).

The stress-strain relationship for this material is given by

$$\sigma = \frac{1}{2} H_{A0} \left(\frac{\lambda^2 - 1}{\lambda^{2\beta + 1}} \right) e^{\beta(\lambda^2 - 1)} \tag{4.19}$$

where σ is the total stress in the tissue, H_{A0} is the zero-strain aggregate modulus and can be considered as the modulus in confined compression, λ is the axial stretch and β is a non-dimensional parameter which measures the sensitivity of σ to large strains.

4.3.4.2.   *Permeability constitutive relation*

Both the biphasic and triphasic models adopt the same permeability constitutive relation for modelling the strain-dependent permeability of the tissue. The chosen

model is based on the non-linear framework of Holmes and Mow (1990) and is given by

$$k(\lambda) = k_0 \left(\frac{\lambda-\phi_0}{1-\phi_0}\right)^{\kappa} e^{\frac{1}{2}M(\lambda^2-1)} \tag{4.21}$$

where λ is the axial stretch, k_0 is the zero strain permeability, M and κ are non-dimensional parameters relating k to λ, and ϕ is the tissue porosity; the subscript 0 indicates zero strain values. Heneghan and Riches (2008a) validated this strain-dependent permeability model by fitting it to data obtained from permeation experiments on bovine NP tissue, and found an excellent fit. The parameters required for this fit were implemented into the current model.

4.3.5. Material properties of biphasic and triphasic models

Biphasic and triphasic elastic and poroelastic material properties were obtained from the literature (Table 4.1 and Table 4.2 for biphasic and triphasic properties respectively).

Poisson's ratio, v, was defined as zero to simplify the conversion between zero strain aggregate modulus, H_{A0}, and Young's modulus, E. This simplification is valid when considering the permeation protocol being modelled because the sample is confined laterally. The diffusion coefficient of solutes, D^{α}, such as small ions, in the disc and AC are smaller than those in aqueous solutions, D_0^{α} (Burstein et al., 1993, Garcia et al., 1996, Leddy and Guilak, 2003, Maroudas, 1975, Quinn et al., 2000, Torzilli et al., 1987, Urban et al., 1978). For small solutes, the diffusion coefficient in disc tissue and AC is approximately 35−60% of the coefficient in aqueous solution, with

these coefficients reducing with increased tissue compression (Burstein et al., 1993, Leddy and Guilak, 2003). As such, this scaling factor has been used to determine D_0^{α}. The solubility term, κ^{α}, used in the model represents the fraction of the pore volume which may be occupied by the solute. Therefore, since the relative solute to solvent volume fraction is negligible, $\kappa^{\alpha} = 1$ in the standard state (the full pore volume is available to the solute).

Biphasic Material Property	Units	Value	Source
$\varnothing_0$	-	0.2	Roberts et al. (1989)
H_{A0}	MPa	0.3	Périé et al. (2005)
ν	-	0	-
β	-	0.256	Heneghan and Riches (2008b)
k_o	mm^4/N.s	0.002	Farrell and Riches (2012)
M	-	2.41	Heneghan and Riches (2008b)
κ	-	0.48	Heneghan and Riches (2008b)
Φ	-	0.971	Frijns et al. (2003)
D_0^+	mm^2/s	1.00×10^{-03}	Scaled from D$^+$
D^+	mm^2/s	4.40×10^{-04}	Frijns et al. (2003)
κ^+	-	1	-
D_0^-	mm^2/s	1.60×10^{-03}	Scaled from D$^-$
D^-	mm^2/s	6.70×10^{-04}	Frijns et al. (2003)
κ^-	-	1	-

Table 4.1 Material properties of the biphasic FE model.

Triphasic Material Property	Units	Value	Source
$\varnothing_0$	-	0.2	Roberts et al. (1989)
FCD in reference state	mEq/L	130	Stokes et al. (2010)
H_{A0}	MPa	0.3	Périé et al. (2005)
ν	-	0	-
β	-	0.256	Heneghan and Riches (2008b)
k_o	mm^4/N.s	0.002	Farrell and Riches (2012)
M	-	2.41	Heneghan and Riches (2008a)
κ	-	0.48	Heneghan and Riches (2008a)
Φ	-	0.971	Frijns et al. (2003)
D_0^+	mm^2/s	1.00×10^{-03}	Scaled from D^+
D^+	mm^2/s	4.40×10^{-04}	Frijns et al. (2003)
κ^+	-	1	-
D_0^-	mm^2/s	1.60×10^{-03}	Scaled from D^-
D^-	mm^2/s	6.70×10^{-04}	Frijns et al. (2003)
κ^-	-	1	-

Table 4.2 Material properties of the triphasic FE model.

4.3.6. Geometry and constraints

Both the biphasic and triphasic models were modelled as a cube of side 1mm which was confined along the x and y axes. The downstream surface (A) was fully confined on all axes. The upstream surface (B) was first compressed before a fluid pressure gradient was applied to produce permeation. A mesh gradient was incorporated to reduce computational time with a finer spacing employed towards the boundaries due to hypothesised strain gradients developing in these regions.
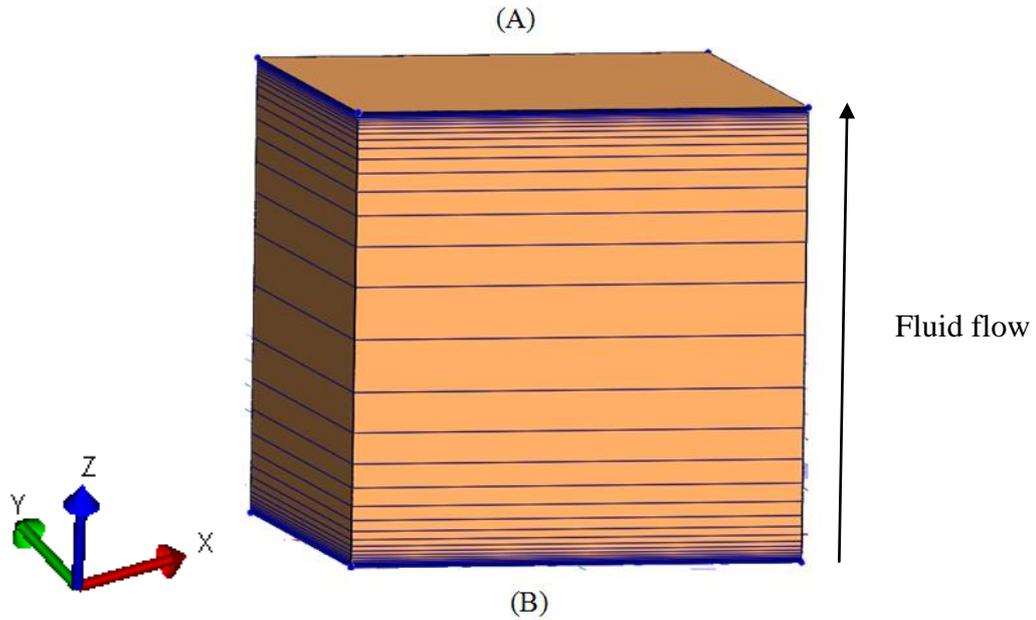
Figure 4.2 Geometry of biphasic and triphasic permeation models.

A steady-state analysis was performed on both models. The biphasic analysis consisted of 2 steps; compressive displacement of 0.1mm in the z direction on the upstream surface to create slight compressive deformation mimicking contact from the upper platen in the experimental setup, followed by the application of a fluid pressure over and above the ambient conditions on the upstream surface whilst maintaining the downstream surface pressure to zero to induce permeation. The triphasic analysis included an additional first step which ramped the FCD from 0 to -130 mEq/L, producing a Donnan osmotic pressure in the fluid as well as a Donnan electric potential in the mixture.

Each model was subjected to 30, 45 and 60kPa of fluid pressure difference on the upstream surface, and a range of external bath NaCl salinities from 0M to 3M which was in keeping with the experimental protocol conducted in chapter 3. It was not possible to replicate 0M NaCl due to the requirement of $\tilde{c}^{\alpha}>0$ to satisfy the triphasic

governing equations thus 0.001M NaCl was considered an acceptable alternative and would demonstrate similar results to the 0M case. The triphasic model required the implementation of additional initial conditions as a result of the significantly more complex governing equations employed by the material model. The initial effective solute concentrations (Na^+ and Cl^-) were set in accordance with the desired solution salinity. The effective fluid pressure, P_e, was calculated from

$$P_e = ambient\ pressure - RT\Phi \cdot osm \qquad (4.22)$$

where osm is the external solution osmolarity. The ambient fluid pressure was assumed to be zero. Table 4.3 shows the required alterations in effective pressure with changing solution osmolarity and applied fluid pressure as calculated from Eq. (4.22). Each model parameter was adjusted accordingly before computation. Ionic compounds such as sodium chloride dissociate in solution into their constituent ions, where the osmolarity is the measure of solute concentration (osm/L). NaCl dissociates into Na^+ and Cl^-, resulting in two osmoles within the solution (1M NaCl = 2Osm NaCl).

Ambient pressure	R (mJ/nmol·K)	T (K)	mM	Φ	Osm	P_e (kPa)	30kPa	45kPa	60kPa
0	8.31E-06	293	0.001	0.971	0.002	-4.73E-06	0.029995	0.044995	0.059995
0	8.31E-06	293	150	0.971	300	-0.709607	-0.67961	-0.66461	-0.64961
0	8.31E-06	293	500	0.971	1000	-2.365358	-2.33536	-2.32036	-2.30536
0	8.31E-06	293	1000	0.971	2000	-4.730716	-4.70072	-4.68572	-4.67072
0	8.31E-06	293	2000	0.971	4000	-9.461432	-9.43143	-9.41643	-9.40143
0	8.31E-06	293	3000	0.971	6000	-14.19215	-14.1621	-14.1471	-14.1321

Table 4.3 Effective fluid pressures for permeation models.

4.3.7. Data analysis

4.3.7.1. Mesh convergence analysis

In FE modelling, a finer mesh typically yields more accurate results. However, as mesh coarseness is reduced, the computational time increases which may be undesirable. A balance between mesh fineness and computational time is therefore required via a mesh convergence analysis. The method of conducting a mesh convergence analysis involved plotting the curve of a critical result, in this case fluid velocity and FCD gradient, against the mesh fineness and computational time. Figure 4.3 shows the results for the mesh convergence analysis conducted for the triphasic model which was chosen for analysis due its higher level of complexity compared to the biphasic model. Graph A indicates that there was much variance in FCD gradient until the model contained upwards of 140 nodes. Graph B, which plots the percentage change in fluid flux with increasing nodal steps, indicates there was no significant difference in results between 160 and 180 nodes (4 to 5 on x-axis). Graph C indicates that the difference in computational time was relatively small between 160 and 180 nodes. Therefore, a 180 node model was considered appropriate for this particular study, resulting in a run time of ~20 minutes on a Dell Studio laptop.

(A)

(B)

(C)
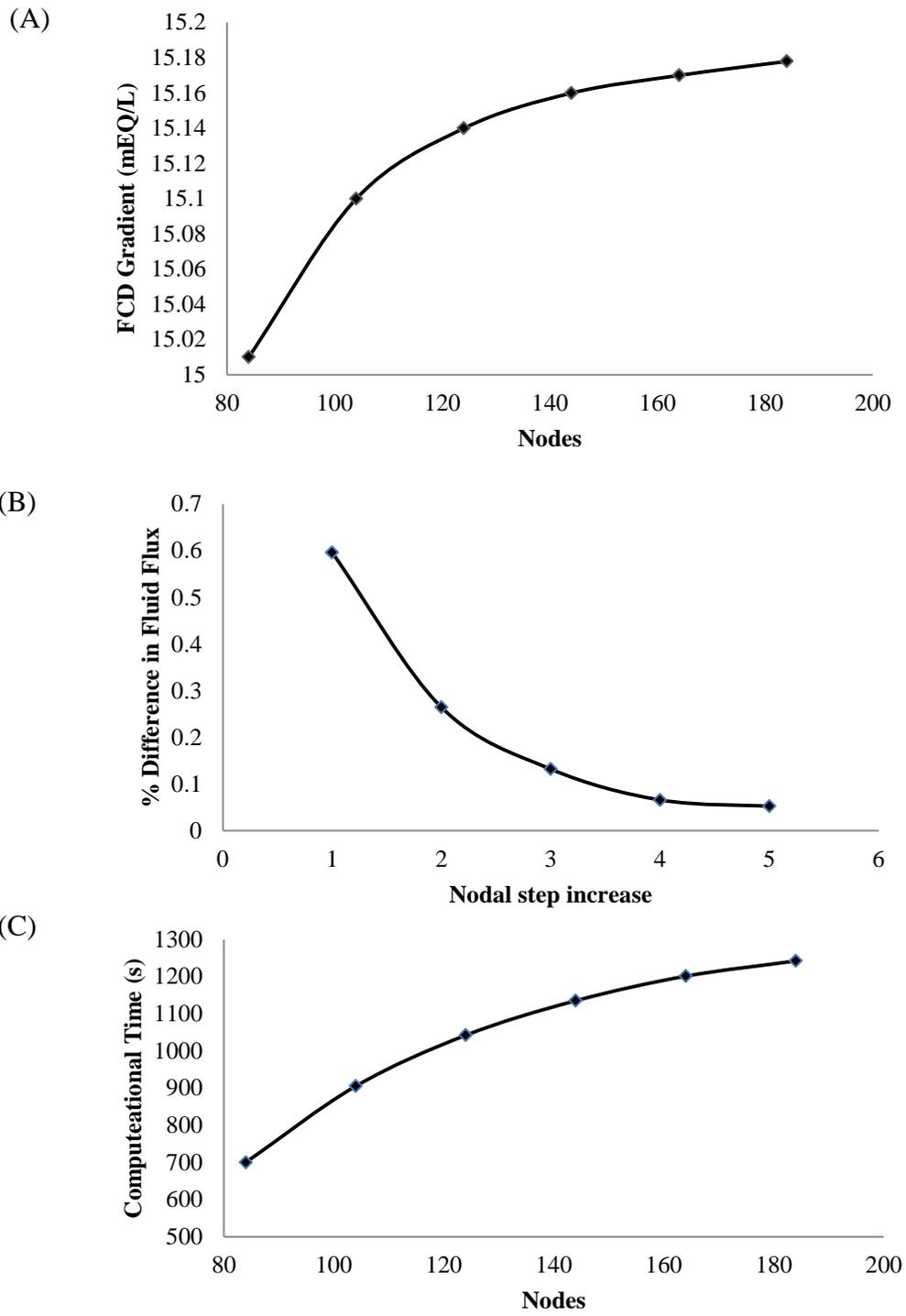
Figure 4.3 Mesh convergence results for triphasic permeation model.

4.3.8. Data analysis

A paired two sample t-test was used to for comparison between FE results and experimental data. Significance was set at $p \leq 0.05$.

4.4. Results

In this section numerical results from the biphasic-solute poroelastic (BP) model and the triphasic-solute poroelastic (TP) model are compared to the permeation experimental data presented in chapter 3. Since the FE models performed steady-state analyses, all numerical fluid velocity results are compared to experimental fluid velocities at equilibrium.

4.4.1. Biphasic poroelastic model results

The BP model demonstrated qualitative agreement with experimental results for fluid velocity, with all results falling within the same order of magnitude for all fluid pressures and solute concentrations (Figure 4.4). The experimentally observed trend in increased fluid velocities, for all solute concentrations, with increasing fluid pressure was reproduced by the model, as was the reduction in fluid velocity when the hypertonic solution was permeated compared to the hypotonic solution for all fluid pressures (Figure 4.4). However, the model failed to replicate experimental fluid velocity in the hypertonic case or the experimentally observed increase in fluid velocity associated with isotonic permeation. Figure 4.5 illustrates that fluid velocity was found to decrease non-linearly with increasing solute concentration. The effect of fluid pressure on fluid velocity was lower in the hypertonic case and highest in the hypotonic case. Model fluid velocity also appeared to be more sensitive to applied

fluid pressure than the experimental data, especially in the hypotonic and isotonic cases.

(A)

(B)

(C)
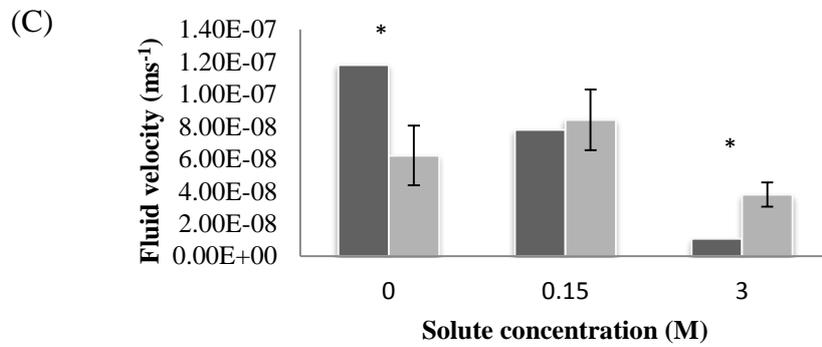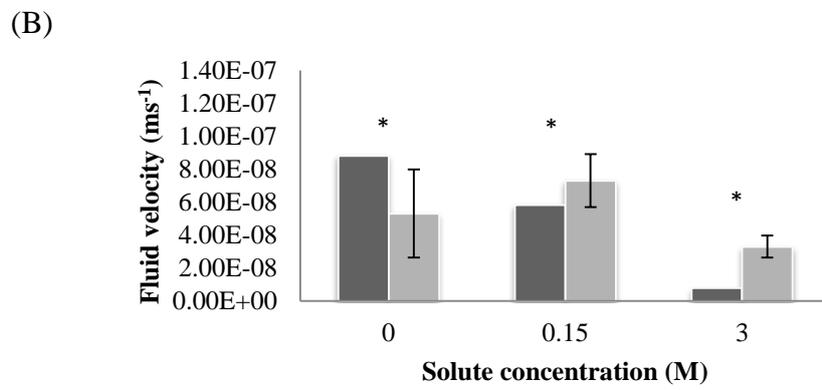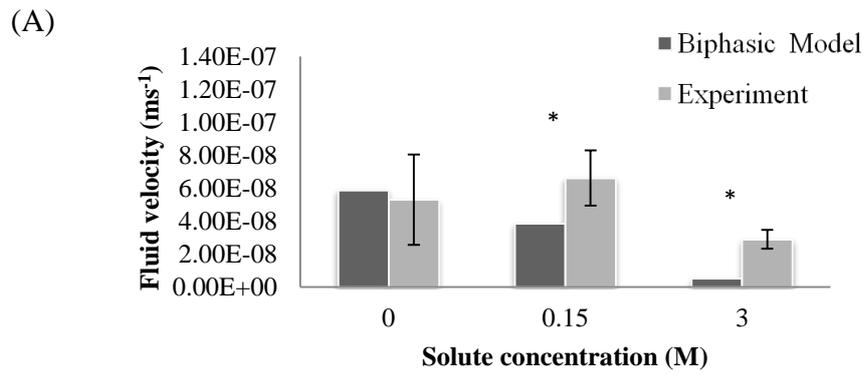
Figure 4.4 Experimental and biphasic model results. (A) 30kPa, (B) 45kPa, (c) 60kPa.
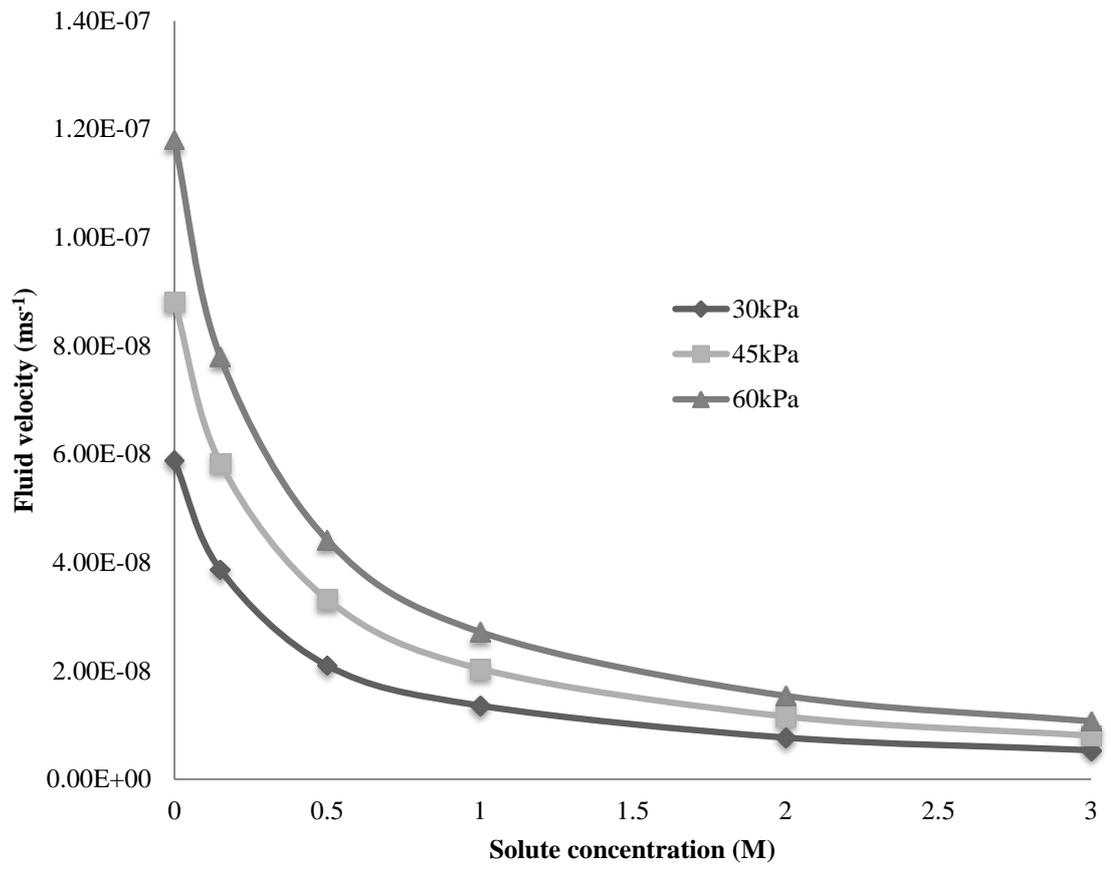
Figure 4.5 Biphasic model fluid velocity in relation to solute concentration.

4.4.2. Triphasic poroelastic model results

The TP model demonstrated agreement with experimental results for fluid velocity, with all results falling within the same order of magnitude (Figure 4.6). The experimentally observed trend in increased fluid velocities, for all solute concentrations, with increasing fluid pressure was reproduced by the model, as was the reduction in fluid velocity when the hypertonic solution was permeated compared to the hypotonic solution (Figure 4.6). Fluid velocities for the hypotonic and isotonic case were lower than those predicted by the BP model, whereas fluid velocities for the hypertonic case were similar. The agreement with experimental data reported in chapter 3 and literature values (Heneghan and Riches, 2008a) for this tissue lends confidence to the use of the TP model for the prediction of global fluid flow in the NP. However, as was the case with the BP model, it failed to accurately predict fluid velocity in the hypertonic case or the increased fluid velocity associated with isotonic permeation even though mechano-chemical effects are accounted for.

Figure 4.7 illustrates how the FCD gradient (difference between FCD concentration at upstream and downstream boundaries) varied with applied fluid pressure and solute concentration. For all concentrations, there was a linear increase in FCD gradient with increasing fluid pressure. Additionally, there was a non-linear increase in FCD gradient, for all fluid pressures, with increasing solute concentration with the greatest increase between 0M and 0.5M concentrations. Figure 4.8 illustrates that fluid velocity decreased non-linearly with increasing solute concentration. In keeping with results from the BP model, the effect of fluid pressure on fluid velocity was lower in the hypertonic case and highest in the hypotonic case. However, the TP model fluid velocity showed lesser sensitivity to applied fluid pressure than the BP

model, and consequently is more akin to the experimental data. Figure 4.9 illustrates

that a negative correlation exists between global fluid velocity and FCD.

(A)
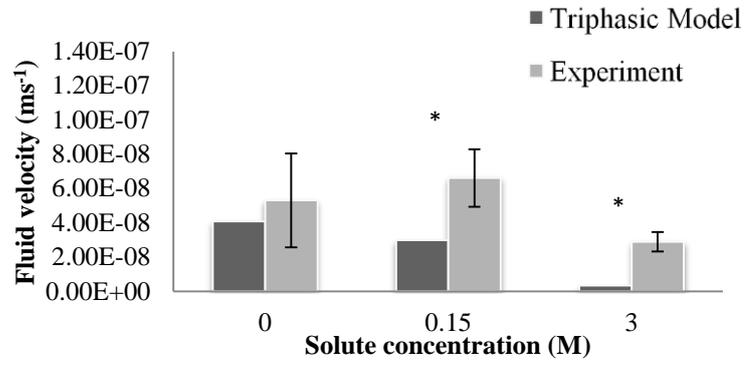
(B)
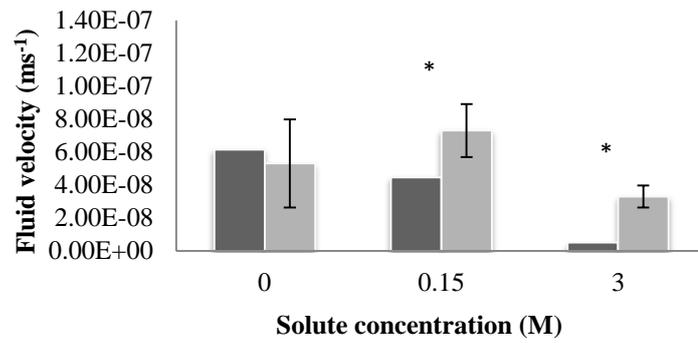
(C)
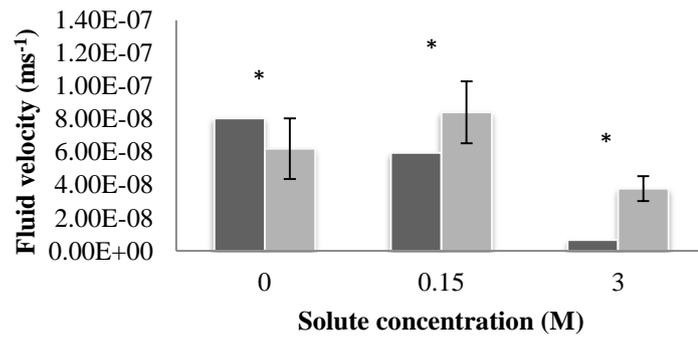
Figure 4.6 Experimental and triphasic model results. (A) – 30kPa, (B) – 45kPa, (c) – 60kPa.
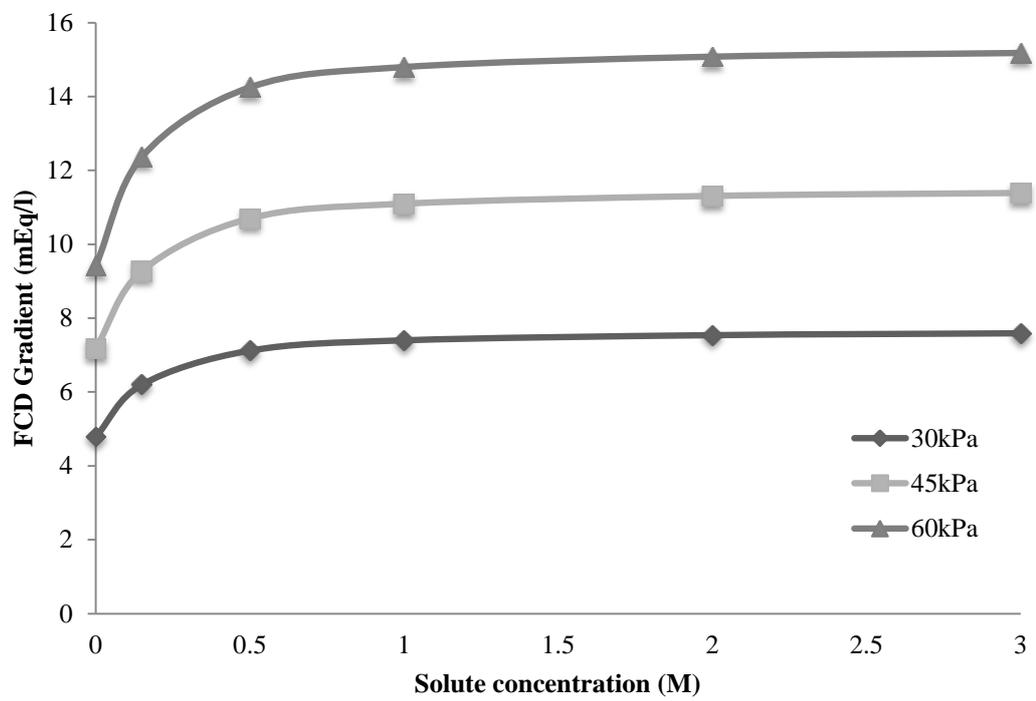
Figure 4.7 Triphasic model FCD gradient (Δ upstream vs downstream) in relation to solute concentration.
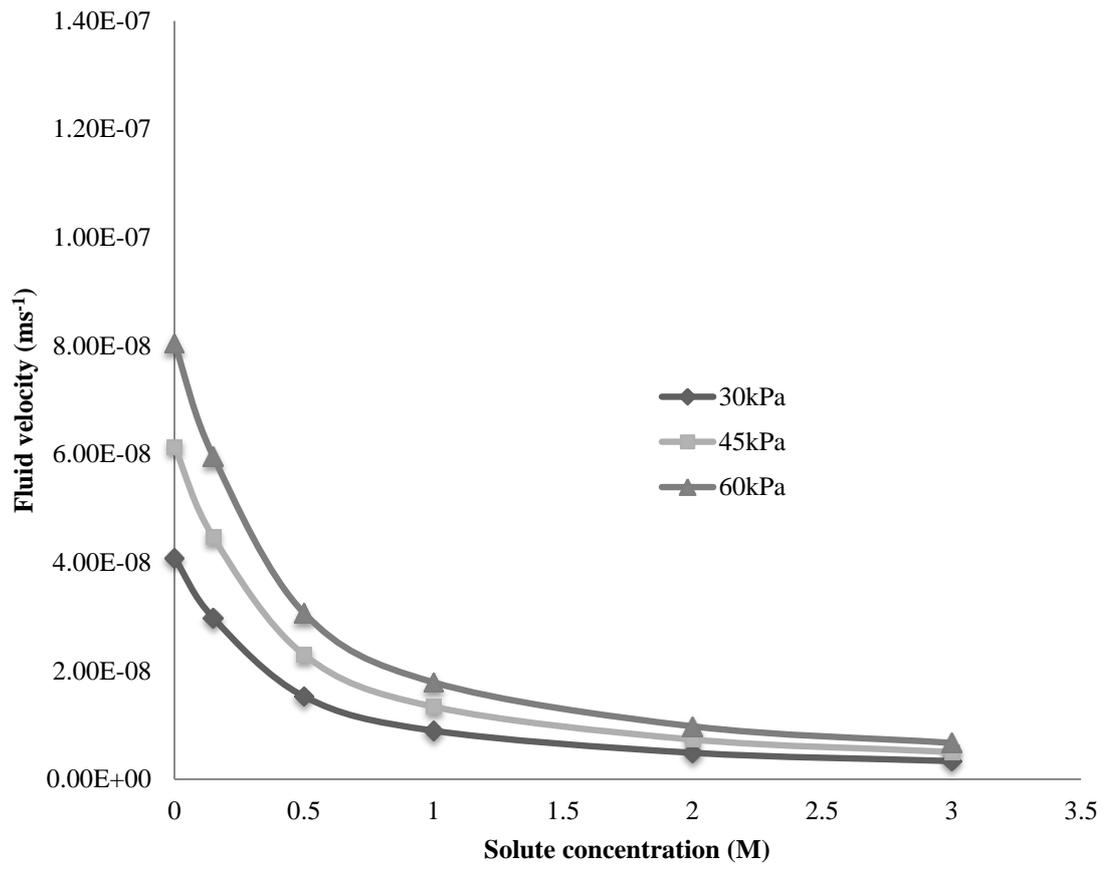
Figure 4.8 Triphasic model fluid velocity in relation to solute concentration.
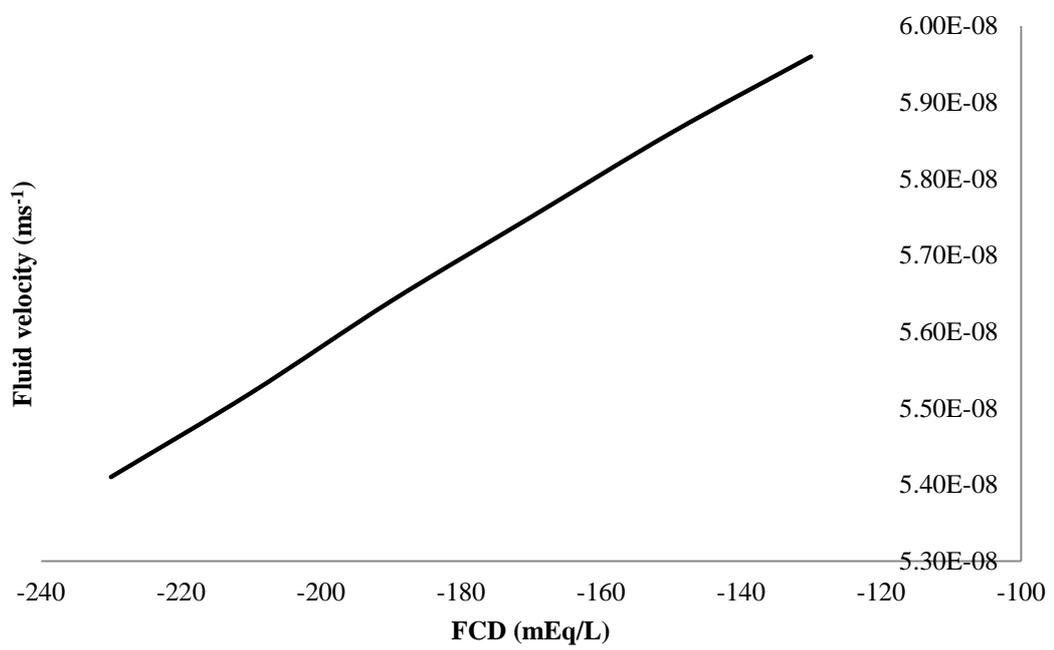
Figure 4.9 Triphasic model fluid velocity in relation to FCD.

Figure 4.10 illustrates how deformation gradients, resulting from the applied fluid pressure, affect strain, effective fluid pressure and FCD within the tissue for each of the permeation solutions at 60kPa. Images were only taken for this pressure gradient as it yielded the greatest tissue deformation allowing for more obvious mechano-electrochemical gradients. Table 4.4, Table 4.5 and Table 4.6 document the magnitudes and gradient of strain, effective fluid pressure, FCD, electric potential, Na^+ and Cl^- concentrations for both models at 60kPa (only strain and effective fluid pressure data available for biphasic model). Both models demonstrated positive strain toward the upstream surface and negative strain toward the downstream surface, for all permeating solutions, and the greatest strain occurring toward the downstream boundary. The TP model demonstrated greater strain gradients compared to the biphasic model. The TP model strain gradient throughout the tissue was found to increase with increasing solute concentration. Both models showed identical effective pressure results with the 0M case exhibiting a swelling potential, while the effective fluid pressure was 60kPa for all solute concentrations. All cases showed a FCD gradient throughout the tissue thickness with the highest concentration toward the downstream surface. The magnitude of the FCD gradient was found to increase with increasing solution concentration; the upstream FCD concentration decreased while the downstream FCD concentration increased.

Figure 4.11 illustrates how deformation gradients, resulting from the applied fluid pressure and chemical gradients, affected electric potential and Na^+ and Cl^- concentrations within the tissue for each of the permeating solutions at 60kPa. There was a significant reduction in electric potential with increasing solute concentration. However, an electric potential gradient existed for all permeating solutions, with

greater potential toward the downstream surface. The magnitude of the gradient, however, was found to reduce with increasing NaCl concentration (Table 4.5).

A higher concentration of Na^+ compared to Cl^- was found for all permeating solutions. This concentration increased substantially with increasing solute concentration with the difference between 0M and 0.15M being lesser that that of the 3M case. An ionic concentration gradient existed, for both Na^+ and Cl^- in all permeating solution cases with the greatest Na^+ concentration found toward the downstream surface and the greatest Cl- concentration found toward the upstream surface (Table 4.6). Na^+ concentration was found equal that of FCD in the 0M case.
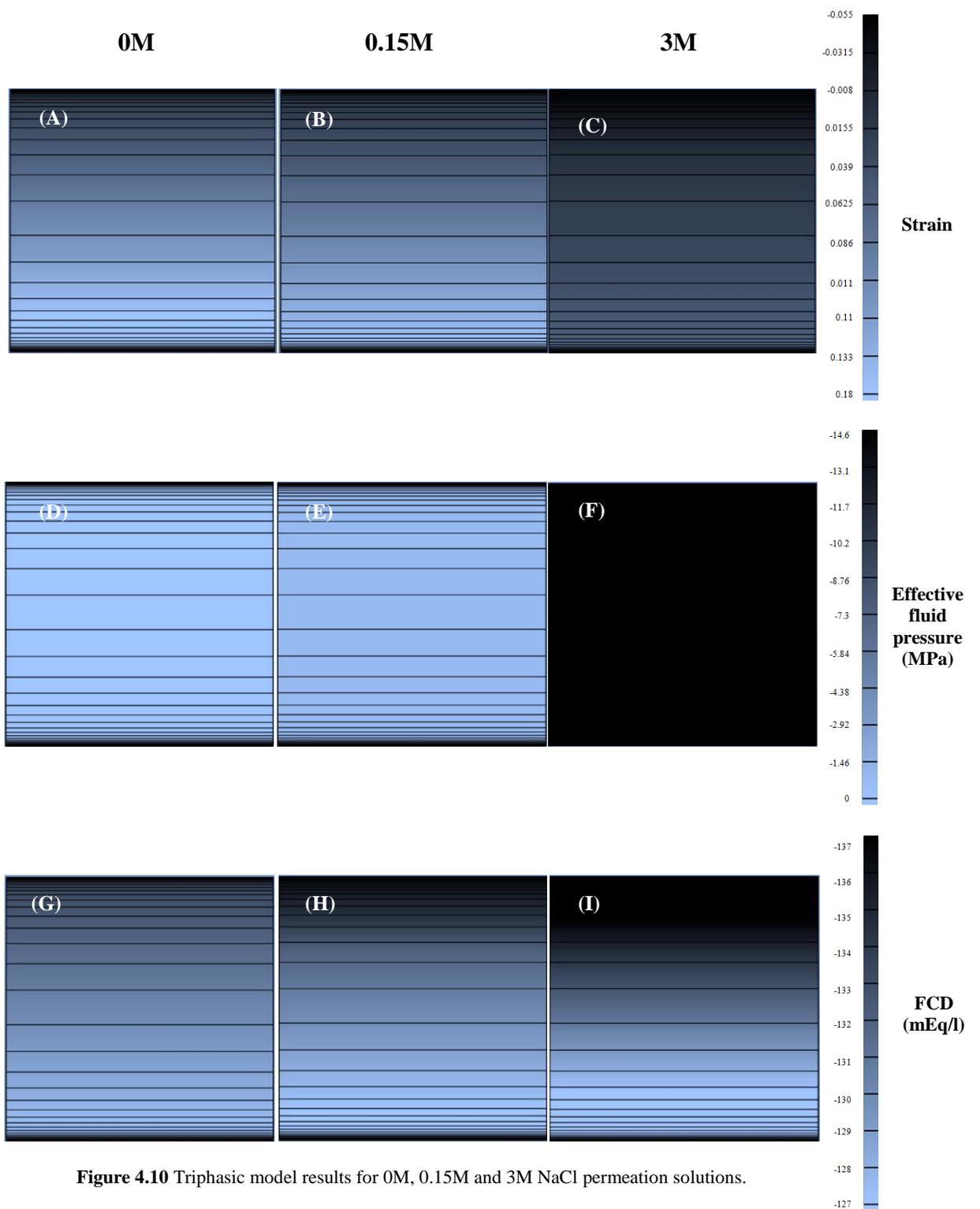
Figure 4.10 Triphasic model results for 0M, 0.15M and 3M NaCl permeation solutions.
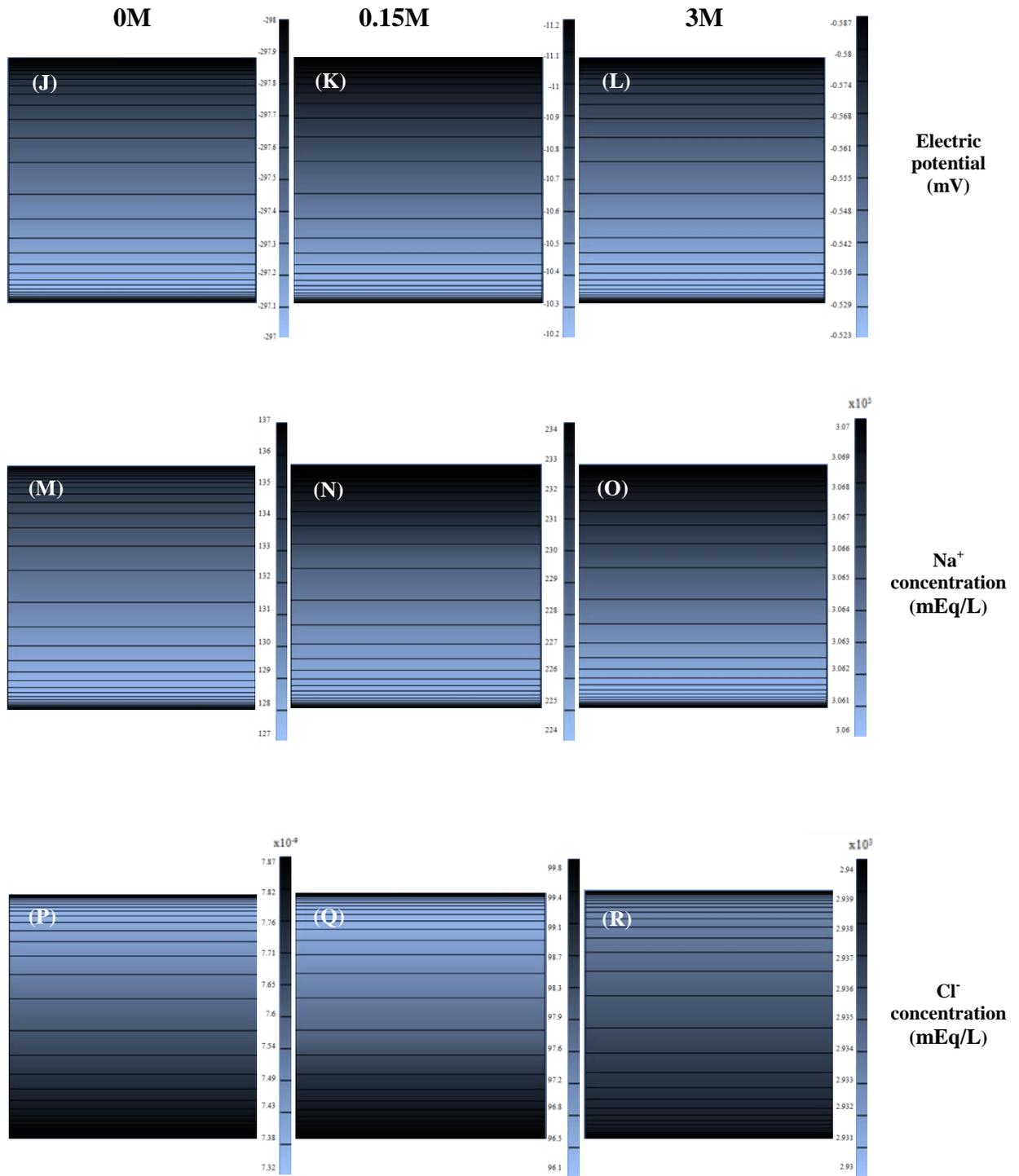
Figure 4.11 Triphasic model results for 0M, 0.15M and 3M NaCl permeation solutions.

	Strain			Effective Fluid Pressure (MPa)		
	0M	**0.15M**	**3M**	**0M**	**0.15M**	**3M**
Upstream	0.0032	0.0032	0.0031	0.06	-0.671	-14.56
Downstream	-0.0167	-0.0167	-0.0167	0	-0.731	-14.62
Gradient	0.0135	0.0135	0.0136	0.06	0.06	0.06

Table 4.4 Biphasic model results for upstream and downstream surfaces. Negative strain values indicate compressive strain and negative effective fluid pressure values are the result of osmotic loading offset occurring during the first step.

	Strain			Effective Fluid Pressure (MPa)			FCD (mEq/L)		
	0M	**0.15M**	**3M**	**0M**	**0.15M**	**3M**	**0M**	**0.15M**	**3M**
Upstream	0.0183	0.0278	0.0374	0.06	-0.671	-14.56	-127	-126	-124
Downstream	-0.0376	-0.0456	-0.0529	0	-0.731	-14.62	-137	-138	-139
Gradient	0.0559	0.0734	0.0903	0.06	0.06	0.06	10	12	15

Table 4.5 Triphasic model results for upstream and downstream surfaces. Negative strain values indicate compressive strain and negative effective fluid pressure values are the result of osmotic loading offset occurring during the first step.

	Electric Potential (mV)			Na^+ Concentration (mEq/L)			Cl^- Concentration (mEq/L)		
	0M	**0.15M**	**3M**	**0M**	**0.15M**	**3M**	**0M**	**0.15M**	**3M**
Upstream	-297	-10.3	-0.523	127	225	3.06E+03	7.87E-09	99.8	2.94E+03
Downstream	-298	-11.2	-0.587	137	234	3.07E+03	7.32E-09	96.1	2.93E+03
Gradient	1	0.9	0.064	10	9	10	-5.5E-10	-3.7	-10

Table 4.6 Triphasic model results for upstream and downstream surfaces.

4.5. Discussion

Biphasic and triphasic poroelastic finite element models were developed to investigate the mechanisms affecting fluid flow in the NP by simulating the permeation experiment of chapter 3. This study has provided insight to the effect of mechano-electrochemical phenomena such as electric potential and FCD gradients. The models were compared with experimental data presented in chapter 3.

Both the BP and the TP models demonstrated agreement with experimental data which lends confidence to the literature sourced material properties. The TP model predicted slightly lower fluid velocities than the BP model for all fluid pressure gradients (Figure 4.12) and solute concentrations as a result of the influence of mechano-electrochemical effects. The mechano-electrochemical phenomenon responsible for this reduction in fluid velocity is the frictional interaction between the interstitial fluid and the counter ions which are electrostatically linked to the fixed charges (Frijns et al., 1997). In additional to structural changes, disc degeneration is associated with a loss in FCD (Urban and Roberts, 2003) and resultant increase in permeability, as demonstrated by the TP model (Figure 4.9). This may impact on the disc's ability to behave hydrostatically (Adams et al., 1996); however, it may also contribute to a self-preservation mechanism whereby nutrient transport to the cells is enhanced to maintain biosynthesis.
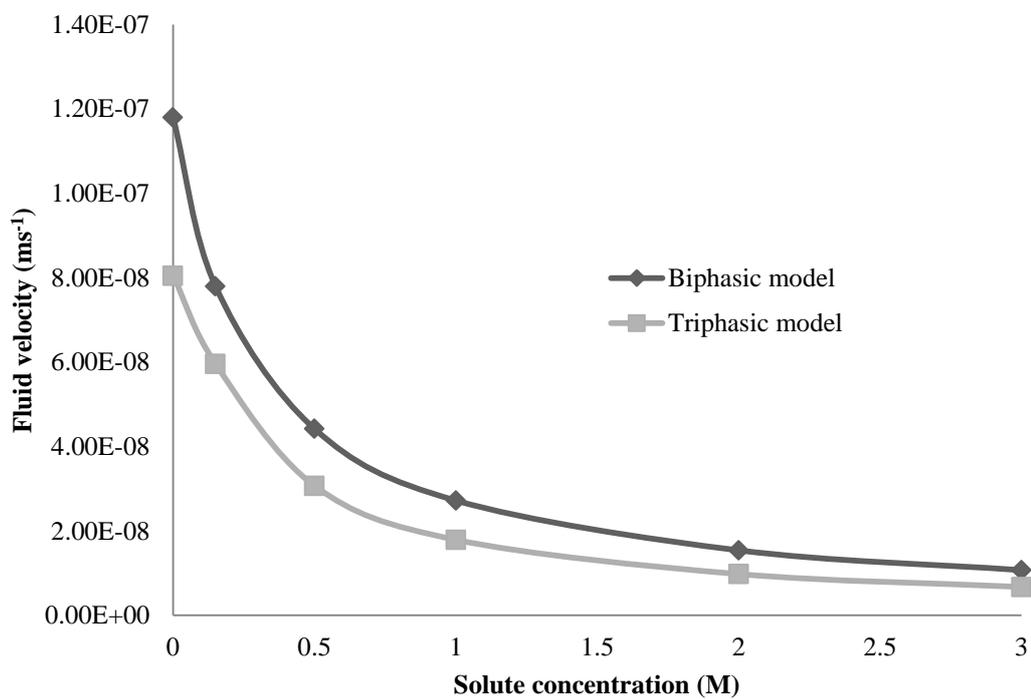
Figure 4.12 Comparison of fluid velocities obtained from the biphasic and triphasic models (60kPa).

The decrease in the BP model fluid velocity with increasing solute concentration can be attributed solely to the frictional interactions between the solid matrix and solute. However, the reduction in fluid velocity with increasing solute concentration, seen in the TP model, can be attributed to both greater flow induced compaction of the solid matrix as a result of a chemically reduced compressive modulus, as well as solute-solid frictional interactions. This mechano-electrochemical occurrence serves to maintain the tissue's low permeability which is essential for allowing the disc to maintain its structural integrity under physiological loading. The agreement between experimental results and TP model results lends confidence to the use of an extended quadriphasic Darcy's law (Huyghe and Janssen, 1997) which accounts for mechano-electrochemical effects, when considering the apparent permeability of cartilaginous tissue:

$$n^f v^{fs} = -K \cdot [\nabla_0 p - RT[(2\phi^f - \phi^+ - \phi^-)\nabla_0 c^+ + (\phi^f - \phi^-)\nabla_0 c^{fc}] - Fc^{fc}\nabla_0 \xi] \qquad (4.23)$$

In both the BP and the TP models, the effect of fluid pressure on fluid velocity was lowest in the hypertonic case and highest in the hypotonic case as a result of high solute-solid frictional interactions in the former. Additionally, the magnitudes of fluid velocities for all pressure gradients in the hypertonic case were similar between the two models. This observation is the result of ionic effects in the TP model being negated in the hypertonic environment, resulting in fluid flow being governed solely by the applied fluid pressure and solute-solid interactions. This finding supports the hypothesis in chapter 3 that all gradients, other than fluid pressure, are rendered negligible in a hypertonic external solution.

The TP model predicted that a FCD and resultant electric potential gradient exists as a result of applied fluid pressure, with the greatest concentrations occurring toward the downstream surface which is in keeping with the experimental hypothesis in chapter 3. The increase in FCD toward the downstream surface observed in the hypertonic case indicates a loss of compressive stiffness which is in agreement with the triphasic investigation of Lai et al. (2000) who reported that FCD gradient is positively correlated to aggregate modulus (Figure 4.13). The model predicted that the change in FCD gradient plateaus in solute concentrations greater than 1M (Figure 4.7), which indicates that this concentration was sufficient to negate the model's ionic modulus. This is supported by the finding that the change in strain gradient was greatest between 0M and 0.15M and lowest between 0.15M and 3M. The literature indicates that 3M NaCl is required to negate all ionic effects in the bovine NP (Mow and Schoonbeck, 1984, Heneghan and Riches, 2008b) which is substantially greater than that required for the TP model. This may indicate that the FCD content used in the TP model, which was based on values measured in mildly to moderately degenerate human discs (Stokes et al., 2010), was lower than what was present in the experimentally permeated healthy bovine samples; Jackson et al., (2009) reported a PG content in this tissue of 190mEq/L. This finding emphasises the sensitivity of FCD when modelling both the healthy and degenerate disc.

Although the FCD gradient was found to increase with increasing solute concentration as a result of flow induced deformation gradients, there was a significant decrease in electric potential gradient with increasing solute concentration as a result of ionic gradients being rendered negligible in such environments (Mow and Schoonbeck, 1984). The source of the electric potential gradient is the ion

concentration gradients associated with an inhomogeneous FCD distribution. The concentration of cations (Na^+) was found to opposite that of anions (Cl^-) due to the Donnan exclusion effect (Gu et al., 1999a) which is consistent with previous analytical studies (Gu et al., 1993, Lai et al., 2000). The diffusion tendency of the cations and the anions are in opposite directions when an inhomogeneous distribution of FCD exists in the tissue, resulting in a separation of the oppositely charged ions and subsequently inducing a diffusion potential opposing this tendency for separation (Lai et al., 2000). Even though the cations and anions have a propensity to drift apart, creating the diffusion potential, all ions move in the direction of flow due to the net fluid flow. These findings are entirely consistent with the triphasic permeation analysis of Gu et al. (1993). A combination of the fluid pressure induced streaming potential and the diffusion potential (which acts in the opposite direction), results in the overall electric potential gradient which plays an important role in governing both global and localised interstitial fluid transport as described numerically by Gu et al. (1993) and experimentally in chapter 3. An interesting finding, however, is that the polarity of the electric potential is more negative toward the downstream surface for all solute concentrations which, according to Lai et al. (2000), is the result of the tissues low aggregate modulus ($H_A = 0.3MPa$) and indicates that the electric field is dominated by the diffusion potential. Had the polarity been more positive toward the downstream surface then the electric field would have been dominated by streaming potential which is the case for tissues with $H_A > 0.54MPa$. This finding indicates that FCD gradients have a considerable influence on electric potential dependent fluid flow within disc tissue with low aggregate modulus such as the NP and that degenerative adaptations may impact on the polarity of electric fields.
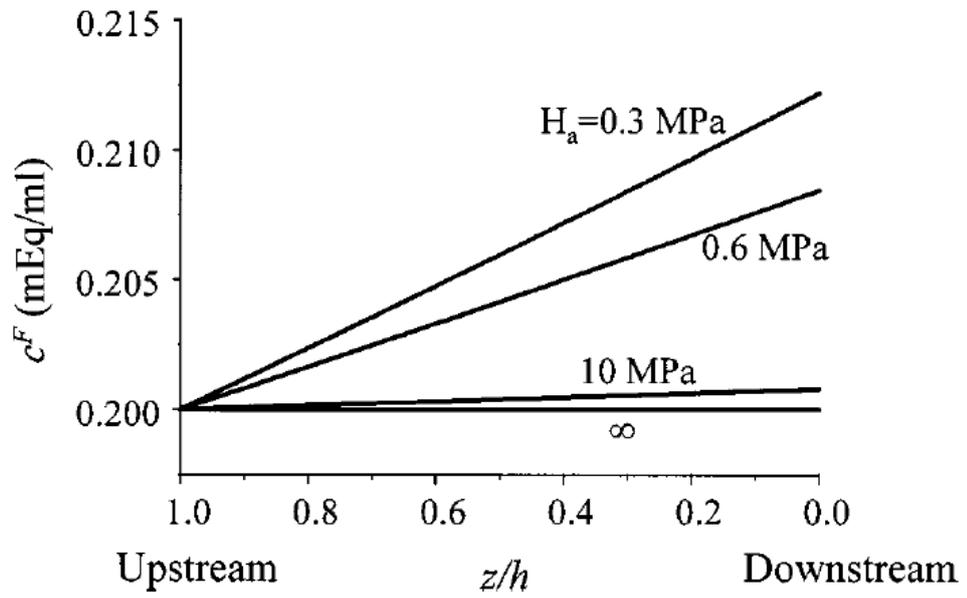
Figure 4.13 FCD gradient is related to aggregate modulus. FCD increases toward the downstream surface due to drag-induced compaction during permeation (Lai et al., 2000).
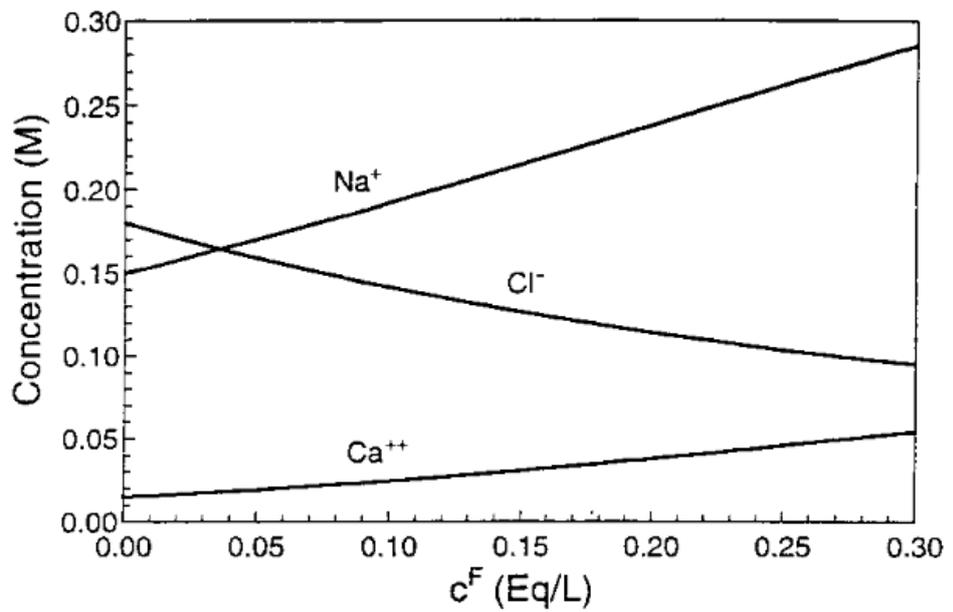
Figure 4.14 Concentration of ions within charged hydrated tissue as a function of fixed charge density (Gu et al., 1999a).

The finding that model fluid velocity results do not match experimental data with regards to isotonic flow augmentation may indicate that the governing equations do not account for the full set of micromechanical phenomena which influence fluid flow within the disc. If we consider the solvent, w, and solute, j^{α}, flux relations, as discussed in section 4.3.3, and substitute in the partition coefficient (Eq. 4.15) and effective solute concentration (Eq. 4.14), we find

$$w = -\tilde{k} \cdot \left(\nabla \tilde{p} + R\theta \sum_{\beta \neq s,w} \frac{\hat{\kappa}^{\beta} exp\left(-\frac{z^{\beta} Fc\psi}{R\theta}\right)}{d_0^{\beta}} d^{\beta} \cdot \nabla \tilde{c}^{\beta} \right) \qquad (4.24)$$

and

$$j^{\alpha} = \tilde{\kappa}^{\alpha} d^{\alpha} \cdot \left(-\varphi^w \nabla + \frac{c^{\alpha}/\hat{\kappa}^{\alpha} exp\left(\frac{-z^{\alpha} Fc\psi}{R\theta}\right)}{d_0^{\alpha}} w \right) \qquad (4.25)$$

It is evident that these relations are directly dependent on effective fluid pressure gradients, $\nabla \tilde{p}$, effective solute concentration gradients, $\nabla \hat{c}^{\beta}$, and electric potential, ψ, which is consistent with quadriphasic theory (Huyghe and Janssen, 1997). Even though FCD gradients are not explicitly accounted for in the solvent flux relationship, electric potential and FCD are fundamentally linked. However, the extended quadriphasic Darcy's law (Eq. 4.23), which provides a possible explanation for experimental data, as discussed in chapter 3, considers both phenomena as separate terms. Since the experimentally observed isotonic flow augmentation can be attributed to the aggregate of fluid pressure gradients, solute concentration gradients, electric potential gradients *and* FCD gradients, this may provide an explanation as to

why the TP model failed to mimic such experimental phenomenon. The hypothesis in chapter 3, regarding the flow augmentation mechanism was that all gradients are left in situ in the isotonic case, only. If the FCD gradient is not accounted for then the isotonic flow is still influenced by one more gradient than the hypotonic case; the mobile ion concentration gradient. This would perhaps indicate that isotonic flow augmentation should still be accounted for by the TP model. However, it is the fundamental interaction between FCD gradients and mobile ions which creates the electric field dominating diffusion potential. The omission of the FCD gradient term may serve to negate the effect of mobile ion gradients on flow, thus leaving the isotonic case reliant on the same gradients as present in the hypotonic case; effective fluid pressure and electric potential. This would result in fluid velocity being greater in the hypotonic case than the isotonic case due to a combination of the increased permeability and reduced solid-fluid frictional interactions associated with hypotonic solution permeation. The importance of the FCD gradient term is highlighted by Gu et al. (1993) who found, via application of triphasic theory to a permeation study on AC, that localised fluid and ion velocity is greater toward the downstream surface of the tissue as a result of the high concentration of FCD in the this region. Additionally, the finding in this study that diffusion potential dominates the electric field within the tissue indicates that FCD gradients contribute significantly to fluid flow and, thus, must be considered in the constitutive behaviour. Further investigation is required to identify how the transport of charged ions the disc is extrapolated to the transport of interstitial fluid which may indicate where another discrepancy lies between experimental and numerical results. Additionally, the other parameters in the model were not best fitted to experimental data. Potential

nonlinearities associated with other parameters may provide better agreement with data.

Currently, there is no experimental data which documents the change in electric potential of disc tissue with degeneration. However, Gu (1999a) showed that tissue conductivity increases with increasing hydraulic permeability if the FCD remains constant. Therefore the decrease in streaming potential in Figure 4.15 indicates that changes in FCD, permeability and electrical conductivity in relation to degeneration, will affect streaming potential. The reduction in streaming potential with advancing degenerative grade is most prominent in the axial direction, which may have important ramifications for the NP which relies heavily on axial nutrient transport.
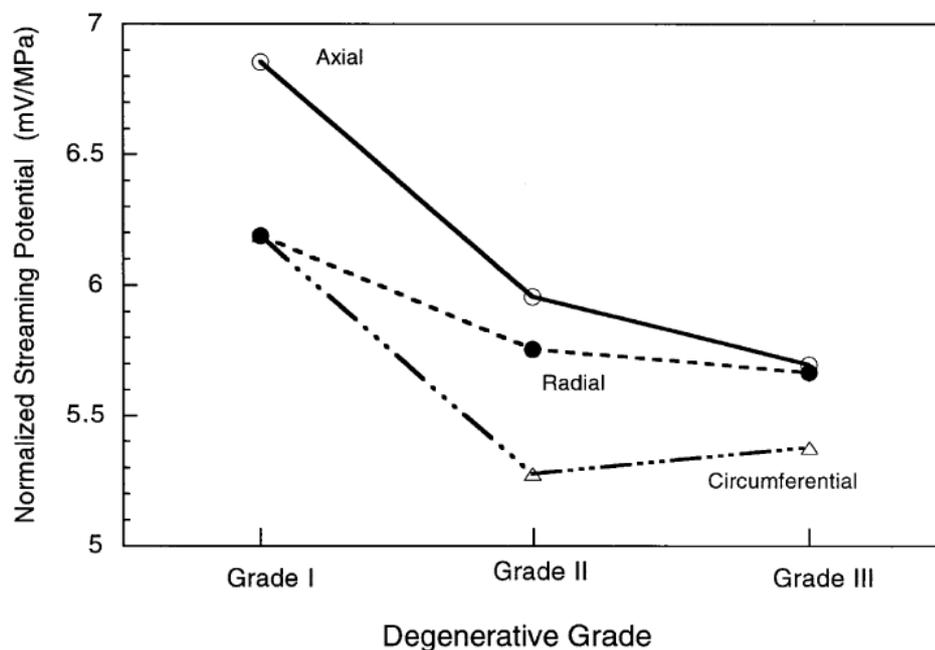
Figure 4.15 Effects of degeneration and sample orientation on the static streaming potential of the AF. The streaming potential is orientation dependent (anisotropic) for grades I and II but not for grade III (Gu et al., 1999c).

4.6. Conclusions

This chapter has confirmed the hypothesis from chapter 3 that mechano-electrochemical phenomena influence fluid transport in the disc. Models which account for such interactions must be used to accurately investigate fluid flow and solute transport in the disc. Even though the TP model did not accurately describe the apparent mechano-electrochemical fluid augmentation mechanisms seen experimentally, the global fluid velocity results were in agreement. A future avenue open to investigation with the TP model is the parametrical alteration of FCD to evaluate the effect of degeneration on fluid flow and electric potential. Whilst this method may not provide completely accurate results when considering extreme cases of degeneration due to the associated plethora of structural changes, it may provide valuable insight to the changes in mechano-chemical interactions during the early stages of degenerative adaptations.

5. Experimental determination of the Poisson's ratio of the IVD

5.1. Introduction

As discussed in section 2.4.6, the Poisson's effect is caused by the movement of molecules and molecular bonds within a matrix to accommodate stress. Historically, the measurement of Poisson's ratio in cartilaginous tissue has proved particularly challenging due to the viscid nature of the tissue, resulting in a lack of empirical evidence of this fundamental material property. Mechanically, the NP has been well-characterised in confined compression (Heneghan and Riches, 2008b, Johannessen and Elliott, 2005, Perie et al., 2005) with regards to permeability and aggregate modulus, however, the Poisson's ratio, ν, of this tissue remains a relative unknown with numerical models typically adopting values between 0.35 and 0.49 (Meakin and Hukins, 2001, Kulak et al., 1976, Iatridis et al., 2003, Lu et al., 1998, Argoubi and Shirazi-Adl, 1996, Goel et al., 1993, Lee et al., 2000, Natarajan et al., 1994). Only one study has directly determined the Poisson's ratio of the NP and reported a significantly higher value of 0.62 ± 0.15 (Cloyd et al., 2007).

The majority of previous studies have referred to a single Poisson's ratio value which encompasses the mechanical response of both the solid and fluid phases, however, as briefly mentioned in section 2.4.6, the Poisson's effect in cartilaginous tissue is a far more complex phenomenon. Classically, Poisson's ratio is a material constant, deformation independent and applicable to small strain deformations in linearly elastic solids. In this regard, the use of the term Poisson's ratio, when considering the mechanical response of cartilaginous tissue, is a gross simplification.

Biphasic theory suggests that low permeability cartilaginous tissues instantaneously deform without volume change and behave as an incompressible elastic solid in unconfined compression between impermeable platens (Armstrong et al., 1984), which has led to an assumed Poisson's ratio, v, of 0.5. However, radial strain may be augmented as a result of radial viscous drag forces due to the relative movement of fluid and solid resulting in v possibly exceeding 0.5. Alternatively, if hydraulic permeability is sufficiently high and/or the strain-rate slow enough, radial fluid exudation may not impose significant radial stress on the solid phase allowing for Poisson's ratio to be more dependent on the Poisson's ratio of the solid phase alone and potentially lower than 0.5 in the ramp phase (Wong et al., 2000). Thus, it is clear that experimental conditions influence the Poisson's ratio at the end of a ramp phase. In this thesis the ratio of circumferential to axial strain at the end of the ramp phase is defined as the biphasic-Poisson's ratio, v_B. This is the Poisson's ratio of both the solid and fluid phases in combination and is deformation dependent, pore pressure dependent and deformation-rate dependent. During the hold phase, radial fluid flow allows the pore pressure to equilibrate with the external environment (Armstrong et al., 1984). The tissue may also radially recoil during the hold phase due to the relaxation of flow induced tensile radial elastic stresses in the matrix. The equilibrium deformation is determined by the Poisson's ratio of the solid phase which, for the purposes of this thesis, is defined as the matrix-Poisson's ratio, v_M; considered constant for small strain deformations and deformation-rate independent.

One adopted method to measure the Poisson's ratio of cartilaginous tissue is an unconfined compression experiment whereby a cylindrical tissue specimen is compressed between two smooth, impermeable platens. In this configuration, the

sample is compressed along the z-direction which results in radial expansion (Armstrong et al., 1984). This allows unrestrained lateral displacement and free fluid flow exudation and/or imbibition across the cylindrical surface (Figure 5.1). Optical measurement techniques may then be employed to measure the initial lateral displacement, v_B, and subsequent recoil, v_M, during a stress-relaxation experiment. However, due to unavoidable non-ideal tissue-platen conditions, interfacial shear stresses may significantly impact measured values from their true levels. Additionally, the fluid pressurisation related lubrication mechanisms associated with AC (the reader is referred to the review by Ateshian (2009) for a fuller description of this extensive field) may also occur during the unconfined compression of the NP thus possibly influencing measured Poisson's ratio values.
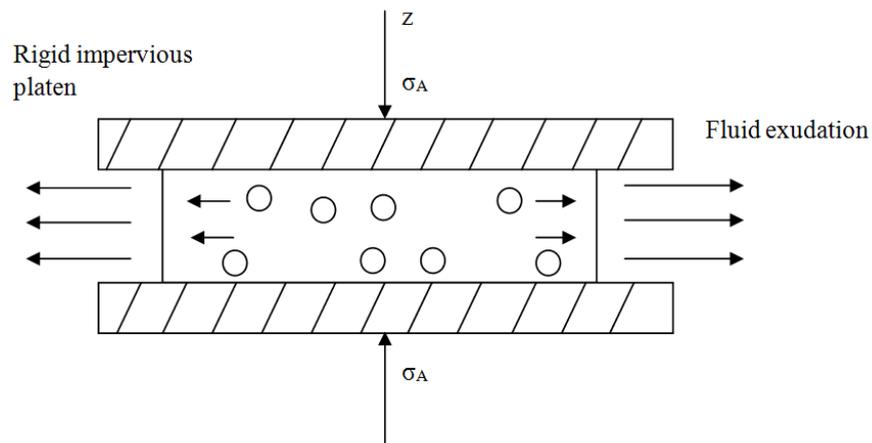
Figure 5.1 Schematic diagram of a tissue sample being compressed via a rigid impervious smooth platen for measurement of Poisson's ratio. Based on Fig 1b from (Armstrong et al., 1984).

Variation in the Poisson's ratio of AC has been attributed to collagen fibre orientation (Jurvelin et al., 1997, Kiviranta et al., 2006, Chegini and Ferguson, 2010). Jurvelin et al. (1997) used an optical measurement technique to characterise the depth-dependent Poisson's ratio in AC and found that results were lowest in the superficial zone. Collagen fibres are orientated parallel to the articular surface in this region which may have inhibited lateral expansion which is in keeping with the finding that the tissue exhibits high lateral tensile stiffness in this zone (Akizuki et al., 1986).

Additionally, rat tail collagen fibres, and type I collagen which can be found in soft tissues such as the NP, have been found to be viscoelastic and nonlinear (Betsch and Baer, 1980, Haut and Little, 1972, Rajini et al., 2001, Sanjeevi, 1982). The contribution of collagen viscoelasticity to cartilage mechanics has been observed in tensile testing where fluid pressurisation is negligible (Roth and Mow, 1980). Since radially orientated collagen fibres in the NP will be stressed in tension during unconfined compression, similar contributions may occur whereby the transient response is not only globally viscoelastic, but incorporates contributions from fluid flow within collagen fibres (Li and Herzog, 2004a, Silver et al., 2002). Cartilaginous tissue is known to demonstrate profound transient mechanical behaviour via strain-rate dependency which may be influenced by the aforementioned solid matrix viscoelasticity. A number of studies have reported that it is the global fluid-flow mechanism which dominates the transient behaviour (Li et al., 2003, Li and Herzog, 2004b, Mukherjee and Wayne, 1998, Setton et al., 1993, Soltz and Ateshian, 1998), whilst others have suggested a significant influence from solid matrix viscoelasticity (DiSilvestro and Suh, 2001, DiSilvestro et al., 2001b, DiSilvestro et al., 2001a,

Huang et al., 2001, Huang et al., 2003, Khalsa and Eisenberg, 1997, Mak, 1986a, Mak, 1986b). The influence of solid matrix viscoelasticity on disc mechanics in unconfined compression is yet to be fully determined.

Collagen orientation is considered to be homogeneous in the NP indicating that Poisson's ratio may be homogeneous and isotropic, however, there appears to be an organised distribution of elastic fibres (Yu et al., 2002) making up ~1.7% of the dry weight (Mikawa et al., 1986). In the centre of the disc elastic fibres have been found to run predominantly radially, whereas they are seen to run predominantly vertically towards the endplates, anchoring the disc to the cartilage endplates (Yu et al., 2002). This reported organisation may play a small role in governing lateral expansion and recoil during unconfined compression and relaxation.

In vivo, the disc relies on its heterogeneous structure, comprising of the NP, AF and CEPs, to transfer large multi-axial loads (O'Connell et al., 2011). As such, the NP is neither fully confined nor fully unconfined due to the mechanical contribution of the AF. The highly organised structure of the AF allows it to perform a complex role in disc mechanics whereby it counteracts shear and bugling effects whilst enabling the NP to develop a high hydrostatic pressure to resist compressive loading. Even under simple axial compression, complex loading conditions are generated throughout the disc via AF tensile hoop stresses, AF radial bulging, and the mechanical interactions between the NP and the surrounding AF (Heuer et al., 2008, Laible et al., 1993, O'Connell et al., 2007b). Experimentally, internal disc deformations have previously been measured using radiographic and optical measurement techniques (Tsantrizos et al., 2005, Costi et al., 2007, O'Connell et al., 2007a, Seroussi et al., 1989), demonstrating that the AF bulges outward during compression and the NP migrates

within the disc space (O'Connell et al., 2011). However, these studies relied on the insertion of physical markers, resulting in significant tissue disruption which may have introduced artefacts to the results. Due to difficulties in measuring internal disc behaviour without compromising structural integrity (O'Connell et al., 2011), the interaction between the NP and AF in unconfined compression and the possible internal Poisson's ratio related strain distributions is yet to be fully understood. Since degeneration is thought to initiate via annular defects (Osti et al., 1990), the transference of stress from the NP to the AF may be important, and the Poisson's ratio of the NP is a key parameter in this mechanism.

5.2. Aims and hypotheses

The lack of characterisation of disc biomechanics in unconfined compression has led to assumed values of Poisson's ratio being utilised in disc modelling. This chapter, therefore, aims to characterise the biphasic and matrix Poisson's ratio of the NP, determine any variation in these properties due to axial location and strain-rate, and to investigate the interaction between the NP and AF in unconfined compression with minimal tissue disruption. It is hypothesised that the Poisson's ratio of the NP is both strain-dependent and strain-rate-dependent, there is a significant effect of axial location and the AF will provide a confining effect to the NP and reduce the overall Poisson's ratio of the disc.

5.3. Methods

5.3.1. Development of the testing configuration and experimental protocol

An optical measurement technique, coupled with an unconfined compression experiment was considered the most appropriate method to characterise the Poisson's ratio of the disc. Variations of this technique have previously been used to measure the lateral expansion of both AC (Jurvelin et al., 1997, Kiviranta et al., 2006, Wang et al., 2003) and disc tissue (Cloyd et al., 2007). Due to the tissue's inherent viscous nature, a range of experimental obstacles, including the influence of interfacial shear stresses, had to be overcome to allow accurate measurement of both biphasic and matrix Poisson's ratios.

To allow for the investigation of the effects of strain-rate, a materials characterisation system (Electroforce 3200 series, Bose, USA) was used as the base unit to which a custom built unconfined compression rig and accompanying biaxial video extensometer (Prosilica GE video camera, Allied Vision Technologies, USA) was attached. The unconfined rig consisted of an upper platen, which was able to apply displacements in the z-direction, and a stationary lower platen. Highly polished toughened borosilicate glass was used as the platen material to allow video extensometer visualisation of the tissue's inferior surface through the lower platen, and for its low friction coefficient which was considered essential to allow unrestrained lateral expansion and recoil during a stress-relaxation experiment. An engineering drawing of the lower platen configuration, which was designed to allow characterisation of both isolated disc samples and full disc sections and to be attached to the Bose 3200 system's adjustable crosshead, is shown in Figure 5.2.
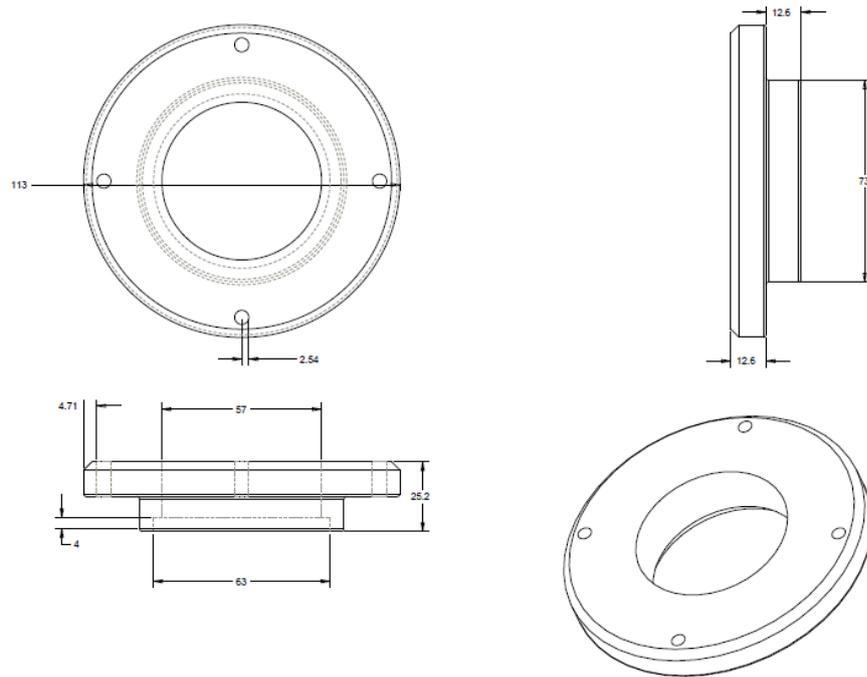
Figure 5.2 Engineering drawing of custom built lower glass platen (all dimensions are in mm).

A lubricating gel was used to reduce interfacial shear stresses whilst also acting as a hydrating medium. The gel also allowed for the regulation of ionic environment by varying the concentration of NaCl in the mixture. A readily available inert aqueous lubricant was (Boots Pharmaceuticals, UK) mixed with NaCl solution. The optimum concentration of lubricant to solution was determined via friction experiments whereby tissue samples were positioned on a lubricated glass angled ramp (comparable to platens) (Figure 5.3), and the tan of the angle of motion initiation was equal to the static friction coefficient and the tan of the angle of motion cessation being equal to the kinetic friction coefficient. Each concentration of lubricant was tested 3 times and the resultant coefficients of friction recorded. The results of the lubricating gel test are presented in Table 5.1.
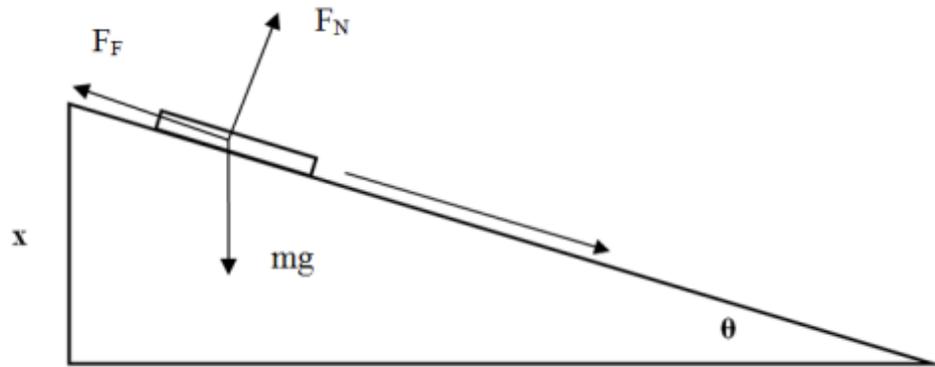
Figure 5.3 Schematic of angled ramp procedure to determine the static and dynamic coefficient of friction of a tissue sample on a glass platen.

$$F_F = \mu F_N \tag{5.1}$$

$$\mu = \frac{F_F}{F_N} \tag{5.2}$$

$$F_N = mg\,cos\theta \tag{5.3}$$

$$F_F = mg\,sin\theta \tag{5.4}$$

$$\mu = \frac{sin\theta}{cos\theta} = tan\theta \tag{5.5}$$

Ratio (Lubricating gel : Saline)	Initial coefficient	Cessation coefficient
1:0	0.57 ± 0.08	0.5 ± 0.1
1:2	0.37 ± 0.02	0.33 ± 0.02
1:3	0.38 ± 0.04	0.34 ± 0.04

Table 5.1 Ratio of lubricating gel to saline frictional coefficient.

The biaxial video extensometer was positioned below the moveable crosshead of the materials testing system, and orientated so as the inferior surface of the sample was visible for tracking (Figure 5.4 and Figure 5.5). This configuration allowed for Poisson's ratio measurement across the diameter of a sample, enabling analysis of both isolated tissue and full discs. The biaxial video extensometer determined strain in two orthogonal directions, denoted ε_{11} and ε_{22}. The video image from the camera was integrated into the WinTest software (Bose, USA) which tracked a sequence of prepositioned India ink dots on the surface of the tissue. This method of marking was chosen as it allowed for the sample to remain intact as the ink adhered to the sample surface. A novel method was developed to allow the accurate positioning of ink markings on a sample surface whereby a focused beam of light was directed through a PTFE template of the desired marker configuration and onto a sample surface. A rounded syringe tip was then used to apply India ink to the sample in the configuration of the projected light (Figure 5.6 to Figure 5.9).
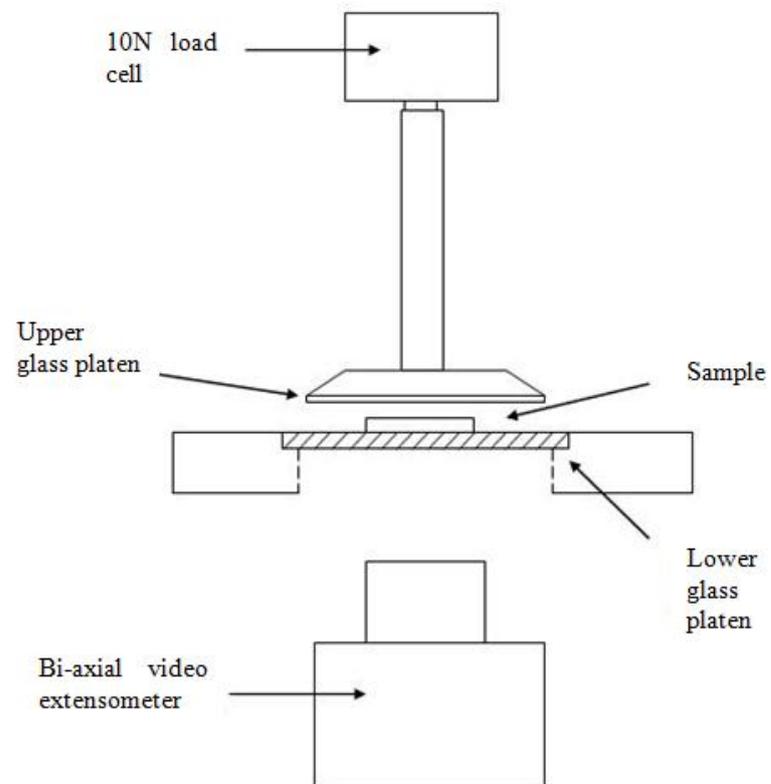
Figure 5.4 Schematic of unconfined compression rig coupled with bi-axial video extensometer.
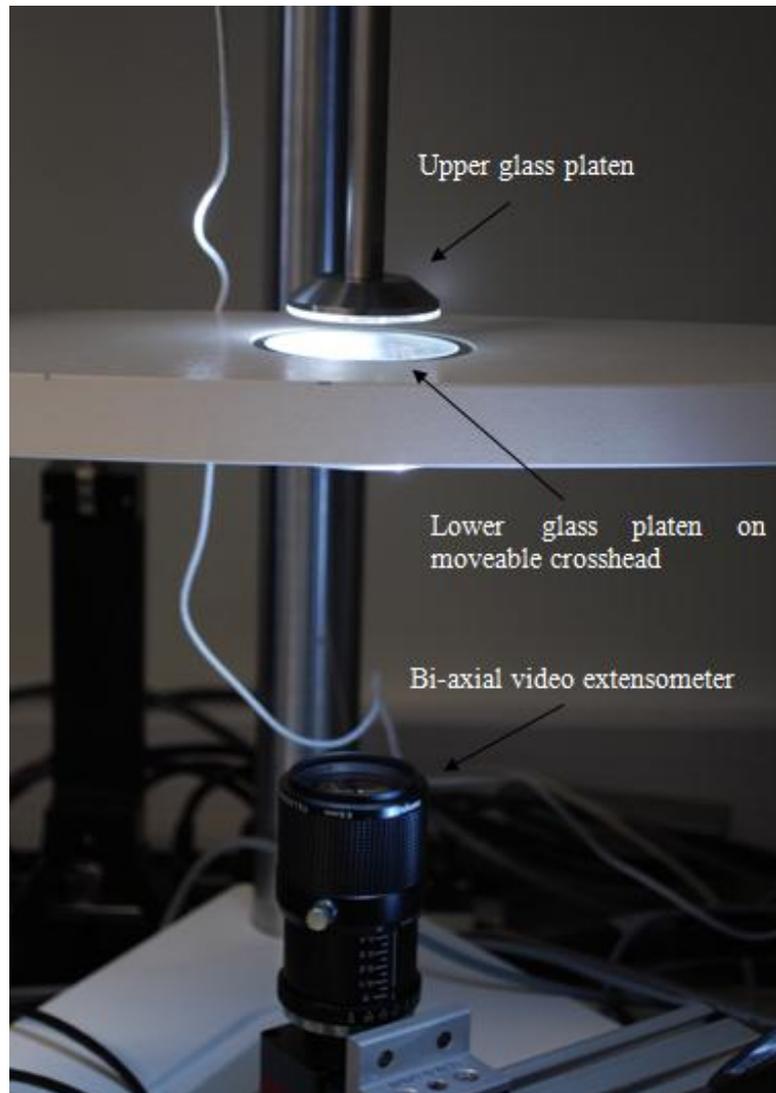
Figure 5.5 Unconfined compression rig coupled with bi-axial video extensometer.
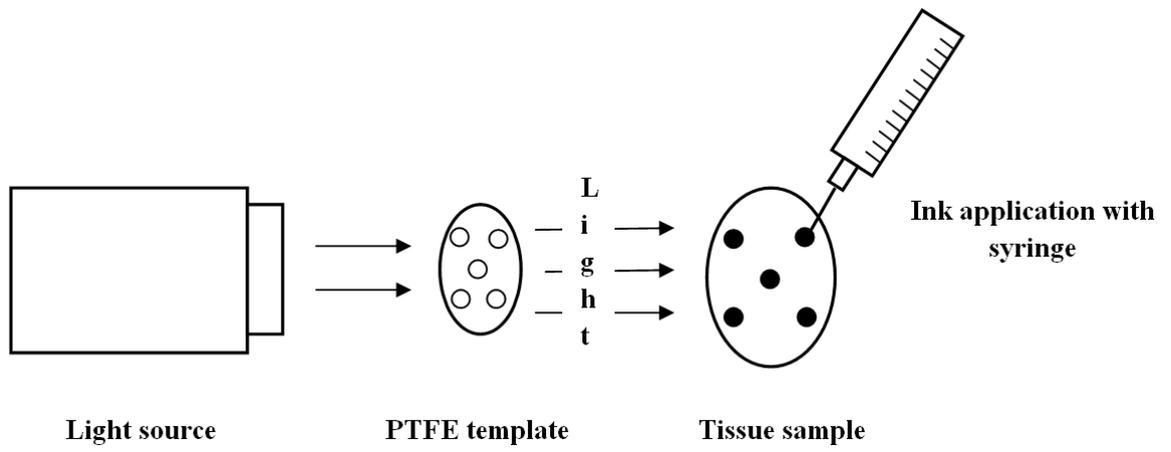
Figure 5.6 Marker positioning protocol.
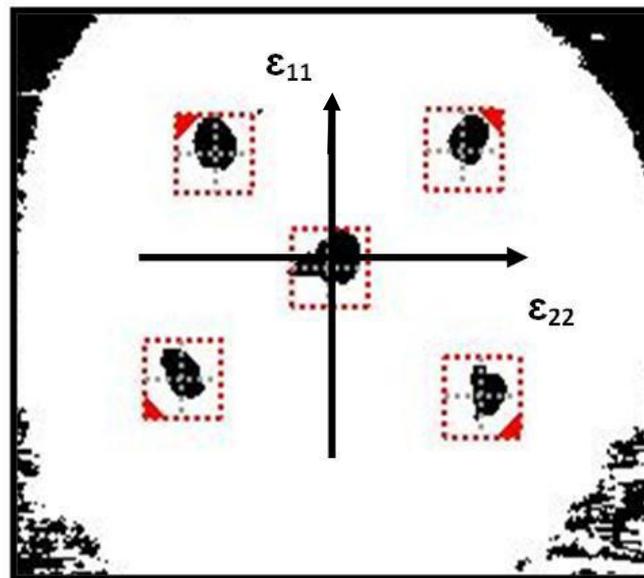
Figure 5.7 Marker configuration and software tracking system.
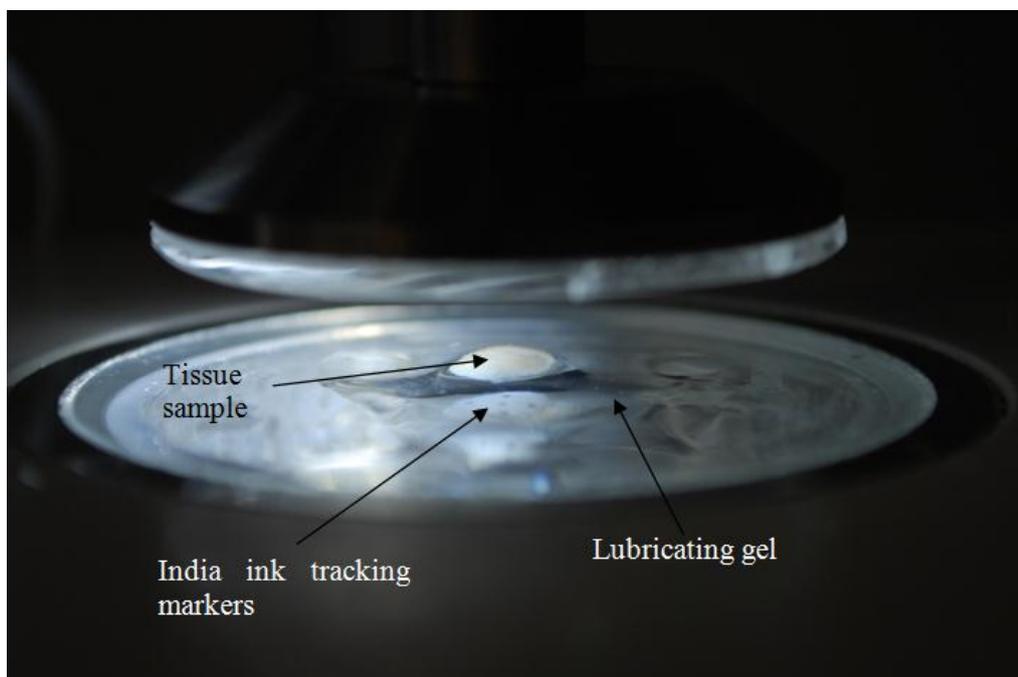
Figure 5.8 Tissue sample in lubricating gel.
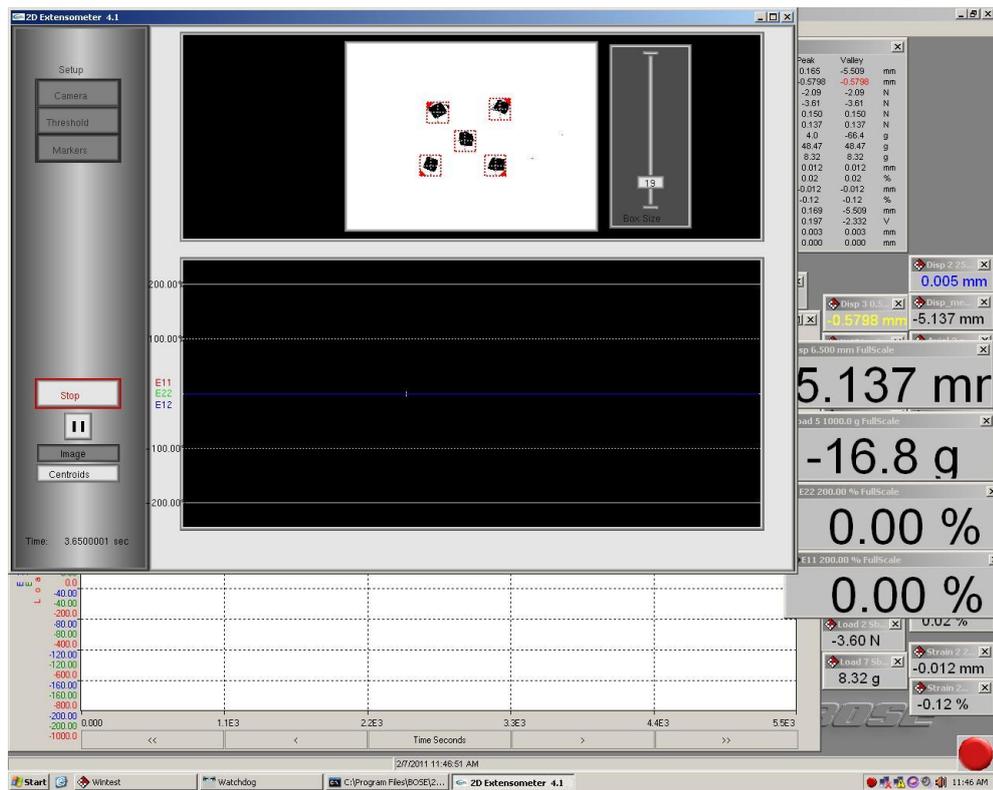
Figure 5.9 Screen shot of Bose WinTest tracking software.

In order to validate the experimental configuration, a pilot test on a silicon plug was performed, followed by similar tests on AC. Firstly, the silicone plug (ø10mm, 4mm thick) was tested by compressing to 20% axial strain, and comparing the resultant Poisson's ratio to the predicted outcome for this incompressible material ($v = 0.5$). Secondly, the protocol was repeated on a sample of AC and the results compared to literature reported values, $v_M = 0.185 \pm 0.065$ (Jurvelin et al., 1997). The testing configuration adopted for these experiments was identical to those used for the final testing of disc tissue. The results verified that the proposed method for measuring Poisson's ratio was suitable due to the silicon plug demonstrating $v \approx 0.5$ and AC demonstrating $v_B = 0.5$ and $v_M = 0.15$ (Figure 5.10 and Figure 5.11).
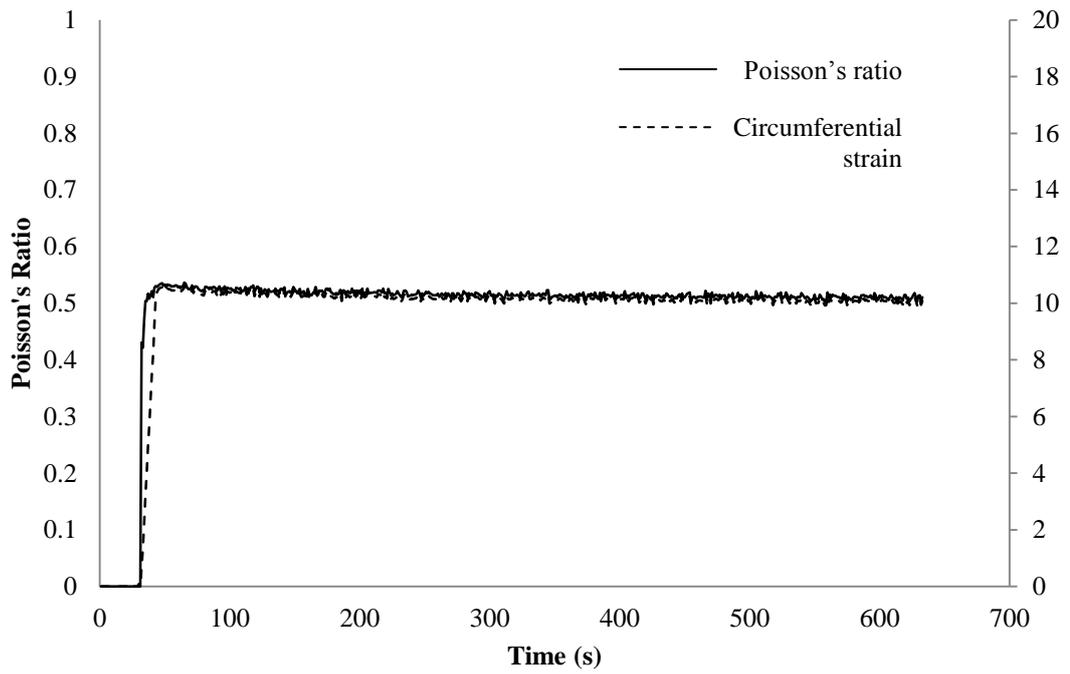
Figure 5.10 Poisson's ratio and circumferential strain results for a silicon plug.
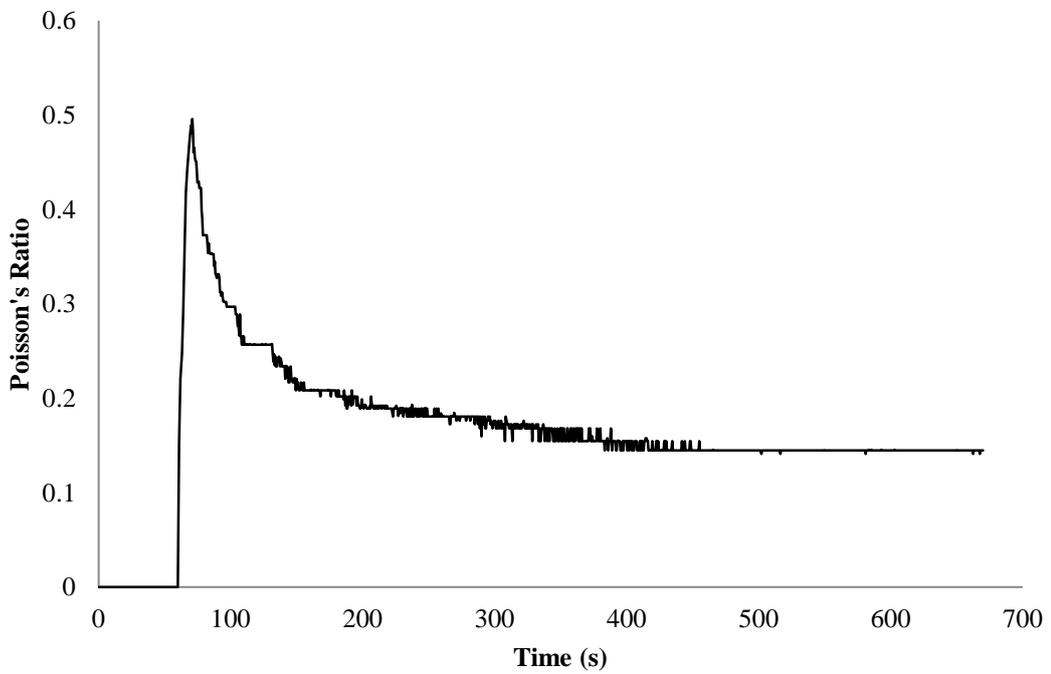
Figure 5.11 Poisson's ratio results for a sample of AC.

Due to the significant swelling potential of disc tissue, artefacts may be introduced to an unconfined compression experiment when attempting to measure lateral expansion. However, mixing the lubricating gel with saline of sufficient concentration to negate the swelling potential allows for more accurate determination of the Poisson's ratio of the solid matrix during unconfined compression (Recuerda et al., 2011). A pilot study was conducted to quantify the swelling of the NP in physiological saline, in terms of radial strain. A NP sample was positioned in the unconfined rig and held at $\lambda = 1$ for 3h whilst immersed in 0.15M NaCl lubricating gel. The sample showed significant lateral expansion during the initial 1h before reaching equilibrium indicating that significant artefacts in Poisson's ratio measurements may be introduced in such an environment (Figure 5.12). 3M NaCl has been shown to negate ionic effects in healthy bovine tissue (Heneghan and Riches, 2008b), therefore, the lubricating gel was mixed with NaCl and distilled water until a concentration of 3M was achieved. Recuerda (2011) investigated the effect of experimental protocol on the mechanical properties of the IVD in unconfined compression and found that an initial semi-confined swelling phase with no preload and ramp increments of 5% was most accurate when testing the NP. The viscous properties of NP allow for larger swelling than AF and AC tissue and the semi-confined swelling induces compressive stress comparable to a preload. This set of guidelines was considered appropriate for the current study.
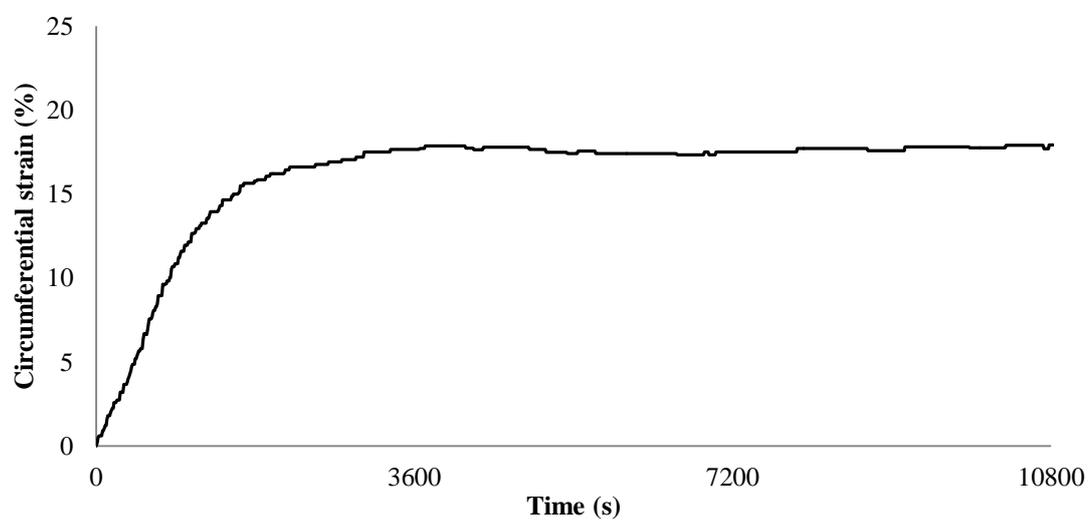
Figure 5.12 Circumferential swelling of NP sample bathed in 0.15M NaCl lubricant.

5.3.2. Materials

5.3.2.1.   *Isolated nucleus pulposus*

Due to biochemical similarities between bovine tail and human lumbar discs (Demers et al., 2004), IVDs from bovine tails (aged 14-30 months) were harvested, within 4h of slaughter, with a scalpel. Spilker et al. (1990) investigated the effect of sample aspect ratio (diameter/height, *d/h*) on the frictional coefficient at the sample/platen interface and reported that effects were significant for specimens with large aspect ratios. Consequently, a 5.5 mm diameter punch was used to remove 5-6mm thick NP plugs from the 4 largest discs with each plug subsequently sectioned into four $1544 \pm 252\mu m$ (mean $\pm$ S.D). This allowed for a balance between economical tissue removal, maintenance of structural integrity, sufficient surface area to allow optical tracking and relatively low aspect ratio, *d/h* = ~3.6. Samples were grouped into inner (inner zone of the NP) (N=16) and outer (adjacent to the CEP) (N=16) samples (Figure 5.13). The samples were stored frozen at -20°C. Upon thawing, five ink dots of side 3mm were marked on one side of the tissue in the configuration outlined in section 5.3.1.
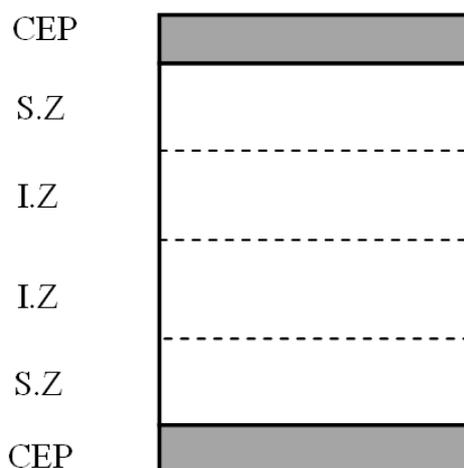
Figure 5.13 Sectioning plan of isolated NP plugs. S.Z – Superficial zone, I.Z – Inner zone.

To allow an understanding of the possible factors influencing the biphasic Poisson's ratio and recovery of the tissue after deformation, an analysis of the collagen and elastic fibre orientation was conducted. Three plugs of NP (ø10mm) material were harvested from bovine tails and fixed in 10% formalin for 48 hours. Each plug was then sectioned in the axial-radial plane at the midpoint of the sample with a cryostat (ThermoElectron Corporation, Cheshire, U.K.) which was maintained at -14°C. Plugs were bonded to mounting die using a low temperature embedding resin (Shandon Cryomatrix, Thermo Fisher Scientific) and one 5μm thick sample was harvested per plug and dual stained for collagen and elastic fibres. Full plug thickness (end-plate to end-plate) sections were stained to allow analysis of the axial homogeneity of each component.

Sectioned samples were brought to water via xylene and ethanol followed by a Mallory bleach with 0.25% potassium permanganate for 10 min. Samples were then rinsed in 95% ethanol before being submerged in Miller's solution for ~3h. Samples were then re-rinsed in 95% ethanol and tap water. A counter stain with iron hematoxylin and van Gieson was added. Samples were finally dehydrated with ethanol, cleared with xylene and mounted (Miller, 1971). Imaging was conducted with a light microscope (Zeiss Axio Imager.Z1) at 40x magnification. Staining was performed by technicians at the School of Veterinary Medicine, University of Glasgow.

5.3.2.2.   *Full disc*

Due to biochemical similarities between bovine tail and human lumbar discs (Demers et al., 2004) IVD's from bovine tails (aged 14-30 months) were harvested within 4h of slaughter. A microtome blade was used to remove the three largest discs which were subsequently frozen at -20 ^{o}C. The following day a 16mm punch was

used to produce uniform plugs containing both the NP and AF before being taken to a cryostat (ThermoElectron Corporation, Cheshire, U.K.) which was maintained at -14°C. Discs were bonded to mounting die using a low temperature embedding resin (Shandon Cryomatrix, Thermo Fisher Scientific). ~20µm slices were removed from each disc until a flat surface was obtained. Each disc was then rotated 180° and the same process applied on the opposite surface to obtain two parallel flat surfaces, resulting in 16 discs of 2330 ± 600 µm thickness. Discs were then stored at -20 ^{o}C until testing when they were thawed slowly at room temperature (~1800s) and subsequently clamped between two polished aluminium plates. The clamps were then submerged in 3M NaCl to allow semi-confined swelling for 2h, whilst maintaining surface finish and parallelism (Figure 5.14). India ink marker dots were then applied to thawed discs using the technique described in 5.3.1. Two spacing configurations were used; square of side 3mm (on the NP only) termed *inner* (n=8), and square of side 10mm (on the AF and central dot on NP) termed *outer* (n=8).
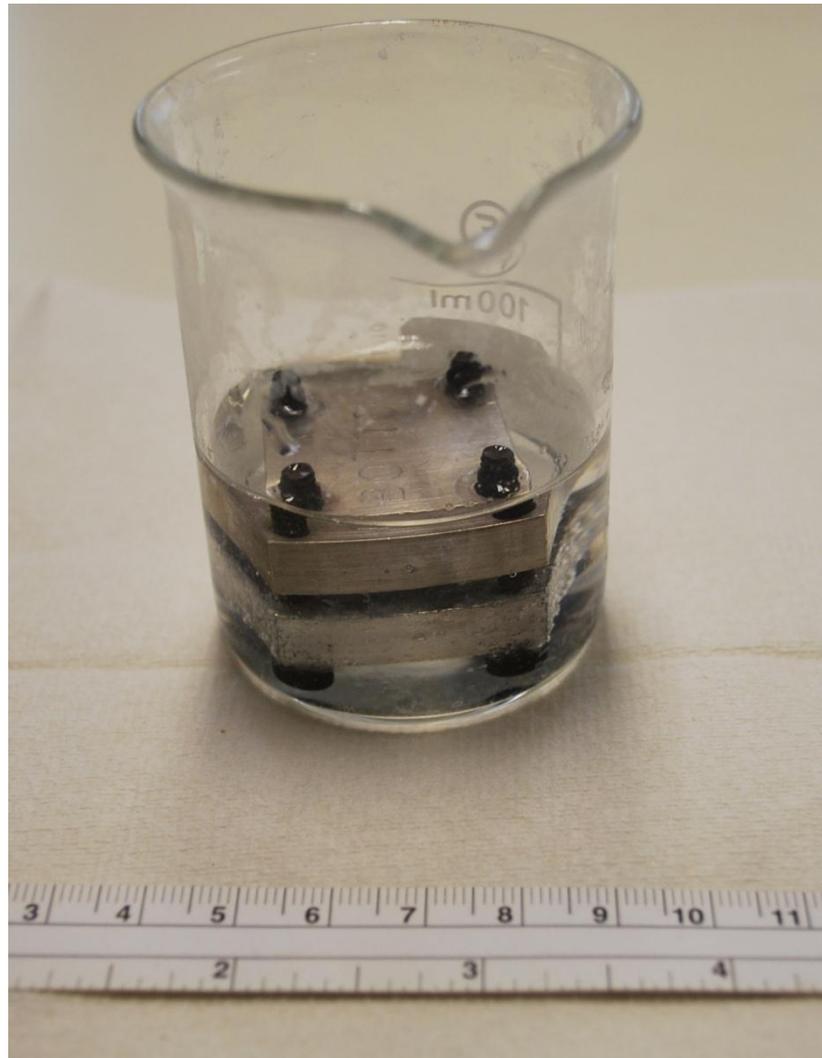
Figure 5.14 Clamping system for full disc semi-confined swelling.
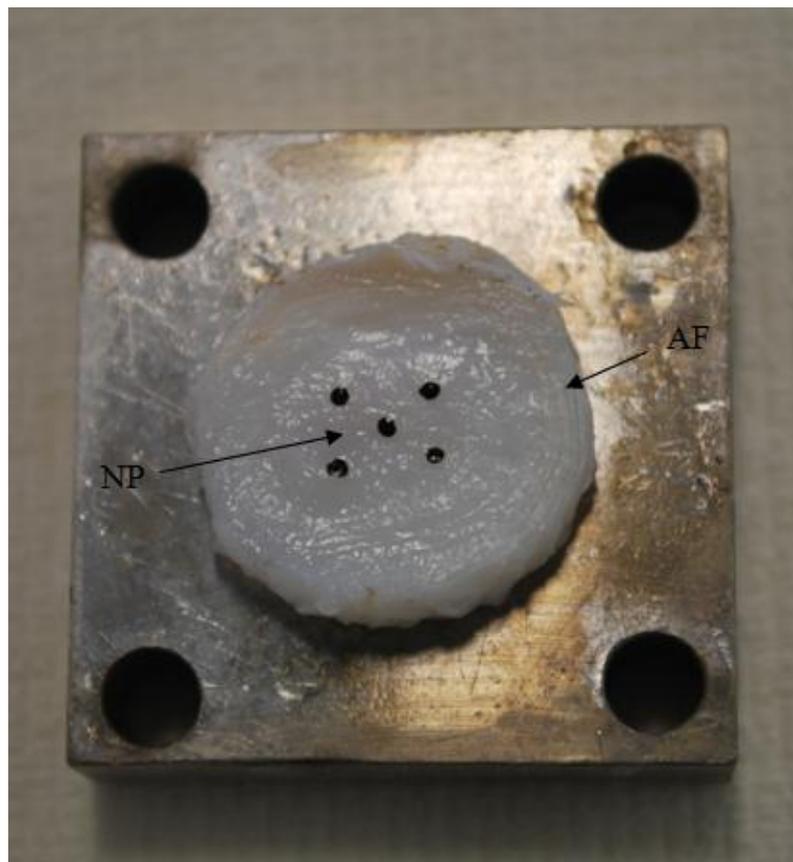
Figure 5.15 India ink dots applied to full disc surface (inner marking configuration of side 3mm shown).

5.3.3. Mechanical testing

5.3.3.1.　　　Depth and strain-rate dependent Poisson's ratio of the isolated NP

Axial displacements were applied to each sample (Electroforce 3200 series, Bose, USA), whilst a Prosilica GE video camera (Allied Vision Technologies, USA) determined strain in two orthogonal directions (denoted ε_{11} and ε_{22}) which were then used to calculate circumferential strain and Poisson's ratio. Ramp-hold experiments were conducted in displacement control whilst measuring the circumferential strains. Each sample was subjected to 5% strain increments up to 20% axial strain at either 30μm/s ($\varepsilon_{zz} \approx 0.02s^{-1}$) or 0.3μm/s ($\varepsilon_{zz} \approx 0.0002s^{-1}$) with one hour hold periods which, in pilot studies, was found to be sufficient for full stress relaxation. The slow strain rate was chosen to keep the tissue in constant equilibrium; and the fast strain rate chosen as it was x100 greater than the velocity of the slow ramp which was considered sufficient to allow the tissue to demonstrate any strain rate dependency. Therefore, there were four experimental groups (inner/outer; fast/slow strain rate) with N=8 in each group. Circumferential strain data was recorded at 2Hz during the hold phases, using a 10Hz low-pass filter to counter motor noise. Static and dynamic coefficients of friction between NP samples and the lubricated glass platens were determined using an angled ramp as described in section 5.3.1.

5.3.3.2.　　　Region / strain dependent Poisson's ratio of the full disc

Axial displacements were applied to each sample and the resultant circumferential strain and Poisson's ratio determined as outlined in section 5.3.1. Ramp-hold experiments were conducted in displacement control whilst measuring the circumferential strains. Each sample was subjected to 5% strain increments up to

20% axial strain at 30μm/s ($\varepsilon_{zz} \approx 0.02s^{-1}$) with one hour hold periods which, in pilot studies, was found to be sufficient for full stress relaxation. Therefore, there were two experimental groups (inner markers/outer markers) with N=8 in each group.

5.3.3.3.   *The effect of interfacial shear stress*

The protocol outlined in section 5.3.2.1 was repeated with no lubricant to deliberately introduce high friction between the sample and platens. Each sample was allowed to equilibrate for 2 hours prior to placement in the unconfined compression rig. Circumferential strain and resultant Poisson's ratios were calculated for each axial strain with N=3.

5.3.4. Data analysis

Circumferential strain, $\varepsilon_{\theta\theta}$, was calculated using

$$\varepsilon_{\theta\theta} = \sqrt{\frac{(\varepsilon_{11}^2 + \varepsilon_{22}^2)}{2}} \tag{5.6}$$

The derivation of Eq. (5.6) and how circumferential strain is related to radial strain is documented in Appendix 9.3. The global Poisson's ratio was subsequently calculated from

$$v = -\frac{\varepsilon_{\theta\theta}}{\varepsilon_{zz}} \tag{5.7}$$

where v is the Poisson's ratio, $\varepsilon_{\theta\theta}$ is the resultant circumferential strain and ε_{zz} is the applied axial strain. v_B was defined as v at the end of the ramp phase, whilst v_M was defined as v at the end of the hold phase. Strain, strain-rate, zone and AF dependency

were analysed using repeated measures ANOVA, with significant differences assumed when $p \leq 0.05$.

5.4.   Results

5.4.1. Mechanical testing

The static coefficient of friction of the NP-glass interface was 0.44 ± 0.08, and 0.26 ± 0.05 (mean ± SD) for the silicone-glass interface. The dynamic coefficient of friction of the NP-glass interface was 0.34 ± 0.08, and 0.17 ± 0.04 for the silicone-glass interface which is in keeping with previous investigations of the friction coefficient between soft tissue specimens and glass platens during unconfined compression (Wu et al., 2004).

All samples exhibited swelling (~1% circumferential strain) during the initial hold phase; however, equilibrium was always achieved before the first ramp phase and data sets were corrected for swelling by zeroing circumferential strain data immediately before the first ramp. For nearly all isolated NP samples, the maximum circumferential strain was recorded immediately after the ramp phase, which was followed by partial radial recoil of the tissue during the hold phase. Radial recoil resulted in v_M being less than v_B ($p < 0.001$) (Figure 5.16). v_M and v_B were strain-dependant ($p < 0.001$) for both the 0.3µm/s and 30µm/s strain-rates, with both measures of v increasing linearly with increasing axial strain. Poisson's ratio values for the slower strain-rate were significantly greater than those for the faster strain-rate ($p < 0.001$). Poisson's ratios for the outer zone at both strain-rates were greater than those of the inner zone for all strains although not significantly so ($p = 0.625$) (Figure 5.17). Results for the isolated NP when high interfacial shear stresses were

induced via the omission of lubricant showed no redial recoil and significantly greater v_B when compared to the low friction case, for all strains (p = 0.025) (Figure 5.21).
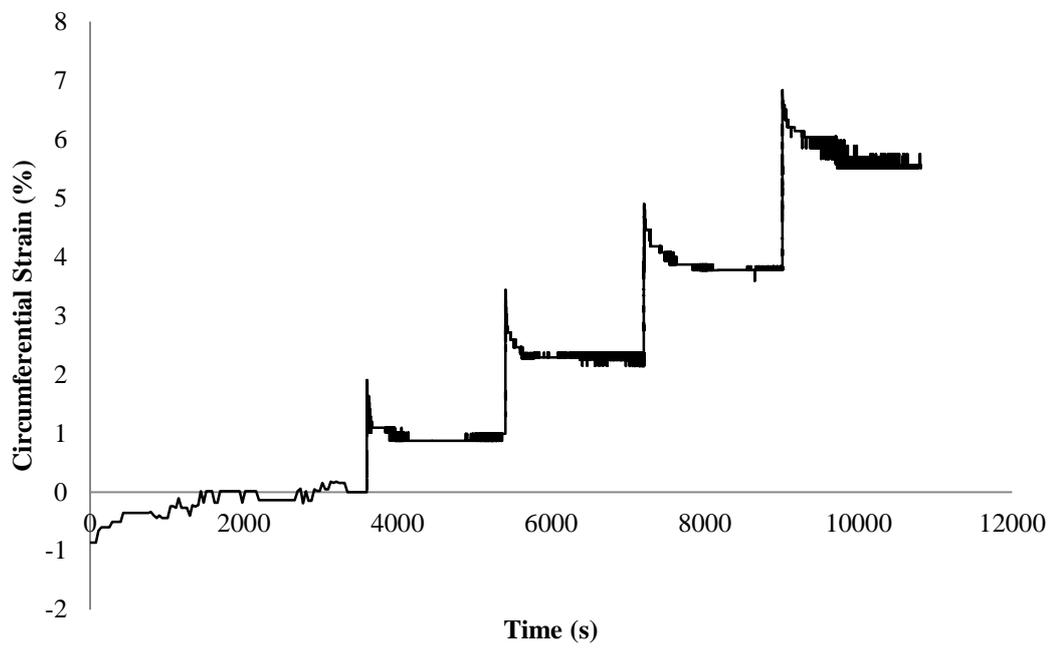
Figure 5.16 Example of circumferential strain results for the isolated NP demonstrating radial recoil.
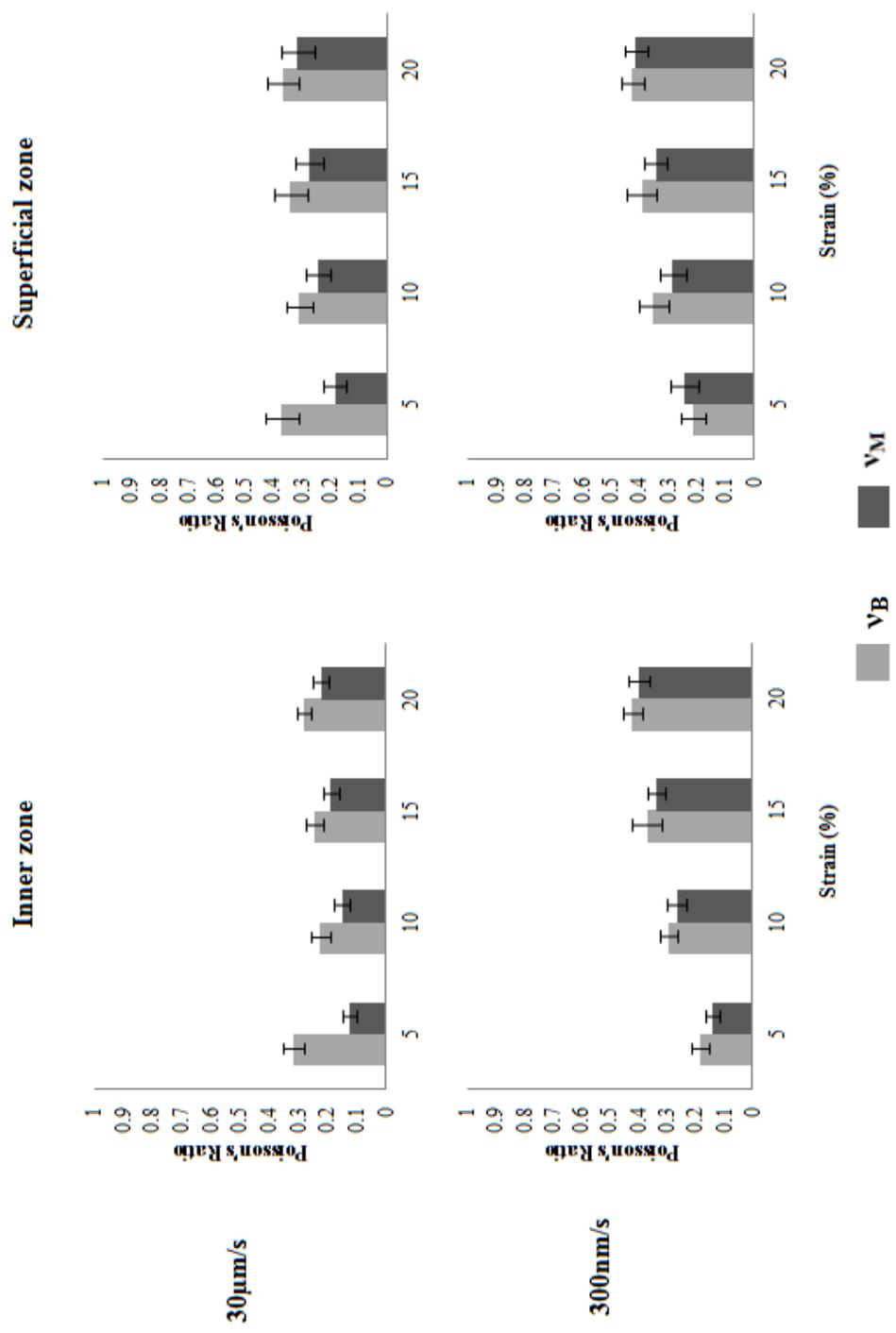
Figure 5.17 Poisson's ratio results for the isolated NP.

No significant lateral recoil was observed for either inner or outer marker positions for the full disc tests (p = 0.619), with $v_M \approx v_B$ (Figure 5.18). Accordingly, only one Poisson's ratio (v_B) will be referred to when discussing the full disc. Poisson's ratio was found to increase linearly with increasing axial strain, for both marker positions, in a similar fashion to that observed for the isolated NP. Results for the inner marker position, even though not significantly (p = 0.247), were greater and demonstrated greater variance than results for the outer position (Figure 5.19). Inner marker results (NP with confining effect of AF) were greater than results for the isolated NP for most axial strains even though not significantly so (p = 0.173) (Table 5.2) and demonstrated greater strain dependence (Figure 5.20). Superficial zone results for isolated NP have been chosen for this comparison due to the comparable location of measurement with the full disc inner marker configuration (markers were positioned on inferior surface of full disc).

The load cell used in this study was chosen as it offered the highest resolution available at the time whilst allowing for the weight of the upper platen (300g). Unfortunately it did not offer a resolution capable of measuring the stress-relaxation during unconfined compression experiments, and the lubricating gel introduced undesirable artefacts to reaction force data, so this has not been included in this chapter.
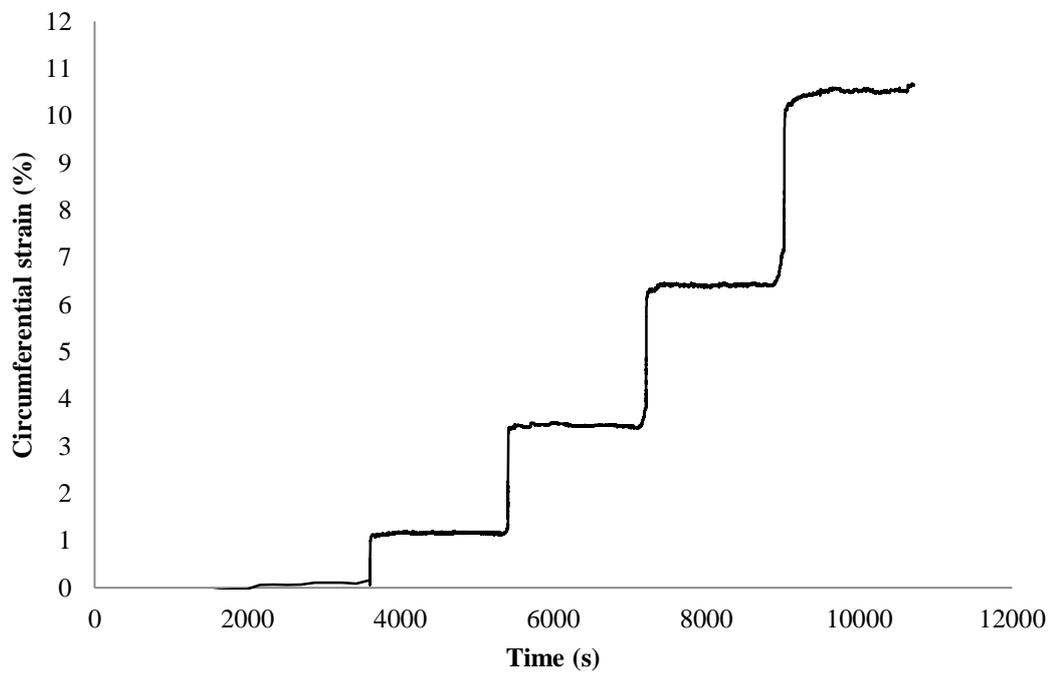
Figure 5.18 Circumferential strain results for full disc (inner markers).
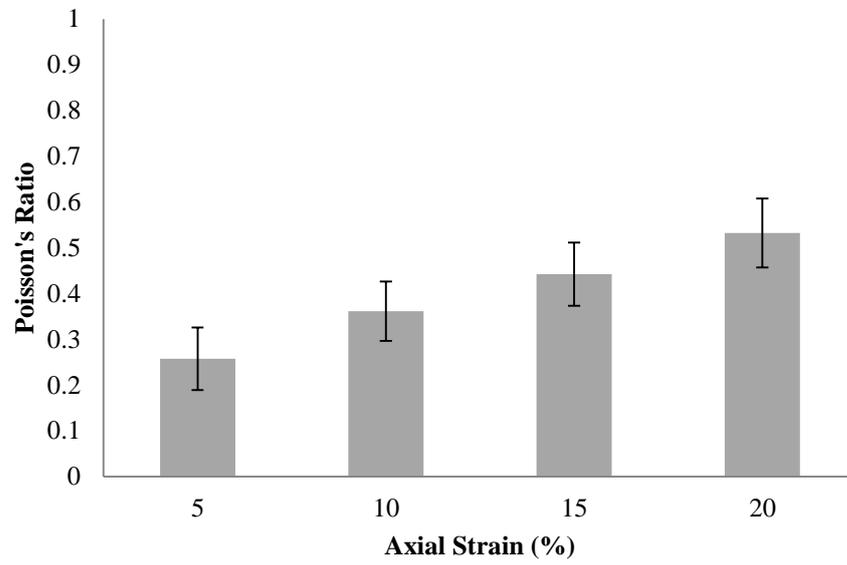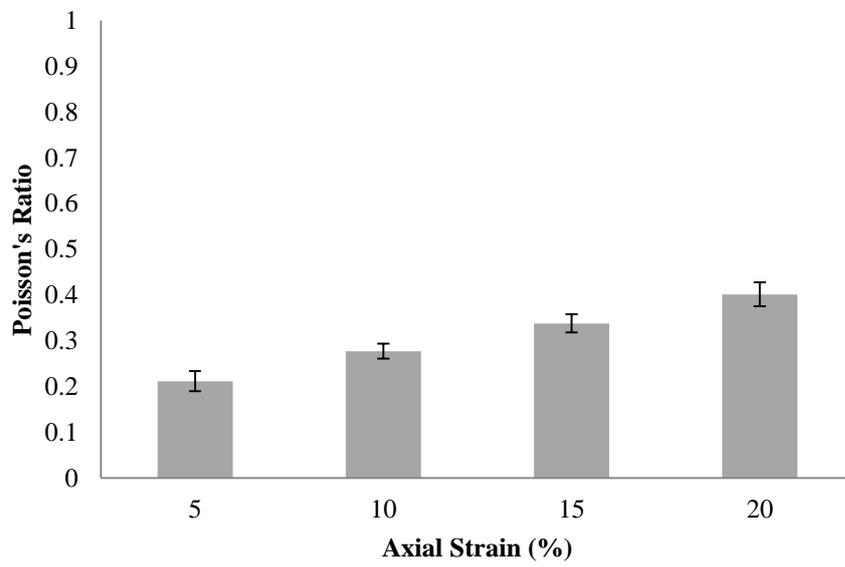
Figure 5.19 Poisson's results for full disc (A - inner markers, B – outer markers).

Strain (%)	NP (with AF)	Isolated NP
5	0.26 ± 0.07	0.37 ± 0.06
10	0.36 ± 0.06	0.31 ± 0.05
15	0.44 ± 0.07	0.34 ± 0.06
20	0.53 ± 0.08	0.37 ± 0.06

Table 5.2 Biphasic Poisson's ratio results for NP (full disc and isolated NP).
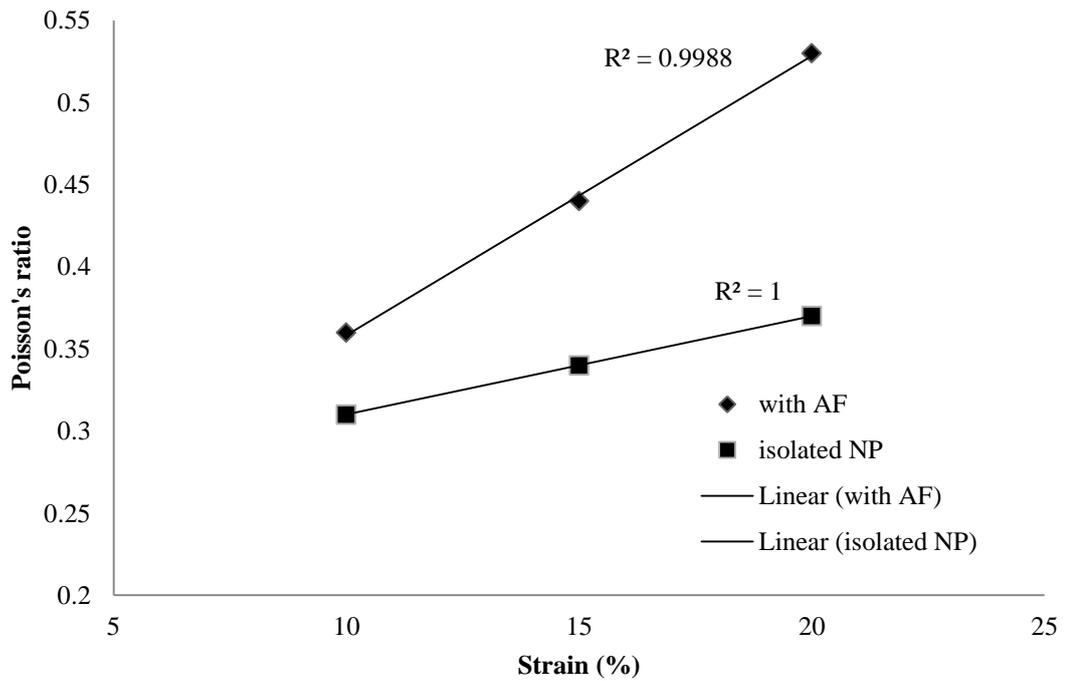
Figure 5.20 vB obtained from i) NP confined by AF and ii) isolated NP for strains >10%.
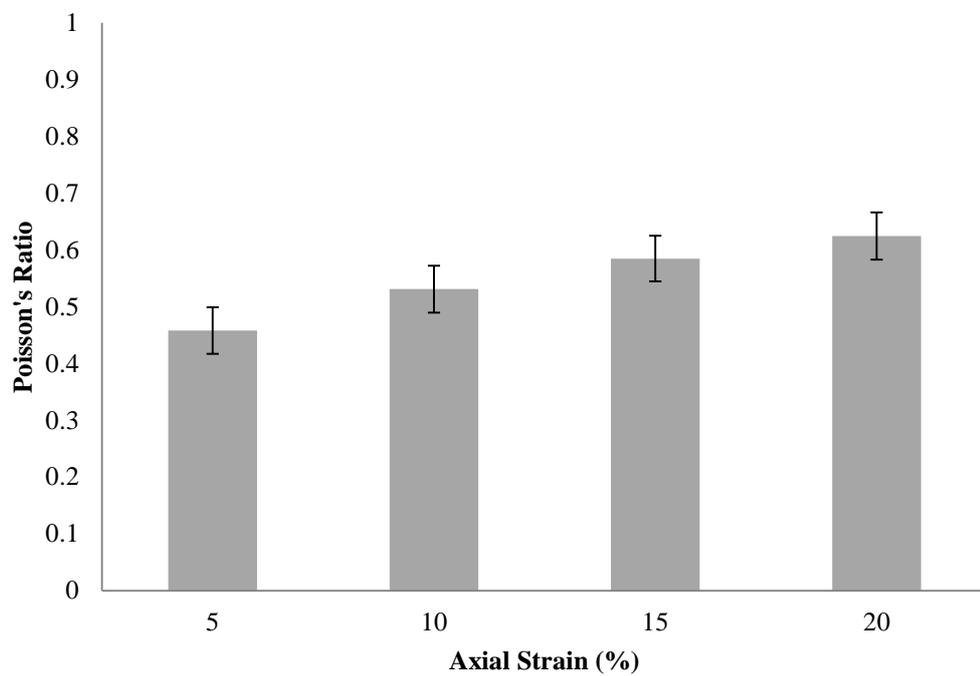
Figure 5.21 Isolated NP biphasic-Poisson's ratio results with high interfacial shear stresses.

5.4.2. Histology

Histology results indicate that the collagen network in the NP appears to be unorganised and homogenous, as previously reported (Szirmai, 1970, Inoue and Takeda, 1975, Inoue, 1981), with no obvious difference between superficial and inner zones. However, long elastic fibres (20-50μm) were found to be straight and run predominantly perpendicularly to the cartilage endplate in the superficial zone (A) whilst run predominantly radially in the inner zones (B) (Figure 5.22) which is in keeping with the study investigating collagen and elastic fibre orientation in bovine discs by Yu and co-workers (2002).
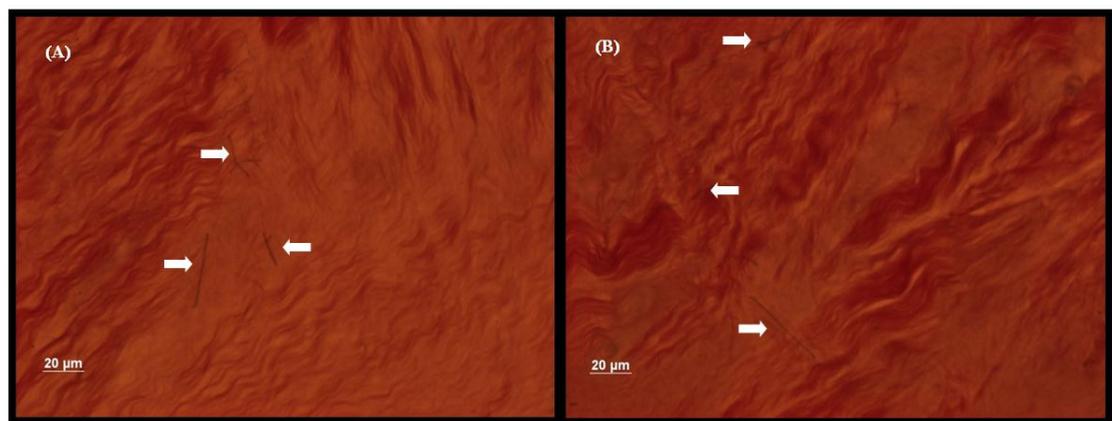
Figure 5.22 Collagen (red) and elastic fibre (black) orientation for (A) superficial and (B) inner zones. Elastic fibres are indicated by arrows.

5.5. Discussion

For multiphasic modelling of the IVD, ν_M is a necessary parameter in all but confined compression analyses. Similar methodologies of the measurement of Poisson's ratio have been reported previously for both AC (Jurvelin et al., 1997, Korhonen et al., 2002, Wang et al., 2003) and NP (Cloyd et al., 2007) with the latter reporting $\nu = 0.62 \pm 0.15$. However, this chapter has reported that ν_M of the isolated

NP is strain-dependent with results varying between 0.12 and 0.44. The significant discrepancy between the current results and those reported by Cloyd et al. (2007) may be due to methodological and/or sample differences. Cloyd et al. (2007) determined ν at the end of the hold phase via a single shot optical recording of lateral displacement which did not allow for quantification of radial recoil (if any) or friction effects which, if present, may have resulted in the reporting of ν_B and not ν_M. They also bathed their specimens in physiological saline which may have significantly swollen the tissue. Both of these issues may be ascribed to their comparatively high result. Additionally, anisotropic materials can sometimes exhibit a Poisson's ratio greater than 0.5 in some directions; therefore if the tissue expanded non-uniformly, an over prediction of lateral expansion at a region of high displacement may have occurred. The discrepancy between current and previous results highlights the sensitivity of experimental protocol to the characterisation of disc properties.

The friction tests found the silicon-glass interface to have lower static and dynamic coefficients of friction than the NP-glass interface. The Poisson's ratio of silicone was found to be 0.52 ± 0.008 suggesting friction effects did not reduce the measurement of ν for silicone. Due to the non-porous nature of silicone there was no radial recoil, however the existence of radial recoil for the isolated NP samples in the hold phase indicates that solid matrix radial tensile stresses were sufficient to overcome the interfacial shear stresses.

For the fast ramp condition ν_B may be considered constant at approximately 0.35 across the axial strain range. Linear biphasic theory (Armstrong et al., 1984) predicts that $\nu_B = 0.5$ at the start of each ramp phase due to the assumption of solid and fluid

phase incompressibility and zero friction. However, depending on the radial permeability and/or the applied strain-rate, the Poisson's ratio at the end of the ramp phase may deviate from this value. Slow ramps allow more time for fluid gradients to diffuse away and therefore the tissue would be closer to equilibrium at the end of the ramp. Additionally, the use of the lubricating gel as a fluid film may have allowed for fluid flow through the superior and inferior surfaces of the tissue sample during compression thus causing significant deviation from the boundary conditions outlined in the biphasic unconfined compression theoretical work of Armstrong et al, (1984). The effect of this mechanism may have served to reduce fluid pressurisation in the tissue and thus reduce v_B.

The increase in v_M with axial strain may be due to the compaction of the tissue; as voids collapse the tissue becomes denser. However, v_M results for the slower strain-rate were significantly greater than those for the faster strain-rate. One explanation may be the intrinsic viscoelasticity of the collagen fibres, whereby increased radial stress relaxation of the fibres in the slow condition compared to the fast would reduce the strain energy in the collagen thus reducing the work they could do in recoiling against friction. Additionally, it has been reported that collagen fibre viscoelasticity may weaken fluid pressurisation in unconfined compression, especially at moderate strain rates (Li and Herzog, 2004a), which may indicate an additional mechanism resulting in the low values of v_B. Such a phenomenon may be modelled using poroviscoelasticity theory (Suh and DiSilvestro, 1999). In the disc, NP matrix viscoelasticity may be a mechanism which serves to reduce the radial stress experienced at the NP-AF interface during compressive loading.

Isolated NP results show no significant difference between superficial and inner zones, however, it should be noted that results for the former are higher for all strains and strain-rates, and the lack of statistical significance may be due to the experiment being under-powered. Analysis of elastic fibre orientation, by way of histology, indicated that elastic fibres run predominantly radially in the inner zone and predominantly perpendicularly to the CEPs in the superficial zones which is consistent with previous work (Yu et al., 2002). Since elastic fibres will only demonstrate mechanical contribution in tension, this may provide an explanation as to why both v_B and v_M results for the inner zone were lower than those obtained in the superficial zones.

Full disc Poisson's ratio results demonstrate no lateral recoil, which may be a result of increased interfacial artefacts due to the high sample aspect ratio (d/h = ~7). Nevertheless, some interesting results were obtained. In keeping with isolated tissue results, a linear increase in Poisson's ratio was observed with increasing axial strain for both marker configurations as a result of tissue consolidation. Results for the outer marker position were lower than results obtained for the inner marker configuration which may be a result of the latter measurements being taken from the AF; tissues with higher modulus such as AC and AF have been shown to exhibit low Poisson's ratios (Jurvelin et al., 1997, Kiviranta et al., 2006). Results obtained for the inner marker configuration represent the Poisson's ratio of the NP in situ with the confining effect of the AF, and were found to be greater than comparable v_B results for the isolated NP which may be the result of fluid pressurisation mechanisms. Since friction effects were evident in the full disc experiments, only a biphasic value has been obtained which is highly dependent on radial permeability during an unconfined compression experiment. Since the AF exhibits a significantly lower permeability than the NP, this will serve to increase fluid pressurisation during the ramp phase and subsequently increase v_B. The

finding that Poisson's ratio results for the inner marker configuration were greater than results obtained for the outer configuration may indicate to an important strain distribution mechanism which allows the NP to expand to accommodate stress, by distributing it to the stiffer AF. This mechanism may also serve to lessen localised strain concentrations at the NP-AF boundary, where cell density is high, whilst disc bulging is kept to a minimum via the comparatively stiffer AF.

The finding that increased interfacial shear stresses, induced via lubricant omission, resulted in greater biphasic Poisson's ratio results may suggest non-uniform lateral expansion under such conditions. Since circumferential strain was recorded via the relative movement of markers, anisotropic expansion may have resulted in large localised deformations thus distorting results. This finding, however, lends confidence to the experimental set up where lower Poisson's ratio and radial recoil were observed when the lubricant was included. Further work into this anomaly, by way of surface strain mapping which allows for the recording of localised radial strains, may confirm this hypothesis but was not conducted as part of current work.

5.6. Experimental artefacts

The current experimental set up has provided an improvement on previously adopted optical measurement techniques by maintaining the structural integrity of the tissue. Previously, physical markers have been inserted to the tissue which may have resulted in significant alterations to tissue structure. However, the sagittal sectioning of the disc conducted in this study may have depressurised the NP and thus released the AF circumferential pre-stress (O'Connell et al., 2011) indicating that current ν_B results may be lower than what exist in vivo.

The use of a hypertonic external environment during the experiment may have served to reduce radial permeability; however, the effect of this will only have influenced the transient behaviour and not the equilibrium results. Since biphasic results are in fact lower than predicted (<0.5) the effect of reduced permeability was not considered significant. The other implication associated with the hypertonic environment is the possible dehydration of the tissue over the long test durations which may explain the findings of Khalsa and Eisenberg (1997) who found that the Poisson ratio of AC decreased with increasing saline concentration. However, circumferential strain was recorded throughout each full test and any artefacts associated with dehydration, such as radial contraction during the initial hold phase, were not observed. Ideally, an isotonic environment would have been used, however, for reasons outlined in section 5.3.1 it was decided that a hypertonic environment was most suitable for the characterisation of Poisson's ratio effects.

Over such long testing durations, the leaching of PG's from the tissue is a possible source of experimental error. However, it has been shown that when the tissue is subjected to solutions of high osmotic pressure then leaching is significantly reduced (Urban and Maroudas, 1981). Since 3M NaCl was used in this experimental set up, minimal leaching is expected to have occurred.

5.7. Conclusions

This chapter has shown that the Poisson's ratio of the isolated NP is strain and strain-rate dependent with solid matrix viscoelasticity playing an important role in describing its variation with strain-rate. The AF has been found to play in important role in enabling the disc to absorb compressive loads by allowing the NP to expand radially, whilst maintaining minimal global disc bulging. For future modelling of the disc, it is suggested that the matrix-Poisson's ratio values determined at low strain but high strain-rate may be the most characteristic of this tissue and poroviscoelasticity theory may have to be included to account for strain-rate effects.

6. Finite element modelling of the nucleus pulposus in unconfined compression: the effect of mechano-electrochemical phenomena

6.1. Introduction

The unconfined compression test is a commonly used material characterisation method for investigating the mechanical properties of cartilaginous tissue and explants in tissue engineering studies. As presented in chapter 5, it allows for the elucidation of global material properties such as Poisson's ratio and Young's modulus; however, there is occasional discrepancy between experimental and numerical results. This form of mechanical test does not allow for the analysis of the micromechanical interactions which occur during loading of the tissue, which may reveal where any disagreement originates. Additionally, such experimental analyses do not provide detailed information on how such deformations may impact tissue mechanics at the cellular level.

Disc cells exist in a complex environment whereby variations in nutrient supply and physical signals can significantly impact on their activity (Horner and Urban, 2001, Urban, 2002). Structural remodelling may result from changes in the matrix which is governed by the environment-sensitive cellular response. The reaction of the IVD to mechanical loading and its effect on cellular activity has been an area of extensive research in recent years; however, it has proved experimentally challenging due to complex physical stimuli. Mechano-electrochemical interactions within the extra-cellular matrix such as stress, strain, ion concentration, fluid pressure, electric potential and fluid flow combine to create the complex physiochemical environment

in which cells exist, and the interactions of such stimuli are almost impossible to determine experimentally.

The formulation of the biphasic mixture model (Mow et al., 1980), where cartilaginous tissue is modelled as an intrinsically incompressible porous-permeable solid matrix filled with an incompressible interstitial fluid, has been used extensively in the tissue mechanics literature. Armstrong et al. (1984) delivered the first mathematical framework for the unconfined biphasic creep and stress-relaxation of AC which detailed the mechanical responses within a cylindrical specimen compressed between two frictionless and impermeable platens. Subsequently, more complex unconfined compression conditions and material properties have been modelled (Spilker et al., 1990, Cohen et al., 1998) and the incorporation of the solid matrix tension–compression nonlinearity proved a significant step in allowing the biphasic model to better describe the response of cartilaginous tissue in unconfined compression (Cohen et al., 1998, Soulhat et al., 1999, Soltz and Ateshian, 2000).

However, as highlighted in chapters 3 and 5, discrepancy can also exist between biphasic theory and experimental results, likely due to the existence of negatively charged proteoglycans entrapped within the solid matrix. As discussed in chapter 4, proteoglycans are responsible for the existence of mechano-electrochemical phenomena in the disc which significantly influence disc mechanics via electric potentials (Frank et al., 1987) and reduced permeability (Gu et al., 1993). Consequently, triphasic models have been used to investigate the mechanical, electrical, and chemical behaviours of cartilaginous tissue (Iatridis et al., 1998, Gu et al., 1999c, Gu et al., 1999b, Argoubi and Shirazi-Adl, 1996, Best et al., 1994, Frijns

et al., 1997, Laible et al., 1993, Iatridis et al., 1997a) by explicitly modelling such mechano-electrochemical phenomena.

As discussed in chapter 4, an electric potential is generated in a charged tissue via deformation induced gradients in FCD, cation and anion concentrations coupled with convective ion transport induced by interstitial fluid flow (Sun et al., 2004). Sun et al., (2004) investigated the effect of FCD on the unconfined compression of AC via a triphasic FE model and reported that the apparent Young's modulus and biphasic Poisson's ratio of a charged tissue is greater than the intrinsic Young's modulus and intrinsic Poisson's ratio (Poisson's ratio measured with the sample bathed in a hypertonic solution, a method adopted in chapter 5) of an uncharged tissue. The study also reported, in agreement with the triphasic permeation analysis results presented in chapter 4, that during unconfined stress-relaxation the diffusion potential and the streaming potential compete against each other for dominance of the overall electric potential. The study of Sun and co-workers (2004) was, however, completely numerical and model results were not compared to experimental results, nor did it consider the well-known effects of strain-dependent permeability. Kim et al., (1995) investigated the radially directed streaming potentials during dynamic unconfined compression of cartilage discs and reported that flow-induced electric fields may influence chondrocyte metabolism. Yao and Gu (2007a) investigated the mechanical and chemical response as well as the electrical signals in the IVD during an unconfined compression test via a 3D homogeneous triphasic FE model and demonstrated that fluid pressurisation and stresses are most pronounced at the NP-AF boundary and that the distribution of fluid pressure, effective stress and electrical potential are more uniform in the NP than in the AF.

Since unconfined compression has previously been used to determine material properties of disc, AC and tissue engineered explants, it is important to understand the mechano-electrochemical interactions which influence both the macro and micro responses of the tissue during such a test. A comparison between experimental and numerical data is required to validate each model and allow a thorough understanding of the mechanisms which govern the mechanical response of the NP in unconfined compression. Modelling such a configuration with both biphasic and triphasic framework is important due to the frequency of usage of each in the literature (Ateshian et al., 2004).

6.2.   Aims and hypotheses

Geometrically simple FE models must be developed to investigate the complex intrinsic mechanical and biological properties prior to the incorporation of more complex geometries to disassociate the mechanical and geometrical effects on disc behaviour. This chapter, therefore, aims to investigate Poisson's ratio effects in the NP through FE simulations of an unconfined compression analysis and elucidate the transient and equilibrium mechano-electrochemical interactions which occur during such loading. In a similar fashion to the investigation discussed in chapter 4, biphasic and triphasic models will be developed and analysed with ionic environment a key variable. Material properties and configuration constraints are taken from those identified in chapter 5. It is hypothesised that the ionic environment has a significant effect on results and mechano-electrochemical interactions play an important role in governing tissue response in an unconfined compression experiment.

6.3. Methods

6.3.1. FEBio

As used in chapter 4.3.1, the nonlinear finite element program FEBio was chosen as the most suitable platform to model the unconfined compression of the NP.

6.3.2. FEBio Biphasic material

The biphasic material, as discussed in chapter 4.3.2, may be used to model a non-charged mixture of a porous solid matrix and interstitial fluid. The mixture is compressible as the pores of the solid matrix are collapsible. Quasi-static conditions were assumed for momentum balance by neglecting inertia effects.

A change in mixture volume may occur when interstitial fluid enters or leaves the porous solid matrix. According to continuum kinematics, each constituent, α, of a mixture (α = s for the solid and α = w for the fluid) has a separate motion with the movement of α = s particularly important to the current study. Since the mixture is porous, the Cauchy stress, σ, is given by

$$\sigma = -p\mathrm{I} + \sigma_e \qquad (6.1)$$

Where p is the fluid pressure, I is the identity tensor, and σ_e is the effective stress resulting from the deformation of the solid matrix. Conservation of mass for the mixture requires that

$$div(v^s + w) = 0 \qquad (6.2)$$

where v^s is the solid matrix velocity and w is the fluid flux relative to the solid. To relate the relative fluid flux, w, to the fluid pressure and solid deformation, the equation of conservation of linear momentum for the fluid is

$$-\varphi^w \nabla p + \hat{P}_d^w = 0 \qquad (6.3)$$

Where $-\varphi^w$ is the porosity of the solid matrix and $\hat{P}_d^w$ is the momentum exchange between the solid and fluid phases. The most common constitutive relation employed in the biphasic material is

$$\hat{P}_d^w = -\varphi \text{k}^{-1} \cdot w \qquad (6.4)$$

where k is the hydraulic permeability. When combined with (Eq.6.3), it gives the familiar Darcy's law:

$$w = -\text{k} \cdot \nabla p \qquad (6.5)$$

These equations are combined with the constitutive relations for the solid to provide the full biphasic theory.

6.3.3. FEBio Triphasic material

A triphasic material is an extension to the biphasic material whereby charged or neutral solutes may be contained in the mixture. Additionally, the solid matrix may also be charged (allowing for the incorporation of FCD) affecting the interaction between solute and solid matrix considerably. The triphasic material model is based on the mixture theory of Lai et al. (1991) and considers the charged solid phase, the

incompressible fluid phase, and ion phase with two monovalent ion species, i.e., anion (-) and cation (+) (Sun et al., 1999). The reader is referred to section 4.3.3 for a full description of the theory.

6.3.4. Biphasic and Triphasic solid and permeability constitutive relations

6.3.4.1. *Solid phase constitutive relation*

Both the biphasic and triphasic models adopt the same solid constitutive relation for modelling the deformable solid matrix of the tissue, whilst incorporating the additional properties discussed above. The chosen relation is based on the non-linear framework of Holmes and Mow (1990) which allows for the modelling of strain-dependent stiffness. This isotropic, hyper elastic material model has been successfully implemented in modelling the solid matrix of both AC (Holmes and Mow, 1990, Ateshian et al., 1997) and IVD tissue (Iatridis et al., 1998, Heneghan and Riches, 2008b). The reader is referred to section 4.3.4.1 for a fuller description of the theory.

6.3.4.2. *Permeability constitutive relation*

Both the biphasic and triphasic models adopt the same permeability constitutive relation for modelling the strain-dependent permeability of the tissue. The reader is referred to section 4.3.4.2 for a fuller description of the theory.

6.3.5. Material properties of biphasic and triphasic models

Biphasic and triphasic elastic and poroelastic material properties were obtained from the literature (Table 6.1 and Table 6.2 for biphasic and triphasic properties respectively). Although triphasic effects will have some influence on transient mechanical properties, the term biphasic-Poisson's ratio will be used to describe the Poisson's ratio at the end of the ramp phase for continuity with the work presented in Chapter 5. The matrix-Poisson's ratio, v_M, was taken from experimental results obtained in chapter 5 whereby Poisson's ratio data obtained at low strain and strain rates may be most representative of the NP. E was calculated via Eq. (2.6). The ion diffusion coefficients, D^α, used in the triphasic model were significantly scaled up from the literature values as a pilot model required in excess of 15000s to reach equilibrium which was not in keeping with experimental data. The reason for this disparity will be discussed in section 6.5. The sourcing and calculation of triphasic properties was discussed in section 4.3.5.

Biphasic Material Property	Units	Value	Source
$\emptyset_0$		0.2	Roberts et al. (1989)
E	MPa	0.29	-
v_M		0.12	-
β		0.256	Heneghan and Riches (2008b)
k_o	mm^4/N.s	0.002	Farrell and Riches (2012)
M		2.41	Heneghan and Riches (2008b)
κ		0.48	Heneghan and Riches (2008b)

Table 6.1 Material properties of the biphasic analytical model.

Triphasic Material Property	Units	Value	Source
$\varnothing_0$		0.2	Roberts et al. (1989)
FCD in reference state	mEq/L	130	Stokes et al. (2010)
E	MPa	0.29	-
ν_M		0.12	-
β		0.256	Heneghan and Riches (2008b)
k_o	$mm^4/N.s$	0.002	Farrell and Riches (2012)
M		2.41	Heneghan and Riches (2008b)
κ		0.48	Heneghan and Riches (2008b)
Φ		0.971	Frijns et al. (2003)
D_0^+	mm^2/s	1.00×10^{-03}	Scaled from Na^+ D
D^+	mm^2/s	4.40×10^{-04}	Frijns et al. (2003)
κ^+		1	-
D_0^-	mm^2/s	1.60×10^{-03}	Scaled from Cl^- D
D^-	mm^2/s	6.70×10^{-04}	Frijns et al. (2003)
κ^-		1	-

Table 6.2 Material properties of the triphasic analytical model.

6.3.6. Geometry and constraints

Both the biphasic and triphasic models were modelled as a symmetric quarter cylinder to reduce computational time. The model had a radius of 2.75mm and height of 1.5mm, consistent with the experimental sample geometry in chapter 5 (Figure 6.1).
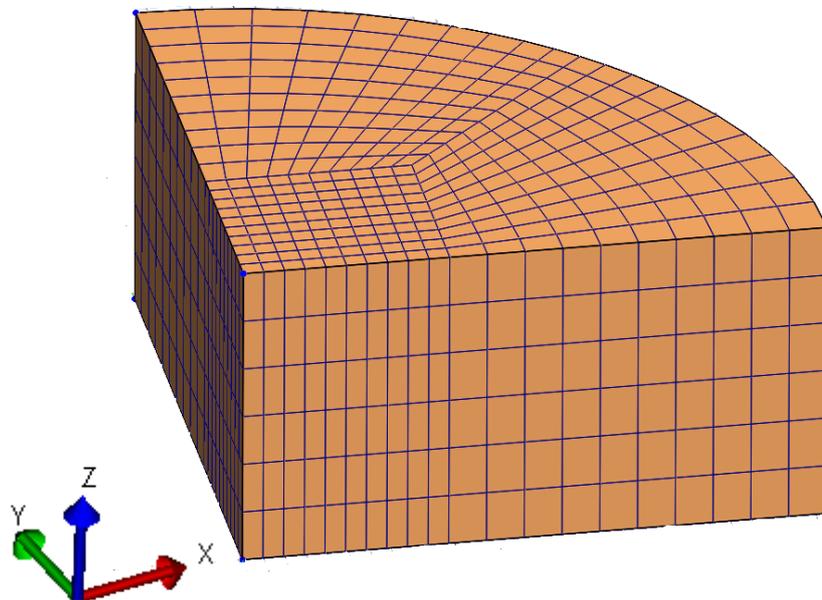
Figure 6.1 Unconfined FEA model.

The circumferential boundary was free draining (fluid pressure = 0), however, fluid pressure throughout the rest of the model was dependent on the applied loading conditions. The nodes in the x-z plane were constrained in the y- direction and the nodes in the y-z plane were constrained in the x-direction. The inferior surface was constrained in z-direction.

After deforming the sample, the axial displacement was held constant to allow the tissue to relax in the radial direction due to interstitial fluid flow.

A steady-state analysis was performed on both models. Both the biphasic and triphasic analyses consisted of a compressive displacement of 0.075mm in the z direction on the superior surface at either 2.5s or 250s ($\varepsilon_{zz} \approx 0.02 s^{-1}/\varepsilon_{zz} \approx 0.0002 s^{-1}$) to model the strain-rate dependency seen experimentally, followed by a hold phase. 5% axial strain was chosen due to findings in chapter 5 that Poisson's ratio results determined at low strain are most characteristic of this tissue. The triphasic analysis included an additional first step which ramped the FCD from 0 to -130 mEq/L, producing a Donnan osmotic pressure in the fluid as well as a Donnan electric potential in the mixture.

The triphasic model was subjected to both isotonic and hypertonic external bath NaCl salinities (0.15M and 3M). The latter of which is in keeping with the experimental protocol conducted in chapter 5. The triphasic model required the implementation of additional initial conditions as a result of the significantly more complex governing equations employed by the material model. These are discussed in full in chapter 4.

The initial effective solute concentrations (Na^+ and Cl^-) and effective pressures were set in accordance with the desired external solution concentration. The calculation of these parameters was discussed in chapter 4.

6.3.7. Data analysis

6.3.7.1.   Mesh convergence analysis

As discussed in section 4.3.7.1, a finer mesh typically yields more accurate results. The method of conducting a mesh convergence analysis involved plotting a curve of a critical result, in this case peak radial fluid velocity against the mesh fineness and computational time. Figure 6.2 shows the results for the mesh convergence analysis conducted for the triphasic model which was chosen for analysis due its higher level of complexity compared to the biphasic model. Graph A indicates that there was much variance in peak radial fluid velocity until the model contained upward of 2500 nodes. Graph B plots the computational time against the number of nodes, and illustrates that the difference in time was reduced upwards of 3000 nodes. Therefore, a 2500 node model was considered optimum for this application.

(A)
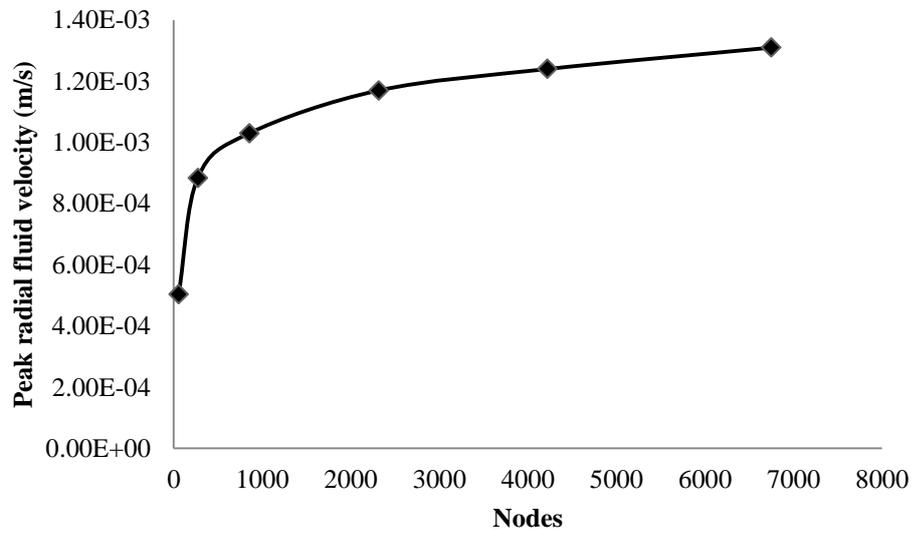
(B)
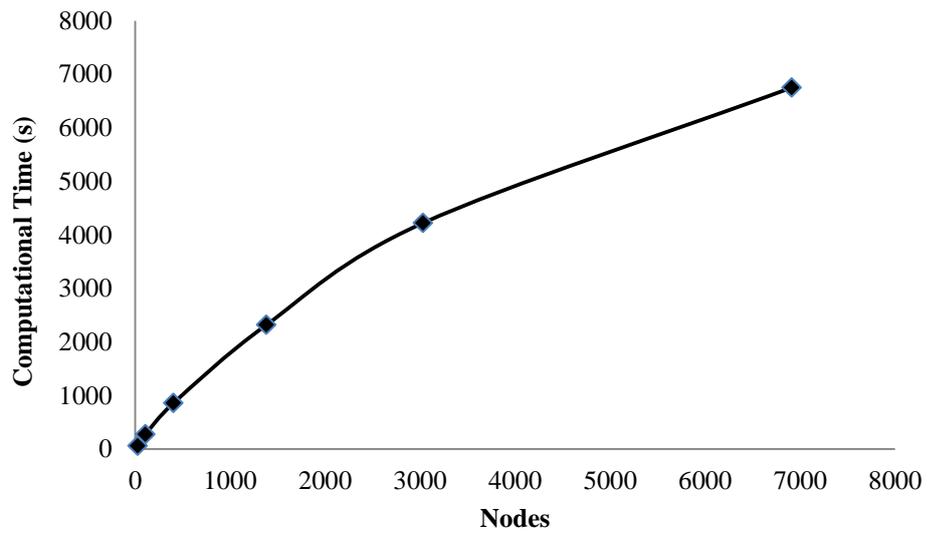
Figure 6.2 Unconfined compression model mesh convergence analysis.

6.3.7.2.   *Calculation of Poisson's ratio*

Data was recorded at 3 different nodes located from the circumferential edge of each model, donated I, II and III (Figure 6.3). Results were obtained from these nodes to elucidate any radial variation in mechanical response.
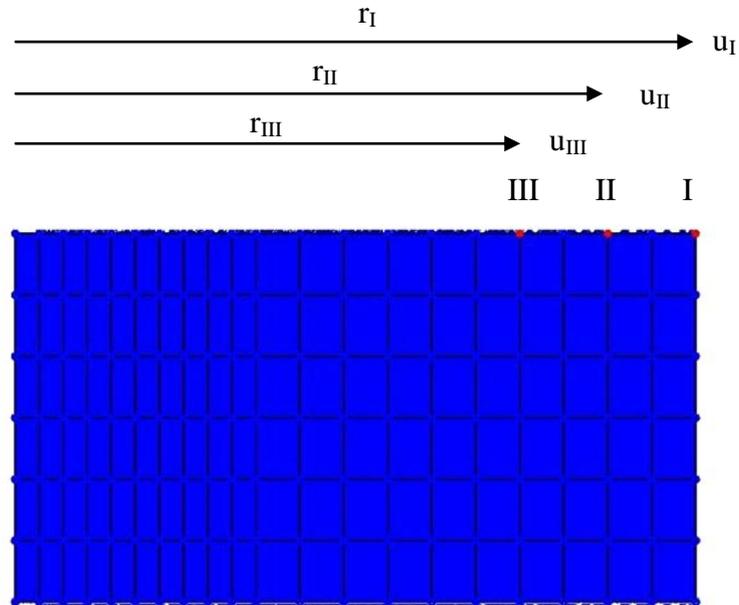
Figure 6.3 Nodes used for recording of model results.

To match experimental data, and in a similar fashion to the method adopted by Cloyd et al., (2007), lateral strain was globally defined as the change in diameter over the initial diameter of a cylindrical sample. Poisson's ratio was calculated from

$$\varepsilon_{rr\alpha} = \frac{u_\alpha}{r_\alpha} \tag{6.6}$$

where

$$\nu_\alpha = -\frac{\varepsilon_{rr\alpha}}{\varepsilon_{zz}} \tag{6.7}$$

u_α is the nodal radial displacement, r_α is the initial radial position of the node ($r_I =$ 2.75mm, $r_{II} = 2.39$mm, $r_{III} = 2.04$mm), and ε_{zz} is the applied axial strain. All other measures, such as fluid velocity, were obtained directly from the modelling program and no post analysis was required.

An alternative local definition of ε_{rr} is

$$\varepsilon_{rr\alpha} = \frac{\partial u}{\partial r}\bigg|_\alpha \tag{6.8}$$

This was not used since it could not be matched to experimental values.

6.3.7.3.   *Data analysis*

A paired two sample t-test was used to for comparison between FE results and experimental data. Significance was set at $p \le 0.05$.

6.4.   Results

In this section, numerical results from the biphasic poroelastic model (BP) and the triphasic poroelastic model (TP) will be compared to each other with particular interest paid to Poisson's ratio, fluid pressure, fluid flux, axial stress and the electrochemical phenomena such as electric potential and FCD. Firstly, the general macro-mechanical responses applicable to both models will be discussed. Each model will then be further analysed by examining nodal variations in response during an unconfined stress-relaxation experiment with strain-rate and external solution concentration being key factors. Finally, each model will be compared directly to one another and to the experimental data presented in chapter 5.

6.4.1. General results (Biphasic and Triphasic models)

Both the BP and TP models demonstrated significant time-dependent variation in radial displacement, fluid pressure and radial fluid flux for both strain rates (Figure 6.4).
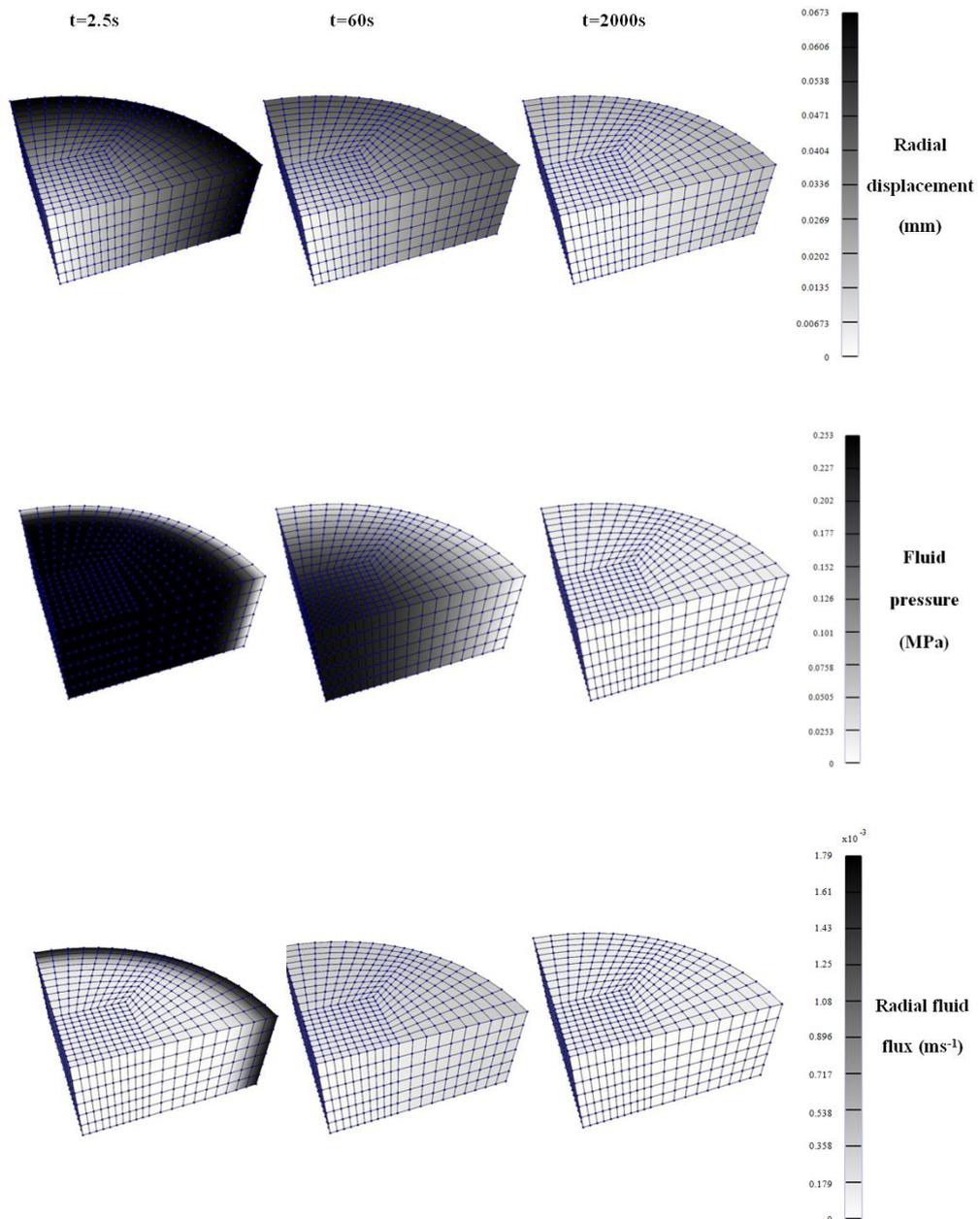
Figure 6.4 Results representative of both the BP and TP models, demonstrating significant time-dependent variations. Images were taken from the biphasic model with $\dot{\varepsilon}_{zz} \approx 0.02s^{-1}$.

Under the assumption of frictionless, impermeable platens, the lateral movement of the tissue was uniform across the lateral edge of the tissue (Sun et al., 2004). At the end of the ramp phase, t=2.5s for the $\dot{\varepsilon}_{zz} \approx 0.02 s^{-1}$ ramp, the greatest radial displacement occurred, indicating lateral expansion, which is in keeping with the experimental results obtained in chapter 5. At this point, the greatest fluid pressure also occurred toward the centre of the model with the circumferential edge remaining at zero pressure, by definition. The greatest radial fluid flux was also achieved immediately after the ramp phase with the circumferential edge experiencing the greatest outward flow. During the hold phase, t=2.5s to t=2000s, radial displacement continued in the negative direction, creating radial recoil until equilibrium was achieved, again in keeping with experimental data. Fluid pressure dissipated slowly from the circumferential edge until a homogeneous pressure was achieved at equilibrium. Additionally, radial fluid flux reduced significantly during the hold phase until equilibrium (zero flow). Figure 6.5 plots the compressive displacements applied to each model for both strain rates.
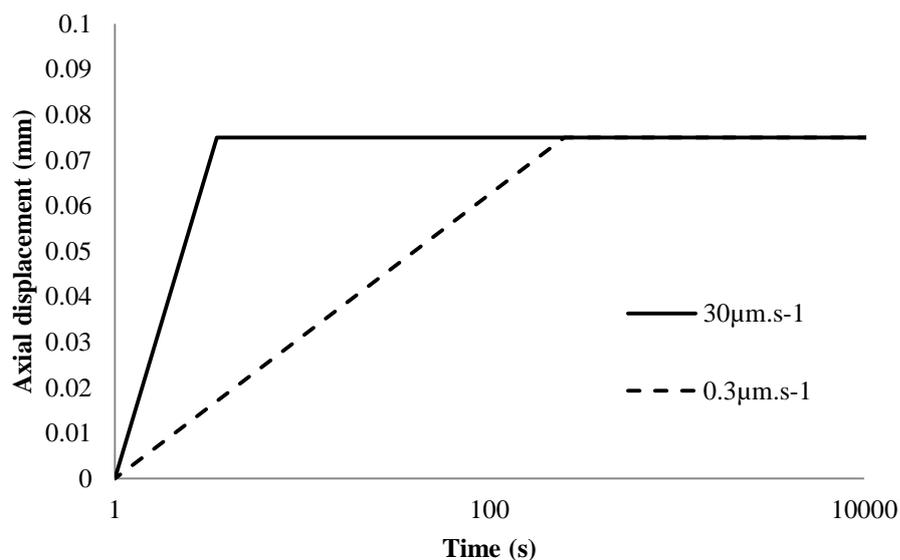
Figure 6.5 Compressive displacement plots for both strain rates.

6.4.2. Biphasic poroelastic (BP) model results

The BP model demonstrated both time-dependent and nodal variation in measures of Poisson's ratio, fluid pressure, radial fluid flux and axial stress (Figure 6.6). Results indicate that $v_{B\ I} = 0.49$, $v_{B\ II} = 0.517$ and $v_{B\ III} = 0.519$. $v_M = 0.12$ at all nodes. All nodes demonstrated an increase in fluid pressure during the ramp phase with the greatest peak fluid pressure occurring at node III with P = 0.0071MPa. An increase in fluid flux was observed at node I during the ramp phase with the greatest measure occurring immediately after the ramp phase with $w = 1.14\text{x}10^{-4}\text{mm}^3.\text{s}^{-1}$. Both nodes II and node III demonstrated an initial increase and subsequent reduction in fluid flux before following a similar trend to that observed at node I. All measures of fluid flux dissipated to zero during the hold phase. The peak axial stress was observed immediately after the ramp phase before stress relaxation occurred until equilibrium was achieved, at all nodes. A variation in peak axial stress was observed between nodes, with node II experiencing the greatest peak stress (19.89kPa) with node I experiencing the lowest (18.24kPa). No radial variation in equilibrium stress occurred with $\sigma_e = 14.77\text{kPa}$.
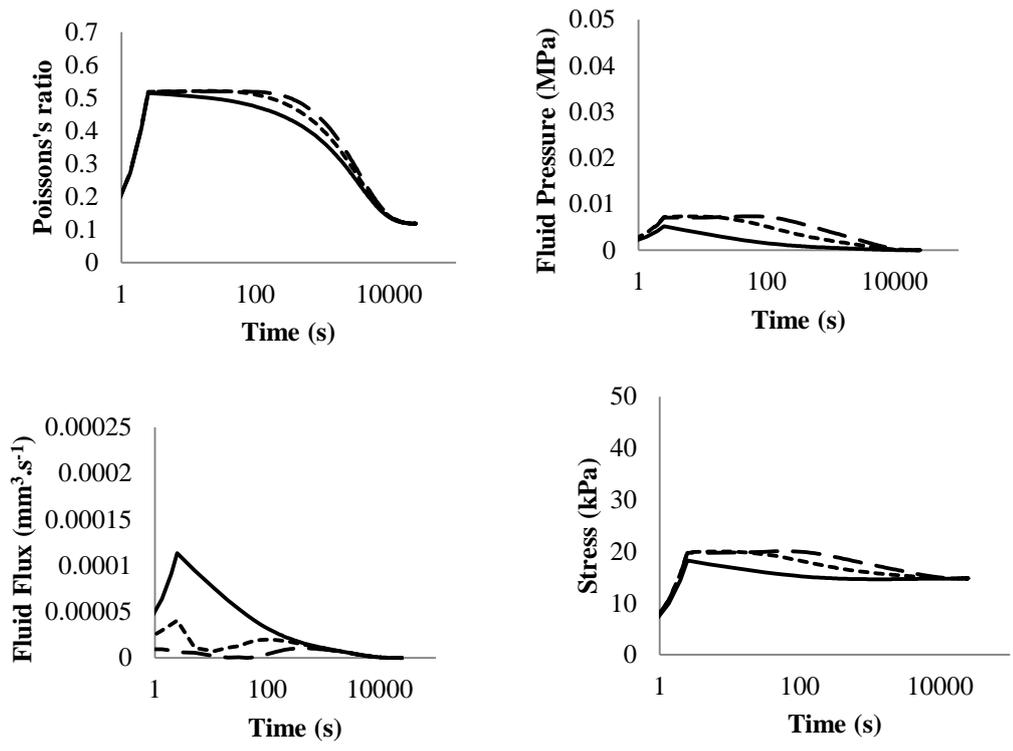
Figure 6.6 BP model results for 30µm/s ramp.

I
II
III

The slower strain-rate resulted in a variation in non-equilibrium measures of Poisson's ratio, fluid pressure, and radial fluid flux when compared to the fast strain-rate (Figure 6.7). There was no strain-rate dependency on equilibrium measures. A reduction in biphasic Poisson's ratio was observed for the $0.3 \mu ms^{-1}$ compared to the $30 \mu ms^{-1}$ ramp with $v_{B\ I} = 0.47$, $v_{B\ II} = 0.51$ and $v_{B\ III} = 0.52$. Peak fluid pressures, and radial fluid fluxes were lower in the slow ramp compared to the fast ramp. A nodal variation in peak axial stress was observed, with node III experiencing the greatest stress (19.8kPa) and node I experiencing the lowest (15.3kPa). No stress relaxation occurred at node I, however a slight increase in axial stress during the hold phase was observed. No difference in equilibrium stress was observed between nodes as expected with $\sigma_e = 14.77$kPa.
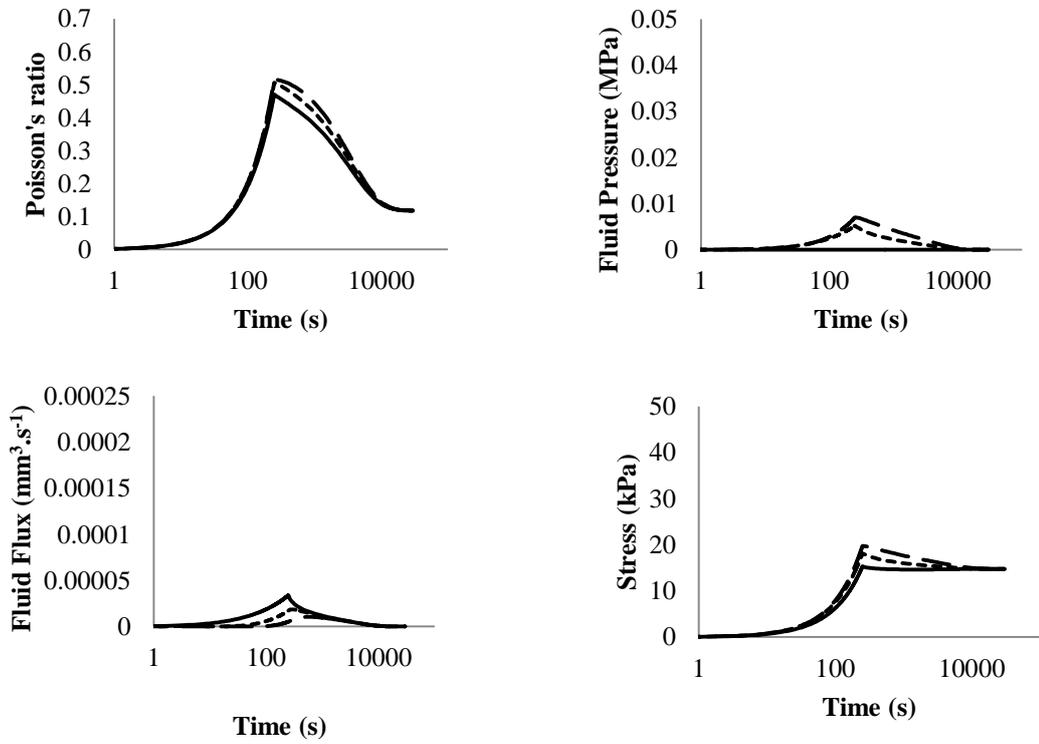
Figure 6.7 BP model results for 0.3μm/s ramp.

I
II
III
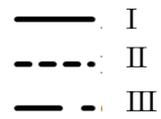
6.4.3. Triphasic poroelastic (TP) model results

6.4.3.1.   0.15M NaCl external solution

Similarly to the BP model, the TP model demonstrated both time-dependent and nodal variation in measures of Poisson's ratio, fluid pressure, radial fluid flux and as well as electrochemical phenomena such as FCD and electric potential (Figure 6.8). Results indicate that $v_{B\ I} = 0.57$, $v_{B\ II} = 0.58$ and $v_{B\ III} = 0.58$. $v_M = 0.22$ at all nodes. All nodes demonstrated an increase in fluid pressure during the ramp phase with the greatest peak fluid pressure occurring at node III with P = 0.045MPa and the lowest fluid pressure at node I with P = 0.043MPa. Fluid pressure did not dissipate to zero, which was the case in the BP model, instead all nodal fluid pressures tended to 0.04MPa. An increase in fluid flux was observed at node I during the ramp phase with the greatest measure occurring immediately after the ramp with $w = 2.3 \times 10^{-4}$ mm^3.s^{-1}. Both nodes II and node III demonstrated an initial increase and subsequent reduction in fluid flux before following a similar trend to that observed at node I. All measures of fluid flux dissipated to zero during the hold phase. The peak axial stress was observed immediately after the ramp before stress relaxation occurred and equilibrium was achieved, for all nodes. A variation in peak axial stress was observed between nodes, with node III experiencing the greatest stress (46.9kPa) and node I experiencing the lowest (45.1kPa). No difference in equilibrium stress was observed between nodes as expected. An increase in FCD was observed from the initiation of the ramp continuing through the hold phase until equilibrium was achieved, with a concomitant transient nodal variation. The electric potential response followed a similar trend with $\psi_e = -8.43$mV.
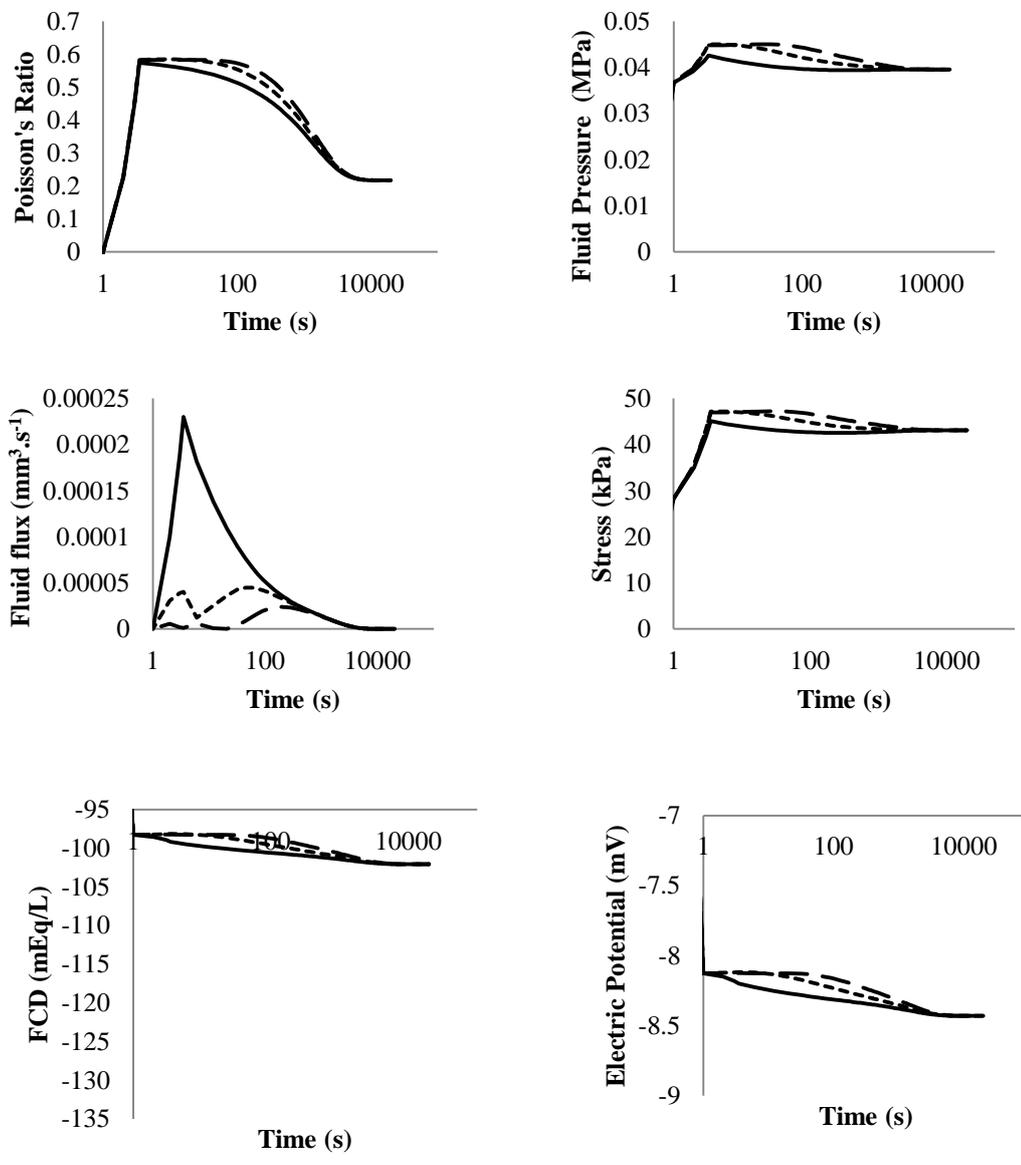
Figure 6.8 TP model results for 0.15M NaCl / 30μms^{-1} ramp.

I

II

III

In a similar fashion to the BP model, the slower strain-rate TP model resulted in a variation in non-equilibrium measures of Poisson's ratio, fluid pressure, radial fluid flux, FCD and electric potential when compared to the faster ramp (Figure 6.9). There was no strain-rate dependency on equilibrium measures. A reduction in biphasic Poisson's ratio was observed for the $0.3\mu ms^{-1}$ compared to the $30 \mu ms^{-1}$ ramp with $v_{B\ I} = 0.51$, $v_{B\ II} = 0.55$ and $v_{B\ III} = 0.57$. Peak fluid pressure and radial fluid flux were lower in the $0.3\mu ms^{-1}$ ramp. All measures of fluid flux dissipated to zero during the hold phase. The peak axial stress was observed immediately after the ramp phase before stress relaxation occurred until equilibrium was achieved. A variation in peak axial stress was observed between nodes, with node III experiencing the greatest stress (46.39kPa) and node I experiencing the lowest (42.72kPa). No difference in equilibrium stress was observed between nodes with σ_e = 43.1kP. An increase in FCD was observed from the initiation of the ramp continuing through the hold phase until equilibrium was achieved with a concomitant transient nodal variation. The peak electric potential demonstrated a similar time dependent response with ψ_e = -8.43mV.
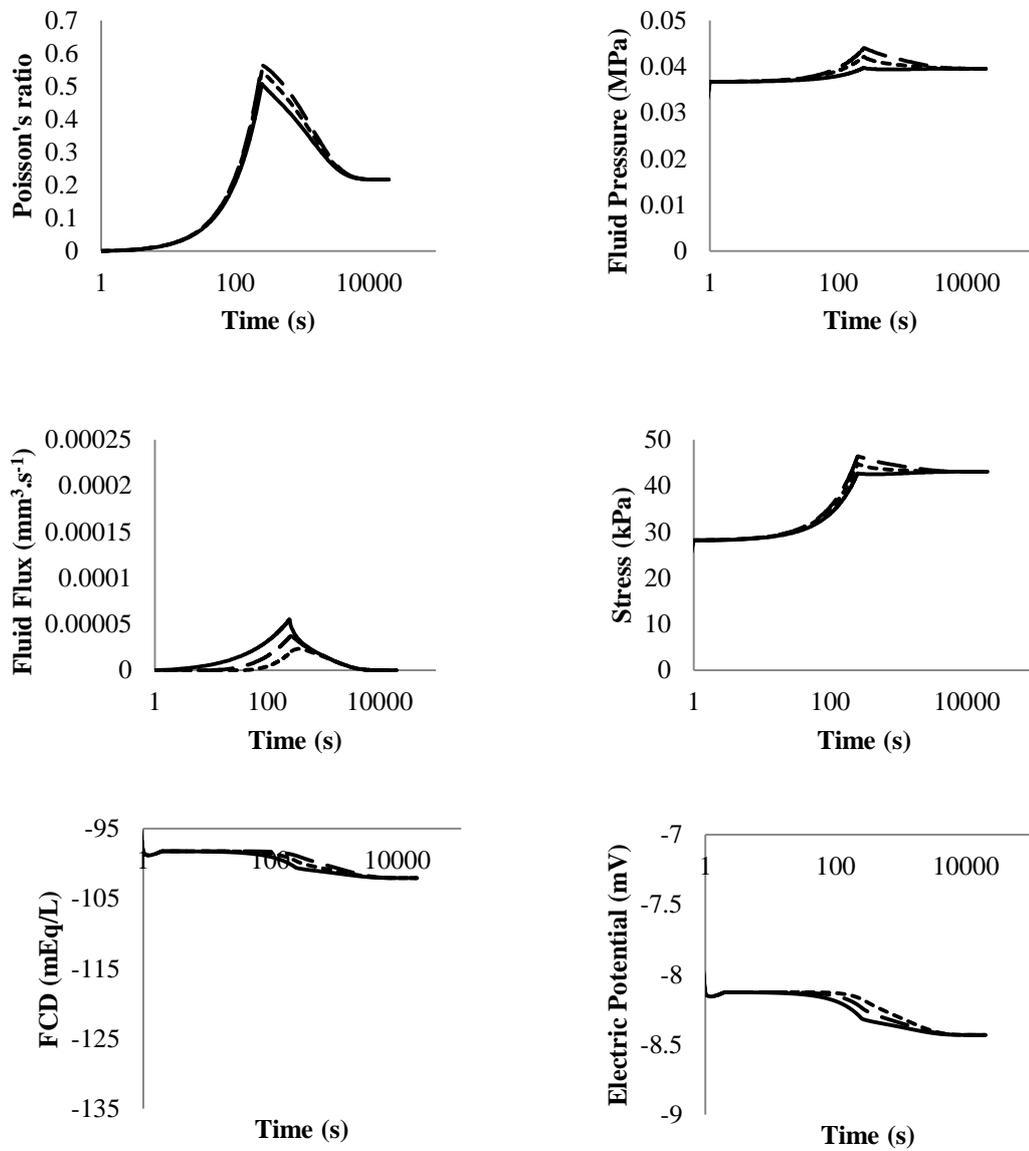
Figure 6.9 TP model results for 0.15M NaCl / 0.3μms^{-1} ramp.

6.4.3.2.   3M NaCl external solution

The 3M TP model demonstrated both time-dependent and nodal variation in measures of Poisson's ratio, fluid pressure, radial fluid flux axial stress, FCD and electric potential (Figure 6.10). Results indicate that $v_{B\ I} = 0.52$, $v_{B\ II} = 0.53$ and $v_{B\ III} = 0.53$. $v_M = 0.13$ at all nodes. All nodes demonstrated with an initial pressure of 0.0052MPa. The greatest pressure thereafter was recorded immediately after the ramp phase at node II with P = 0.0125MPa. Fluid pressure did not dissipate to zero as was observed in the biphasic model, rather all nodal fluid pressures tended to 0.0055MPa. An increase in fluid flux was observed at all nodes during the ramp phase with the greatest measure occurring immediately after the ramp phase at node I with $w = 1.2 \times 10^{-4}$ mm^3.s^{-1}. Both nodes II and node III demonstrated an initial increase and subsequent reduction in fluid flux before following a similar trend to that observed at node I. All measures of fluid flux dissipated to zero during the hold phase. The peak axial stress was observed immediately after the ramp phase before stress relaxation occurred until equilibrium was achieved, at all nodes. A variation in peak axial stress was observed between nodes, with node II experiencing the greatest stress (23.76kPa) and node I experiencing the lowest (21.98kPa). No difference in equilibrium stress was observed between nodes as expected with $\sigma_e = 18.65$kPa. An increase in FCD was observed from the initiation of the ramp continuing through the hold phase until equilibrium was achieved with a concomitant transient nodal variation. The peak electric potential demonstrated a similar time dependent response with $\psi_e = -0.55$mV.
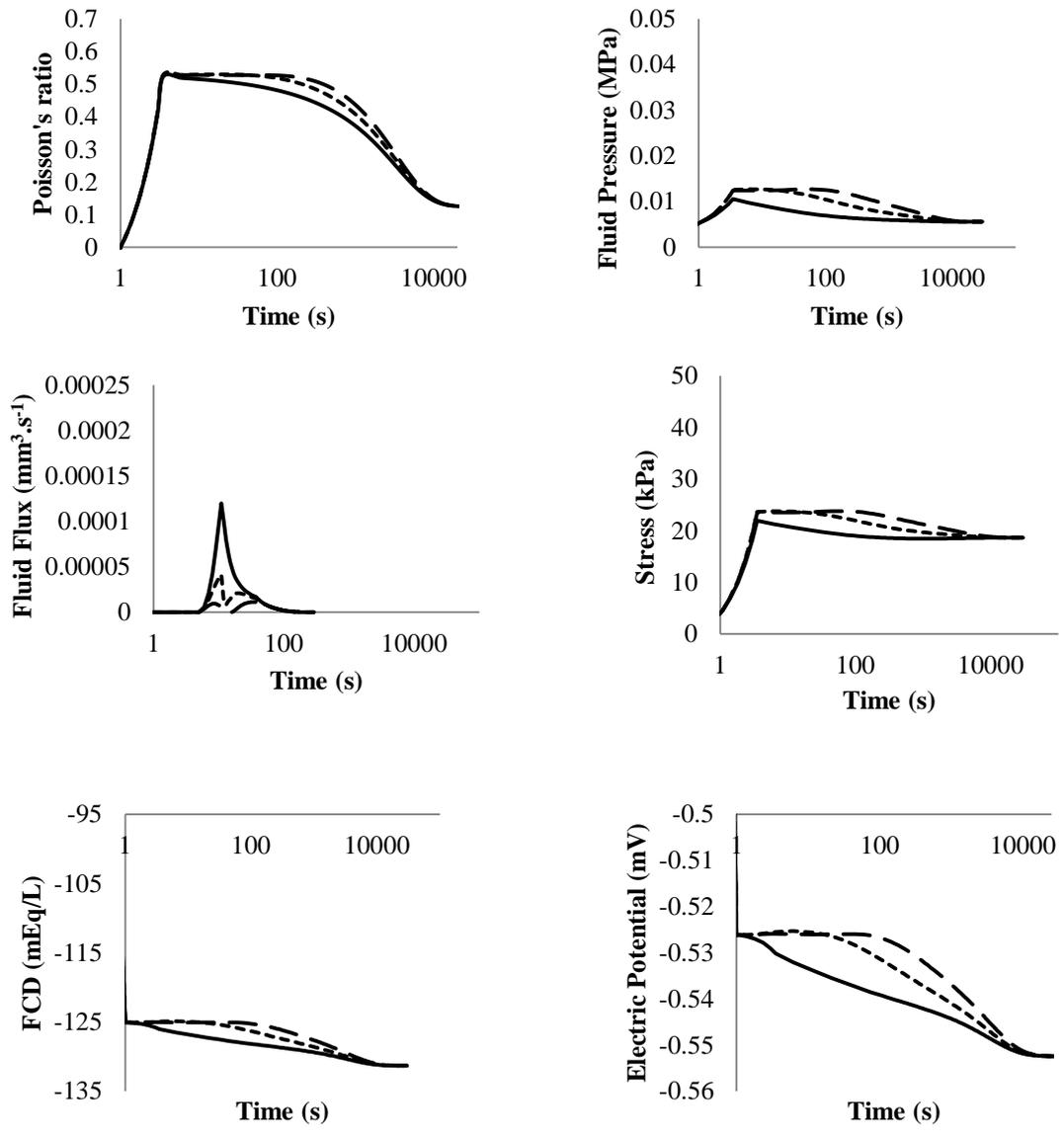
Figure 6.10 TP model results for 3M NaCl / 30μms⁻¹ ramp.

I

II

III

| 190

The slower strain-rate 3M TP model resulted in variation in non-equilibrium measures of Poisson's ratio, fluid pressure, radial fluid flux, FCD and electric potential (Figure 6.11) when compared to the fast ramp. There was no strain-rate dependency on equilibrium measures. A slight reduction in biphasic Poisson's ratio was observed for the $0.3\mu ms^{-1}$ compared to the 30 μms^{-1} ramp with $v_{B\,I} = 0.51$, $v_{B\,II} = 0.51$ and $v_{B\,III} = 0.52$. The greatest pressure was recorded immediately after the ramp phase at node III with P = 0.012MPa, with an equilibrium fluid pressure of 0.005MPa. Peak radial fluid flux was observed at node I with $w = 3.5\text{x}10^{-5}$ mm^3.s^{-1}. All measures of fluid flux dissipated to zero during the hold phase. The peak axial stress was observed immediately after the ramp phase before stress relaxation occurred until equilibrium was achieved. A variation in peak axial stress was observed between nodes, with node III experiencing the greatest stress (23.5kPa) and node I experiencing the lowest (19.1kPa). No difference in equilibrium stress was observed between nodes with $\sigma_e = 18.65$kP. An increase in FCD was observed from the initiation of the ramp continuing through the hold phase until equilibrium was achieved with a concomitant transient nodal variation. The peak electric potential demonstrated a similar time dependent response with $\psi_e = -0.55$mV.

Figure 6.11 TP model results for 3M NaCl / 0.3μms⁻¹ ramp.

I
II
III
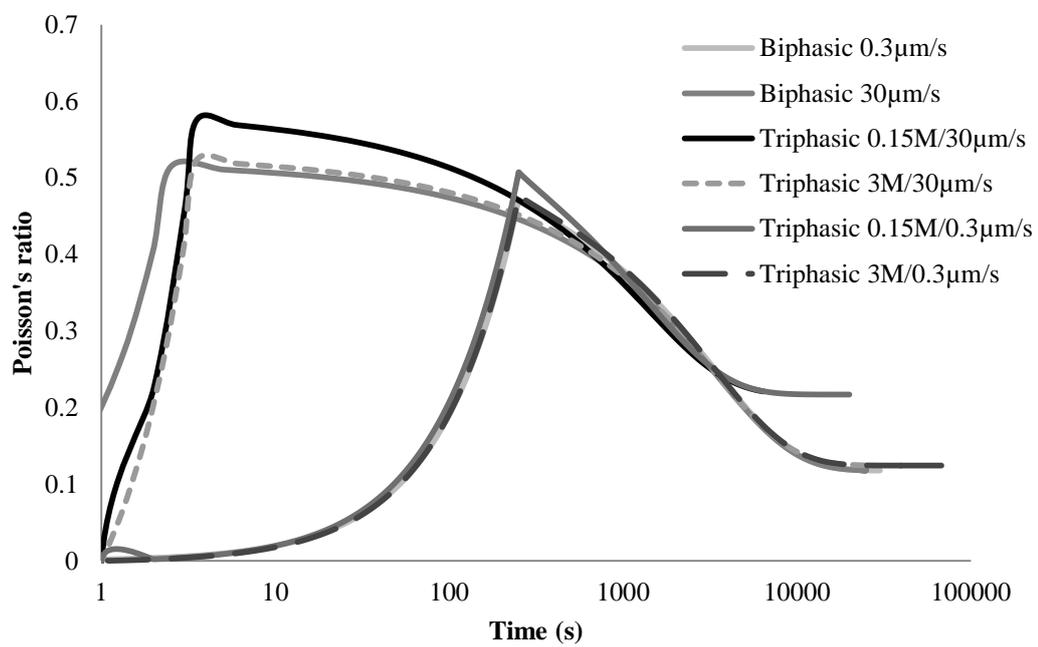
Figure 6.12 BP and TP model Poisson's ratio results for $30\mu ms^{-1}$ and $0.3\mu ms^{-1}$ ramp speeds / 0.15M and 3M NaCl external solutions.
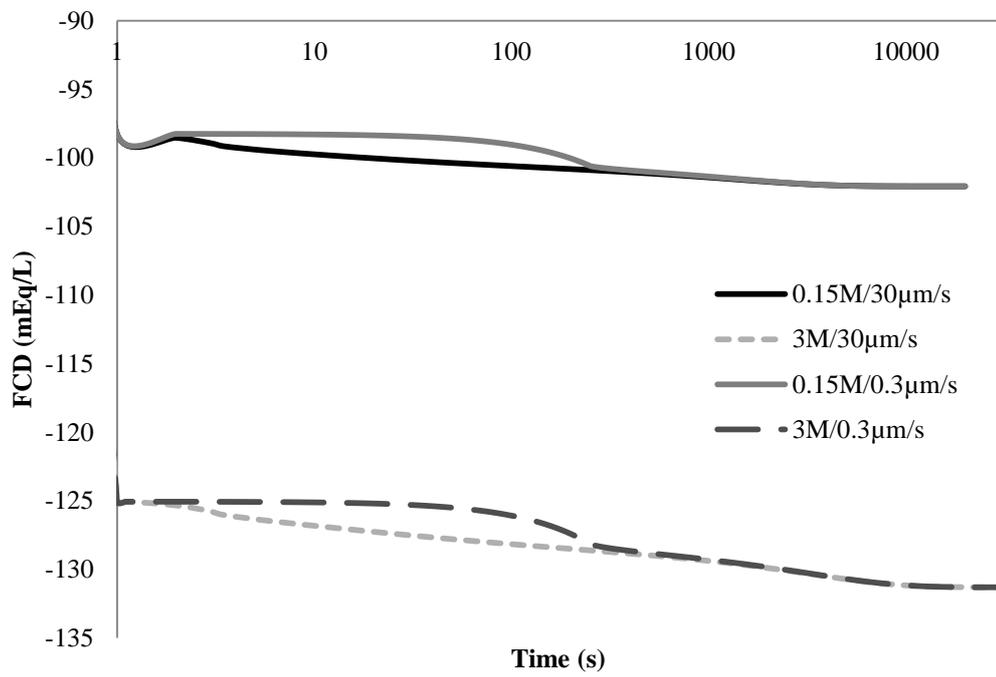
Figure 6.13 TP model FCD results for 30µms^{-1} and 0.3µms^{-1} ramps / 0.15M and 3M NaCl external solutions.

	Biphasic		Triphasic			
	$30\mu ms^{-1}$	$0.3\mu ms^{-1}$	$30\mu ms^{-1}$		$0.3\mu ms^{-1}$	
			0.15M	3M	0.15M	3M
ν_B	0.49	0.47	0.57	0.52	0.51	0.51
ν_M	0.12	0.12	0.22	0.12	0.22	0.12
Peak fluid pressure (MPa)	0.005	0.0016	0.043	0.012	0.0397	0.012
Equilibrium fluid pressure (MPa)	0	0	0.04	0.005	0.04	0.005
Peak radial fluid flux ($mm^3.s^{-1}$)	$1.14x10^{-4}$	$3.39x10^{-5}$	$2.3x10^{-4}$	$1.2x10^{-4}$	$5.52x10^{-5}$	$3.5x10^{-5}$
Equilibrium fluid flux ($mm^3.s^{-1}$)	0	0	0	0	0	0
Peak stress (kPa)	18.24	15.3	45.1	22.0	42.7	19.1
Equilibrium stress (kPa)	14.77	14.77	43.1	18.65	43.1	18.65
Post ramp FCD (mEq/L)	-	-	-99.2	-126	-100.6	-128.1
Equilibrium FCD (mEq/L)	-	-	-102.1	-131.31	-102.1	-131.31
Post ramp electric potential (mV)	-	-	-8.2	-0.53	-8.31	-0.53
Equilibrium electric potential (mV)	-	-	-8.43	-0.552	-8.43	-0.552

Table 6.3 Summary of BP and TP model results obtained at node I.

6.4.4. TP – experimental results

Figure 6.14 plots experimentally determined v_B and v_M results for both strain-rates against model results obtained at node I. For the fast strain rate, all models demonstrated poor agreement with experimental data for v_B, with the $TP_{0.15M}$ model demonstrating the poorest agreement. In agreement with experimental data, the slow strain-rate resulted in a reduction in measures of v_B for all models; however there was poor agreement between absolute values. The BP and TP_{3M} model results provided closest agreement with experimental v_M results for both strain-rates.
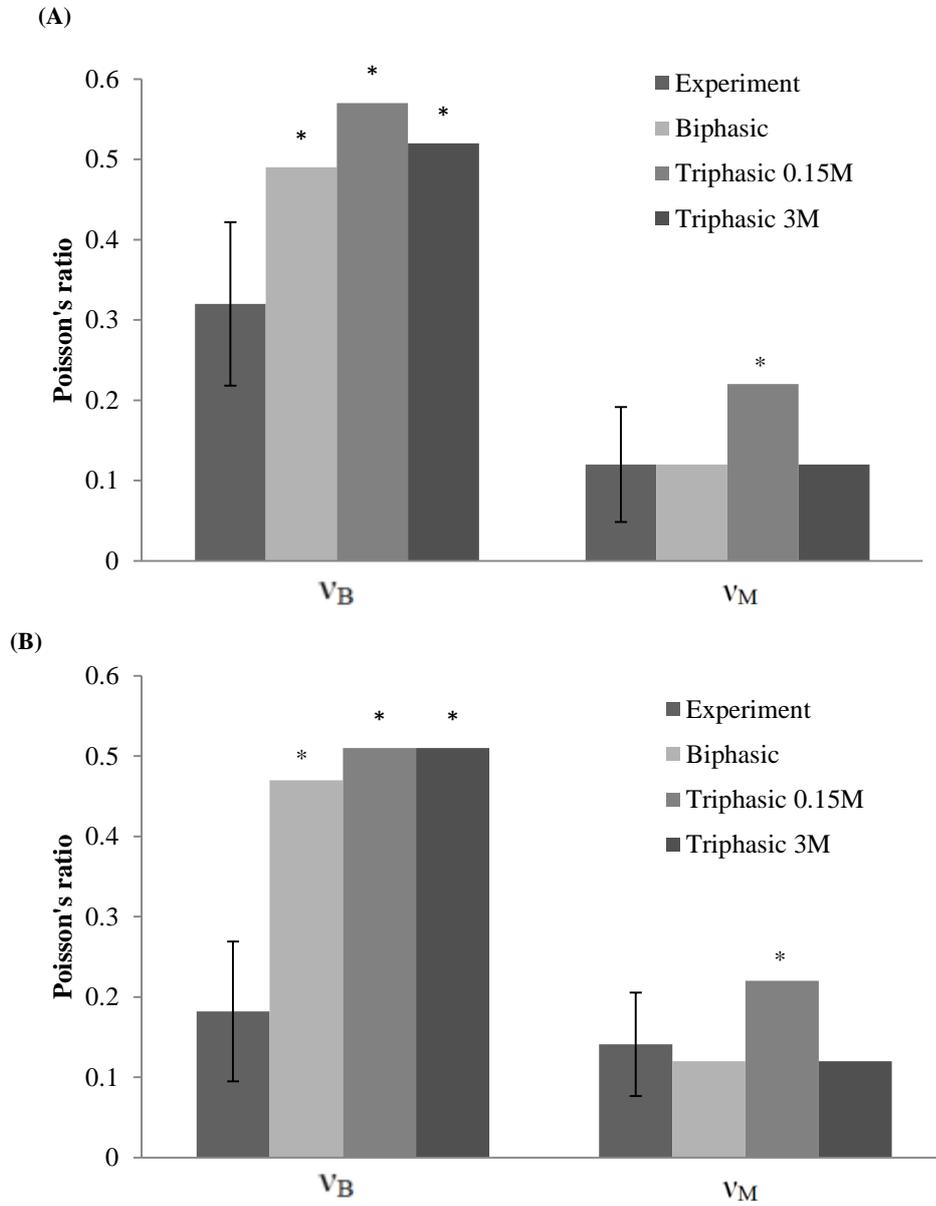
Figure 6.14 Experimental results compared to BP and TP model Poisson's ratio results for (A) $30 \mu ms^{-1}$ and (B) $0.3 \mu ms^{-1}$.

6.5. Discussion

Biphasic and triphasic poroelastic (BP and TP respectively) FE models were developed to investigate the mechanisms affecting the mechanical response of the NP during an unconfined compression experiment. The transient and equilibrium mechano-electrochemical interactions which occur during such loading conditions were investigated and results compared to the experimental Poisson's ratio data presented in chapter 5. Both the BP and TP models were able to predict the global time-dependent response of the tissue in unconfined compression which lends confidence to the literature sourced material properties. Differences were identified between the models which indicate that the selection of numerical framework is crucial when modelling cartilaginous tissue.

Due to the inclusion of swelling effects in the isotonic triphasic model, $v_B = 0.57$ resulting from substantial volumetric increase. This finding suggests that any experimental data obtained during an unconfined compression experiment on cartilaginous tissue when an isotonic external solution is used may contain significant swelling artefacts. Indeed, one of the suggested reasons for the comparatively lower Poisson's ratio results presented in chapter 5 compared to the earlier work of Cloyd et al, (2007) is that the authors of the earlier study bathed their specimens in physiological saline, thus possibly introducing significant swelling. The biphasic Poisson's ratio result predicted by the $TP_{0.15M}$ model is very much in keeping with the result presented by Cloyd and co-workers suggesting that swelling was indeed the source of their comparatively higher value ($v_B = 0.62$). These findings

lend confidence to the use of a hypertonic external solution during the unconfined compression of cartilaginous tissue and to the results presented in chapter 5.

Significant radial variation in v_B was observed for both models and both strain-rates. Results obtained at node I for the fast strain-rate are entirely in keeping with biphasic and triphasic theory, whereby the tissue behaves as an incompressible with $v_B = {\sim}0.5$. However, the higher values of v_B obtained at nodes II and III were the result of a greater hydrostatic fluid pressure developing toward the centre of the disc during axial compression. The greater v_B results obtained from the TP model when compared to the BP model is due to the charged model developing a greater fluid pressure, particularly in the isotonic case; hypertonic environments render the majority of the ionic swelling component negligible. The swelling potential of the $TP_{0.15M}$ model resulted in v_M being higher than the BP model result for the same conditions, leading to a poor agreement with experimental data whilst the TP_{3M} v_M results matched experimental data. In the BP and TP_{3M} models the tissue's equilibrium lateral displacement is governed by the intrinsic mechanical properties of the solid matrix, whereas in the $TP_{0.15M}$ model, the incorporation of FCD results a greater equilibrium lateral displacement due to the additional Donnan osmotic pressure, a result which is in keeping with earlier work (Sun et al., 2004). These findings lend confidence to the use of a hypertonic external solution for the investigation of the Poisson's ratio of the solid matrix as conducted in chapter 5.

For all models, the slower strain-rate resulted in lower v_B as fluid pressure gradients are allowed to diffuse away during slow ramps which is entirely consistent with the experimental data presented in chapter 5. This is confirmed by the weakened fluid pressurisation which occurred during the slow ramp when compared to the fast ramp.

However, the effect of strain-rate was least pronounced on 3M TP v_B results causing poor agreement with experimental data in the slow condition (Figure 6.14); perhaps due to a significant reduction in permeability. Strain-rate had no effect on v_M, for all models, which does not agree with experimental data. This may have been a result of solid matrix viscoelasticity - hypothesised in chapter 5 to play an important role in the strain-rate dependency of this tissue during an unconfined compression experimental - not being taken into account in any of the models. The TP model demonstrated a slower rate of recoil than the BP model, with the effect most apparent in the 3M case indicating that this is a direct result of reduced radial permeability. The influence of mechano-electrochemical phenomena on the measurement of Poisson's ratio in unconfined compression, as outlined in this chapter, is entirely consistent with the earlier triphasic analysis of Sun et al., (Sun et al., 2004)

As expected, strain-rate had no effect on equilibrium stress, for both models; however, the concentration of the external solution used in the TP model had a significant effect with the 0.15M case demonstrating greater stiffness as a result of the additional ionic osmotic pressure; the compressive load being supported by both the intrinsic stiffness of the solid matrix and the ionic osmotic pressure at equilibrium. The 3M case demonstrated a lower equilibrium stress as a result of the negation of ionic contributions and the addition of osmotic loading, which is in keeping with the earlier study of Heneghan and Riches (2008b) who investigated the contribution of ionic osmotic pressure to the NP load bearing mechanism. The load bearing mechanism of the BP model was, as expected, determined primarily by the intrinsic modulus of the solid matrix which is why the BP and TP_{3M} σ_e are similar.

The maximum fluid pressure was observed at the end of the ramp phase, for both models and strain-rates. However, the $TP_{0.15M}$ model demonstrated greater fluid pressurisation than the BP model due to reduced radial permeability caused by the incorporation of the hydrophilic FCD. Additionally, the BP model fluid pressure reduced to zero at equilibrium whilst the $TP_{0.15M}$ model fluid pressure remained elevated at equilibrium with the magnitude of the equilibrium value representing the Donnan osmotic pressure. The TP_{3M} model also demonstrated lower fluid pressures than the $TP_{0.15M}$ model due to the negation of the ionic swelling pressure. The magnitude of the hypertonic equilibrium fluid pressure represents 12% of that obtained for the isotonic case due to ~85% of total pressure magnitude being rendered negligible in such environments (Urban et al., 1979).

Interesting and unexpected radial fluid flux variations were observed for the fast strain rate, for all models, whereby nodes II and III demonstrated an initial increase in flux, followed by a reduction toward the end of the ramp phase before following the same trend as node I until equilibrium. This finding may have been the result of strain rate effects influencing radial permeability via reduced porosity during radial recoil; as the tissue consolidates at a quicker rate in the fast ramp compared to the slow then internal fluid flux may be reduced. This phenomenon is also highlighted by the significantly slower reduction in fluid pressure at nodes II and III compared to node I.

The TP model demonstrated that FCD and ionic gradients can generate an electric potential within the tissue during unconfined compression which has been suggested to have the ability to influence disc mechanics and biological functioning, as discussed in chapter 4. For both strain-rates and external solutions, an increase in

FCD was observed during the ramp phase resulting from axial compression of the solid matrix. The increase in FCD coupled with the increase in pressure dependent fluid chemical potential during the ramp phase resulted in the concomitant increase in electric potential. In agreement with the work of Yao and Gu (2007b) (Figure 6.15), FCD continued to increase during the hold phase, albeit at a slower rate, as a result of lateral recoil further consolidating the solid matrix until equilibrium was achieved. This effect may act to expedite the recovery of the disc after a period of compressive loading by encouraging flow into the disc and restricting outward flow. In agreement with early work on membrane streaming potentials in gall-bladder tissue (Diamond and Harrison, 1966), equilibrium electric potential was found to decrease considerably with an increase in external solution concentration resulting from changes in NaCl concentration (Figure 6.16), with the 3M case resulting in a 93% reduction when compared to results predicted in the 0.15M case. This phenomenon is the result of reduced fluid flow in the presence of high salt concentrations, as discussed in chapter 4.
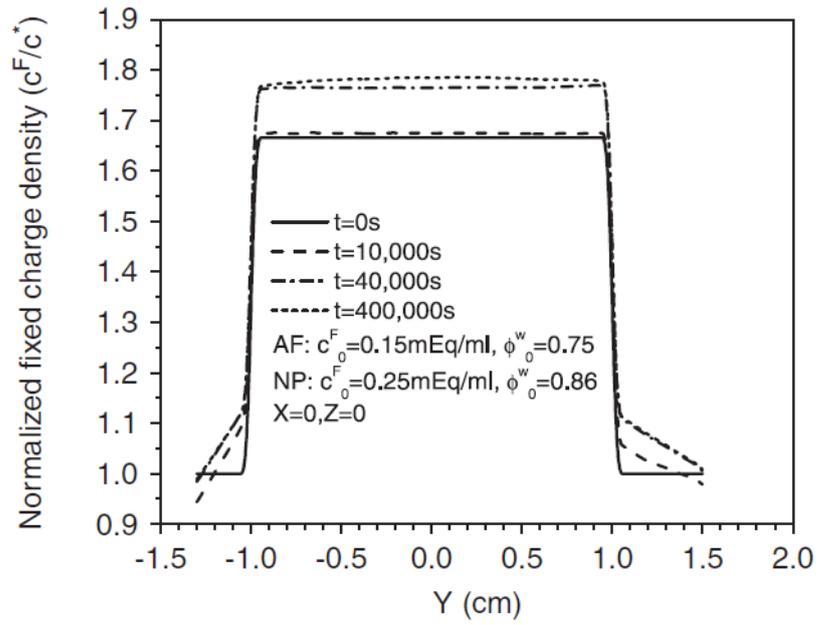
Figure 6.15 Transient response of normalised FCD during unconfined compression stress-relaxation (Yao and Gu, 2007b).
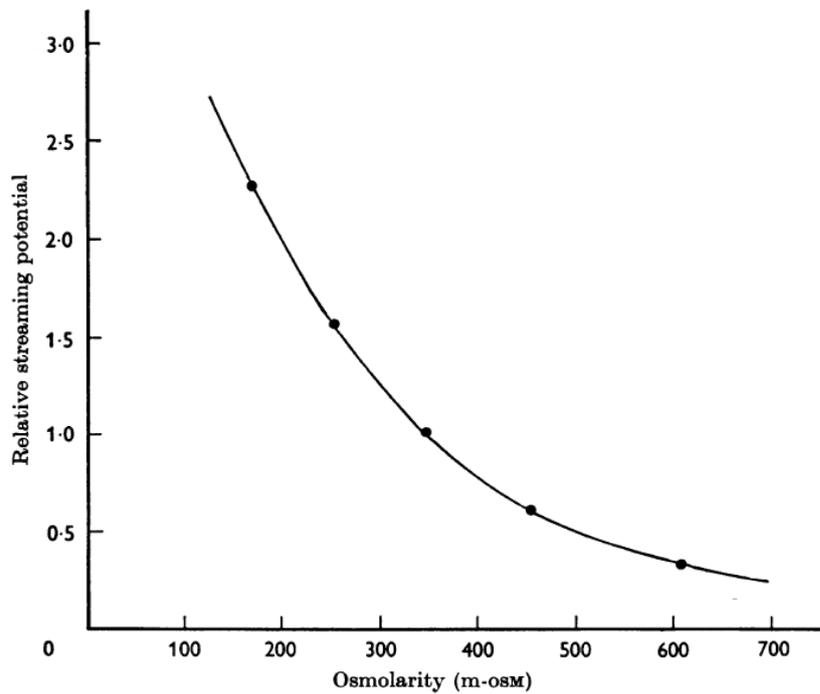
Figure 6.16 The effect of osmolarity upon streaming potentials in a gallbladder (Diamond and Harrison, 1966).

A radial gradient in FCD was found with the greatest concentration occurring toward the circumferential edge of the sample. This observed radial variation in FCD is in keeping with a previous study who reported that the greatest PG and collagen synthesis was observed toward to the radial periphery of cartilage discs during unconfined compression (Kim et al., 1994). It was hypothesised that certain fields and fluid-matrix interactions were responsible for this observation during dynamic unconfined compression. The radial variation in FCD concentration and electric potential found in this study during the transient phase of unconfined compression may indicate that mechano-electrochemical gradients may play an important role in the delivery of nutrients to chondrocytes in cartilaginous tissue.

Solid matrix viscoelasticity was not taken into account in this study due to the Holmes-Mow solid type utilised in both models; coupling a Holmes-Mow solid with a viscoelastic solid in the current configuration would not have allowed for the conversion of Young's modulus and Poisson's ratio to Lamé constants which are required to evaluate the stress and elasticity tensors. Due to the importance of strain-dependent mechanisms in cartilaginous tissue (Heneghan and Riches, 2008a, Heneghan and Riches, 2008b), the Holmes-Mow solid was prioritised ahead of the incorporation of solid matrix viscoelasticity. A potential future study into the triphasic unconfined compression of cartilaginous tissue would be to combine both strain-dependent and viscoelastic solid mechanisms which may elucidate a clearer understanding of the micromechanical phenomena which influence the strain-rate dependent properties of the tissue.

A pilot model demonstrated that the use of literature sourced ion diffusion coefficients resulted in an extremely long relaxation time which required an up-

scaling to better match experimental data. The source of this disparity may be the use of a solid matrix definition which did not account for the difference between the tensile and compressive moduli (Ateshian, 2013). In unconfined compression, the tensile modulus of the tissue governs the time constant via

$$w \ \alpha \ \frac{r^2}{H_a k} \tag{6.9}$$

where w is the fluid flux, r is the model radius, H_A is the tensile modulus and k is the hydraulic permeability. Whilst the ion diffusion rate is governed by

$$\dot{D} \ \alpha \ \frac{r^2}{D^\alpha} \tag{6.10}$$

where D^α is the diffusion coefficient of solute α. Since r and H_A are constant, by increasing D^α, it was possible to reduce the time constant to provide a better agreement with experimental data. Accounting for this disparity in the future by incorporating the differences in tensile and compressive moduli may allow for the use of more realistic ion diffusivities whilst also replicating experimental hold times. Nonetheless, this parametric adjustment still allowed for the analysis of the mechanisms which influence the Poisson's ratio of this tissue. Making adjustments to model properties is a common method to obtain a better agreement with experimental results as highlighted by Stokes et al (2010).

Another potential future study could involve the inverse engineering of triphasic theory to optimise material properties when modelling the NP in unconfined compression as well as the incorporation of tension-compression non-linearity.

One important point to consider when investigating Poisson's ratio effects via a FE model is the method in which radial strain is determined; recording nodal radial displacements, as done here, or recording the radial normal strain. The former method was adopted here as it mimicked the experimental protocol of chapter 5 thus allowing direct comparison of data. Both methods will yield identical v_M results; however, the transient behaviour will be significantly different. The selection of analysis method must be determined by defining the objectives of the study.

6.6.   Conclusions

This chapter has investigated the mechano-electrochemical interactions which occur during the unconfined compression of the NP. Results indicate that appropriate selection of numerical framework and analysis protocol is essential when investigating disc mechanics. External solution concentration was found to significantly influence disc mechanics as hypothesised, with the TP$_{3M}$ validating the experimental protocol presented in chapter 5. Strain-rate was found to significantly influence the transient response of the tissue, only, thus resulting in poor agreement with experimental data which may have been the result of solid matrix viscoelasticity omission. Radial variations in mechano-electrochemical interactions were found which may influence radial nutrient transport when the disc is subject to axial loading. Since the investigation of cartilaginous tissue biomechanics via unconfined compression is commonly reported in the literature, the current analysis may be beneficial in interpreting such data, especially when considering the influence of electro-chemical effects in charged hydrated tissues.

7. Confined compression of the human nucleus pulposus: mechano-chemical effects in the degenerate case

7.1.   Introduction

As discussed in previous chapters, the mechano-chemical effects resulting from the high concentration of PG's significantly influence the response of the NP to deformation. However, the relationship between ionic effects and the significant adaptations which occur in the disc throughout the degenerative cascade has not been fully investigated.

In vivo, the NP is partially confined by the AF which has led to many studies adopting a confined compression experimental configuration for the investigation of the mechanical properties of this tissue. The confined compression experiment, however, only allows for the direct measurement of the time-dependent load response of a viscoelastic material. The subsequent inverse curve fitting of this data to a biphasic model allows for the elucidation of hydraulic permeability and aggregate modulus, the latter of which is a measure of the tissue's compressive stiffness in confined compression. Such parameterisation of a constitutive equation is often conducted to allow future scaling to multi-dimensional models (Riches, 2012).

The majority of NP confined compression studies have been conducted on healthy animal tissue (Perie et al., 2005, Perie et al., 2006a, Perie et al., 2006b, Heneghan and Riches, 2008b). Only one study has comprehensively investigated the mechanics of human tissue in confined compression (Johannessen and Elliott, 2005) and

determined the aggregate modulus and hydraulic permeability of both the healthy and the degenerate NP for a single strain level. IVD degeneration is a complex physiochemical process which results in significantly altered disc mechanics, predominantly via the loss of aggrecan; the primary PG in the NP (Urban et al., 1979, Urban and McMullin, 1988). Since the tissue's compressive modulus is highly dependent on mechano-chemical phenomena arising from the high concentration of negatively charged PG's in healthy tissue, it has been suggested that a loss of the hydrophilic PG results in a significant reduction in H_A and a concomitant increase in hydraulic permeability (Johannessen and Elliott, 2005). Ateshian et al, (2004) investigated the importance of PG content on the compressive modulus of AC in confined compression by fitting experimental results to a triphasic model and reported that 98% of the H_A was contributed to by ionic effects. Heneghan and Riches (2008b) later apportioned the strain-dependent osmotic pressure and stiffness of the bovine NP into ionic and non-ion contributions and reported the former represented 70% of the applied load at equilibrium. This study negated the ionic pressure by subjecting their specimens to various concentrations of saline; a method used extensively in previous chapters of this thesis. Massey et al., (2012) parametrically altered an osmo-poroelastic FE model to determine the effect of degeneration on the disc during the diurnal cycle and found significant stress increase occurred in the centre. The importance of ionic contributions to the compressive modulus of the NP is evident; however, the significant reduction in PG content associated with degeneration and the possible related changes in electrochemical mechanisms may have a significant impact on the tissue and the applicability of current models when investigating human samples.

Knowledge of the compressive properties of the degenerate human NP is essential for the development of new models of the disc and for the enhancement of existing ones (Johannessen and Elliott, 2005). Understanding the mechano-chemical interactions which occur during the deformation of degenerate tissue may help to improve engineered replacement devices and tissue, whilst also providing insight to possible new treatment strategies and to the mechanical aetiology of the degenerative cascade.

By subjecting the degenerate tissue to both isotonic and hypertonic external solutions during a confined compression experiment in a similar protocol to that adopted by Heneghan and Riches (2008b), and subsequently curve fitting the load response to a biphasic model thus allowing elucidation of E and k_0, the effect of degeneration on mechano-chemical effects may be examined.

7.2. Aims and hypotheses

The aim of this chapter was to subject degenerate human NP samples to confined compression in both isotonic and hypertonic external solutions and subsequently apply inverse analytical methods to determine the effect of degeneration on mechano-chemical phenomena. It was hypothesised there would be minimal effect of external solution on the mechanical response of the tissue as a result of diminished mechano-chemical interactions occurring in the degenerate case.

7.3. Methods

7.3.1. Materials

All procedures were approved by the University Ethics Committee. One fresh human lumbar spine was obtained from the Department of Life Sciences and Human Biology, University of Glasgow, Glasgow, and was wrapped in saline soaked gauze before being frozen at -20°C until testing. A hand held saw was then used to cut the spine into 3 motion segments (L1-L4) before a sagittal section was made toward the periphery of the segment to aid visualisation of the discs (Figure 7.1).

3 lumbar discs were removed from the separated motion segments whilst frozen by a hand saw at the superior and inferior endplates before a plug of NP was removed via a cork borer (ø 10mm). Using a modified Thompson scale, the discs were assigned a degenerative grade (scale 1-5; Grade 1 – non degenerate; to Grade 5 – severely degenerate) based on observations of gross morphology (Figure 7.2). Frozen NP plugs were then sectioned into 16 1631 ± 212 μm (mean ± SD) thick plugs of NP tissue, orientated in the axial direction, using a custom built tissue sectioning device.
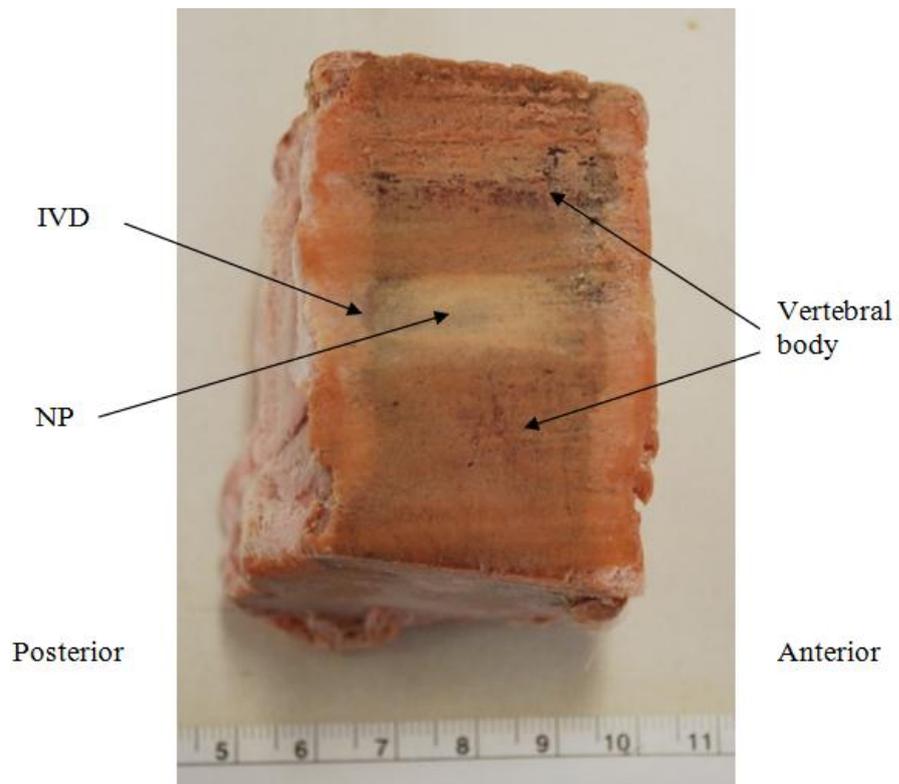
Figure 7.1 Human lumbar motion segment.

Figure 7.2 L1 – L3 lumbar discs removed from spinal column and central plug of NP removed for testing. Thomson grading: L1 – 4, L2 – 4, L3 – 3.

7.3.2. Mechanical testing

A schematic diagram and photographs of the confined compression apparatus used are shown in Figure 7.3 to Figure 7.6. The configuration consisted of an impermeable stainless steel confining chamber (ø10mm) with an upper compression platen made from rigid and porous sintered stainless steel. The upper platen was connected to the actuator of a materials characterisation system (Electroforce 3200 series, Bose, USA) via a 450N load cell (425100-0100, Bose, USA) which was used to continuously measure reaction force. The full configuration was submerged within a heated water bath filled with saline and held at 37°C. Temperature stability is plotted in Figure 7.7.

With the confining chamber empty, the upper platen was lowered in load control until 0.5N was detected and the actuator position noted. A sample was then positioned within the confining chamber, and the upper platen lowered again until a compressive load of 0.2N was detected. The specimen thickness was calculated from the new grip-to-grip displacement, with this reference position defined as zero strain ($\lambda = 1$). The external bath was then filled with either 0.15M NaCl (n = 6) or 3M NaCl (n = 6) and heated to the desired temperature and a saline filled syringe used to flood the upper chamber and ensure platen saturation. An initial 2hr hold phase (z = 0) allowed each sample to reach equilibrium and an increase in compressive load was observed during this time, indicating that the sample had swollen into the cavity of the confining chamber and platen. Displacement controlled ramp-hold cycles were then administered with displacements corresponding to $\lambda = 0.95$, 0.9 and 0.85 at 2µm.s^{-1} with dwell times of 2000, 2500 and 3000s. The current strain range was chosen as the overall compressive strain in the disc has been found to be below 0.2

(Botsford et al., 1994). Dwell times were based on previous confined compression experiments on healthy NP tissue which has been previously (Heneghan and Riches, 2008b) shown to exhibit lower permeability than degenerate human tissue (Heneghan and Riches, 2008a).
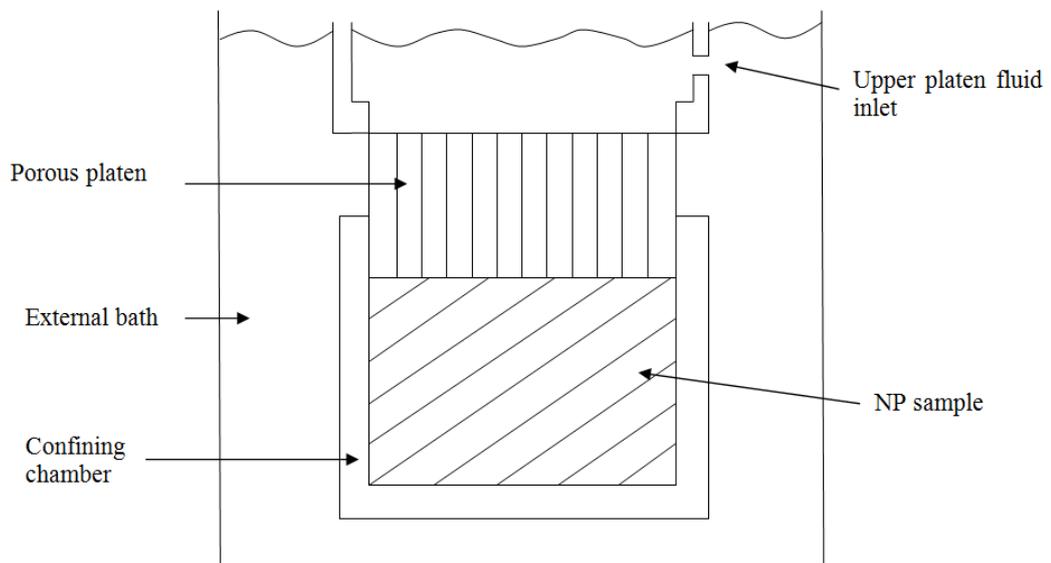
Figure 7.3 Confined compression schematic.
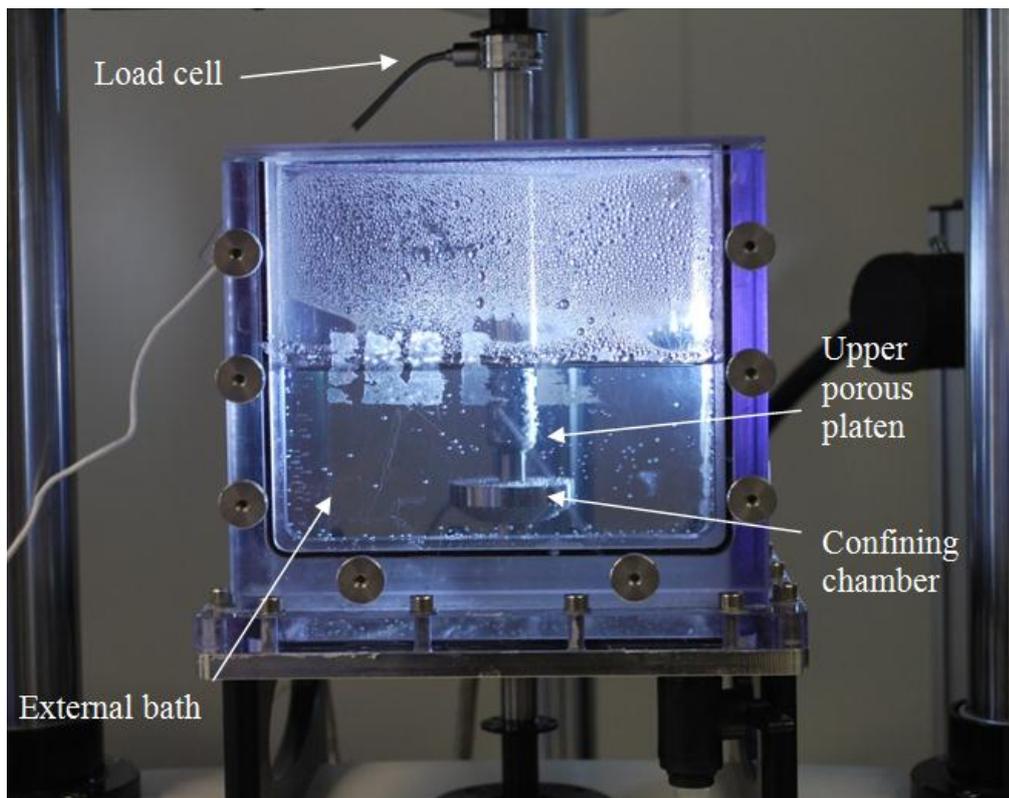
Figure 7.4 Photograph of confined compression experimental configuration.
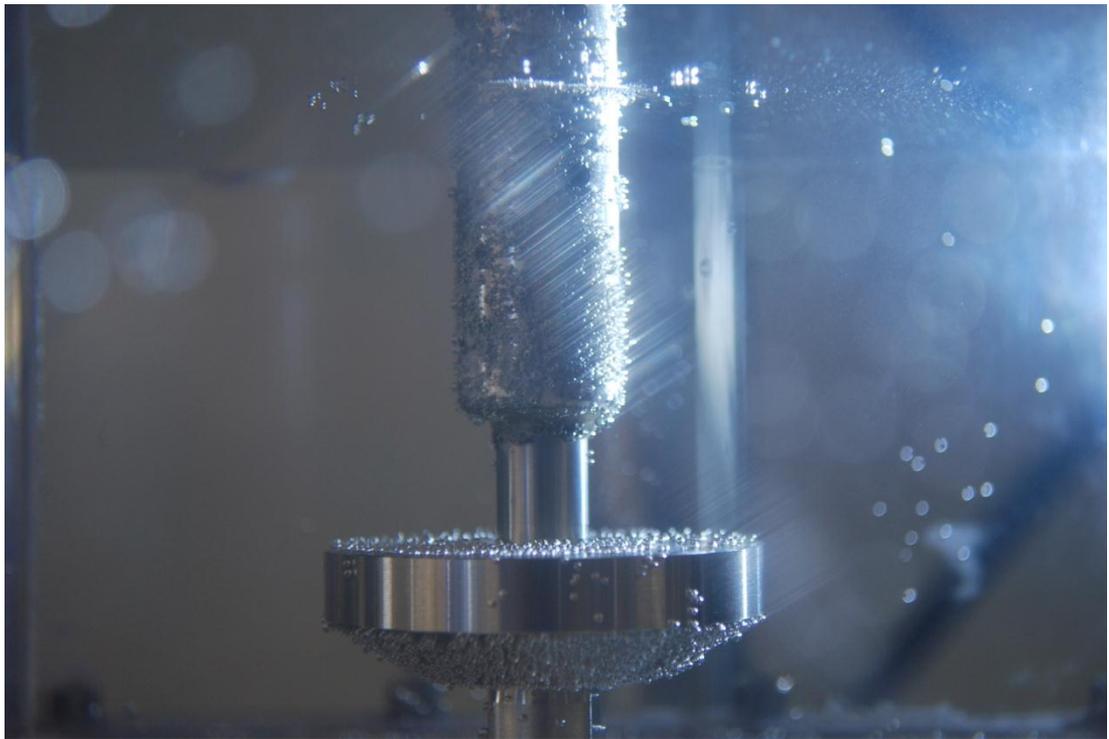
Figure 7.5 Photograph of upper platen and confining chamber submerged within external bath.
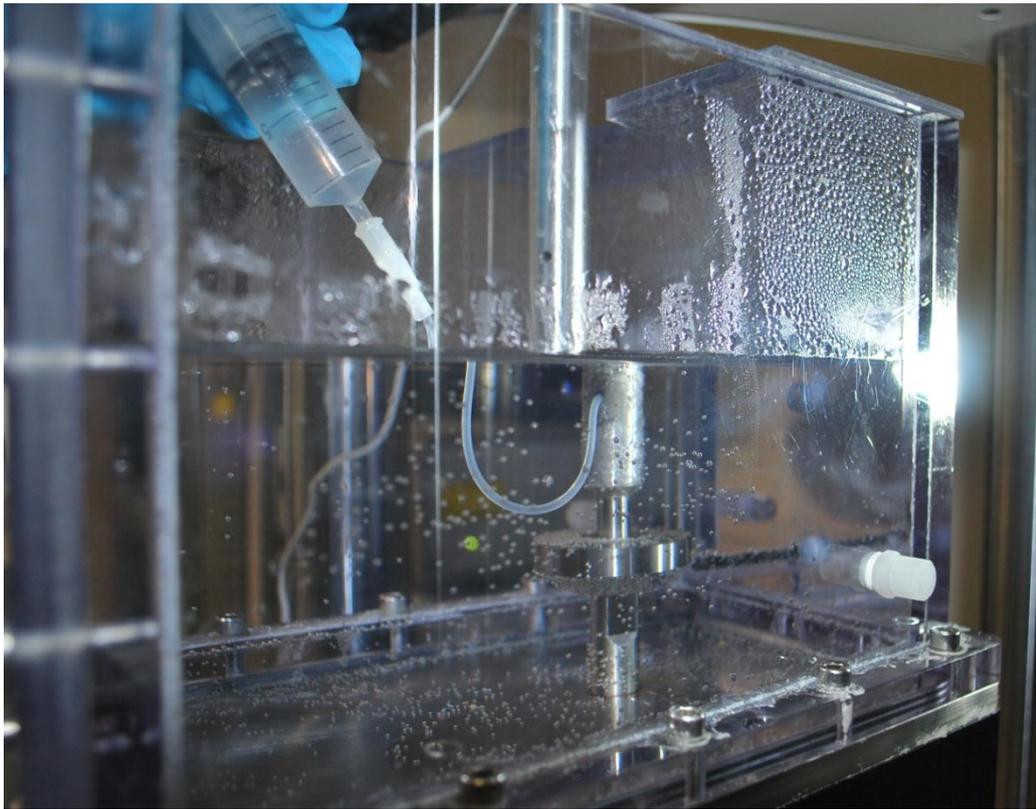
Figure 7.6 Use of a syringe to flood the upper chamber with saline and vent air.
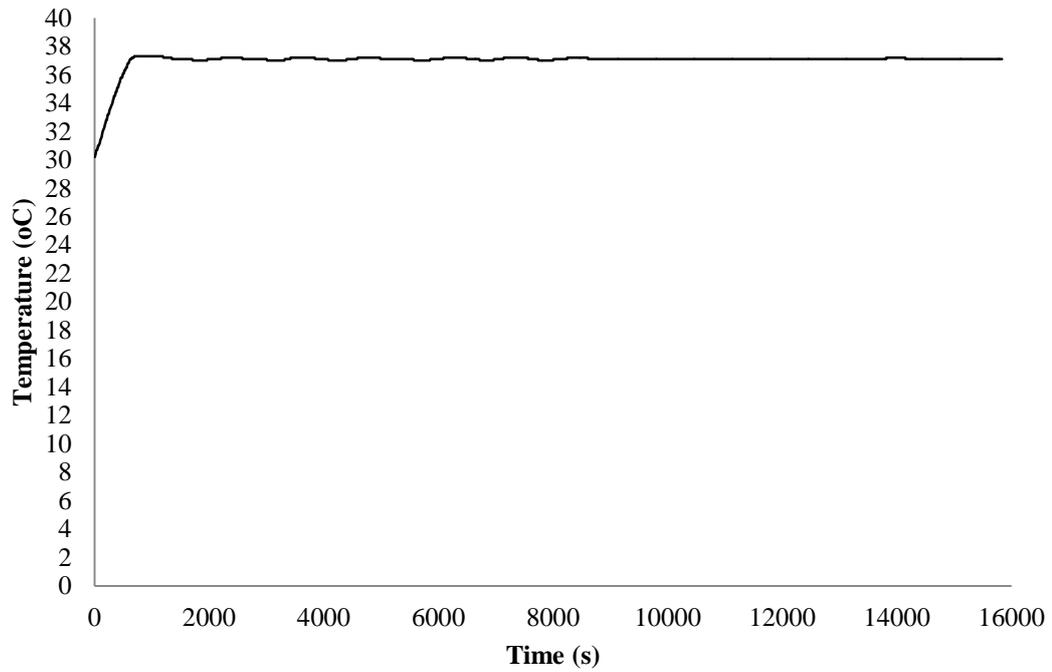
Figure 7.7 Plot of external bath fluid temperature throughout a test duration. Temperature was set to 37°C.

To analyse the equilibrium response of the tissue, the non-linear biphasic equation for finite deformation (Holmes and Mow, 1990) was fitted to the experimental load data obtained in both external solutions. This technique has been previously utilised for the analysis of cartilaginous tissues (Ateshian et al., 1997, Iatridis et al., 1998, Perie et al., 2005, Perie et al., 2006a, Perie et al., 2006b, Heneghan and Riches, 2008b). The compressive stress at equilibrium is related to λ by

$$\sigma_e = \frac{1}{2} H_{A0} \left(\frac{\lambda^2 - 1}{\lambda^{2\beta + 1}} \right) e^{\beta(\lambda^2 - 1)} \tag{7.1}$$

where σ_e is the equilibrium stress, H_{A0} is the aggregate modulus at zero strain and β is a non-dimensional constant which measures the sensitivity of σ_e to large strains. Heneghan and Riches (2008b) included the term σ_0 to account for the initial swelling stress of the tissue. However, since this study is only interested in H_A, which is a

| 219

derivative of σ_e, this addition was not included. Instead, in a similar method to previous studies, all stress data was set to zero before the first ramp (Iatridis et al., 1998, Perie et al., 2005, Perie et al., 2006a, Perie et al., 2006b). To calculate H_{A0} and β ordinary least squares regression was used in Excel via the solver tool.

7.3.3. FE modelling

7.3.3.1. *Model properties*

For each sample, the transient stress response was fitted to a biphasic FE confined compression model which incorporated strain-dependent stiffness (Eq. 7.1) and permeability; both of which are based on the non-linear framework of Holmes and Mow (1990). The strain-dependent permeability, $k(\lambda)$, is given by

$$k(\lambda) = k_0 \left(\frac{\lambda - \phi_0}{1 - \phi_0}\right)^{\kappa} e^{\frac{1}{2}M(\lambda^2 - 1)} \tag{7.2}$$

where λ is the axial stretch, k_0 is the zero strain permeability, M and κ are non-dimensional parameters relating k to λ, and ϕ is the tissue porosity; the subscript 0 indicates zero strain values. By inputting the reaction force obtained experimentally, it was possible to solve an inverse FE problem that recreated the reaction force curve by altering the material parameters; thus providing k_0, M and κ.

As used in previous chapters, the nonlinear finite element program FEBio was chosen as the most suitable platform to model the confined compression of the NP. Table 7.1 contains the initial material parameters required for the model.

By defining $\nu = 0$, which is applicable to a confined compression experiment,

$$H_a = E(1 - v)/[(1 + 2v)(1 - 2v)] \tag{7.3}$$

reduces to

$$H_a = E \tag{7.4}$$

Model material properties were either taken from the literature or from the analysis outlined above (Table 7.1).

Material Property	Units	Value	Source
$\emptyset_0$		0.2	Roberts et al. 1989
E	MPa	-	Calculated from H_{A0}
v		0	-
β		-	Obtained from ordinary least squares regression

Table 7.1 Material properties used in biphasic confined compression model.

7.3.3.2. *Geometry and constraints*

A cuboidal model of side 1mm consisting of 84 nodes and 20 elements was created (Figure 7.8), with all faces confined in all axes other than the superior surface which was free in the z-axis and free-draining (ideal condition). An indenter was modelled as a rigid body and was connected via a rigid interface to the superior surface ($z = 1$) of the cuboid. Z displacement was applied to the indenter to induce deformation of 5% strain.

After deforming the sample, the axial displacement was held constant to allow the tissue to relax due to interstitial fluid flow. A steady-state analysis was performed which consisted of a compressive displacement of 0.05mm in the z direction on the superior surface at a rate replicating experimental conditions. The curve-fit was performed on the reaction force, Fz, of the indenter.
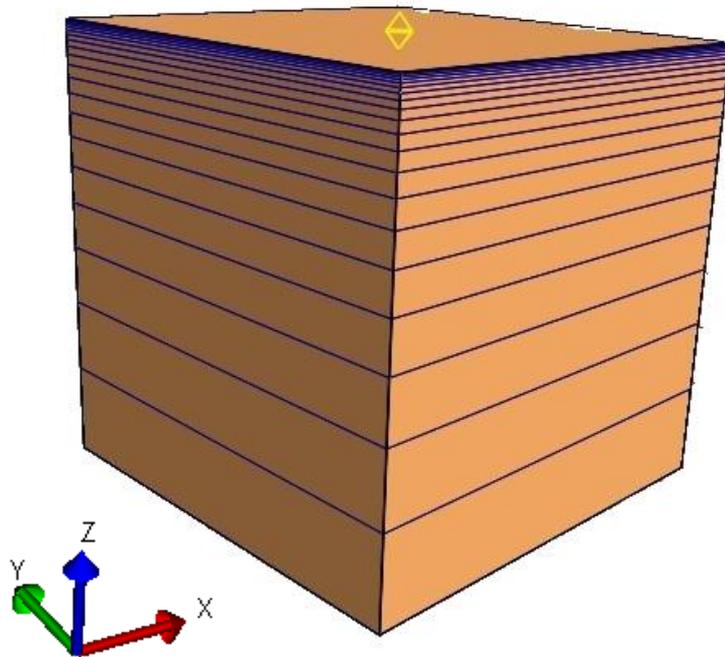
Figure 7.8 Confined compression FE model.

7.3.4. Data analysis

To examine the effect of external solution on the parameters H_{A0}, β, K_0 and M, a paired two sample t-test was used. Significance was set at $p \leq 0.05$.

7.4. Results

All samples experienced an increase in compressive load during each of the ramp phases, with the peak load occurring immediately after displacement. Stress relaxation then followed during each of the hold phases. The typical load and stress responses obtained are shown in Figure 7.9 and Figure 7.10 respectively. Figure 7.11 plots the equilibrium stress, σ_e, against λ for samples tested in both 0.15M and 3M NaCl solutions. Almost all samples, for both external solutions, demonstrated a non-linear increase in σ_e with increasing strain. The effect of external solution was not significant (P = 0.367). Figure 7.12 plots the experimental and model stress response over time, with an excellent equilibrium fit and poor transient fit. Figure 7.13 and Figure 7.14 plot k against λ, for both external solutions, obtained inversely via the FE model. k was found to decrease with decreasing λ. A significant reduction in k_0 was observed (p = 0.05) for samples bathed in the hypertonic solution compared to those in the isotonic solution. Table 7.2 shows the calculated parameters H_{AO}, β and M. The effect of external solution on these parameters was not significant (P > 0.2). No correlation was found between H_{A0} and k_0 and disc level or degenerative grade (Figure 7.15).
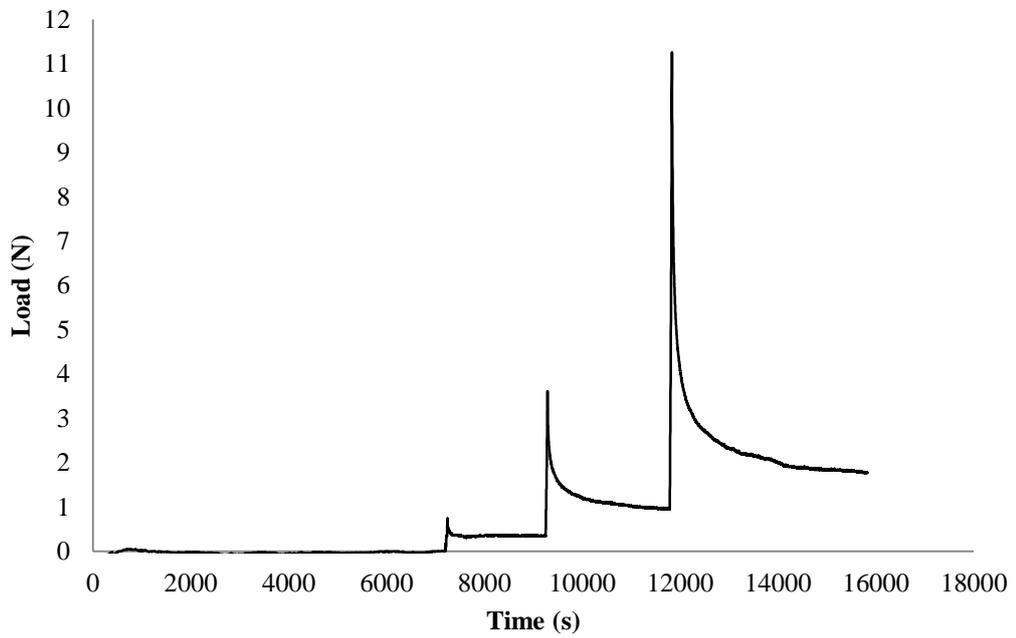
Figure 7.9 Typical plot of multiple strain experimental load response over time.
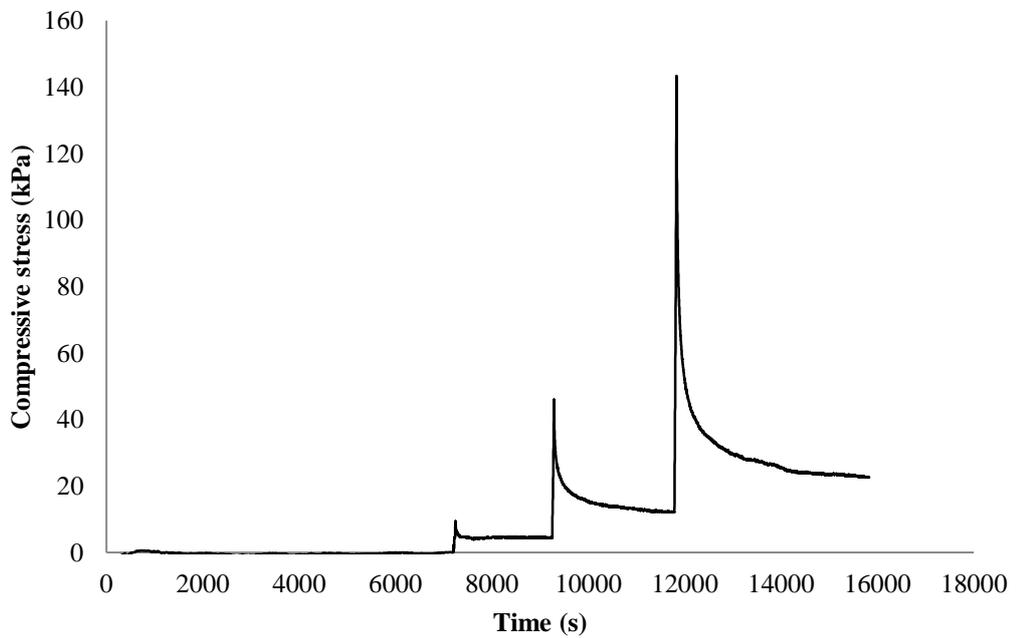
Figure 7.10 Typical plot of multiple strain experimental stress response over time. Positive stress indicates compression.

(A)

(B)
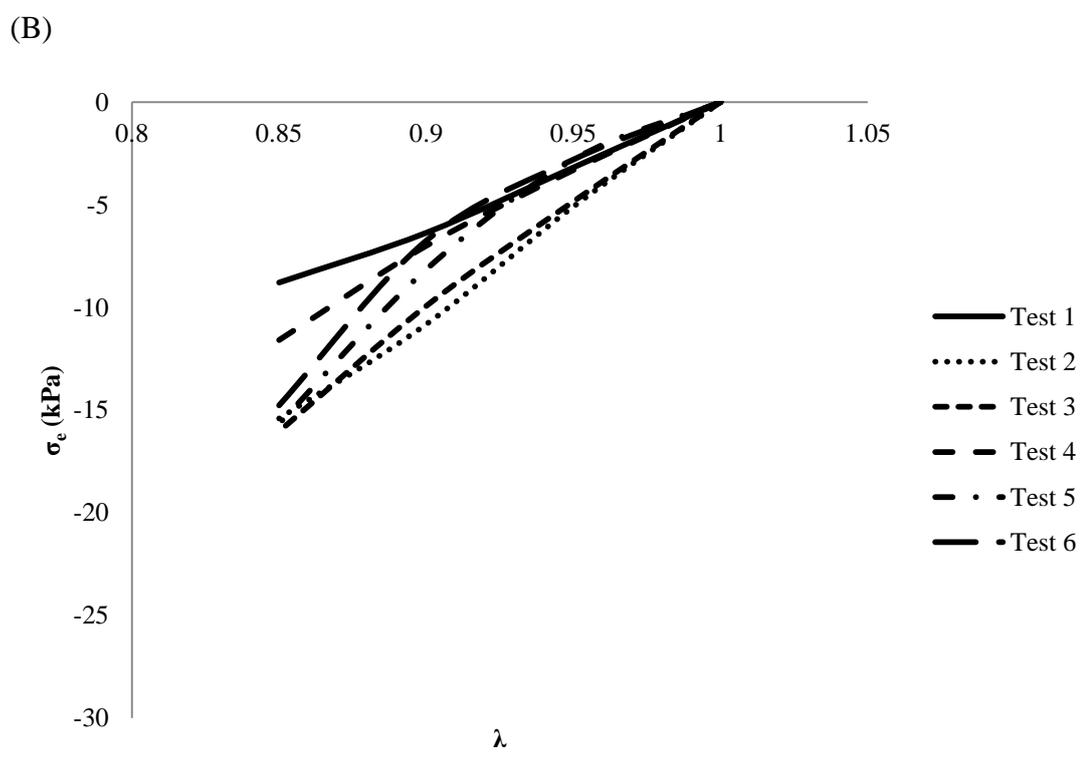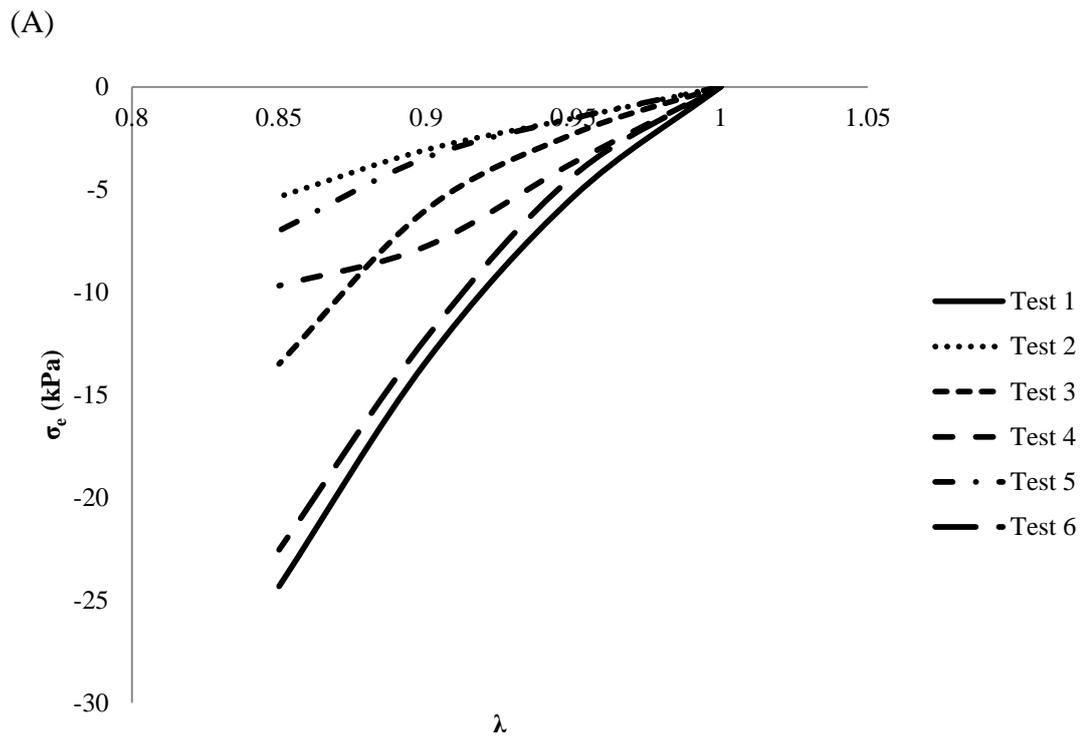
Figure 7.11 Plots of σ against λ for samples bathed in A) 0.15M NaCl and B) 3M NaCl
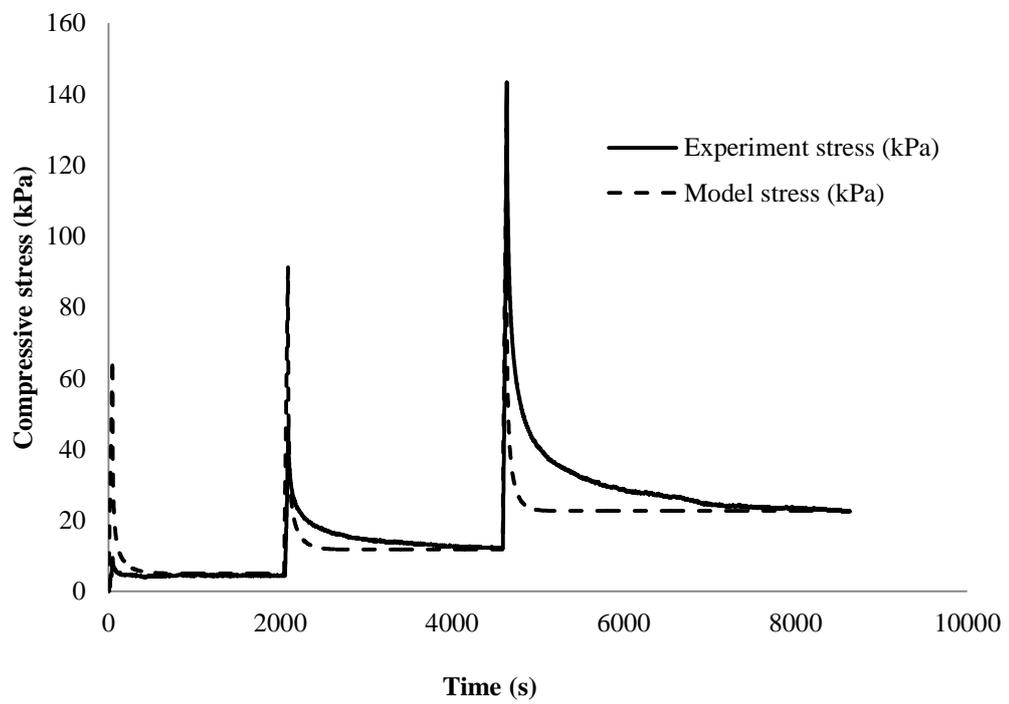
Figure 7.12 Biphasic FE model σ fit to experimental data. Positive stress indicates compression.

(A)

(B)
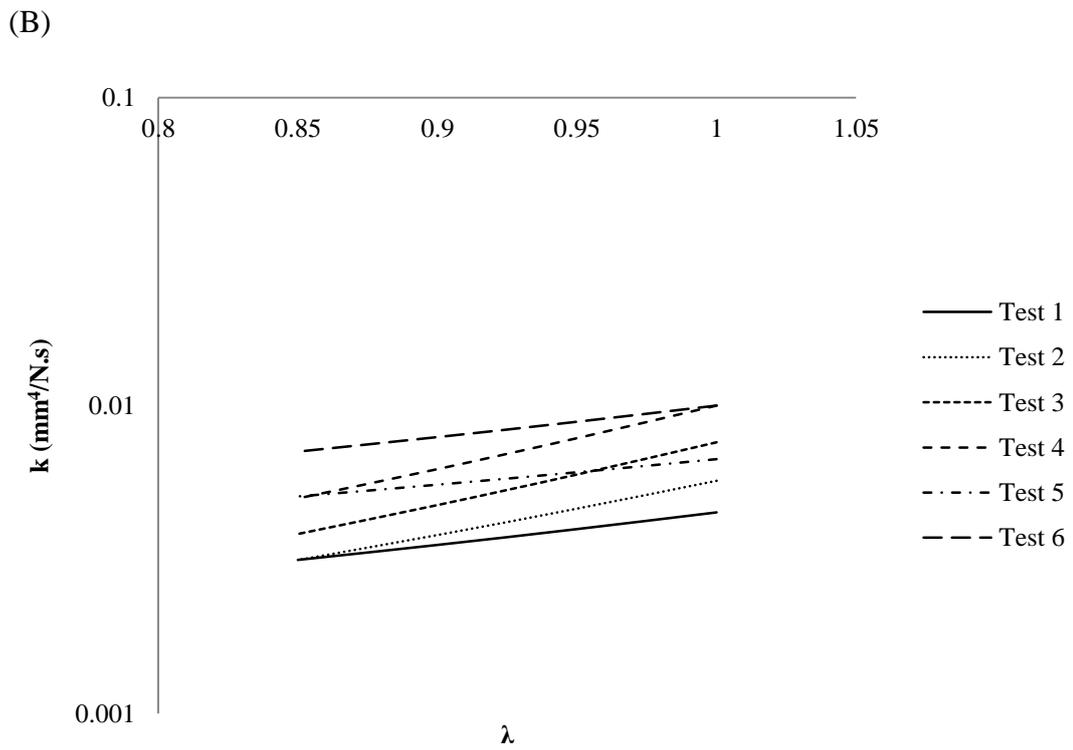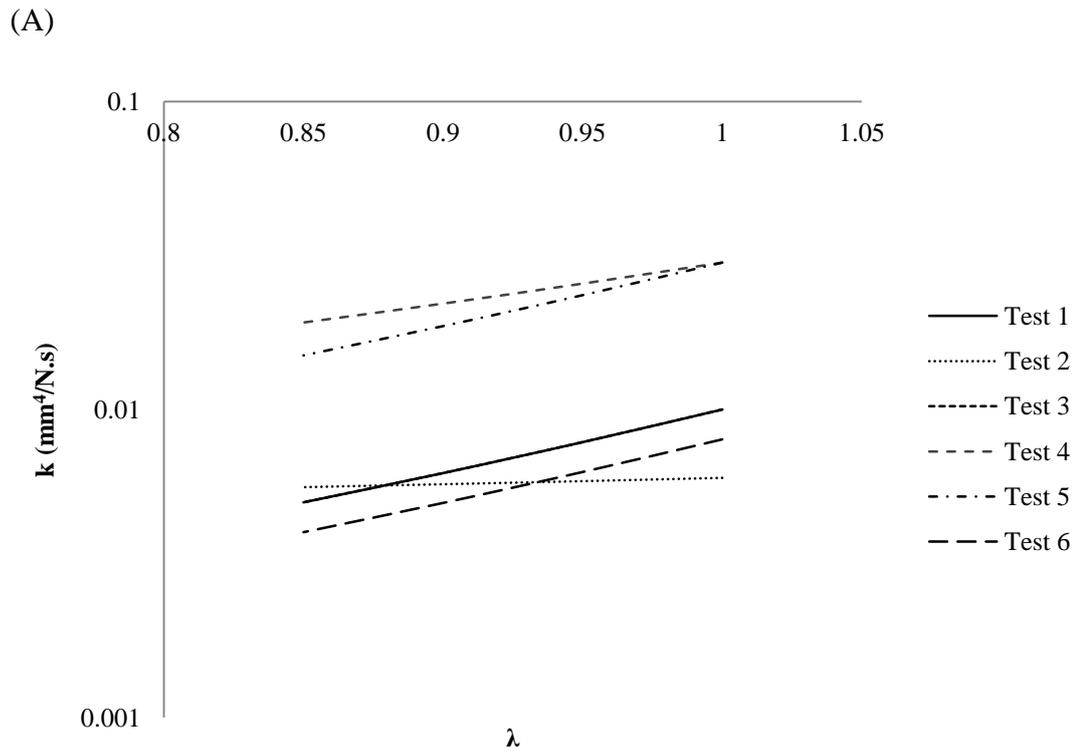
Figure 7.13 Plots of k against λ for samples bathed in A) 0.15M NaCl and B) 3M NaCl.
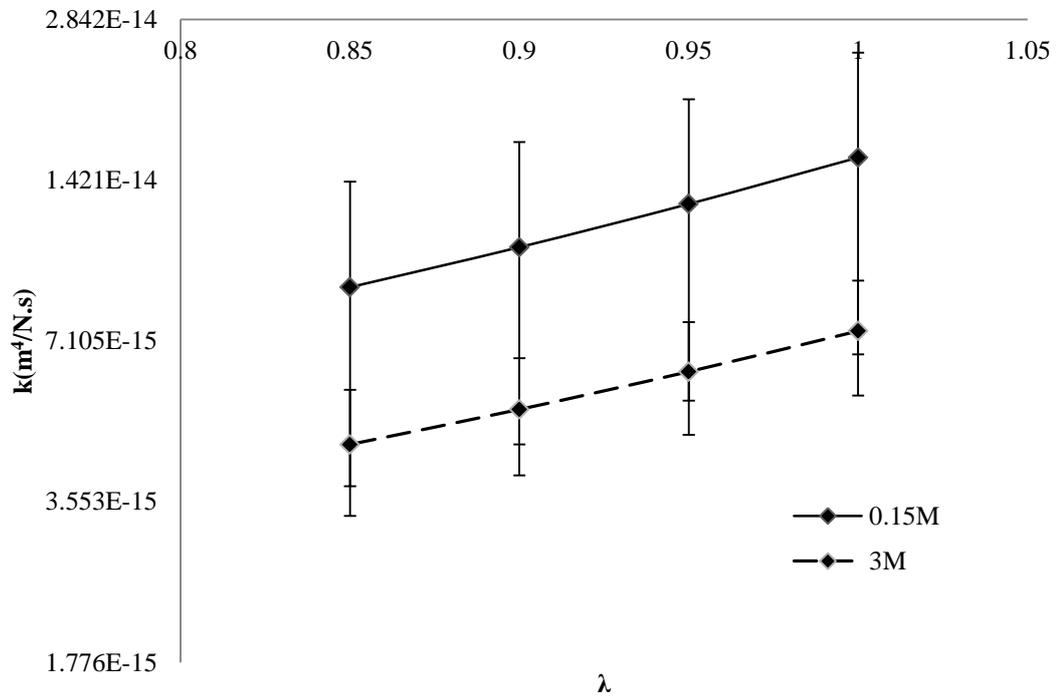
Figure 7.14 Plot of average k against λ for both external solutions. Error bars indicate S.D.

	0.15M	3M
H_{A0} (kPa)	62.73 ± 33.04	69.79 ± 19.75
β	5.78 ± 3.31	4.35 ± 5.43
k_0 (mm^4/N.s)	0.0157± 0.011	0.0074 ± 0.0023
M	3.96 ± 1.83	3.21 ± 1.35
R^2	0.993	0.998

Table 7.2 Comparison of H_{A0}, β, k_0, and M for both external solutions.

(A)
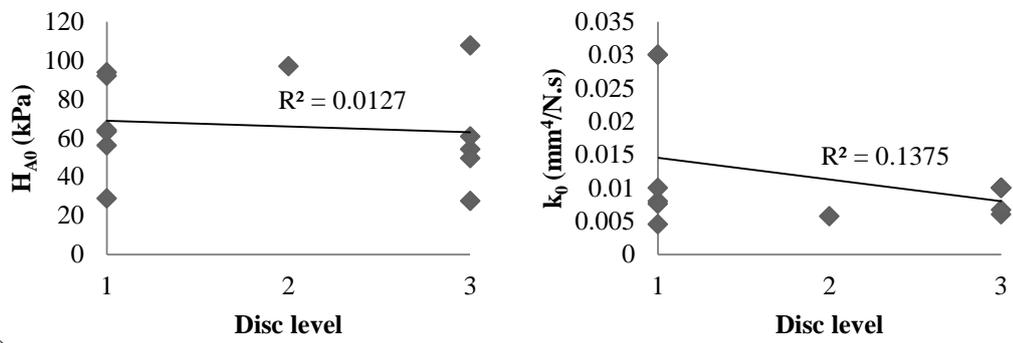
(B)
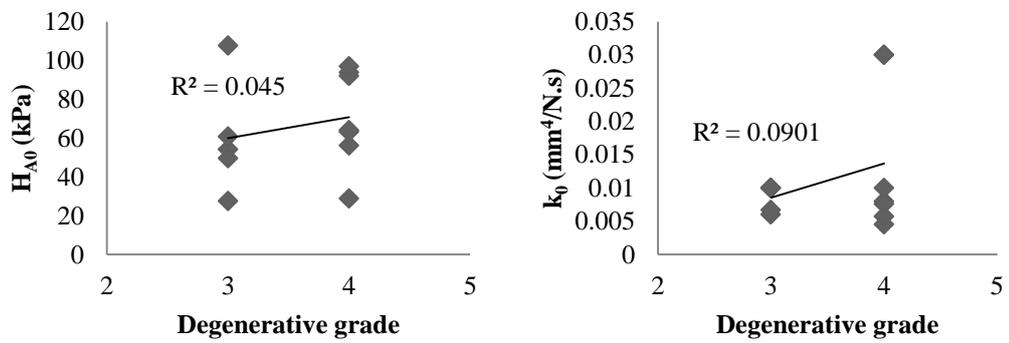
Figure 7.15 Correlation between H_{A0} and k_0 with A) Disc level and B) Degenerative grade

7.5. Discussion

Degeneration is an irreversible disorder that compromises the mechanical function of the disc (O'Connell et al., 2011) and is often implicated in lower back pain thus placing a significant burden on health organisations. Therefore, multiple strain confined compression experiments were conducted on human NP samples with the aim of establishing how degenerative alterations in electrochemical mechanisms affect the load bearing capacity of the tissue. Inverse curve fitting of the tissue's load response in both isotonic and hypertonic external solutions to the biphasic theory allowed an elucidation of H_{A0}, k_0 and the multiple strain parameters: β and M.

Experimental results indicate that solid matrix stresses are greater in the degenerate case than in healthy tissue which may have important ramifications for the biomechanical characteristics and possible remodelling of the degenerate disc. In the healthy case, load is supported by an aggregate of hydrostatic fluid pressure (Oloyede et al., 1998, Wilke et al., 1999), an osmotic pressure resulting from the high concentration of PG and a solid matrix stress. However, results indicate that in the degenerate case the primary load bearing contribution comes from the solid matrix, which is in keeping with the poroelastic and chemical electric model (PEACE) predictions of Iatridis et al., (2003) who investigated the effect of PG content and distribution on disc mechanics.

There was no significant difference in H_{A0} between samples bathed in isotonic and hypertonic solutions. Since hypertonic solutions negate the ionic component of the swelling pressure, this finding indicates a significant loss of PG and associated electro-chemical interactions in the degenerate tissue. This finding is in keeping with

previous studies which reported a loss of PG content with advancing degenerative grade (Buckwalter, 1995, Johannessen and Elliott, 2005). Current results for H_{A0} were greater than hypothesised, for both external solutions, perhaps as a result of the degenerate tissue's fibrotic (Buckwalter, 1995) and highly non-linear nature. Indeed, the current results are remarkably similar to those obtained by Heneghan and Riches (2008b) via similar experiments on bovine NP.

A poor transient fit was obtained between the non-linear biphasic FE model and experimental data (Figure 7.12), indicating that this theoretical framework may not be appropriate for modelling degenerate NP tissue. Although the current permeability values are in keeping with previous work (Johannessen and Elliott, 2005) they cannot be taken as absolute. The source of disagreement with biphasic theory is evident in the significantly lower peak-to-equilibrium ratio obtained during the first ramp compared to the second and third ramps. This may, partly, have been the result of experimental issues when investigating degenerate tissue. Although tissue samples were prepared to the exact diameter of the confining chamber, the total chamber volume may not have been occupied due to low tissue swelling resulting from the tissue's low PG content (Ateshian, 2013). This may indicate that degenerate tissue requires an initial tare load to ensure the full chamber is occupied during a confined compression experiment. To this end, the model was retrospectively fitted to the second and third ramps only, after appropriately zeroing the load and displacement, and the initial ramp treated as a tare load. A slightly improved fit was obtained (Figure 7.16); however, it remains apparent that the non-linear biphasic framework, as implemented in FEBio, is unable to accurately predict the response of this tissue

suggesting that this possible experimental issue are not the only source of disagreement.
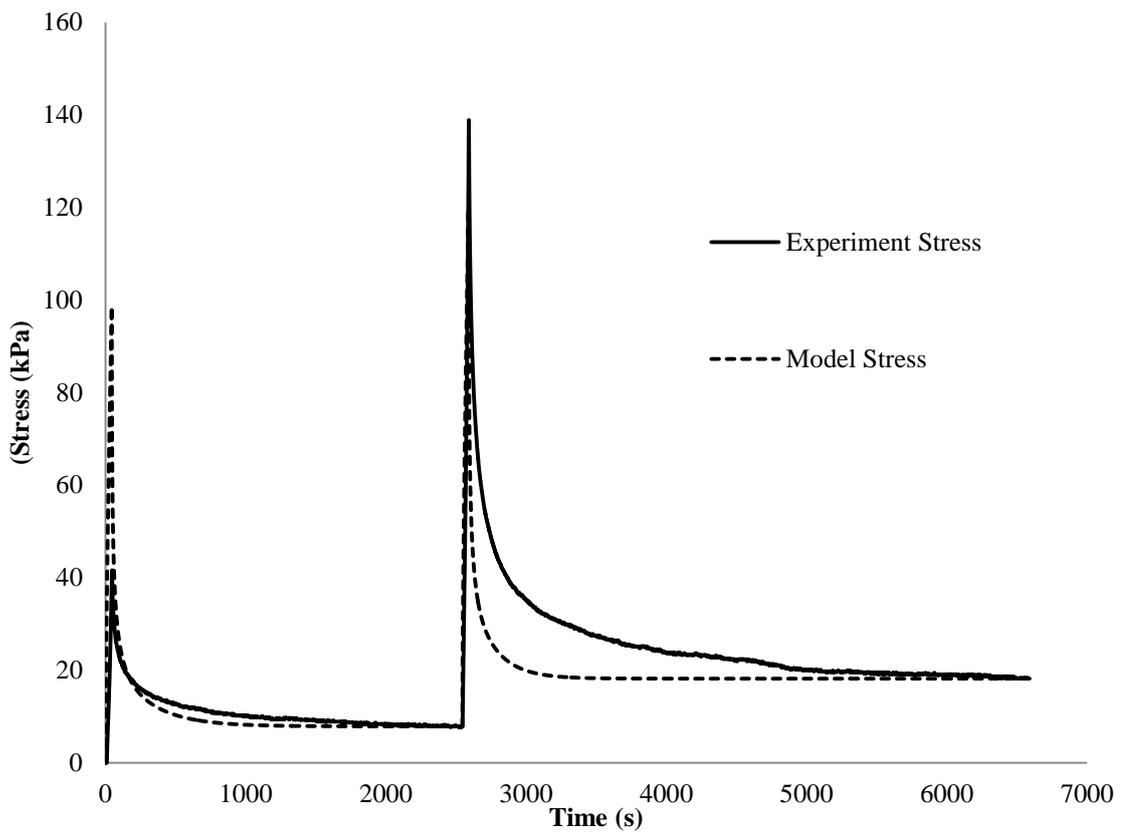
Figure 7.16 Biphasic FE model σ fit to experimental data for second and third ramps only.

An additional explanation is that this tissue may exhibit a dual permeability phase via a degenerate heterogeneous structure; fissures (evident in degenerate NP which appears granular after dissection) allow for high permeability channels whilst the granulated high density regions of tissue exhibit lower permeability. This phenomenon may explain why the homogeneous single permeability model was not able to capture the transient response of the tissue in confined compression. This theory is also in keeping with the finding that both σ_e and k appear to be highly dependent on deformation as highlighted by the high values of β (exponential stiffening coefficient) and the long hold time required for the third ramp compared to the first and second. Indeed, the current values of β are significantly greater than previously reported for healthy tissue (Heneghan and Riches, 2008a). A significantly reduced ionic swelling pressure and fissured heterogeneous structure in may result in an initial reduced load bearing capacity (at low strain). However, as compression continues during a sequence of ramps, the solid matrix consolidates to a greater extent than what is likely to occur in the healthy state due to reduced water content and the closure of fissures. This is highlighted by the low peak stresses observed at 5% strain and 10% compared to the subsequent high peak stresses observed at 15% strain. This significant consolidation of tissue serves to reduce permeability, via reduced fissures space and pore size, increase PG concentration and reduce FCD charge-to-charge distance, all of which may combine to increase tissue stiffness during significant deformation.

The significant exponential reduction in permeability and increase in stiffness with increasing strain may suggest that an important self preservation mechanism exists which counteracts the mechanical adaptations which occur with advancing stages of

degeneration. The tissue loses PG content with aging; consequently losing its ability to withstand compressive loading. However, the tissue appears to have the ability to become consolidate thus reducing permeability and increasing PG concentration; possibly compensating for mechanical degenerative adaptations to some extent.

Samples bathed in the hypertonic solution demonstrated a significant reduction in k_0 despite low PG content. This may be a result of strain gradients whereby higher localised PG concentrations toward the upstream surface create an electric potential gradient in the same direction as fluid flow in the current configuration. In the 0.15M case only, these chemical gradients may provide a flow augmenting mechanism as described in chapter 3. The higher PG concentration toward top boundary, in the 0.15M case, may encourage fluid to this region which will serve to maintain pore inflation and increase permeability. This may indicate that PG content, even though significantly diminished, may still play a significant role in disc mechanics and nutrient transport in the degenerate case by facilitating electro-chemical interactions.

The greater sample variation in H_{A0} and k_0 results obtained in the 0.15M case compared to the 3M case indicates significant variation in sample PG content. In the 0.15M case, the PG's are able to contribute to the tissues compressive stiffness, therefore samples with greater PG content will demonstrate greater H_{A0} and reduced k_0. However, the 3M case negates the effect of PG, so samples demonstrate less variation in H_{A0} and k_0 because these properties are reliant solely on solid matrix compaction. No correlation was found between $H_{A0,}$ k_0 to disc level and degenerative grade ($p > 0.05$) (Figure 7.15) which may be a result of the low sample population. A larger population study is required to investigate these relationships in more depth.

7.6. Experimental artefacts

The significant variability observed in data may be a result of the experiment being under powered and significant inter-specimen variability. Stokes et al (2010) also found substantial specimen variability when conducting force-relaxation experiments on human IVDs. However, this variability was not explained by differences in disc physical dimensions or degeneration. Further investigation is required to elucidate which degeneration sensitive biochemical alterations may affect such experiments.

As discussed, the non-linear biphasic theory does not appear to be able to accurately predict the transient response of the severely degenerate NP. In addition to the previously discussed potential experimental issue arising during the first ramp whereby the specimen does not occupy the full chamber volume, and the potential dual permeability phenomenon, solid matrix viscoelasticity may also be a factor (Ateshian, 2013). Based on previous work on NP tissue (Heneghan and Riches, 2008b) a high strain-rate was used, this however may have excited the well documented viscoelastic behaviour of the solid matrix. Since the effect of this phenomenon in the current configuration is as yet unknown and since the FE model did not cater for such interactions it must be considered as a possible contributory factor to the poor transient fit.

7.7. Conclusions

Human NP samples were subjected to confined compression in both isotonic and hypertonic environments to investigate the effect of degenerative mechano-chemical adaptations on the tissue's load bearing capacity. Results indicate that solid matrix stresses are greater in the degenerate case than in healthy tissue which may have

important ramifications when considering the proneness of the degenerate disc to traumatic injury. External solution concentration was not found to significantly affect the stiffness of the tissue suggesting that PG content was highly diminished. Results also indicate that the degenerate NP stiffness is sensitive to deformation via heightened consolidation mechanisms and may exhibit a dual permeability phase which resulted in poor agreement with non-linear biphasic theory. These findings suggest that this tissue may not be suitably modelled using this mathematical framework. Although PG content was significantly reduced, mechano-chemical phenomena may still play important role in disc mechanics and cell biosynthesis. The inverse modelling techniques outlined in this work should be extended to the triphasic domain for a fuller understanding of the mechanisms.

8. Thesis discussion, limitations and recommendations

8.1. Discussion

This thesis has investigated the mechanical response of the NP to external loading with particular interest paid to the mechano-electrochemical interactions which develop during such conditions. Experimental results have been complimented with multiphasic FE modelling which has allowed for a fuller investigation of the micromechanical relationships which exist within this tissue.

In chapter 3, a direct permeation study was conducted to determine the effect of external solution concentration on fluid flow within the NP. Results indicated that the tissue is most permeable to physiological saline (0.15M NaCl) and least to a hypertonic solution (3M NaCl). By comparing quadriphasic theory to experimental data, a potential flow augmenting mechanism was identified which serves to increase fluid flow by up to 55% of the applied fluid pressure. This phenomenon was attributed to deformation induced ionic osmotic pressure gradients which consist of FCD, mobile ion and electrical potential gradients. This chapter demonstrated the importance of using a constitutive equation that includes mobile ions and fixed charges as separate phases when modelling this tissue. The considerable influence of mechano-electrochemical effects may have ramifications when considering the transport of nutrients within the disc and the signals which control disc cell biosynthesis.

Chapter 4 modelled a direct permeation experiment on the NP via multiphasic FE analysis. Results agreed with the hypothesis in chapter 3 that mechano-electrochemical interactions significantly influence fluid transport within the disc. Accordingly, models which account for such interactions must be used when investigating fluid and solute transport within cartilaginous tissue; however, there remains some work to allow closer agreement with experimental data. The triphasic model was not able to replicate the apparent flow augmenting mechanism found experimentally in chapter 3 which may have been a result of FCD and electric potential gradients not being considered as separate terms in the governing equations. Nonetheless, good agreement was obtained with experimental data for global fluid velocities and localised mechano-electrochemical interactions were investigated.

Chapter 5 sought to investigate Poisson's ratio effects within the IVD via unconfined compression experiments. Results indicated that the Poisson's ratio of the NP is strain-dependent and that solid matrix viscoelasticity may play an important role in disc mechanics at moderate strain-rates. Poisson's ratio results were significantly lower than what were previously reported for the human NP which is perhaps due to methodological differences; highlighting the sensitivity of experimental set up when mechanically testing cartilaginous tissue. Unconfined compression experiments on the full disc indicated that the AF plays an important role in enabling the disc to absorb compressive loads by allowing the NP to expand radially, whilst maintaining minimal global disc bulging.

Chapter 6 investigated the mechano-electrochemical interactions which occur within the NP during unconfined compression. The selection of numerical framework was found to be crucial when investigating disc mechanics. In keeping with previous

chapters, the effect of external solution concentration was found to significantly influence the tissue's response to mechanical loading; the TP_{3M} results validating the experimental protocol adopted in chapter 5. Strain-rate was found to significantly influence the transient response of the tissue, only, thus resulting in poor agreement with experimental data which may have been the result of solid matrix viscoelasticity omission. Radial variations in mechano-electrochemical interactions were found which may influence radial nutrient transport when the disc is subject to axial loading.

The analysis presented in chapter 7 involved subjecting degenerate human NP samples to confined compression and varying external solution concentrations to establish the effect of degenerative mechano-chemical adaptations on the tissue's load bearing capacity. Solid matrix stresses were found to be greater in degenerate tissue than in healthy tissue which may have important ramifications when considering the proneness of the disc to traumatic injury such as prolapse. The effect of external environment was significantly reduced in degenerate tissue as a result of low PG content. However, the degenerate NP was found to be highly sensitive to deformation, perhaps via newly observed consolidation mechanisms. Although PG content is reduced with advancing degeneration, this important constituent has been found to continue to contribute to disc mechanics and possibly cell biosynthesis in the degenerate state. The non-linear biphasic theory was unable to accurately predict the transient mechanical behaviour, possibly as a result of the degenerate tissue exhibiting a heterogeneous structure and dual permeability phase, suggesting that this framework is not suitable when investigating the degenerate NP.

This work has also compared the open source FE software "FEBio" to experimental data, which has not been previously reported in the literature. Although slight discrepancy was found when analysis mechano-chemical effects via the triphasic theory, potentially due to the difficulty in parameterising these tissues, global results were in agreement with the experimental data obtained in chapters 3 and 5 which lends confidence to the use of this program for the modelling of the IVD.

8.2. Novel contributions

This study has aimed to investigate the micromechanical interactions which influence disc mechanics, particularly in the NP, via a series of experiments and complementary FE modelling. The novel contributions to the literature are summarised as follows:

I. A fuller understanding of the mechano-electrochemical influences on fluid flow within the nucleus pulposus.

II. Development of a novel method to characterise the Poisson's ratio of the disc via unconfined compression and optical analysis.

III. In depth investigation of the Poisson's ratio of the NP and the confining effect of the AF.

IV. Insight to the potential ramifications of degeneration on mechano-electrochemical effects.

V. Comparison between biphasic and triphasic theory application to NP mechanics.

It is apparent that many challenges remain when modelling cartilaginous tissue, particularly when considering the artefacts associated with experimental boundary

conditions. Although current models are yet to fully predict the mechanical response of the NP to deformation and external influences such as chemical loading, the results presented in this thesis have highlighted the importance in adopting the correct mathematical framework when conducting such investigations. Whether or not the additional computational expense associated with the implementation of the more complex frameworks, such as triphasic and quadriphasic theory, is required, depends very much on the objectives of the study in question.

In addition to informing future models of the disc, the work presented in this thesis may also aid the development of artificial NP implants and total disc replacement devices. To allow for improved functionality of a degenerate disc, the replacement device must behave in a similar mechanical fashion to the healthy NP. The results in this thesis provide a suitable benchmark for potential replacement materials to be critiqued against, particularly in terms of permeability and fluid pressurisation which are crucial to the load bearing capacity of the tissue.

8.3.   Limitations

The major limitation of this work was the use of bovine tail discs for the majority of experiments. This animal model was chosen due to its similar constituents, size and mechanical response to the human lumbar disc as well as its availability. The variances between the bovine tail disc and human disc have been discussed throughout this thesis, with reference to the possible associated issues with the presented data. However, the deformation and external environment sensitivities highlighted throughout can also be expected in the human case.

The low sample population for the work on degenerate human tissue is another limitation. It was considered essential that fresh human discs were obtained as opposed to using fixed tissue which would have introduced a plethora of mechanical artefacts. Unfortunately, only one fresh human spine became available during the investigation period and only a small number of samples were able to be harvested from the discs due to their reduced thickness resulting from degeneration. However, all results obtained from human tissue are highly valuable and the results presented in this thesis may have established some previously unreported mechanical behaviour in the degenerate case.

Two of the three experimental chapters in this thesis were conducted at room temperature (19-24°C). The complexity of these experimental configurations did not cater for the regulation of external solution temperature. Whilst it is more representative of the physiological condition to maintain the samples at body temperature, it was out with the scope of these experimental chapters which were interested in the sensitivity of the discs response to mechanical and chemical loading. The determination of the absolute values of mechanical properties was not the focus of this research.

8.4.   Recommendations for future work

Whilst much has been achieved in this thesis, there remains a significant amount of work to be carried out in the subject area. The investigation of disc mechano-electrochemical interactions is highly complex and has only been briefly investigated both experimentally and numerically in this volume of work. Effort should be made to develop our multiphasic modelling capabilities as it has been shown that the

current implementation of the various frameworks may be underestimating fluid flow in the physiological condition. Additionally, modelling which couples solid matrix viscoelasticity in addition to the well documented non-linear behaviour of this tissue is required for a fuller description of strain-rate effects. It has also been shown that the major source of disparity between experimental data and numerical results is the poor replication of boundary conditions and unavoidable associated artefacts. Future modelling must, therefore, be conducted whereby limiting factors, such as interfacial shear stresses in an unconfined compression experiment, are accurately accounted for in simulations thus allowing for a closer correlation to in vitro tests. The unconfined experimental protocol outlined in chapter 5 provided the first comprehensive analysis of matrix Poisson's ratio effects in the NP. This work should be continued to encompass the degenerate case. Although the unconfined compression analysis of the full disc yielded interesting strain distribution mechanisms, the effect of friction was significant and the absolute values for Poisson's ratio must be further validated via another experimental set up. The confined compression of the degenerate human tissue conducted in this thesis was severely limited by sample size and a wider population study is required to lend confidence to the current results. The development of heterogeneous poroelastic models may capture the potential dual permeability phase of the degenerate NP found in this study and should be explored. By combining two elastic material definitions within a single solid phase, each with a different permeability value, the influence of granular channels in degenerate tissue may be captured; channels will demonstrate high permeability and dense tissue regions will demonstrate low permeability. Additionally, the inverse FE modelling conducted in this study should be extrapolated to the triphasic domain for a fuller

understanding of the mechano-electrochemical interactions which occur during the deformation of the degenerate NP.

All of the numerical analyses conducted in this study adopted material properties from the literature; many of which were obtained from experimental conditions which were non-comparable with those modelled in this work. By conducting parametric studies on the input parameters used in the numerical chapters of this thesis, a closer agreement with the experimental data may be achieved. One potentially important parametric study may involve a sensitivity analysis and optimisation of FCD. FCD has been shown in this thesis to be extremely important in regulating the mechanical properties of the disc. However, the FCD values used in the current FE models were obtained from mildly to moderately degenerate human tissue which is significantly different in composition to the bovine tissue used for the experiments conducted in this thesis. By inversely fitting experimental data to a triphasic FE model it may be possible to determine a more appropriate FCD value and thus provide better agreement with empirical data.

Furthermore, this form of study should not be limited to only FCD as the mechanical response of the disc may be highly sensitive to other material properties such as aggregate modulus, ion diffusivity and the non-dimensional parameters which relate permeability to deformation in a biphasic tissue.

By continuing the work presented in this thesis, further insight to the control of fluid flow and nutrient transport within the disc and the mechanical response dependent on such mechanisms will be obtained which may lead to a better understanding of the

mechanisms influencing disc degeneration and perhaps allow us to develop possible

treatments or, indeed, prevent it.

References

ADAMS, M. A. & DOLAN, P. 2005. Spine biomechanics. *J Biomech,* 38, 1972-83.

ADAMS, M. A. & HUTTON, W. C. 1982. PROLAPSED INTERVERTEBRAL-DISK - A HYPERFLEXION INJURY. *Spine,* 7, 184-191.

ADAMS, M. A. & HUTTON, W. C. 1983. The effect of posture on the fluid content of lumbar intervertebral discs. *Spine (Phila Pa 1976),* 8, 665-71.

ADAMS, M. A., MCNALLY, D. S. & DOLAN, P. 1996. 'Stress' distributions inside intervertebral discs. The effects of age and degeneration. *J Bone Joint Surg Br,* 78, 965-72.

ADAMS, M. A. & ROUGHLEY, P. J. 2006. What is intervertebral disc degeneration, and what causes it? *Spine,* 31, 2151-2161.

AGUIAR, D. J., JOHNSON, S. L. & OEGEMA, T. R. 1999. Notochordal cells interact with nucleus pulposus cells: Regulation of proteoglycan synthesis. *Experimental Cell Research,* 246, 129-137.

AKIZUKI, S., MOW, V. C., MULLER, F., PITA, J. C., HOWELL, D. S. & MANICOURT, D. H. 1986. TENSILE PROPERTIES OF HUMAN KNEE-JOINT CARTILAGE .1. INFLUENCE OF IONIC CONDITIONS, WEIGHT BEARING, AND FIBRILLATION ON THE TENSILE MODULUS. *Journal of Orthopaedic Research,* 4, 379-392.

ANDERSSON, G. B. J. 1999. Epidemiological features of chronic low-back pain. *Lancet,* 354, 581-585.

ANTONIOU, J., STEFFEN, T., NELSON, F., WINTERBOTTOM, N., HOLLANDER, A. P., POOLE, R. A., AEBI, M. & ALINI, M. 1996. The human lumbar intervertebral disc - Evidence for changes in the biosynthesis and denaturation of the extracellular matrix with growth, maturation, ageing, and degeneration. *Journal of Clinical Investigation,* 98, 996-1003.

ARGOUBI, M. & SHIRAZI-ADL, A. 1996. Poroelastic creep response analysis of a lumbar motion segment in compression. *J Biomech,* 29, 1331-9.

ARMSTRONG, C. G., LAI, W. M. & MOW, V. C. 1984. An analysis of the unconfined compression of articular cartilage. *J Biomech Eng,* 106, 165-73.

ARUN, R., FREEMAN, B. J. C., SCAMMELL, B. E., MCNALLY, D. S., COX, E. & GOWLAND, P. 2009. 2009 ISSLS Prize Winner: What Influence Does Sustained Mechanical Load Have on Diffusion in the Human Intervertebral Disc? An In Vivo Study Using Serial Postcontrast Magnetic Resonance Imaging. *Spine,* 34, 2324-2337.

ATESHIAN, G. A. 2009. The role of interstitial fluid pressurization in articular cartilage lubrication. *Journal of Biomechanics,* 42, 1163-1176.

ATESHIAN, G. A. 2013. Personal communication.

ATESHIAN, G. A., ALBRO, M. B., MAAS, S. & WEISS, J. A. 2011. Finite Element Implementation of Mechanochemical Phenomena in Neutral Deformable Porous Media Under Finite Deformation. *Journal of Biomechanical Engineering-Transactions of the Asme,* 133.

ATESHIAN, G. A., CHAHINE, N. O., BASALO, I. M. & HUNG, C. T. 2004. The correspondence between equilibrium biphasic and triphasic material properties in mixture models of articular cartilage. *Journal of Biomechanics,* 37, 391-400.

ATESHIAN, G. A., LAI, W. M., ZHU, W. B. & MOW, V. C. 1994. AN ASYMPTOTIC SOLUTION FOR THE CONTACT OF 2 BIPHASIC CARTILAGE LAYERS. *Journal of Biomechanics,* 27, 1347-1360.

ATESHIAN, G. A., LIKHITPANICHICUL, M. & HUNG, C. T. 2006. A mixture theory analysis for passive transport in osmotic loading of cells. *Journal of Biomechanics,* 39, 464-475.

ATESHIAN, G. A., WARDEN, W. H., KIM, J. J., GRELSAMER, R. P. & MOW, V. C. 1997. Finite deformation biphasic material properties of bovine articular cartilage from confined compression experiments. *J Biomech,* 30, 1157-64.

AYOTTE, D. C., ITO, K., PERREN, S. M. & TEPIC, S. 2000. Direction-dependent constriction flow in a poroelastic solid: the intervertebral disc valve. *J Biomech Eng,* 122, 587-93.

AYOTTE, D. C., ITO, K. & TEPIC, S. 2001. Direction-dependent resistance to flow in the endplate of the intervertebral disc: an ex vivo study. *J Orthop Res,* 19, 1073-7.

BAILEY, A. J. 1978. Collagen and elastin fibres. *J Clin Pathol Suppl (R Coll Pathol),* 12, 49-58.

BARBIR, A., MICHALEK, A. J., ABBOTT, R. D. & IATRIDIS, J. C. 2010. Effects of enzymatic digestion on compressive properties of rat intervertebral discs. *J Biomech,* 43, 1067-73.

BATTIE, M. C., HAYNOR, D. R., FISHER, L. D., GILL, K. & GIBBONS, L. E. 1995. SIMILARITIES IN DEGENERATIVE FINDINGS ON MAGNETIC-RESONANCE IMAGES OF THE LUMBAR SPINES OF IDENTICAL-TWINS. *Journal of Bone and Joint Surgery-American Volume,* 77A, 1662-1670.

BELYTSCH.T, KULAK, R. F., SCHULTZ, A. B. & GALANTE, J. O. 1974. FINITE-ELEMENT STRESS ANALYSIS OF AN INTERVERTEBRAL-DISK. *Journal of Biomechanics,* 7, 277-285.

BENDIX, T., KJAER, P. & KORSHOLM, L. 2008. Burned-Out Discs Stop Hurting Fact or Fiction? *Spine,* 33, E962-E967.

BEST, B. A., GUILAK, F., SETTON, L. A., ZHU, W., SAED-NEJAD, F., RATCLIFFE, A., WEIDENBAUM, M. & MOW, V. C. 1994. Compressive

mechanical properties of the human anulus fibrosus and their relationship to biochemical composition. *Spine (Phila Pa 1976),* 19, 212-21.

BETSCH, D. F. & BAER, E. 1980. STRUCTURE AND MECHANICAL-PROPERTIES OF RAT TAIL TENDON. *Biorheology,* 17, 83-94.

BIOT, M. A. 1941. General theory of three-dimensional consolidation. *Journal of Applied Physics,* 12, 155-164.

BIOT, M. A. 1962. MECHANICS OF DEFORMATION AND ACOUSTIC PROPAGATION IN POROUS MEDIA. *Journal of Applied Physics,* 33, 1482-&.

BODEN, S. D., MCCOWIN, P. R., DAVIS, D. O., DINA, T. S., MARK, A. S. & WIESEL, S. 1990. Abnormal magnetic-resonance scans of the cervical spine in asymptomatic subjects. A prospective investigation. *J Bone Joint Surg Am,* 72, 1178-84.

BORENSTEIN, D. G., O'MARA, J. W., BODEN, S. D., LAUERMAN, W. C., JACOBSON, A., PLATENBERG, C., SCHELLINGER, D. & WIESEL, S. W. 2001. The value of magnetic resonance imaging of the lumbar spine to predict low-back pain in asymptomatic subjects - A seven-year follow-up study. *Journal of Bone and Joint Surgery-American Volume,* 83A, 1306-1311.

BOTSFORD, D. J., ESSES, S. I. & OGILVIE-HARRIS, D. J. 1994. In vivo diurnal variation in intervertebral disc volume and morphology. *Spine (Phila Pa 1976),* 19, 935-40.

BRINCKMANN, P., FROBIN, W., HIERHOLZER, E. & HORST, M. 1983. Deformation of the vertebral end-plate under axial loading of the spine. *Spine (Phila Pa 1976),* 8, 851-6.

BUCKWALTER, J. A. 1995. Aging and degeneration of the human intervertebral disc. *Spine (Phila Pa 1976),* 20, 1307-14.

BURSTEIN, D., GRAY, M. L., HARTMAN, A. L., GIPE, R. & FOY, B. D. 1993. DIFFUSION OF SMALL SOLUTES IN CARTILAGE AS MEASURED BY NUCLEAR-MAGNETIC-RESONANCE (NMR) SPECTROSCOPY AND IMAGING. *Journal of Orthopaedic Research,* 11, 465-478.

BUSCHMANN, M. D. & GRODZINSKY, A. J. 1995. A MOLECULAR-MODEL OF PROTEOGLYCAN-ASSOCIATED ELECTROSTATIC FORCES IN CARTILAGE MECHANICS. *Journal of Biomechanical Engineering-Transactions of the Asme,* 117, 179-192.

CAO, L., GUILAK, F. & SETTON, L. A. 2011. Three-dimensional finite element modeling of pericellular matrix and cell mechanics in the nucleus pulposus of the intervertebral disk based on in situ morphology. *Biomechanics and Modeling in Mechanobiology,* 10, 1-10.

CARNEY, S. L. & MUIR, H. 1988. THE STRUCTURE AND FUNCTION OF CARTILAGE PROTEOGLYCANS. *Physiological Reviews,* 68, 858-910.

CHEGINI, S. & FERGUSON, S. J. 2010. Time and depth dependent Poisson's ratio of cartilage explained by an inhomogeneous orthotropic fiber embedded biphasic model. *J Biomech,* 43, 1660-6.

CHELBERG, M. K., BANKS, G. M., GEIGER, D. F. & OEGEMA, T. R. 1995. IDENTIFICATION OF HETEROGENEOUS CELL-POPULATIONS IN NORMAL HUMAN INTERVERTEBRAL DISC. *Journal of Anatomy,* 186, 43-53.

CHEN, A. C., BAE, W. C., SCHINAGL, R. M. & SAH, R. L. 2001. Depth- and strain-dependent mechanical and electromechanical properties of full-thickness bovine articular cartilage in confined compression. *J Biomech,* 34, 1-12.

CHEN, A. C., NGUYEN, T. T. & SAH, R. L. 1997. Streaming potentials during the confined compression creep test of normal and proteoglycan-depleted cartilage. *Annals of Biomedical Engineering,* 25, 269-277.

CHEUNG, K. M. C., KARPPINEN, J., CHAN, D., HO, D. W. H., SONG, Y. Q., SHAM, P., CHEAH, K. S. E., LEONG, J. C. Y. & LUK, K. D. K. 2009. Prevalence and Pattern of Lumbar Magnetic Resonance Imaging Changes in a Population Study of One Thousand Forty-Three Individuals. *Spine,* 34, 934-940.

CHOW, D. H. K., LI, M. F., LAI, A. & POPE, M. H. 2011. Effect of load carriage on spinal compression. *International Journal of Industrial Ergonomics,* 41, 219-223.

CLOYD, J. M., MALHOTRA, N. R., WENG, L., CHEN, W., MAUCK, R. L. & ELLIOTT, D. M. 2007. Material properties in unconfined compression of human nucleus pulposus, injectable hyaluronic acid-based hydrogels and tissue engineering scaffolds. *Eur Spine J,* 16, 1892-8.

COHEN, B., LAI, W. M. & MOW, V. C. 1998. A transversely isotropic biphasic model for unconfined compression of growth plate and chondroepiphysis. *J Biomech Eng,* 120, 491-6.

COSTI, J. J., STOKES, I. A., GARDNER-MORSE, M., LAIBLE, J. P., SCOFFONE, H. M. & IATRIDIS, J. C. 2007. Direct measurement of intervertebral disc maximum shear strain in six degrees of freedom: Motions that place disc tissue at risk of injury. *Journal of Biomechanics,* 40, 2457-2466.

DAGENAIS, S., CARO, J. J. & HALDEMAN, S. 2008. A systematic review of low back pain cost of illness studies in the United States and internationally. *Value in Health,* 11, A160-A161.

DE SCHEPPER, E. I. T., DAMEN, J., VAN MEURS, J. B. J., GINAI, A. Z., POPHAM, M., HOFMAN, A., KOES, B. W. & BIERMA-ZEINSTRA, S. M. 2010. The Association Between Lumbar Disc Degeneration and Low Back Pain The Influence of Age, Gender, and Individual Radiographic Features. *Spine,* 35, 531-536.

DEMERS, C. N., ANTONIOU, J. & MWALE, F. 2004. Value and limitations of using the bovine tail as a model for the human lumbar spine. *Spine,* 29, 2793-2799.

DIAMOND, J. M. & HARRISON, S. C. 1966. EFFECT OF MEMBRANE FIXED CHARGES ON DIFFUSION POTENTIALS AND STREAMING POTENTIALS. *Journal of Physiology-London,* 183, 37-&.

DISILVESTRO, M. R. & SUH, J. K. 2002. Biphasic poroviscoelastic characteristics of proteoglycan-depleted articular cartilage: simulation of degeneration. *Ann Biomed Eng,* 30, 792-800.

DISILVESTRO, M. R. & SUH, J. K. F. 2001. A cross-validation of the biphasic poroviscoelastic model of articular cartilage in unconfined compression, indentation, and confined compression. *Journal of Biomechanics,* 34, 519-525.

DISILVESTRO, M. R., ZHU, Q. & SUH, J. K. 2001a. Biphasic poroviscoelastic simulation of the unconfined compression of articular cartilage: II--Effect of variable strain rates. *J Biomech Eng,* 123, 198-200.

DISILVESTRO, M. R., ZHU, Q., WONG, M., JURVELIN, J. S. & SUH, J. K. 2001b. Biphasic poroviscoelastic simulation of the unconfined compression of articular cartilage: I--Simultaneous prediction of reaction force and lateral displacement. *J Biomech Eng,* 123, 191-7.

DONNAN, F. G. 1924. The theory of membrane equilibria. *Chemical Reviews,* 1, 73-90.

DROST, M. R., WILLEMS, P., SNIJDERS, H., HUYGHE, J. M., JANSSEN, J. D. & HUSON, A. 1995. Confined compression of canine annulus fibrosus under chemical and mechanical loading. *J Biomech Eng,* 117, 390-6.

EBARA, S., IATRIDIS, J. C., SETTON, L. A., FOSTER, R. J., MOW, V. C. & WEIDENBAUM, M. 1996. Tensile properties of nondegenerate human lumbar anulus fibrosus. *Spine (Phila Pa 1976),* 21, 452-61.

EHLERS, W., KARAJAN, N. & MARKERT, B. 2009. An extended biphasic model for charged hydrated tissues with application to the intervertebral disc. *Biomechanics and Modeling in Mechanobiology,* 8, 233-251.

EYRE, D. R. 1980. COLLAGEN - MOLECULAR DIVERSITY IN THE BODYS PROTEIN SCAFFOLD. *Science,* 207, 1315-1322.

EYRE, D. R. & MUIR, H. 1976. Types I and II collagens in intervertebral disc. Interchanging radial distributions in annulus fibrosus. *Biochem J,* 157, 267-70.

FARRELL, M. D. & RICHES, P. E. 2012. THE POISSON'S RATIO OF THE NUCLEUS PULPOSUS IS STRAIN DEPENDENT. *Journal of Biomechanics,* 45, Supplement 1, S566.

FERGUSON, S. J., ITO, K. & NOLTE, L. P. 2004. Fluid flow and convective transport of solutes within the intervertebral disc. *J Biomech,* 37, 213-21.

FRANK, E. H., GRODZINSKY, A. J., KOOB, T. J. & EYRE, D. R. 1987. Streaming potentials: a sensitive index of enzymatic degradation in articular cartilage. *J Orthop Res,* 5, 497-508.

FRASER, R. D., OSTI, O. L. & VERNON-ROBERTS, B. 1993. Intervertebral disc degeneration. *Eur Spine J,* 1, 205-13.

FREBURGER, J. K., HOLMES, G. M., AGANS, R. P., JACKMAN, A. M., DARTER, J. D., WALLACE, A. S., CASTEL, L. D., KALSBEEK, W. D. & CAREY, T. S. 2009. The Rising Prevalence of Chronic Low Back Pain. *Archives of Internal Medicine,* 169, 251-258.

FREEMONT, A. J., PEACOCK, T. E., GOUPILLE, P., HOYLAND, J. A., OBRIEN, J. & JAYSON, M. I. V. 1997. Nerve ingrowth into diseased intervertebral disc in chronic back pain. *Lancet,* 350, 178-181.

FRIJNS, A. J. H., HUYGHE, J. M. & JANSSEN, J. D. 1997. A validation of the quadriphasic mixture theory for intervertebral disc tissue. *International Journal of Engineering Science,* 35, 1419-1429.

FRIJNS, A. J. H., HUYGHE, J. M., KAASSCHIETER, E. F. & WIJLAARS, M. W. 2003. Numerical simulation of deformations and electrical potentials in a cartilage substitute. *Biorheology,* 40, 123-131.

GALBUSERA, F., SCHMIDT, H., NOAILLY, J., MALANDRINO, A., LACROIX, D., WILKE, H. J. & SHIRAZI-ADL, A. 2011. Comparison of four methods to simulate swelling in poroelastic finite element models of intervertebral discs. *Journal of the Mechanical Behavior of Biomedical Materials,* 4, 1234-1241.

GARCIA, A. M., FRANK, E. H., GRIMSHAW, P. E. & GRODZINSKY, A. J. 1996. Contributions of fluid convection and electrical migration to transport in cartilage: Relevance to loading. *Archives of Biochemistry and Biophysics,* 333, 317-325.

GARCIA, A. M., LARK, M. W., TRIPPEL, S. B. & GRODZINSKY, A. J. 1998. Transport of tissue inhibitor of metalloproteinases-1 through cartilage: Contributions of fluid flow and electrical migration. *Journal of Orthopaedic Research,* 16, 734-742.

GOEL, V. K., KONG, W., HAN, J. S., WEINSTEIN, J. N. & GILBERTSON, L. G. 1993. A combined finite element and optimization investigation of lumbar spine mechanics with and without muscles. *Spine (Phila Pa 1976),* 18, 1531-41.

GROEN, G. J., BALJET, B. & DRUKKER, J. 1990. Nerves and nerve plexuses of the human vertebral column. *Am J Anat,* 188, 282-96.

GRUBER, H. E. & HANLEY, E. N. 1998. Analysis of aging and degeneration of the human intervertebral disc - Comparison of surgical specimens with normal controls. *Spine,* 23, 751-757.

GU, W. Y., LAI, W. M. & MOW, V. C. 1993. TRANSPORT OF FLUID AND IONS THROUGH A POROUS-PERMEABLE CHARGED-HYDRATED TISSUE, AND STREAMING POTENTIAL DATA ON NORMAL BOVINE ARTICULAR-CARTILAGE. *Journal of Biomechanics,* 26, 709-723.

GU, W. Y., LAI, W. M. & MOW, V. C. 1998. A mixture theory for charged-hydrated soft tissues containing multi-electrolytes: Passive transport and swelling behaviors. *Journal of Biomechanical Engineering-Transactions of the Asme,* 120, 169-180.

GU, W. Y., LAI, W. M. & MOW, V. C. 1999a. Transport of multi-electrolytes in charged hydrated biological soft tissues. *Transport in Porous Media,* 34, 143-157.

GU, W. Y., MAO, X. G., FOSTER, R. J., WEIDENBAUM, M., MOW, V. C. & RAWLINS, B. A. 1999b. The anisotropic hydraulic permeability of human lumbar anulus fibrosus. Influence of age, degeneration, direction, and water content. *Spine (Phila Pa 1976),* 24, 2449-55.

GU, W. Y., MAO, X. G., RAWLINS, B. A., IATRIDIS, J. C., FOSTER, R. J., SUN, D. N., WEIDENBAUM, M. & MOW, V. C. 1999c. Streaming potential of human lumbar anulus fibrosus is anisotropic and affected by disc degeneration. *Journal of Biomechanics,* 32, 1177-1182.

HAUT, R. C. & LITTLE, R. W. 1972. CONSTITUTIVE EQUATION FOR COLLAGEN FIBERS. *Journal of Biomechanics,* 5, 423-&.

HAYNES, W. M. 2010. *Handbook of Chemistry and Physics*, CRC Press.

HEIKKILA, J. K., KOSKENVUO, M., HELIOVAARA, M., KURPPA, K., RIIHIMAKI, H., HEIKKILA, K., RITA, H. & VIDEMAN, T. 1989. GENETIC AND ENVIRONMENTAL-FACTORS IN SCIATICA - EVIDENCE FROM A NATIONWIDE PANEL OF 9365 ADULT TWIN PAIRS. *Annals of Medicine,* 21, 393-398.

HENEGHAN, P. & RICHES, P. 2008a. Determination of the strain-dependent hydraulic permeability of the compressed bovine nucleus pulposus. *Journal of Biomechanics,* 41, 903-906.

HENEGHAN, P. & RICHES, P. 2008b. The strain-dependent osmotic pressure and stiffness of the bovine nucleus pulposus apportioned into ionic and non-ionic contributors. *Journal of biomechanics,* 41, 2411-2416.

HEUER, F., SCHMIDT, H. & WILKE, H. J. 2008. Stepwise reduction of functional spinal structures increase disc bulge and surface strains. *J Biomech,* 41, 1953-60.

HICKEY, D. S. & HUKINS, D. W. L. 1980. RELATION BETWEEN THE STRUCTURE OF THE ANNULUS FIBROSUS AND THE FUNCTION AND FAILURE OF THE INTERVERTEBRAL-DISK. *Spine,* 5, 106-116.

HOLM, S., MAROUDAS, A., URBAN, J. P., SELSTAM, G. & NACHEMSON, A. 1981. Nutrition of the intervertebral disc: solute transport and metabolism. *Connect Tissue Res,* 8, 101-19.

HOLMES, M. H. 1986. Finite deformation of soft tissue: analysis of a mixture model in uni-axial compression. *J Biomech Eng,* 108, 372-81.

HOLMES, M. H. & MOW, V. C. 1990. The nonlinear characteristics of soft gels and hydrated connective tissues in ultrafiltration. *J Biomech,* 23, 1145-56.

HORNER, H. A., ROBERTS, S., BIELBY, R. C., MENAGE, J., EVANS, H. & URBAN, J. P. 2002. Cells from different regions of the intervertebral disc: effect of culture system on matrix expression and cell phenotype. *Spine (Phila Pa 1976),* 27, 1018-28.

HORNER, H. A. & URBAN, J. P. G. 2001. 2001 Volvo Award winner in basic science studies: Effect of nutrient supply on the viability of cells from the nucleus pulposus of the intervertebral disc. *Spine,* 26, 2543-2549.

HOUBEN, G. B., DROST, M. R., HUYGHE, J. M., JANSSEN, J. D. & HUSON, A. 1997. Nonhomogeneous permeability of canine anulus fibrosus. *Spine (Phila Pa 1976),* 22, 7-16.

HUANG, C. Y., MOW, V. C. & ATESHIAN, G. A. 2001. The role of flow-independent viscoelasticity in the biphasic tensile and compressive responses of articular cartilage. *Journal of Biomechanical Engineering-Transactions of the Asme,* 123, 410-417.

HUANG, C. Y., SOLTZ, M. A., KOPACZ, M., MOW, V. C. & ATESHIAN, G. A. 2003. Experimental verification of the roles of intrinsic matrix viscoelasticity and tension-compression nonlinearity in the biphasic response of cartilage. *J Biomech Eng,* 125, 84-93.

HUYGHE, J. M. & JANSSEN, J. D. 1997. Quadriphasic mechanics of swelling incompressible porous media. *International Journal of Engineering Science,* 35, 793-802.

IATRIDIS, J. C., LAIBLE, J. P. & KRAG, M. H. 2003. Influence of fixed charge density magnitude and distribution on the intervertebral disc: applications of a poroelastic and chemical electric (PEACE) model. *J Biomech Eng,* 125, 12-24.

IATRIDIS, J. C., MACLEAN, J. J., O'BRIEN, M. & STOKES, I. A. 2007. Measurements of proteoglycan and water content distribution in human lumbar intervertebral discs. *Spine (Phila Pa 1976),* 32, 1493-7.

IATRIDIS, J. C., SETTON, L. A., FOSTER, R. J., RAWLINS, B. A., WEIDENBAUM, M. & MOW, V. C. 1998. Degeneration affects the anisotropic and nonlinear behaviors of human anulus fibrosus in compression. *J Biomech,* 31, 535-44.

IATRIDIS, J. C., SETTON, L. A., WEIDENBAUM, M. & MOW, V. C. 1997a. Alterations in the mechanical behavior of the human lumbar nucleus pulposus with degeneration and aging. *J Orthop Res,* 15, 318-22.

IATRIDIS, J. C., SETTON, L. A., WEIDENBAUM, M. & MOW, V. C. 1997b. The viscoelastic behavior of the non-degenerate human lumbar nucleus pulposus in shear. *J Biomech,* 30, 1005-13.

INOUE, H. 1981. Three-dimensional architecture of lumbar intervertebral discs. *Spine (Phila Pa 1976),* 6, 139-46.

INOUE, H. & TAKEDA, T. 1975. 3-DIMENSIONAL OBSERVATION OF COLLAGEN FRAMEWORK OF LUMBAR INTERVERTEBRAL DISKS. *Acta Orthopaedica Scandinavica,* 46, 949-956.

ISHIHARA, H., MCNALLY, D. S., URBAN, J. P. & HALL, A. C. 1996. Effects of hydrostatic pressure on matrix synthesis in different regions of the intervertebral disk. *J Appl Physiol,* 80, 839-46.

ISHIHARA, H., WARENSJO, K., ROBERTS, S. & URBAN, J. P. 1997. Proteoglycan synthesis in the intervertebral disk nucleus: the role of extracellular osmolality. *Am J Physiol,* 272, C1499-506.

JACKSON, A. R., YUAN, T. Y., HUANG, C. Y. & GU, W. Y. 2009. A Conductivity Approach to Measuring Fixed Charge Density in Intervertebral Disc Tissue. *Ann Biomed Eng*.

JENSEN, M. C., BRANTZAWADZKI, M. N., OBUCHOWSKI, N., MODIC, M. T., MALKASIAN, D. & ROSS, J. S. 1994. MAGNETIC-RESONANCE-IMAGING OF THE LUMBAR SPINE IN PEOPLE WITHOUT BACK PAIN. *New England Journal of Medicine,* 331, 69-73.

JOHANNESSEN, W. & ELLIOTT, D. M. 2005. Effects of degeneration on the biphasic material properties of human nucleus pulposus in confined compression. *Spine (Phila Pa 1976),* 30, E724-9.

JURVELIN, J. S., BUSCHMANN, M. D. & HUNZIKER, E. B. 1997. Optical and mechanical determination of Poisson's ratio of adult bovine humeral articular cartilage. *J Biomech,* 30, 235-41.

KELLGREN, J. H., BIER, F. & LAWRENCE, J. S. 1963. GENETIC FACTORS IN GENERALIZED OSTEO-ARTHROSIS. *Annals of the Rheumatic Diseases,* 22, 237-&.

KHALSA, P. S. & EISENBERG, S. R. 1997. Compressive behavior of articular cartilage is not completely explained by proteoglycan osmotic pressure. *J Biomech,* 30, 589-94.

KIM, Y. J., BONASSAR, L. J. & GRODZINSKY, A. J. 1995. THE ROLE OF CARTILAGE STREAMING POTENTIAL, FLUID-FLOW AND PRESSURE IN THE STIMULATION OF CHONDROCYTE BIOSYNTHESIS DURING DYNAMIC COMPRESSION. *Journal of Biomechanics,* 28, 1055-1066.

KIM, Y. J., SAH, R. L. Y., GRODZINSKY, A. J., PLAAS, A. H. K. & SANDY, J. D. 1994. MECHANICAL REGULATION OF CARTILAGE BIOSYNTHETIC BEHAVIOR - PHYSICAL STIMULI. *Archives of Biochemistry and Biophysics,* 311, 1-12.

KIVIRANTA, P., RIEPPO, J., KORHONEN, R. K., JULKUNEN, P., TOYRAS, J. & JURVELIN, J. S. 2006. Collagen network primarily controls Poisson's ratio of bovine articular cartilage in compression. *J Orthop Res,* 24, 690-9.

KORHONEN, R. K., LAASANEN, M. S., TOYRAS, J., RIEPPO, J., HIRVONEN, J., HELMINEN, H. J. & JURVELIN, J. S. 2002. Comparison of the equilibrium response of articular cartilage in unconfined compression, confined compression and indentation. *J Biomech,* 35, 903-9.

KULAK, R. F., BELYTSCHKO, T. B., SCHULTZ, A. B. & GALANTE, J. O. 1976. NONLINEAR BEHAVIOR OF HUMAN INTERVERTEBRAL-DISK UNDER AXIAL LOAD. *Journal of Biomechanics,* 9, 377-386.

KUSLICH, S. D., ULSTROM, C. L. & MICHAEL, C. J. 1991. THE TISSUE ORIGIN OF LOW-BACK-PAIN AND SCIATICA - A REPORT OF PAIN RESPONSE TO TISSUE STIMULATION DURING OPERATIONS ON THE LUMBAR SPINE USING LOCAL-ANESTHESIA. *Orthopedic Clinics of North America,* 22, 181-187.

KWAN, M. K., LAI, W. M. & MOW, V. C. 1990. A finite deformation theory for cartilage and other soft hydrated connective tissues--I. Equilibrium results. *J Biomech,* 23, 145-55.

LAI, W. M., HOU, J. S. & MOW, V. C. 1991. A triphasic theory for the swelling and deformation behaviors of articular cartilage. *J Biomech Eng,* 113, 245-58.

LAI, W. M., MOW, V. C., SUN, D. D. & ATESHIAN, G. A. 2000. On the electric potentials inside a charged soft hydrated biological tissue: Streaming potential versus diffusion potential. *Journal of Biomechanical Engineering-Transactions of the Asme,* 122, 336-346.

LAIBLE, J. P., PFLASTER, D. S., KRAG, M. H., SIMON, B. R. & HAUGH, L. D. 1993. A poroelastic-swelling finite element model with application to the intervertebral disc. *Spine (Phila Pa 1976),* 18, 659-70.

LEDDY, H. A. & GUILAK, F. 2003. Site-specific molecular diffusion in articular cartilage measured using fluorescence recovery after photobleaching. *Annals of Biomedical Engineering,* 31, 753-760.

LEE, C. K., KIM, Y. E., LEE, C. S., HONG, Y. M., JUNG, J. M. & GOEL, V. K. 2000. Impact response of the intervertebral disc in a finite-element model. *Spine (Phila Pa 1976),* 25, 2431-9.

LI, L. P., BUSCHMAN, M. D. & SHIRAZI-ADL, A. 2003. Strain-rate dependent stiffness of articular cartilage in unconfined compression (vol 125, pg 161, 2003). *Journal of Biomechanical Engineering-Transactions of the Asme,* 125, 566-566.

LI, L. P. & HERZOG, W. 2004a. The role of viscoelasticity of collagen fibers in articular cartilage: theory and numerical formulation. *Biorheology,* 41, 181-94.

LI, L. P. & HERZOG, W. 2004b. Strain-rate dependence of cartilage stiffness in unconfined compression: the role of fibril reinforcement versus tissue volume change in fluid pressurization. *Journal of Biomechanics,* 37, 375-382.

LI, L. P., SOULHAT, J., BUSCHMANN, M. D. & SHIRAZI-ADL, A. 1999. Nonlinear analysis of cartilage in unconfined ramp compression using a fibril reinforced poroelastic model. *Clinical Biomechanics,* 14, 673-682.

LOVE AE 1944. A treatise on the mathematical theory of elasticity, Dover Publications, New York

LU, Y. M., HUTTON, W. C. & GHARPURAY, V. M. 1998. The effect of fluid loss on the viscoelastic behavior of the lumbar intervertebral disc in compression. *J Biomech Eng,* 120, 48-54.

LUOMA, K., RIIHIMAKI, H., LUUKKONEN, R., RAININKO, R., VIIKARI-JUNTURA, E. & LAMMINEN, A. 2000. Low back pain in relation to lumbar disc degeneration. *Spine,* 25, 487-492.

MAAS, S. A., ELLIS, B. J., ATESHIAN, G. A. & WEISS, J. A. 2012. FEBio: Finite Elements for Biomechanics. *Journal of Biomechanical Engineering-Transactions of the Asme,* 134.

MACGREGOR, A. J., ANDREW, T., SAMBROOK, P. N. & SPECTOR, T. D. 2004. Structural, psychological, and genetic influences on low back and neck pain: A study of adult female twins. *Arthritis & Rheumatism-Arthritis Care & Research,* 51, 160-167.

MAGNIER, C., BOIRON, O., WENDLING-MANSUY, S., CHABRAND, P. & DEPLANO, V. 2009. Nutrient distribution and metabolism in the intervertebral disc in the unloaded state: a parametric study. *J Biomech,* 42, 100-8.

MAK, A. F. 1986a. THE APPARENT VISCOELASTIC BEHAVIOR OF ARTICULAR-CARTILAGE - THE CONTRIBUTIONS FROM THE INTRINSIC MATRIX VISCOELASTICITY AND INTERSTITIAL FLUID-FLOWS. *Journal of Biomechanical Engineering-Transactions of the Asme,* 108, 123-130.

MAK, A. F. 1986b. UNCONFINED COMPRESSION OF HYDRATED VISCOELASTIC TISSUES - A BIPHASIC POROVISCOELASTIC ANALYSIS. *Biorheology,* 23, 371-383.

MANIADAKIS, N. & GRAY, A. 2000. The economic burden of back pain in the UK. *Pain,* 84, 95-103.

MANSOUR, J. M. & MOW, V. C. 1976. The permeability of articular cartilage under compressive strain and at high pressures. *J Bone Joint Surg Am,* 58, 509-16.

MAROUDAS, A. 1975. BIOPHYSICAL CHEMISTRY OF CARTILAGINOUS TISSUES WITH SPECIAL REFERENCE TO SOLUTE AND FLUID TRANSPORT. *Biorheology,* 12, 233-248.

MAROUDAS, A. & BANNON, C. 1981. Measurement of swelling pressure in cartilage and comparison with the osmotic pressure of constituent proteoglycans. *Biorheology,* 18, 619-32.

MAROUDAS, A., BULLOUGH, P., SWANSON, S. A. & FREEMAN, M. A. 1968. The permeability of articular cartilage. *J Bone Joint Surg Br,* 50, 166-77.

MAROUDAS, A., STOCKWELL, R. A., NACHEMSON, A. & URBAN, J. 1975. Factors involved in the nutrition of the human lumbar intervertebral disc: cellularity and diffusion of glucose in vitro. *J Anat,* 120, 113-30.

MASSEY, C. J., VAN DONKELAAR, C. C., VRESILOVIC, E., ZAVALIANGOS, A. & MARCOLONGO, M. 2012. Effects of aging and degeneration on the human intervertebral disc during the diurnal cycle: A finite element study. *Journal of Orthopaedic Research,* 30, 122-128.

MATSUI, H., KANAMORI, M., ISHIHARA, H., YUDOH, K., NARUSE, Y. & TSUJI, H. 1998. Familial predisposition for lumbar degenerative disc disease - A case-control study. *Spine,* 23, 1029-1034.

MAUCK, R. L., HUNG, C. T. & ATESHIAN, G. A. 2003. Modeling of neutral solute transport in a dynamically loaded porous permeable gel: Implications for articular cartilage biosynthesis and tissue engineering. *Journal of Biomechanical Engineering-Transactions of the Asme,* 125, 602-614.

MCMILLAN, D. W., GARBUTT, G. & ADAMS, M. A. 1996. Effect of sustained loading on the water content of intervertebral discs: implications for disc metabolism. *Ann Rheum Dis,* 55, 880-7.

MCNALLY, D. S. & ADAMS, M. A. 1992. INTERNAL INTERVERTEBRAL-DISK MECHANICS AS REVEALED BY STRESS PROFILOMETRY. *Spine,* 17, 66-73.

MCNALLY, D. S., ADAMS, M. A. & GOODSHIP, A. E. 1993. CAN INTERVERTEBRAL DISC PROLAPSE BE PREDICTED BY DISC MECHANICS. *Spine,* 18, 1525-1530.

MEAKIN, J. R. & HUKINS, D. W. L. 2001. Replacing the nucleus pulposus of the intervertebral disk: prediction of suitable properties of a replacement material using finite element analysis. *Journal of Materials Science-Materials in Medicine,* 12, 207-213.

MELROSE, J., ROBERTS, S., SMITH, S., MENAGE, J. & GHOSH, P. 2002. Increased nerve and blood vessel ingrowth associated with proteoglycan depletion in an ovine anular lesion model of experimental disc degeneration. *Spine,* 27, 1278-1285.

MIKAWA, Y., HAMAGAMI, H., SHIKATA, J. & YAMAMURO, T. 1986. ELASTIN IN THE HUMAN INTERVERTEBRAL-DISK - A HISTOLOGICAL AND BIOCHEMICAL-STUDY COMPARING IT WITH ELASTIN IN THE

HUMAN YELLOW LIGAMENT. *Archives of Orthopaedic and Trauma Surgery,* 105, 343-349.

MOORE, R. J., VERNONROBERTS, B., FRASER, R. D. & SCHEMBRI, M. 1996. The origin and fate of herniated lumbar intervertebral disc tissue. *Spine,* 21, 2149-2155.

MOW, V. C., KUEI, S. C., LAI, W. M. & ARMSTRONG, C. G. 1980. Biphasic creep and stress relaxation of articular cartilage in compression? Theory and experiments. *J Biomech Eng,* 102, 73-84.

MOW, V. C. & SCHOONBECK, J. M. 1984. CONTRIBUTION OF DONNAN OSMOTIC PRESSURE TOWARDS THE BIPHASIC COMPRESSIVE MODULUS OF ARTICULAR CARTILAGE. *Orthopaedic Transactions,* 8, 312.

MOW, V. C., ZHU, W. & RATCLIFFE, A. 1991. *STRUCTURE AND FUNCTION OF ARTICULAR CARTILAGE AND MENISCUS.*

MUIR, H. 1983. Proteoglycans as organizers of the intercellular matrix. *Biochem Soc Trans,* 11, 613-22.

MUKHERJEE, N. & WAYNE, J. S. 1998. Load sharing between solid and fluid phases in articular cartilage: I - Experimental determination of in situ mechanical conditions in a porcine knee. *Journal of Biomechanical Engineering-Transactions of the Asme,* 120, 614-619.

NACHEMSON, A. 1960. Lumbar intradiscal pressure. Experimental studies on post-mortem material. *Acta orthopaedica Scandinavica. Supplementum,* 43, 1-104.

NACHEMSON, A. & ELFSTROM, G. 1970. Intravital dynamic pressure measurements in lumbar discs. A study of common movements, maneuvers and exercises. *Scandinavian journal of rehabilitation medicine. Supplement,* 1, 1-40.

NACHEMSON, A., LEWIN, T., MAROUDAS, A. & FREEMAN, M. A. 1970. In vitro diffusion of dye through the end-plates and the annulus fibrosus of human lumbar inter-vertebral discs. *Acta Orthop Scand,* 41, 589-607.

NATARAJAN, R. N., KE, J. H. & ANDERSSON, G. B. 1994. A model to study the disc degeneration process. *Spine (Phila Pa 1976),* 19, 259-65.

NERLICH, A. G., SCHLEICHER, E. D. & BOOS, N. 1997. 1997 Volvo Award winner in basic science studies - Immunohistologic markers for age-related changes of human lumbar intervertebral discs. *Spine,* 22, 2781-2795.

NORDIN, M. & FRANKEL, V. H. 2001. *Basic Biomechanics of the Musculoskeletal System,* Baltimore, Lippincott Williams & Wilkins.

O'CONNELL, G. D., JOHANNESSEN, W., VRESILOVIC, E. J. & ELLIOTT, D. M. 2007a. Human internal disc strains in axial compression measured noninvasively using magnetic resonance imaging. *Spine (Phila Pa 1976),* 32, 2860-8.

O'CONNELL, G. D., JOHANNESSEN, W., VRESILOVIC, E. J. & ELLIOTT, D. M. 2007b. Human internal disc strains in axial compression measured noninvasively using magnetic resonance imaging. *Spine,* 32, 2860-2868.

O'CONNELL, G. D., VRESILOVIC, E. J. & ELLIOTT, D. M. 2011. Human Intervertebral Disc Internal Strain in Compression: The Effect of Disc Region, Loading Position, and Degeneration. *Journal of Orthopaedic Research,* 29, 547-555.

O'HARA, B. P., URBAN, J. P. & MAROUDAS, A. 1990. Influence of cyclic loading on the nutrition of articular cartilage. *Ann Rheum Dis,* 49, 536-9.

OGATA, K. & WHITESIDE, L. A. 1981. NUTRITIONAL PATHWAYS OF THE INTERVERTEBRAL-DISK - AN EXPERIMENTAL-STUDY USING HYDROGEN WASHOUT TECHNIQUE. *Spine,* 6, 211-216.

OLOYEDE, A., BROOM, N. D. & MARTINEZ, J. B. 1998. Experimental factors governing the internal stress state of the intervertebral disc. *Medical Engineering & Physics,* 20, 631-637.

OSHIMA, H., ISHIHARA, H., URBAN, J. P. & TSUJI, H. 1993. The use of coccygeal discs to study intervertebral disc metabolism. *J Orthop Res,* 11, 332-8.

OSTI, O. L., VERNONROBERTS, B. & FRASER, R. D. 1990. ANULUS TEARS AND INTERVERTEBRAL-DISK DEGENERATION - AN EXPERIMENTAL-STUDY USING AN ANIMAL-MODEL. *Spine,* 15, 762-767.

PERIE, D., IATRIDIS, J. C., DEMERS, C. N., GOSWAMI, T., BEAUDOIN, G., MWALE, F. & ANTONIOU, J. 2006a. Assessment of compressive modulus, hydraulic permeability and matrix content of trypsin-treated nucleus pulposus using quantitative MRI. *J Biomech,* 39, 1392-400.

PERIE, D., KORDA, D. & IATRIDIS, J. C. 2005. Confined compression experiments on bovine nucleus pulposus and annulus fibrosus: sensitivity of the experiment in the determination of compressive modulus and hydraulic permeability. *J Biomech,* 38, 2164-71.

PERIE, D. S., MACLEAN, J. J., OWEN, J. P. & IATRIDIS, J. C. 2006b. Correlating material properties with tissue composition in enzymatically digested bovine annulus fibrosus and nucleus pulposus tissue. *Ann Biomed Eng,* 34, 769-77.

POIRAUDEAU, S., MONTEIRO, I., ANRACT, P., BLANCHARD, O., REVEL, M. & CORVOL, M. T. 1999. Phenotypic characteristics of rabbit intervertebral disc cells - Comparison with cartilage cells from the same animals. *Spine,* 24, 837-844.

POLLOCK, R., HENEGHAN, P. & RICHES, P. E. 2008. Under-arm partial body weight unloading causes spinal elongation and vibration attenuation during treadmill walking. *Gait & Posture,* 28, 271-277.

PRESCHER, A. 1998. Anatomy and pathology of the aging spine. *European Journal of Radiology,* 27, 181-195.

QUINN, T. M., KOCIAN, P. & MEISTER, J. J. 2000. Static compression is associated with decreased diffusivity of dextrans in cartilage explants. *Archives of Biochemistry and Biophysics,* 384, 327-334.

RAJ, P. P. 2008. Intervertebral disc: anatomy-physiology-pathophysiology-treatment. *Pain Pract,* 8, 18-44.

RAJINI, K. H., USHA, R., ARUMUGAM, V. & SANJEEVI, R. 2001. Fracture behaviour of cross-linked collagen fibres. *Journal of Materials Science,* 36, 5589-5592.

RAZAQ, S., URBAN, J. P. G. & WILKINS, R. J. 2000. Regulation of intracellular pH by bovine intervertebral disc cells. *Cellular Physiology and Biochemistry,* 10, 109-115.

RECUERDA, M., COTE, S.-P., VILLEMURE, I. & PREIE, D. 2011. Influence of experimental protocols on the mechanical properties of the intervertebral disc in unconfined compression. *Journal of biomechanical engineering,* 133, 071006.

REYNAUD, B. & QUINN, T. M. 2006. Anisotropic hydraulic permeability in compressed articular cartilage. *Journal of Biomechanics,* 39, 131-137.

RICHES, P. E. 2012. Sensitivity analysis of permeability parameters of bovine nucleus pulposus obtained through inverse fitting of the nonlinear biphasic equation: effect of sampling strategy. *Computer Methods in Biomechanics and Biomedical Engineering,* 15, 29-36.

RICHES, P. E., DHILLON, N., LOTZ, J., WOODS, A. W. & MCNALLY, D. S. 2002. The internal mechanics of the intervertebral disc under cyclic loading. *Journal of Biomechanics,* 35, 1263-1271.

RICHES, P. E. & MCNALLY, D. S. 2005. A one-dimensional theoretical prediction of the effect of reduced end-plate permeability on the mechanics of the intervertebral disc. *Proc Inst Mech Eng H,* 219, 329-35.

ROBERTS, S., MENAGE, J., DUANCE, V., WOTTON, S. & AYAD, S. 1991. 1991 Volvo Award in basic sciences. Collagen types around the cells of the intervertebral disc and cartilage end plate: an immunolocalization study. *Spine (Phila Pa 1976),* 16, 1030-8.

ROBERTS, S., MENAGE, J. & URBAN, J. P. 1989. Biochemical and structural properties of the cartilage end-plate and its relation to the intervertebral disc. *Spine (Phila Pa 1976),* 14, 166-74.

ROBERTS, S., URBAN, J. P., EVANS, H. & EISENSTEIN, S. M. 1996. Transport properties of the human cartilage endplate in relation to its composition and calcification. *Spine (Phila Pa 1976),* 21, 415-20.

RODRIGUEZ, A. G., SLICHTER, C. K., ACOSTA, F. L., RODRIGUEZ-SOTO, A. E., BURGHARDT, A. J., MAJUMDAR, S. & LOTZ, J. C. 2011. Human Disc Nucleus Properties and Vertebral Endplate Permeability. *Spine,* 36, 512-520.

ROHLMANN, A., ZANDER, T., SCHMIDT, H., WILKE, H. J. & BERGMANN, G. 2006. Analysis of the influence of disc degeneration on the mechanical behaviour of a lumbar motion segment using the finite element method. *Journal of Biomechanics,* 39, 2484-2490.

ROTH, V. & MOW, V. C. 1980. THE INTRINSIC TENSILE BEHAVIOR OF THE MATRIX OF BOVINE ARTICULAR-CARTILAGE AND ITS VARIATION WITH AGE. *Journal of Bone and Joint Surgery-American Volume,* 62, 1102-1117.

SAMBROOK, P. N., MACGREGOR, A. J. & SPECTOR, T. D. 1999. Genetic influences on cervical and lumbar disc degeneration - A magnetic resonance imaging study in twins. *Arthritis and Rheumatism,* 42, 366-372.

SANJEEVI, R. 1982. A VISCOELASTIC MODEL FOR THE MECHANICAL-PROPERTIES OF BIOLOGICAL-MATERIALS. *Journal of Biomechanics,* 15, 107-109.

SATO, K., KIKUCHI, S. & YONEZAWA, T. 1999. In vivo intradiscal pressure measurement in healthy individuals and in patients with ongoing back problems. *Spine,* 24, 2468-2474.

SCHMIDT, H., SHIRAZI-ADL, A., GALBUSERA, F. & WILKE, H. J. 2010. Response analysis of the lumbar spine during regular daily activities--a finite element analysis. *J Biomech,* 43, 1849-56.

SCHWARZER, A. C., APRILL, C. N. & BOGDUK, N. 1995. The sacroiliac joint in chronic low back pain. *Spine (Phila Pa 1976),* 20, 31-7.

SCHWARZER, A. C., APRILL, C. N., DERBY, R., FORTIN, J., KINE, G. & BOGDUK, N. 1994. The relative contributions of the disc and zygapophyseal joint in chronic low back pain. *Spine (Phila Pa 1976),* 19, 801-6.

SCOTT, J. E., BOSWORTH, T. R., CRIBB, A. M. & TAYLOR, J. R. 1994. The chemical morphology of age-related changes in human intervertebral disc glycosaminoglycans from cervical, thoracic and lumbar nucleus pulposus and annulus fibrosus. *J Anat,* 184 (Pt 1), 73-82.

SEROUSSI, R. E., KRAG, M. H., MULLER, D. L. & POPE, M. H. 1989. INTERNAL DEFORMATIONS OF INTACT AND DENUCLEATED HUMAN LUMBAR DISKS SUBJECTED TO COMPRESSION, FLEXION, AND EXTENSION LOADS. *Journal of Orthopaedic Research,* 7, 122-131.

SETTON, L. A. & CHEN, J. Year. Mechanobiology of the intervertebral disc and relevance to disc degeneration. *In:* Research Sympopsium on Intervertebral Disc Degeneration, Sep 15-18 2005 Chicago, IL. NEEDHAM: Journal Bone Joint Surgery Inc, 52-57.

SETTON, L. A., ZHU, W. & MOW, V. C. 1993. The biphasic poroviscoelastic behavior of articular cartilage: role of the surface zone in governing the compressive behavior. *J Biomech,* 26, 581-92.

SHEN, Z. L. L., KAHN, H., BALLARIN, R. & EPPELL, S. J. 2011. Viscoelastic Properties of Isolated Collagen Fibrils. *Biophysical Journal,* 100, 3008-3015.

SHIRAZIADL, S. A., SHRIVASTAVA, S. C. & AHMED, A. M. 1984. STRESS-ANALYSIS OF THE LUMBAR-DISK BODY UNIT IN COMPRESSION - A 3-DIMENSIONAL NONLINEAR FINITE-ELEMENT STUDY. *Spine,* 9, 120-134.

SILVER, F. H., EBRAHIMI, A. & SNOWHILL, P. B. 2002. Viscoelastic properties of self-assembled type I collagen fibers: Molecular basis of elastic and viscous behaviors. *Connective Tissue Research,* 43, 569-580.

SIVE, J. I., BAIRD, P., JEZIORSK, M., WATKINS, A., HOYLAND, J. A. & FREEMONT, A. J. 2002. Expression of chondrocyte markers by cells of normal and degenerate intervertebral discs. *Molecular Pathology,* 55, 91-97.

SOLTZ, M. A. & ATESHIAN, G. A. 1998. Experimental verification and theoretical prediction of cartilage interstitial fluid pressurization at an impermeable contact interface in confined compression. *Journal of Biomechanics,* 31, 927-934.

SOLTZ, M. A. & ATESHIAN, G. A. 2000. A Conewise Linear Elasticity mixture model for the analysis of tension-compression nonlinearity in articular cartilage. *J Biomech Eng,* 122, 576-86.

SOULHAT, J., BUSCHMANN, M. D. & SHIRAZI-ADL, A. 1999. A fibril-network-reinforced biphasic model of cartilage in unconfined compression. *Journal of Biomechanical Engineering-Transactions of the Asme,* 121, 340-347.

SPILKER, R. L., SUH, J. K. & MOW, V. C. 1990. EFFECTS OF FRICTION ON THE UNCONFINED COMPRESSIVE RESPONSE OF ARTICULAR-CARTILAGE - A FINITE-ELEMENT ANALYSIS. *Journal of Biomechanical Engineering-Transactions of the Asme,* 112, 138-146.

STAIRMAND, J. W., HOLM, S. & URBAN, J. P. 1991. Factors influencing oxygen concentration gradients in the intervertebral disc. A theoretical analysis. *Spine (Phila Pa 1976),* 16, 444-9.

STOCKWELL, R. A. 1979. *BIOLOGICAL STRUCTURE AND FUNCTION VOL. 7 BIOLOGY OF CARTILAGE CELLS*.

STOKES, I. A., LAIBLE, J. P., GARDNER-MORSE, M. G., COSTI, J. J. & IATRIDIS, J. C. 2010. Refinement of Elastic, Poroelastic, and Osmotic Tissue Properties of Intervertebral Disks to Analyze Behavior in Compression. *Ann Biomed Eng*.

SUH, J. K. & DISILVESTRO, M. R. 1999. Biphasic poroviscoelastic behavior of hydrated biological soft tissue. *Journal of Applied Mechanics-Transactions of the Asme,* 66, 528-535.

SUN, D. D., GUO, X. E., LIKHITPANICHKUL, M., LAI, W. M. & MOW, V. C. 2004. The influence of the fixed negative charges on mechanical and electrical

behaviors of articular cartilage under unconfined compression. *J Biomech Eng,* 126, 6-16.

SUN, D. N., GU, W. Y., GUO, X. E., LAI, W. M. & MOW, V. C. 1999. A mixed finite element formulation of triphasic mechano-electrochemical theory for charged, hydrated biological soft tissues. *International Journal for Numerical Methods in Engineering,* 45, 1375-1402.

SZIRMAI, J. 1970. *Structure of the intervertebral disc. In Chemistry and Molecular Biology of the Intercellular Matrix,* New York, Academic Press.

TAYLOR, Z. A. & MILLER, K. 2006. Constitutive modeling of cartilaginous tissues: a review. *J Appl Biomech,* 22, 212-29.

TOMLINSON, N. & MAROUDAS, A. 1980. THE EFFECT OF CYCLIC AND CONTINUOUS COMPRESSION ON THE PENETRATION OF LARGE MOLECULES INTO ARTICULAR-CARTILAGE. *Journal of Bone and Joint Surgery-British Volume,* 62, 251-251.

TORZILLI, P. A., ADAMS, T. C. & MIS, R. J. 1987. TRANSIENT SOLUTE DIFFUSION IN ARTICULAR-CARTILAGE. *Journal of Biomechanics,* 20, 203-214.

TSANTRIZOS, A., ITO, K., AEBI, M. & STEFFEN, T. 2005. Internal strains in healthy and degenerated lumbar intervertebral discs. *Spine,* 30, 2129-2137.

TYRRELL, A. R., REILLY, T. & TROUP, J. D. G. 1985. CIRCADIAN VARIATION IN STATURE AND THE EFFECTS OF SPINAL LOADING. *Spine,* 10, 161-164.

URBAN, J. P., HOLM, S. & MAROUDAS, A. 1978. Diffusion of small solutes into the intervertebral disc: as in vivo study. *Biorheology,* 15, 203-21.

URBAN, J. P., HOLM, S., MAROUDAS, A. & NACHEMSON, A. 1982. Nutrition of the intervertebral disc: effect of fluid flow on solute transport. *Clin Orthop Relat Res*, 296-302.

URBAN, J. P. & MAROUDAS, A. 1981. Swelling of the intervertebral disc in vitro. *Connect Tissue Res,* 9, 1-10.

URBAN, J. P., MAROUDAS, A., BAYLISS, M. T. & DILLON, J. 1979. Swelling pressures of proteoglycans at the concentrations found in cartilaginous tissues. *Biorheology,* 16, 447-64.

URBAN, J. P. & ROBERTS, S. 2003. Degeneration of the intervertebral disc. *Arthritis Res Ther,* 5, 120-30.

URBAN, J. P., SMITH, S. & FAIRBANK, J. C. 2004. Nutrition of the intervertebral disc. *Spine (Phila Pa 1976),* 29, 2700-9.

URBAN, J. P. G. 2002. The role of the physicochemical environment in determining disc cell behaviour. *Biochemical Society Transactions,* 30, 858-864.

URBAN, J. P. G., HOLM, S., MAROUDAS, A. & NACHEMSON, A. 1977. NUTRITION OF INTERVERTEBRAL-DISK - INVIVO STUDY OF SOLUTE TRANSPORT. *Clinical Orthopaedics and Related Research*, 101-114.

URBAN, J. P. G. & MCMULLIN, J. F. 1988. SWELLING PRESSURE OF THE LUMBAR INTERVERTEBRAL DISKS - INFLUENCE OF AGE, SPINAL LEVEL, COMPOSITION, AND DEGENERATION. *Spine,* 13, 179-187.

URBAN, J. P. G., ROBERTS, S. & RALPHS, J. R. 2000. The nucleus of the intervertebral disc from development to degeneration. *American Zoologist,* 40, 53-61.

VAN LOON, R., HUYGHE, J. M., WIJLAARS, M. W. & BAAIJENS, F. P. T. 2003. 3D FE implementation of an incompressible quadriphasic mixture model. *International Journal for Numerical Methods in Engineering,* 57, 1243-1258.

VARLOTTA, G. P., BROWN, M. D., KELSEY, J. L. & GOLDEN, A. L. 1991. FAMILIAL PREDISPOSITION FOR HERNIATION OF A LUMBAR-DISK IN PATIENTS WHO ARE LESS THAN 21 YEARS OLD. *Journal of Bone and Joint Surgery-American Volume,* 73A, 124-128.

VIDEMAN, T., BATTIE, M. C., GIBBONS, L. E., MARAVILLA, K., MANNINEN, H. & KAPRIO, J. 2003. Associations between back pain history and lumbar MRI findings. *Spine (Phila Pa 1976),* 28, 582-8.

VIGNOLLET, J., PEARCE, C. & RICHES, P. 2010. Biphasic swelling model for the nucleus pulposus of the intervertebral disc. *In: 9th International Symposium of Computer Methods in Biomechanics and Biomedical Engineering (CMBBE2010).* Valencia, Spain.

WANG, C. C., CHAHINE, N. O., HUNG, C. T. & ATESHIAN, G. A. 2003. Optical determination of anisotropic material properties of bovine articular cartilage in compression. *J Biomech,* 36, 339-53.

WANG, J. L., PARNIANPOUR, M., SHIRAZI-ADL, A., ENGIN, A. E., LI, S. & PATWARDHAN, A. 1997. Development and validation of a viscoelastic finite element model of an L2/L3 motion segment. *Theoretical and Applied Fracture Mechanics,* 28, 81-93.

WANG, Z. L., TEO, J. C. M., CHUI, C. K., ONG, S. H., YAN, C. H., WANG, S. C., WONG, H. K. & TEOH, S. H. 2005. Computational biomechanical modelling of the lumbar spine using marching-cubes surface smoothened finite element voxel meshing. *Computer Methods and Programs in Biomedicine,* 80, 25-35.

WILKE, H. J., NEEF, P., CAIMI, M., HOOGLAND, T. & CLAES, L. E. 1999. New in vivo measurements of pressures in the intervertebral disc in daily life. *Spine,* 24, 755-762.

WONG, M., PONTICIELLO, M., KOVANEN, V. & JURVELIN, J. S. 2000. Volumetric changes of articular cartilage during stress relaxation in unconfined compression. *J Biomech,* 33, 1049-54.

WU, J. Z., DONG, R. G. & SCHOPPER, A. W. 2004. Analysis of effects of friction on the deformation behavior of soft tissues in unconfined compression tests. *J Biomech,* 37, 147-55.

YANG, Z. C., SMOLINSKI, P., LIN, J. S. & GILBERTSON, L. G. 2011. DYNAMICAL FINITE ELEMENT MODELING OF SOFT TISSUES AS CHEMOELECTRIC POROUS MEDIA. *Journal of Mechanics in Medicine and Biology,* 11, 101-130.

YAO, H. & GU, W. Y. 2007a. Three-dimensional inhomogeneous triphasic finite-element analysis of physical signals and solute transport in human intervertebral disc under axial compression. *Journal of Biomechanics,* 40, 2071-2077.

YAO, H. & GU, W. Y. 2007b. Three-dimensional inhomogeneous triphasic finite-element analysis of physical signals and solute transport in human intervertebral disc under axial compression. *J Biomech,* 40, 2071-7.

YU, J., WINLOVE, P. C., ROBERTS, S. & URBAN, J. P. 2002. Elastic fibre organization in the intervertebral discs of the bovine tail. *J Anat,* 201, 465-75.

9. Appendices

9.1. Custom built tissue sectioning device

To cut parallel sections from tissue plugs for the experiments conducted in chapters 3, 5 and 7, a custom designed cutting tool was manufactured. The gold standard for this procedure is the use of a cryostat which maintains the sample in a frozen state during sectioning. However, this device was not readily available within the department for the majority of the research period thus an alternative was required. It was essential to keep the sample frozen throughout cutting to allow an accurate slice to be sectioned thus the tool was stored within at -20°C prior to use. The tool resembles a guillotine form and was manufactured from stainless steel (Figure 9.1). It allowed circular plugs to be held stationary within a guide whilst a blade performed an accurate section to the desired sample thickness. A 0.23mm thick blade was used within the vertical guides to allow an accurate cut. The guide end-plate was adjustable thus allowing for varying sample thicknesses.
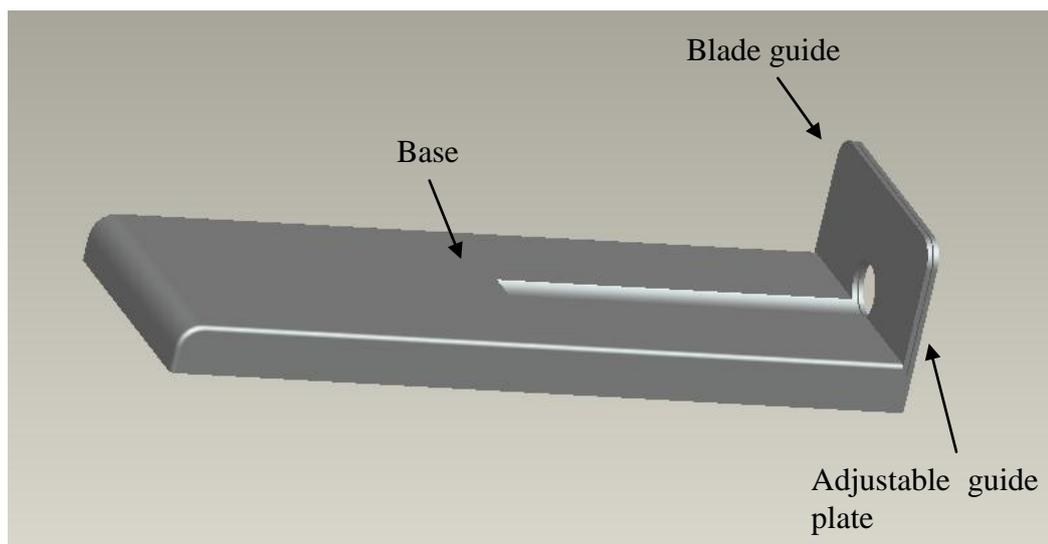

Figure 9.1 Custom built tissue sectioning device.

9.2. Correlation between permeability and run order

To establish whether PG leaching occurred during the direct permeation experiment conducted in chapter 3, permeability was analysed with respect to the running order of each pressure condition. If leaching occurred, one would expect to witness a reduction in permeability with running order. However, there was no significant trend when analysed (Figure 9.2), leading to the conclusion that there was negligible leaching.
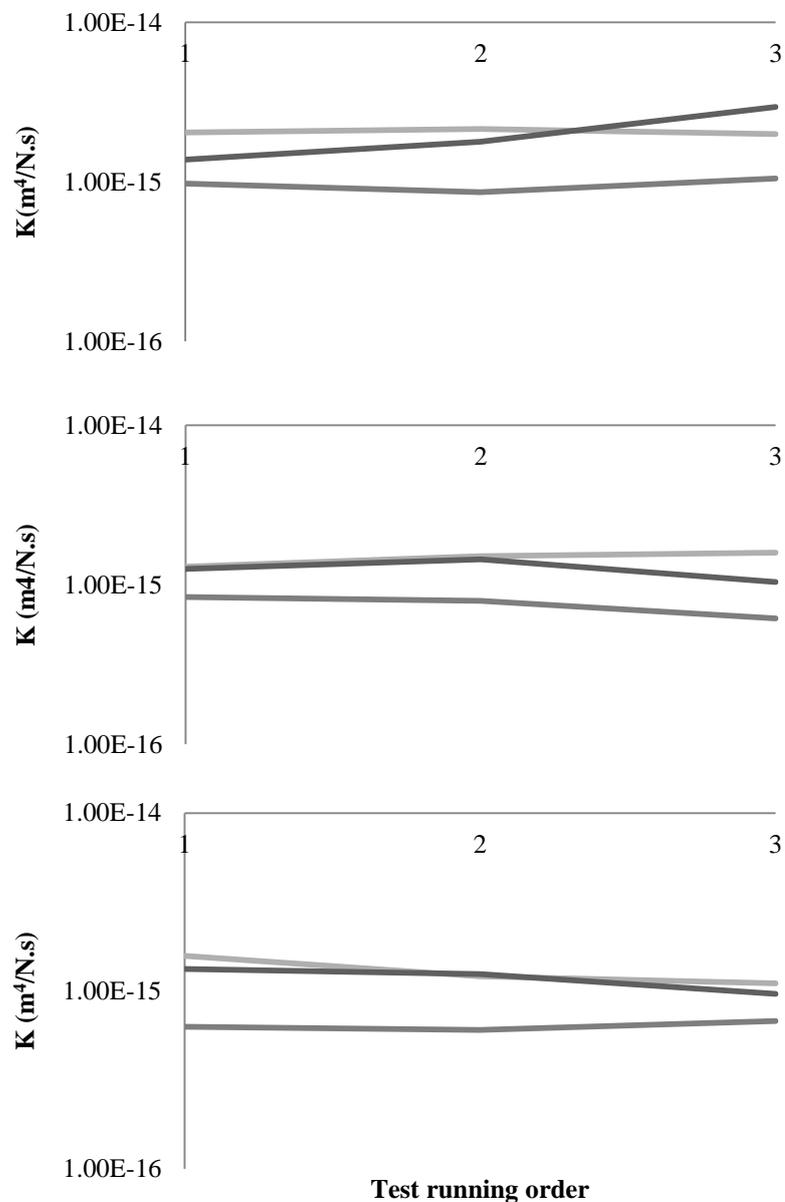

Figure 9.2 Permeability with respect to test running order. A) 30kPa B) 45kPa C) 60kPa

9.3. Derivation of circumferential strain from marker displacements

In cylindrical coordinates, displacements in the radial, circumferential and axial directions may be given by u_r, u_θ and u_z respectively. In this coordinate system, the strains are given by Love AE (1944):

$$\varepsilon_{rr} = \frac{\partial u_r}{\partial r} \qquad \varepsilon_{\theta\theta} = \frac{1}{r}\frac{\partial u_\theta}{\partial r} + \frac{u_r}{r} \qquad \varepsilon_{zz} = \frac{\partial u_z}{\partial z}$$

$$\varepsilon_{\theta z} = \frac{1}{r}\frac{\partial u_z}{\partial \theta} + \frac{\partial u_\theta}{\partial z} \qquad \varepsilon_{zr} = \frac{\partial u_r}{\partial z} + \frac{\partial u_z}{\partial r} \qquad \varepsilon_{r\theta} = \frac{\partial u_\theta}{\partial r} - \frac{u_\theta}{r} + \frac{1}{r}\frac{\partial u_r}{\partial \theta}$$

Assuming displacements are symmetrical about the cylindrical axis, we have $u_\theta = 0$ and $\frac{\partial u_r}{\partial \theta} = \frac{\partial u_z}{\partial \theta} = 0$. Accordingly, the above equations reduce to (Love AE, 1944):

$$\varepsilon_{rr} = \frac{\partial u_r}{\partial r} \qquad \varepsilon_{\theta\theta} = \frac{u_r}{r} \qquad \varepsilon_{zz} = \frac{\partial u_z}{\partial z}$$

$$\varepsilon_{\theta z} = 0 \qquad \varepsilon_{zr} = \frac{\partial u_r}{\partial z} + \frac{\partial u_z}{\partial r} \qquad \varepsilon_{r\theta} = 0$$

The circumferential strain, $\varepsilon_{\theta\theta}$, is equal to the ratio of the radial displacement and original radius. This is exactly the measure as determined by the experimental protocol stated in chapter 5.

Therefore the biphasic and matrix Poisson's ratios determined by the experiment are based on the ratio of two orthogonal strains: circumferential and axial. However, by assuming isotropy of the solid phase, we can assume that: $v = v_{r\theta} = v_{\theta z} = v_{rz}$.

Consequently, for an isotropic material, experimental radial displacement gradients are unnecessary to determine the Poisson's ratio through compression.
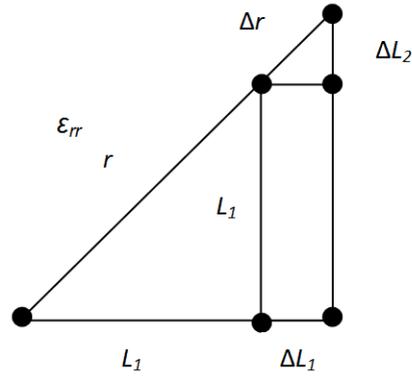

Figure 9.3 Determination of circumferential strain from marker displacements.

$$\varepsilon_{\theta\theta} = \frac{\Delta_r}{r}$$

$$\varepsilon_{\theta\theta}^2 = \frac{\Delta l_1^2 + \Delta l_2^2}{l_1^2 + l_2^2}$$

$$\varepsilon_1 = \frac{\Delta l_1}{l_1}$$

$$\varepsilon_{\theta\theta}^2 = \frac{\varepsilon_1^2 l_1^2 + \varepsilon_2^2 l_2^2}{l_1^2 + l_2^2}$$

$$\varepsilon_2 = \frac{\Delta l_2}{l_2}$$

$$\varepsilon_{\theta\theta}^2 = \frac{\varepsilon_1^2 l_1^2 + \varepsilon_2^2 l_2^2}{2l^2}$$

$$\Delta r^2 = \Delta l_1^2 + \Delta l_2^2$$

$$\varepsilon_{\theta\theta}^2 = \frac{l^2(\varepsilon_1^2 + \varepsilon_2^2)}{2l^2}$$

$$r^2 = l_1^2 + l_2^2$$

$$\Delta l_1^2 = \varepsilon_1^2 l_1^2$$

$$\boldsymbol{\varepsilon_{\theta\theta}} = \sqrt{\frac{(\boldsymbol{\varepsilon_1^2 + \varepsilon_2^2})}{\boldsymbol{2}}}$$

$$\Delta l_2^2 = \varepsilon_2^2 l_2^2$$

Originally square, therefore: $l_1 = l_2 = l$